U.PORTO

DOUTORAMENTO
QUÍMICA ANALÍTICA

Sustainable and task-specific (nano)GUMBOS for chemical and biological analysis

Ana Marta Azevedo

D
2023

U.PORTO
FACULDADE DE FARMÁCIA
UNIVERSIDADE DO PORTO

Sustainable and task-specific (nano)GUMBOS for chemical and biological analysis

Tese do 3º Ciclo de Estudos Conducente ao Grau de Doutoramento em Ciências Farmacêuticas na especialidade de Química Analítica

Trabalho realizado sob a orientação da Professora Doutora Maria Lúcia Marques Ferreira de Sousa Saraiva e coorientação do Professor Doutor João Luís Machado dos Santos

Ana Marta de Oliveira Azevedo

Julho 2023

Ana Marta de Oliveira Azevedo

A todos aqueles que caminharam ao meu lado,
que me deram a mão quando tropecei,
que acreditaram no meu potencial e
que me permitiram chegar aqui.

“Deus quer, o homem sonha, a obra nasce.”

Fernando Pessoa

“Be a bush if you can’t be a tree.
If you can’t be a highway, just be a trail.
If you can’t be a sun, be a star.
For it isn’t by size that you win or fall.
Be the best of whatever you’re.”

Martin Luther King Jr.

Acknowledgments

Ao chegar ao final do percurso, que foi mais longo e acidentado do que o inicialmente previsto, gostaria de agradecer a todos aqueles que, de alguma forma, contribuíram para a concretização deste projeto.

À Faculdade de Farmácia da Universidade do Porto (FFUP) por me ter acolhido como estudante de doutoramento e ter proporcionado as condições necessárias para a realização do trabalho proposto.

À Fundação para a Ciência e Tecnologia (FCT) e ao Fundo Social Europeu (FSE), através do Programa Operacional Regional do Norte, pela concessão da bolsa de doutoramento com a referência SFRH/BD/118566/2016. Agradeço ainda pela atribuição da bolsa para mitigação do impacto da COVID-19 (COVID/BD/151753/2021) e pelo financiamento concedido para realização de atividades de investigação nos Estados Unidos.

À minha orientadora, Professora Doutora Maria Lúcia Saraiva, por, desde cedo, ter acreditado no meu potencial e investido nele. Sou grata por me ter ajudado a encontrar a confiança necessária para enfrentar os desafios que iam surgindo e por nunca ter desistido de mim. O meu sincero agradecimento pelo inestimável apoio, pelas palavras de incentivo e pelos preciosos conselhos.

Ao Professor Doutor João Santos por ter aceitado a coorientação deste trabalho, pela disponibilidade e pelas sugestões.

To Professor Isiah Warner for receiving me in his research group at Louisiana State University (LSU) and allowing me to learn more about GUMBOS chemistry. Thank you for all of your guidance and encouragement.

À Doutora Clara Sousa pela colaboração na análise quimiométrica dos dados experimentais e pela disponibilidade para esclarecer todas as minhas dúvidas. Agradeço também por todas as sugestões e palavras de motivação.

À Doutora Catarina Seabra pelo contributo na parte experimental, pela partilha de conhecimentos e pela constante disponibilidade.

À Doutora Cláudia Nunes e à Doutora Tânia Moniz pelo apoio, pela alegria contagiante e pela troca de ideias.

À Professora Doutora Maria João Sousa pela amabilidade com que me recebeu no Departamento de Biologia da Universidade do Minho e pelos conhecimentos transmitidos.

Ao Professor Doutor Rui Lapa pela simpatia, pelo bom humor e pela ajuda sempre que necessária.

À Professora Doutora Salette Reis, à Professora Doutora Marcela Segundo e ao Professor Doutor João Prior pelo carinho, pelos conselhos e pelas palavras de encorajamento. Um

agradecimento de igual modo especial aos restantes Professores do Laboratório de Química Aplicada da FFUP pela cordialidade e pelo apoio.
A todos os membros do meu grupo de investigação pela ajuda e pela partilha de saberes. Agradeço também aos colegas dos outros laboratórios pela simpatia, prestabilidade e flexibilidade no uso dos equipamentos.
À Sara Marques e à Joana Magalhães por me acolherem tão calorosamente, por serem boas ouvintes e conselheiras, e por sempre torcerem por mim.
À Doutora Edite Cunha, à Ana Rita Pinto, à Andreia Granja, ao João Albuquerque e ao Sarmento Mazivila pelo carinho, pelo incentivo e pela força.
À Ana Filipa Neves e ao André Vilaranda pela vontade de aprender e ajudar, pela alegria contagiante e pela boa-disposição.
À Eng.ª Manuela Barros e à Vânia Dias pelo apoio administrativo e técnico.
À Assistente Técnica Cristina Costa, do Departamento de Ciências Biológicas da FFUP, pela simpatia, disponibilidade e ajuda na preparação dos meios de cultura.
À Técnica Superior Andrea Gouveia pela simpatia, recetividade e auxílio na resolução de todas as questões burocráticas.
To the Warner research group, especially to Mi Chen, Dr. Caitlan Ayala, and Dr. Rocío Pérez for making me feel welcome and providing a nourishing environment to learn more about GUMBOS and nanoGUMBOS. Thank you also for all the help, guidance, and support, even after I returned to Portugal.
To Unique Luna and Kelsey Hines for their friendship and support. Thank you for all the rides to St. Francis Xavier Church and the special memories we shared.
À Professora Doutora Graça Vicente pela empatia, pelo incentivo e pela enorme generosidade. Agradeço-lhe também pela disponibilidade que sempre demonstrou e por ter cuidado de mim enquanto estive em Baton Rouge.
Às minhas amigas, Filipa Abreu e Diana Dias, por estarem sempre presentes, prontas para me ouvir e acolher. À Helena Oliveira pelo carinho e por me ter surpreendido com a sua calorosa visita ao Luisiana.
Aos meus pais pelo apoio incondicional e pelos sacrifícios que fizeram para me poder proporcionar melhores condições de vida e um futuro risonho.
À minha irmã por ter estado sempre do meu lado, por me ter motivado e inspirado.
Aos meus tios, Gil, Gaspar, Cesário e Florinda, pelo exemplo de força e determinação, pelo incentivo e pelo carinho.
To Chideha for his endless support and encouragement. Thank you for inspiring me to be the best version of myself.
Ao Gabriel por tudo aquilo que me ensinou em tão pouco tempo.

Em suma, uma palavra de agradecimento a todos aqueles que me acompanharam ao longo desta jornada e a tornaram mais prazerosa.

Abstract

GUMBOS (*g*roup of *u*niform *m*aterials *b*ased on *o*rganic *s*alts) are considered promising candidates for chemical and biological analyses due to their facile synthesis and high tunability. Additionally, GUMBOS can be easily converted into nanomaterials (e.g., nanoGUMBOS), that can exhibit a variety of properties different from their bulk counterparts.

In the first study of this dissertation, erythrosin B (EB) was converted into GUMBOS via simple ion metathesis reactions using several phosphonium and ammonium cations. The ability of EB-based GUMBOS to discriminate individual and binary mixtures of proteins was examined. Moreover, the effect of various values of pH (3.0, 4.5, and 6.0) and reaction times (5, 10, and 15 min) on their discriminatory power was also evaluated. Ultraviolet-visible (UV-Vis) spectra resulting from interactions between GUMBOS and proteins were analyzed using partial least squares discriminant analysis (PLSDA). Correct protein assignments ranged from 86.5% to 100.0%, with the best results achieved using tetrabutylphosphonium- and tetrabutylammonium-erythosin B GUMBOS (i.e, $[P_{4444}]_2[EB]$ and $[N_{4444}]_2[EB]$) at pH 6.0. Under these conditions, it was also possible to discriminate between mixtures of albumin (Alb) and myoglobin (Mb) at different ratios.

Despite the successful use of EB-based GUMBOS to discriminate proteins at 20 μg mL^{-1}, a range of detection limits is necessary to determine the full potential of these GUMBOS for qualitative and quantitative analyses. In this regard, UV-Vis spectra of $[P_{4444}]_2[EB]$ and $[N_{4444}]_2[EB]$ in the presence of Alb, Mb, ribonuclease A (RNAse A), lysozyme (Lyz), and α-chymotrypsin (α-ChT) at concentrations ranging from 0.05 to 20 μg mL^{-1} were analyzed using PLSDA and partial least squares (PLS). The highest percentages of correct protein assignments were obtained using $[N_{4444}]_2[EB]$ for concentrations greater than 0.50 μg mL^{-1} and GUMBOS were most successful for identification of Mb among all proteins studied. It was also found that both GUMBOS can successfully estimate concentrations of Alb, Mb, Lyz, and α-ChT in the range of 0.50–20 μg mL^{-1}.

In a subsequent study, $[P_{4444}]_2[EB]$ GUMBOS was converted into nanoGUMBOS using an ultrasound-assisted reprecipitation method, and evaluated for ability to discriminate and quantify protein analytes. Sonication time (30 s, 5 min, and 15 min) and cyclodextrin templating (α-, 2-HP-β-, and γ-CD) were investigated for impact on discrimination performance of synthesized nanomaterial. Alb, Lyz, hemoglobin (Hb), trypsin (Try), catalase (Cat), and cytochrome c (Cyt c) were selected as target proteins due to their distinct physicochemical properties and levels of abundance. It was possible to achieve 99.6% of correct protein assignments when sonication time was set to 5 min and no template was

used. Moreover, $[P_{4444}]_2$[EB] nanoGUMBOS was able to distinguish proteins at concentrations as low as 2.0 μg mL^{-1} and discriminate mixtures of different ratios of Lyz, Hb, and Cyt c. The PLS model developed for Alb was also determined to be suitable for quantification.

Protein binding to cell membranes plays an important role in several physiological and pathophysiological conditions. In this regard, ANS (8-anilino-1-naphthalenesulfonic acid) was modified to form GUMBOS with distinct cations, and the resulting GUMBOS were investigated as fluorescent probes for membrane binding studies with Lyz, Mb, α-ChT, and RNAse A. Changes in fluorescence intensity were used to monitor protein binding to liposomes of dimyristoyl-*sn*-glycero-phosphocholine (DMPC), which were chosen due to their ability to mimic membrane structure and composition. When compared to the parent ANS dye, $[N_{4444}]$[ANS] and $[P_{4444}]$[ANS] were determined to have improved optical properties and lipophilicity. Distinct fluorescence responses were observed upon addition of proteins to each probe, showing that surface hydrophobicity impacts the binding process. The relative maintenance of binding cooperativity and maximum fluorescence intensity further suggests that proteins compete with GUMBOS for membrane binding sites.

In an attempt to overcome clinical limitations of rose bengal (RB), three novel GUMBOS were strategically designed and synthesized from RB dye via ion metathesis reactions using select cationic antiseptics. RB-based GUMBOS were evaluated for their potential use as antibacterial agents and were investigated against a panel of clinically relevant Gram-positive and Gram-negative bacteria. GUMBOS were determined to have equal efficacy, and in some cases to be more effective than the parent RB dye and cationic antiseptics as well as their unreacted mixtures towards *Staphylococcus aureus* DSM 2569 and *Enterococcus faecalis*. Moreover, chlorhexidine RB ([CHX][RB]) was determined to be active against Gram-negative *Escherichia coli* and produced the lowest percentage of hemolysis (<5%) among all tested compounds and mixtures.

Finally, an automated yeast-based assay was developed to study toxic effects of GUMBOS and other groups of compounds. The assay was implemented using a sequential injection analysis system that relied on the ability of living *Saccharomyces cerevisiae* cells to enzymatically reduce methylene blue dye to a colorless product. Results confirmed the impact of structural elements on compounds' toxicity. Furthermore, the developed method showed satisfactory repeatability and reproducibility, involved consumption of only 40 μL of reagents, and produced less than 2 mL of effluents.

Keywords: Antibacterial activity; Chemometrics; (Nano)GUMBOS; Proteins; Toxicity.

Resumo

A simplicidade da síntese e adaptação das propriedades dos GUMBOS (grupo de materiais uniformes à base de sais orgânicos), tornam estes materiais atrativos para análises químicas e biológicas. Os GUMBOS podem ainda ser convertidos em nanomateriais (i.e., nanoGUMBOS) com a obtenção de propriedades distintas.

No primeiro estudo apresentado, a eritrosina B (EB) foi combinada com catiões fosfónio e amónio através de reações simples de metátese, avaliando-se a capacidade dos GUMBOS sintetizados para diferenciar entre várias proteínas e misturas de proteínas. Além disso, foi estudado o efeito de diferentes valores de pH (3,0; 4,5 e 6,0) e tempos de incubação (5, 10 e 15 min) no poder discriminatório dos GUMBOS. Os espetros de ultravioleta-visível (UV-Vis) resultantes da interação dos GUMBOS com as proteínas foram sujeitos à análise discriminante por regressão de mínimos quadrados parciais (PLSDA). As percentagens de previsão correta das proteínas variaram entre 86,5% e 100,0%, tendo sido obtidos os melhores resultados com o tetrabutilfosfónio- e o tetrabutilamónio-EB ($[P_{4444}]_2[EB]$ e $[N_{4444}]_2[EB]$) a pH 6,0. Foi, ainda, possível discriminar misturas de proteínas com diferentes proporções de albumina (Alb) e mioglobina (Mb).

Apesar dos GUMBOS derivados da EB terem sido capazes de discriminar as proteínas na concentração de 20 μg mL^{-1}, considerou-se importante testar uma ampla gama de concentrações para confirmar o seu potencial para análises qualitativas e quantitativas. Como tal, os espetros de UV-Vis do $[P_{4444}]_2[EB]$ e do $[N_{4444}]_2[EB]$ na presença de Alb, Mb, ribonuclease A (RNAse A), lisozima (Lyz) e α-quimotripsina (α-ChT), nas concentrações compreendidas entre 0,05 e 20 μg mL^{-1}, foram analisados usando a PLSDA e a regressão por mínimos quadrados parciais (PLS). As percentagens mais elevadas de discriminação correta foram obtidas usando o $[N_{4444}]_2[EB]$ para concentrações superiores a 0,50 μg mL^{-1}. Além disso, ambos os GUMBOS foram mais bem sucedidos na identificação da Mb e mostraram ser capazes de estimar as concentrações de Alb, Mb, Lyz e α-ChT no intervalo de 0,50 a 20 μg mL^{-1}.

No estudo subsequente, o $[P_{4444}]_2[EB]$ foi convertido em nanoGUMBOS usando o método de nanoprecipitação combinado com ultrasonicação, sendo avaliada a sua capacidade para discriminar e quantificar várias proteinas. O efeito do tempo de sonicação (30 s, 5 min e 15 min) e do uso de ciclodextrinas (α-, 2-HP-β- e γ-CD) na capacidade discriminatória do nanoGUMBOS foram, adicionalmente, investigados. A Alb, a Lyz, a hemoglobina (Hb), a tripsina (Try), a catalase (Cat) e o citocromo c (Cyt c) foram selecionadas como proteínas-modelo devido às suas propriedades e abundância distintas. Após 5 min de sonicação, e na ausência de CD, foi possível obter uma percentagem de discriminação correta de

proteínas de 99,6%. Verificou-se ainda que o nanoGUMBOS $[P_{4444}]_2$[EB] é capaz de distinguir proteínas em concentrações tão baixas quanto 2,0 μg mL^{-1}, bem como misturas de proteínas contendo diferentes proporções de Lyz, Hb e Cyt c. O modelo de PLS que mostrou ter uma melhor capacidade preditiva da concentração de proteína foi o modelo desenvolvido com a Alb.

A ligação das proteínas às membranas celulares desempenha um papel importante em inúmeros processos fisiológicos e patofisiológicos. Neste contexto, foram obtidos três GUMBOS por reação do ANS (ácido 8-anilino-1-naftalenosulfónico) com diferentes catiões, tendo sido avaliado o seu potencial como sondas fluorescentes, para o estudo das interações proteína-membrana. As variações na intensidade de fluorescência foram usadas para monitorizar a ligação das proteínas (Lyz, Mb, α-ChT e RNAse A) aos lipossomas de 1,2-dimiristoil-*sn*-glicero-fosfocolina (DMPC), os quais foram escolhidos de forma a mimetizar a estrutura e a composição das membranas lipídicas. Verificou-se uma melhoria das propriedades óticas e um aumento da lipofilia do $[N_{4444}]$[ANS] e $[P_{4444}]$[ANS] comparativamente ao ANS. Além disso, foram obtidas diferentes respostas após adição das proteínas a cada uma das sondas, como resultado provável de diferenças na sua hidrofobia da superfície. A relativa manutenção da cooperatividade e da intensidade de fluorescência máxima sugerem ainda que as proteínas e os GUMBOS competem pelos mesmos locais de ligação nas membranas.

Por forma a ultrapassar as limitações clínicas da rosa de bengala (RB), três novos GUMBOS foram sintetizados a partir deste corante e de antisséticos catiónicos selecionados. O seu potencial uso como agentes antibacterianos foi avaliado usando um painel de bactérias Gram-positivas e Gram-negativas clinicamente relevantes. Os GUMBOS mostraram ter igual eficácia e, em alguns casos maior eficácia, do que os precursores e as respetivas misturas contra a *Staphylococcus aureus* DSM 2569 e a *Enterococcus faecalis.* A clorohexidina RB ([CHX][RB]) provou, ainda, ser ativa contra a bactéria Gram-negativa *Escherichia coli* e ser hemocompatível (hemólise < 5%) comparativamente a todos os compostos e misturas em estudo.

Para estudar a toxicidade de GUMBOS e outros compostos foi implementando um método automático, em que se avalia a capacidade de células viáveis de *Saccharomyces cerevisiae* reduzirem o corante azul de metileno a um produto incolor. Este método apresentou repetibilidade e reprodutibilidade satisfatórias, com um consumo de 40 μL de reagentes e produção de cerca de 2 mL de efluentes. Os resultados confirmaram o impacto dos elementos estruturais na toxicidade dos compostos.

Palavras-chave: Atividade antibacteriana; (Nano)GUMBOS; Proteínas; Quimiometria; Toxicidade.

Table of contents

Acknowledgments ..... **v**
Abstract ..... **ix**
Resumo ..... **xi**
List of figures ..... **xviii**
List of tables ..... **xxiv**
List of abbreviations and acronyms ..... **xxviii**
Outline of the dissertation ..... **xxxii**

Chapter 1. Theoretical background **33**
Abstract 34
1.1. Introduction 35
1.2. Ionic liquids 37
1.2.1. Room temperature ionic liquids 37
1.2.2. Frozen ionic liquids 43
1.3. Group of uniform materials based on organic salts (GUMBOS) 45
1.4. Nanomaterials derived from GUMBOS 51
1.4.1. Synthesis of nanoGUMBOS 51
1.4.1.1. Melt-emulsion-quench approach 51
1.4.1.2. Reprecipitation method 52
1.4.1.3. Reverse micelle strategy 53
1.4.1.4. Aerosolization process 54
1.4.1.5. Hydrogel-assisted method 54
1.4.2. Properties and applications 55
1.5. Other examples of solid-phase ILs chemistry 63
1.6. Motivation and goals 63
References 65

Chapter 2. Protein discrimination using erythrosin B-based GUMBOS in combination with UV–Vis spectroscopy and chemometrics **77**
Abstract 78
2.1. Introduction 79
2.2. Material and methods 80
2.2.1. Reagents and solvents 80
2.2.2. Instrumentation 81

2.2.3. Synthesis and structural characterization of GUMBOS 81
2.2.4. Octanol/water partitioning 82
2.2.5. Protein discrimination using the synthesized GUMBOS 83
2.2.6. Data analysis 83
2.2.7. Rationale of the study 84
2.3. Results 84
2.3.1. Structural characterization of EB-based GUMBOS 84
2.3.2. UV-Vis properties of EB-derived GUMBOS 85
2.3.3. Melting point and hydrophobicity of the synthesized materials 85
2.3.4. Protein discrimination using the synthesized GUMBOS 86
2.3.4.1. $[P_{4444}]_2[EB]$ 87
2.3.4.2. $[P_{44416}]_2[EB]$ 89
2.3.4.3. $[N_{4444}]_2[EB]$ 91
2.3.4.4. $[BDHA]_2[EB]$ 93
2.3.5. Discrimination of binary mixtures containing Alb and Mb 94
2.4. Discussion 95
2.5. Conclusions 97
Supplementary Material 99
References 119

Chapter 3. **Exploring the potential of erythrosin B-based GUMBOS for qualitative and quantitative analyses of proteins** **125**
Abstract 126
3.1. Introduction 127
3.2. Material and methods 128
3.2.1. Reagents and solvents 128
3.2.2. Synthesis and characterization of GUMBOS 128
3.2.3. Spectra acquisition 129
3.2.4. Multivariate data analysis 129
3.3. Results and discussion 130
3.3.1. Discrimination of proteins at different concentrations 130
3.3.2. Quantitative analysis of proteins 134
3.4. Conclusions 136
Supplementary Material 137
References 139

Chapter 4. **Combined use of phosphonium-erythrosin B-based nanoGUMBOS, UV-Vis spectroscopy, and chemometrics for discrimination and quantification of proteins** **143**
Abstract 144
4.1. Introduction 145
4.2. Experimental 146
4.2.1. Reagents and solvents 146
4.2.2. Synthesis of nanoGUMBOS 146
4.2.3. Characterization of the synthesized nanoGUMBOS 147
4.2.4. Evaluation of storage stability 147
4.2.5. Discrimination and quantification of proteins using nanoGUMBOS 147
4.2.6. Data analysis 148
4.3. Results and discussion 149
4.3.1. Characterization of the synthesized nanoGUMBOS 149
4.3.2. Experimental optimization 150
4.3.2.1. Sonication time 150
4.3.2.2. CD templating 154
4.3.3. Discrimination of proteins and their concentrations 154
4.3.4. Discrimination of binary and ternary mixtures of Lyz, Cyt c, and Hb 156
4.3.5. Protein quantitative analysis 159
4.4. Conclusions 160
Supplementary Material 161
References 167

Chapter 5. **Studies of protein binding to biomimetic membranes using ANS-based GUMBOS** **171**
Abstract 172
5.1. Introduction 173
5.2. Material and methods 174
5.2.1. Reagents and solvents 174
5.2.2. Instrumentation 174
5.2.3. Synthesis and characterization of GUMBOS 175
5.2.4. GUMBOS partitioning 176
5.2.5. Preparation of DMPC liposomes 177
5.2.6. Protein-membrane binding studies 177
5.3. Results and discussion 178

5.3.1. Structural characterization of the synthesized GUMBOS.....178
5.3.2. Optical properties of ANS-based GUMBOS.....178
5.3.3. Lipophilicity of the synthesized materials.....179
5.3.4. Thermal stability and melting point of ANS-based GUMBOS.....180
5.3.5. Protein-membrane binding studies.....180
5.4. Conclusions.....182
Supplementary Material.....184
References.....201

Chapter 6. **A GUMBOS-based strategy for overcoming therapeutic limitations of rose bengal**.....**207**
Abstract.....208
6.1. Introduction.....209
6.2. Material and methods.....210
6.2.1. Chemicals and solvents.....210
6.2.2. Instrumentation.....210
6.2.3. Synthesis and characterization of GUMBOS.....211
6.2.4. Micellar/water partitioning.....213
6.2.5. Bacterial strains and growth conditions.....213
6.2.6. Antibacterial activities of synthesized GUMBOS.....214
6.2.7. Hemolysis assay.....214
6.3. Results and discussion.....215
6.3.1. Structural characterization and thermal stability of the synthesized GUMBOS.....215
6.3.2. UV-Vis spectral properties of RB-based GUMBOS.....216
6.3.3. Melting point and lipophilicity of the synthesized compounds.....216
6.3.4. Antibacterial activities of RB-based GUMBOS.....219
6.3.5. Hemocompatibility of the synthesized GUMBOS.....221
6.4. Conclusions.....223
Supplementary Material.....224
References.....229

Chapter 7. **Development of an automated yeast-based spectrophotometric method for toxicity screening: application to ionic liquids, GUMBOS, and deep eutectic solvents**.....**235**
Abstract.....236
7.1. Introduction.....237

7.2. Materials and methods 238
7.2.1. Reagents 238
7.2.2. Synthesis of GUMBOS and DESs 239
7.2.3. Yeast strain and culture conditions 239
7.2.4. Toxicity assessment 240
7.2.5. Flow apparatus 240
7.2.6. Sequential injection procedure 241
7.3. Results and discussion 242
7.3.1. Optimization of the automated yeast-based assay 242
7.3.2. Application of the automated spectrophotometric assay for toxicity evaluation of ILs, GUMBOS, and DESs 244
7.3.2.1. ILs 247
7.3.2.2. GUMBOS 248
7.3.2.3. DESs 248
7.4. Conclusions 249
Supplementary Material 250
References 252

Chapter 8. Concluding remarks and future perspectives 257
8.1. Concluding remarks 257
8.2. Future perspectives 259

List of figures

Chapter 1. Theoretical background

Fig. 1.1. Schematic representation of the change in ion packing from (a) NaCl to (b) [C_2im][Cl].....35

Fig. 1.2. pH dependent colorimetric response of $[P_{66614}]_2$[FL] nanodroplets in (a) water and buffers of pH (b) 7.4, (c) 5.4, (d) 4, and (e) 2.2. The color changes from red to orange, orange green, and light green as the pH decreases. Adapted with permission from (63). Copyright (2013) Royal Society of Chemistry.....43

Fig. 1.3. Melting range for RTILs, FILs, and GUMBOS.....46

Fig. 1.4. (a) Average signal intensity plotted against the logarithm of partition coefficient of AP-derived matrices ([AP][Asc], [AP][Cl], and [AP][NTf_2], from left to right). (b) MALDI-MS spectrum in the positive ion mode of equimolar mixture of hydrophilic (angiotensin II) and hydrophobic (valinomycin) peptides using [AP][Asc] matrix. Adapted with permission from Ref. (42). Copyright (2014) Wiley.....49

Fig. 1.5. (a) Fluorescence emission spectra of BG dye and BG-based nanoGUMBOS in water. (b) Second and (c) third harmonic generation spectra of BG dye, [BG][BETI] nanoGUMBOS, and gold nanospheres in water. Adapted with permission from Ref. (48). Copyright (2017) AIP Publishing.....56

Fig. 1.6. Normalized absorbance spectra and TEM micrographs of gold-shelled nanoGUMBOS built around (a) [C_3mim][NTf_2] and (b) [C_3mim][TPB] as core materials. Adapted with permission from Ref. (55). Copyright (2014) Royal Society of Chemistry....57

Fig. 1.7. (a) Relative tumor volume upon treatments with and without CD-based nanoGUMBOS/laser irradiation. (b) In vivo NIR fluorescent imaging of [IR780][TPB] nanoGUMBOS formed in the absence and presence of CD. Adapted with permission from Ref. (61). Copyright (2019) American Chemical Society.....58

Fig. 1.8. (a) Fluorescence emission spectra of HMT-based nanoGUMBOS: [HMT][TFPB] (red); [HMT][AOT] (blue); [HMT][NTf_2] (green); [HMT][BETI] (black); and [HMT][TFP4B] (grey). (b) Fluorescence intensity of nanoGUMBOS in water (blue), ethanolic solutions of GUMBOS (red), and J/H ratio of nanoGUMBOS (green). Adapted with permission from Ref. (44). Copyright (2010) American Chemical Society.....60

Fig. 1.9. Reactivity of the binary [PIC-PC][NTf_2] nanoprobe towards different ROS. Adapted with permission from Ref. (66). Copyright (2018) Elsevier.....62

Chapter 2. **Protein discrimination using erythrosin B-based GUMBOS in combination with UV–Vis spectroscopy and chemometrics**

Fig. 2.1. (A) Chemical structures of the cations used in the synthesis of EB-based GUMBOS. (B) Synthetic diagram of $[P_{4444}]_2[EB]$ GUMBOS 82

Fig. 2.2. UV-Vis spectra of $[Na]_2[EB]$ and EB-based GUMBOS (1 μmol L^{-1}) in DMSO..... 85

Fig. 2.3. Scores plots corresponding to the first three LVs of PLSDA regression models obtained using UV-Vis spectra at pH 3.0 (IA–IC), pH 4.5 (IIA–IIC), and pH 6.0 (IIIA–IIIC) for protein discrimination. $[P_{4444}]_2[EB]$ GUMBOS + RNAse A (◆), Lyz (■), Alb (▲), Mb (▼), and α-ChT (●). Models A, B, and C correspond to 5, 10, and 15 min of reaction 88

Fig. 2.4. Scores plots corresponding to the first three LVs of PLSDA regression models obtained using UV-Vis spectra at pH 3.0 (IA–IC), pH 4.5 (IIA–IIC), and pH 6.0 (IIIA–IIIC) for protein discrimination. $[P_{44416}]_2[EB]$ GUMBOS + RNAse A (◆), Lyz (■), Alb (▲), Mb (▼), and α-ChT (●). Models (A) 5, (B) 10, and (C) 15 min of reaction 90

Fig. 2.5. Scores plots corresponding to the first three LVs of PLSDA regression models obtained using UV-Vis spectra at pH 3.0 (IA–IC), pH 4.5 (IIA–IIC), and pH 6.0 (IIIA–IIIC) for protein discrimination. $[N_{4444}]_2[EB]$ GUMBOS + RNAse A (◆), Lyz (■), Alb (▲), Mb (▼), and α-ChT (●). Models A, B, and C correspond to 5, 10, and 15 min of reaction 92

Fig. 2.6. Scores plots corresponding to the first three LVs of PLSDA regression models obtained using UV-Vis spectra at pH 3.0 (IA–IC), pH 4.5 (IIA–IIC), and pH 6.0 (IIIA–IIIC) for protein discrimination. $[BDHA]_2[EB]$ GUMBOS + RNAse A (◆), Lyz (■), Alb (▲), Mb (▼), and α-ChT (●). Models (A) 5, (B) 10, and (C) 15 min of reaction 93

Fig. 2.7. Scores plots corresponding to the first two LVs of PLSDA regression models developed using the UV-Vis spectra of (A) $[P_{4444}]_2[EB]$ and (B) $[N_{4444}]_2[EB]$ after incubation with binary mixtures of Alb + Mb..... 95

Fig. S2.1. ^{1}H NMR spectrum of $[P_{4444}]_2[EB]$ GUMBOS 100

Fig. S2.2. ^{13}C NMR spectrum of $[P_{4444}]_2[EB]$..... 100

Fig. S2.3. ^{1}H NMR spectrum of $[P_{44416}]_2[EB]$..... 101

Fig. S2.4. ^{13}C NMR spectrum of $[P_{44416}]_2[EB]$ GUMBOS..... 101

Fig. S2.5. ^{1}H spectrum of $[N_{4444}]_2[EB]$..... 102

Fig. S2.6. ^{13}C spectrum of $[N_{4444}]_2[EB]$ in $CDCl_3$ 102

Fig. S2.7. ^{1}H NMR spectrum of $[BDHA]_2[EB]$ GUMBOS..... 103

Fig. S2.8. ^{13}C NMR spectrum of $[BDHA]_2[EB]$ 103

Fig. S2.9. Overlay of FTIR spectra of starting materials (blue and green) and resulting products (red): (A) $[P_{4444}]_2[EB]$, (B) $[P_{44416}]_2[EB]$, (C) $[N_{4444}]_2[EB]$, and (D) $[BDHA]_2[EB]$. 104

Fig. S2.10. DSC thermograms of EB-based GUMBOS 104

Fig. S2.11. Absorbance spectra of (A) $[P_{4444}]_2$[EB], (B) $[P_{44416}]_2$[EB], (C) $[N_{4444}]_2$[EB], and (D) $[BDHA]_2$[EB]: alone (–) and in the presence of RNAse A (–), Lyz (–), Alb (–), Mb (–), and α-ChT (–). Spectra were recorded at pH 6.0 after 5 min of reaction time.....105

Chapter 3. **Exploring the potential of erythrosin B-based GUMBOS for qualitative and quantitative analyses of proteins**

Fig. 3.1. Synthetic diagram of $[N_{4444}]_2$[EB] and $[P_{4444}]_2$[EB] GUMBOS.....129

Fig. 3.2. Total percentages (%) of correct protein assignments (A) and % of correct assignments of Alb (B), RNAse A (C), Mb (D), Lyz (E), and α-ChT (F) at different concentrations, obtained from the confusion matrices of PLSDA regression models (6 LVs) developed using the $[N_{4444}]_2$[EB] GUMBOS.....132

Fig. 3.3. Total percentages (%) of correct assignments (A) and % of correct assignments of Alb (B), RNAse A (C), Mb (D), Lyz (E), and α-ChT (F) at different concentrations obtained from the confusion matrices of PLSDA regression models, which were developed using 6 LVs and $[P_{4444}]_2$[EB] GUMBOS.....133

Fig. 3.4. UV-Vis spectrum of $[P_{4444}]_2$[EB] GUMBOS + Mb (4 μg mL^{-1}) illustrating the four spectral regions (R1, R2, R3, and R4) considered during optimization of PLS models...134

Fig. S3.1. Root mean square error of cross-validation (RMSECV) obtained from the PLS models developed to predict protein concentration using UV-Vis spectra of $[N_{4444}]_2$[EB] GUMBOS in the presence of Alb (A); RNAse A (B); Mb (C); Lyz (D); and α-ChT (E). Legend: ● R1; ● R2; ● R3; ● R4.....137

Fig. S3.2. Root mean square error of cross-validation (RMSECV) obtained from the PLS models developed to estimate the concentration of proteins using UV-Vis spectra of $[P_{4444}]_2$[EB] GUMBOS in the presence of Alb (A); RNAse A (B); Mb (C); Lyz (D); and α-ChT (E). Legend: ● R1; ● R2; ● R3; ● R4.....138

Chapter 4. **Combined use of phosphonium-erythrosin B-based nanoGUMBOS, UV-Vis spectroscopy, and chemometrics for discrimination and quantification of proteins**

Fig. 4.1. Absorbance spectra of $[P_{4444}]_2$[EB] nanoGUMBOS (–) and $[P_{4444}]_2$[EB] nanoGUMBOS in the presence of Alb (–), Hb (–), Try (–), Cat (–), Lyz (–), and Cyt c (–). NanoGUMBOS were obtained after 5 min of sonication without CD.....148

Fig. 4.2. Scores plots corresponding to the first three LVs of PLSDA regression models developed with UV-Vis spectra for protein discrimination: ● Alb, ● Hb, ● Try, ● Cat, ● Lyz, and ● Cyt c. $[P_{4444}]_2$[EB] nanoGUMBOS obtained after 30 s (A), 5 min (B), and 15 min (C) of sonication.....152

Fig. 4.3. Total percentages of correct protein discrimination obtained with the $[P_{4444}]_2[EB]$ nanoGUMBOS synthesized in the absence and presence of three CDs (α, 2-HP-β, and γ) 154
Fig. 4.4. Total percentages of correct protein assignments obtained with the $[P_{4444}]_2[EB]$ nanoGUMBOS at various protein concentrations 155
Fig. 4.5. Scores plots of PLSDA regression models developed with UV-Vis spectra of $[P_{4444}]_2[EB]$ nanoGUMBOS incubated with mixtures of (A) Lyz and Cyt c; (B) Lyz and Hb; (C) Cyt c and Hb; and (D) Lyz, Cyt c, and Hb. Legend: ■ 100% Lyz; ■ 100% Cyt c; ■ 100% Hb; ■ 75% Lyz + 25% Cyt c; ■ 50% Lyz + 50% Cyt c; ■ 25% Lyz + 75% Cyt c; ■ 25% Lyz + 75% Hb; ■ 50% Lyz + 50% Hb; ■ 75% Lyz + 25% Hb; ■ 50% Cyt c + 50% Hb; ■ 75% Cyt c + 25% Hb; ■ 75% Cyt c + 25% Hb; ■ 1:1:1, Lyz:Cyt c:Hb 158
Fig. S4.1. (A) Chemical structures of the ions used to form $[P_{4444}]_2[EB]$ GUMBOS. (B) Scheme of the reprecipitation procedure used for the synthesis of nanoGUMBOS 161
Fig. S4.2. UV–Vis spectra of $[Na]_2[EB]$ and $[P_{4444}]_2[EB]$ nanoGUMBOS (4 μmol L^{-1}) in water. Both non-templated and CD-templated nanoGUMBOS were obtained after 5 min of sonication 161
Fig. S4.3. TEM image of $[P_{4444}]_2[EB]$ nanoGUMBOS (A) and the corresponding particle size distribution histogram with Gaussian fitting (B) 162
Fig. S4.4. Effect of storage time on the hydrodynamic diameter and PDI of $[P_{4444}]_2[EB]$ nanoGUMBOS. Statistical analysis was performed using the non-parametric Kruskal-Wallis test (*P < 0.05 and **P < 0.01) 162
Fig. S4.5. Scores plots corresponding to the first three LVs of PLSDA regression models developed using UV-Vis spectra of $[P_{4444}]_2[EB]$ nanoGUMBOS for protein discrimination: • Alb, • Hb, • Try, • Cat, • Lyz, and • Cyt c. Models A, B, C, and D correspond to nanoGUMBOS synthesized in the absence and presence of α-, 2-HP-β-, and γ-CD, respectively 163
Fig. S4.6. PLS regression results obtained for (A) Alb, Albumin; (B) Hb, Hemoglobin; (C) Try, Trypsin; (D) Cat, Catalase; (E) Lyz, Lysozyme; and (F) Cyt c, Cytochrome c. Panels I refer to the PLS regression model developed for each protein: true protein concentration (measured) *versus* protein concentration predicted by the UV-Vis spectra (predicted). The red and green lines correspond to calibration and cross-validation data, respectively. Panels II show the root mean square error of calibration (RMSEC), cross-validation (RMSECV), and prediction (RMSEP) variation *versus* number of latent variables (LVs) used in the PLS models. Although using a larger number of LVs can lead to lower errors, no significant decrease was observed for LVs > 4 164

Chapter 5. **Studies of protein binding to biomimetic membranes using ANS-based GUMBOS**

Fig. 5.1. (A) Chemical structures of the cations used to form ANS-based GUMBOS. (B) Schematic representation of GUMBOS syntheses 176

Fig. 5.2. (A) UV-Vis and (B) fluorescence spectra of ANS and ANS-based GUMBOS (10 μmol L^{-1}) in ACN 179

Fig. 5.3. Binding isotherms of ANS, $[N_{4444}][ANS]$, and $[P_{4444}][ANS]$ in the absence of proteins (A). Binding isotherms of ANS (B), $[N_{4444}][ANS]$ (C), and $[P_{4444}][ANS]$ (D) in the presence of Lyz, Mb, α-ChT, and RNAse A (20 μg mL^{-1}), along with the estimated binding parameters: binding constant (K_b), binding process cooperativity (b), maximum fluorescence intensity (C_{max}), and coefficient of determination (R^2). Results are presented as the mean and standard deviation of at least three independent assays, with lines representing the best fit to Eq. 3 182

Fig. S5.1. ^1H NMR spectrum of $[N_{4444}][ANS]$ 186

Fig. S5.2. ^{13}C NMR spectrum of $[N_{4444}][ANS]$ GUMBOS 187

Fig. S5.3. HSQC spectrum of $[N_{4444}][ANS]$.....188

Fig. S5.4. HMBC spectrum of $[N_{4444}][ANS]$ and respective inset 189

Fig. S5.5. ^1H spectrum of $[N_{6666}][ANS]$ GUMBOS 190

Fig. S5.6. ^{13}C spectrum of $[N_{6666}][ANS]$ in CD_3OD 191

Fig. S5.7. HSQC spectrum of $[N_{6666}][ANS]$ GUMBOS and respective inset.....192

Fig. S5.8. HMBC spectrum of $[N_{6666}][ANS]$ and respective inset 193

Fig. S5.9. ^1H spectrum of $[P_{4444}][ANS]$ 194

Fig. S5.10. ^{13}C spectrum of $[P_{4444}][ANS]$ GUMBOS 195

Fig. S5.11. HSQC spectrum of $[P_{4444}][ANS]$.....196

Fig. S5.12. HMBC spectrum of $[P_{4444}][ANS]$ and respective inset 197

Fig. S5.13. Overlay of FTIR spectra of starting materials (green and blue) and resulting GUMBOS (grey): (A) $[N_{4444}][ANS]$, (B) $[N_{6666}][ANS]$, and (C) $[P_{4444}][ANS]$.....198

Fig. S5.14. TGA spectra of ANS-based GUMBOS.....199

Chapter 6. **A GUMBOS-based strategy for overcoming therapeutic limitations of rose bengal**

Fig. 6.1. UV-Vis absorption spectra of $[Na]_2[RB]$ and RB-based GUMBOS (2 μmol L^{-1}) in DMSO.....216

Fig. 6.2. (A) Absorption and (B) second derivative spectra of [CHX][RB] (8 μmol L^{-1}) in the absence (**–**) and presence of increasing concentrations of HePC (**–**), and micelles without GUMBOS (**–**). (C) Plot of second derivative values at 560 nm as a function of HePC micellar

concentration and their fit using a nonlinear least squares regression method. Note: Some error bars are smaller than the corresponding markers 218
Fig. 6.3. Percentage of hemolysis (mean ± standard deviation) after incubation of human RBCs with different concentrations of (A) GUMBOS, (B) starting materials, and (C) unreacted mixtures. RBCs in saline solution (0.85%) and Triton^{TM} X-100 (1% v/v) were used as negative and positive controls, respectively. Statistically significant differences between each concentration and the negative control (untreated RBCs) were assessed using the non-parametric Kruskal-Wallis test (*P < 0.05). Dash line represents 5% hemolysis 222
Fig. S6.1. Overlay of FTIR spectra of bulk materials (green and pink) and resulting GUMBOS (grey): (A) $[BDHA]_2[RB]$, (B) $[C_{16}Py]_2[RB]$, and (C) [CHX][RB]..... 225
Fig. S6.2. TGA spectra of RB-based GUMBOS 226

Chapter 7. **Development of an automated yeast-based spectrophotometric method for toxicity screening: application to ionic liquids, GUMBOS, and deep eutectic solvents**
Fig. 7.1. Schematic representation of the SIA system used to evaluate yeast cell viability. C, carrier (phosphate buffer 0.1 mol L^{-1}, pH 5.8); SP, syringe pump (5 mL syringe capacity); HC, holding coil (2 m length); MSV, multiposition selection valve; MB, methylene blue; *S. cerevisiae*, *Saccharomyces cerevisiae* cells; RC, reaction coil (0.15 m length); CH, cuvette holder (connected to the light source and spectrometer via optical fibers); D, detector (664 nm); LS, light source; W, waste..... 241
Fig. 7.2. Percentage of loss of yeast cell viability after 2 h exposure to different concentrations of (a) ILs, (b) GUMBOS, and (c) DESs. Each point and error bar represents the mean and standard deviation of three independent experiments performed in triplicate. Some error bars are smaller than the symbols 245
Fig. 7.3. IC_{50} values (μmol L^{-1}) obtained for (a) ILs, (b) GUMBOS, and (c) DESs. These values were calculated from the dose-response curves shown in Fig. 2. Statistically differences between compounds containing the same cation or anion was assessed by use of GraphPad Prism software *via* one-way ANOVA-Tukey's test or t-test (*P ≤ 0.05, **P ≤ 0.01, ***P ≤ 0.001, and ****P ≤ 0.0001) 246
Fig. S7.1. (a) Chemical structures, names, and abbreviations of the cations and anions reported in this work. (b) Hydrogen bond acceptors and hydrogen bond donors/salt used for synthesis of DESs..... 250
Fig. S7.2. Effect of (a) buffer pH, (b) MB concentration, (c) MB (circles) and yeast (lines) volumes, (d) propulsion flow rate, and (e) RC length on OD signal at 664 nm..... 250

List of tables

Chapter 1. Theoretical background

Table 1.1. Names, abbreviations, and chemical structures of the cations and anions reported in this review.....38

Table 1.2. Comparison of the FIL based hollow-fiber solid-phase microextraction with other reported methods for determination of dichlorodiphenyltrichloroethane and its primary metabolites in real samples. Reprinted with permission from (58). Copyright (2017) Wiley 44

Table 1.3. Summary of the concentration ranges, detection limits, and sensitivities for different volatile organic compounds.....47

Table 1.4. Examples of nano/mesoscale GUMBOS obtained by the reprecipitation method 53

Table 1.5. Protein adsorption efficiency of $[C_{16}mim]_5[Dy(SCN)_8]$ nanoGUMBOS. Adapted with permission from Ref. (59). Copyright (2019) Elsevier.....63

Chapter 2. Protein discrimination using erythrosin B-based GUMBOS in combination with UV–Vis spectroscopy and chemometrics

Table 2.1. Total percentages of correct predictions (%) obtained from the confusion matrices of PLSDA models (4 LVs), which were developed for protein discrimination using the synthesized EB-based GUMBOS.....87

Table S2.1. Yield and ESI-MS analysis of synthesized materials.....106

Table S2.2. Logarithm of the octanol/water partition coefficients ($\log K_{O/W}$) of EB-based GUMBOS.....106

Table S2.3. Molecular weights and isoelectric points of target proteins 106

Table S2.4. Confusion matrices obtained from the PLSDA models developed for protein discrimination at pH 3.0 using the $[P_{4444}]_2[EB]$ GUMBOS. Models A, B, and C correspond to 5, 10, and 15 min of reaction.....107

Table S2.5. Confusion matrices for protein discrimination at pH 4.5 using the $[P_{4444}]_2[EB]$ GUMBOS and acquired from the PLSDA models. (A) 5, (B) 10, and (C) 15 min of reaction 108

Table S2.6. Confusion matrices acquired from the PLSDA models developed for discrimination of proteins at pH 6.0 using the $[P_{4444}]_2[EB]$ GUMBOS. Models A, B, and C correspond to 5, 10, and 15 min of reaction time.....109

Table S2.7. Confusion matrices for discrimination of proteins at pH 3.0 using the $[P_{44416}]_2$[EB] GUMBOS and acquired from PLSDA models: (A) 5, (B) 10, and (C) 15 min of reaction 110
Table S2.8. Confusion matrices obtained from the PLSDA models for protein discrimination at pH 4.5 using the $[P_{44416}]_2$[EB] GUMBOS. Models A, B, and C correspond to 5, 10, and 15 min of reaction period 111
Table S2.9. Confusion matrices for discrimination of proteins at pH 6.0 using $[P_{44416}]_2$[EB] GUMBOS and acquired from the PLSDA models: (A) 5, (B) 10, and (C) 15 min of reaction 112
Table S2.10. Confusion matrices obtained from PLSDA models developed for discrimination of proteins at pH 3.0 using the $[N_{4444}]_2$[EB] GUMBOS. Models A, B, and C correspond to 5, 10, and 15 min of reaction time 113
Table S2.11. Confusion matrices obtained from the PLSDA models developed for discrimination of proteins at pH 4.5 using the GUMBOS $[N_{4444}]_2$[EB]. Models A, B, and C correspond to 5, 10, and 15 min of reaction period 114
Table S2.12. Confusion matrices obtained from the PLSDA models developed for protein discrimination at pH 6.0 using the $[N_{4444}]_2$[EB] GUMBOS. Models A, B, and C: 5, 10, and 15 min of reaction 115
Table S2.13. Confusion matrices generated from the PLSDA models used for protein discrimination at pH 3.0 with the GUMBOS $[BDHA]_2$[EB]. Models A, B, and C correspond to 5, 10, and 15 min of reaction period 116
Table S2.14. Confusion matrices for discrimination of proteins at pH 4.5 using the GUMBOS $[BDHA]_2$[EB] and acquired from PLSDA models: A, B, and C correspond to 5, 10, and 15 min of reaction 117
Table S2.15. Confusion matrices obtained from the PLSDA models developed for protein discrimination at pH 6.0 using the $[BDHA]_2$[EB] GUMBOS. Models A, B, and C: 5, 10, and 15 min of reaction 118

Chapter 3. **Exploring the potential of erythrosin B-based GUMBOS for qualitative and quantitative analyses of proteins**

Table 3.1. Figures of merit corresponding to the optimum PLS models (4 LVs and spectral range from 600 to 290 nm) developed to estimate protein concentrations (0.50–20 μg mL^{-1}) using EB-based GUMBOS 135
Table 3.2. Errors (%) obtained for the calibration (C), cross-validation (CV), and prediction (P) sets used to develop the PLS models for protein quantification 136

Chapter 4. **Combined use of phosphonium-erythrosin B-based nanoGUMBOS, UV-Vis spectroscopy, and chemometrics for discrimination and quantification of proteins**

Table 4.1. Confusion matrices obtained from the PLSDA regression models developed for protein discrimination using the $[P_{4444}]_2[EB]$ nanoGUMBOS. Models A, B, and C correspond to 30 s, 5 min, and 15 min of sonication 153

Table 4.2. Percentages of correct predictions (%) for different concentrations of proteins obtained from the confusion matrices of PLSDA regression models 156

Table 4.3. Figures of merit obtained from the PLS models developed to predict protein concentration ($20.0 \geq [Protein] \geq 2.0$ μg mL^{-1}) using the $[P_{4444}]_2[EB]$ nanoGUMBOS 160

Table S4.1. Hydrodynamic diameter, polydispersity index (PDI), and zeta potential (ZP) of $[P_{4444}]_2[EB]$ nanoGUMBOS obtained after 30 s, 5 min, and 15 min of sonication. Values represent the mean and standard deviation of three batches of nanoGUMBOS 165

Table S4.2. Characterization of CD-templated nanoGUMBOS in terms of hydrodynamic diameter, polydispersity index (PDI), and zeta potential (ZP). Data expressed as mean ± standard deviation (n = 3) 165

Table S4.3. Molecular weights and isoelectric points of target proteins 165

Table S4.4. Confusion matrices obtained from the PLSDA regression models developed for protein discrimination using the $[P_{4444}]_2[EB]$ nanoGUMBOS synthesized in the absence (A) and presence of three CDs: α (B), 2-HP-β (C), and γ (D) 166

Chapter 5. **Studies of protein binding to biomimetic membranes using ANS-based GUMBOS**

Table 5.1. Partition coefficients (expressed as K_p and logD) of parent ANS and ANS-based GUMBOS in micelles of HePC (pH 7.4, 37 ºC). Results are presented as the mean ± standard deviation of three replicates.....180

Table S5.1. ESI-MS analysis of synthesized compounds 200

Table S5.2. Half weight loss temperature ($T_{50\%}$) and melting point of ANS-based GUMBOS 200

Chapter 6. **A GUMBOS-based strategy for overcoming therapeutic limitations of rose bengal**

Table 6.1. Chemical structures and molar ratios of the ions used in GUMBOS synthesis 212

Table 6.2. Partition coefficients (expressed as K_p and logD) of $[Na]_2[RB]$ and RB-based GUMBOS in micelles of HePC at pH 7.4 and 37 ºC. Results are the mean ± standard deviation of three replicates 217

Table 6.3. MICs and MBCs (μg mL^{-1}) of GUMBOS, parent compounds, and unreacted stoichiometric mixtures against Gram-positive and Gram-negative bacteria 220
Table S6.1. Green LED irradiation parameters 227
Table S6.2. ESI-MS analysis of synthesized GUMBOS 227
Table S6.3. TGA data of RB-based GUMBOS. 227
Table S6.4. Melting point range (ºC) of synthesized compounds 227
Table S6.5. MICs and MBCs (μg mL^{-1}) of GUMBOS (A), parent compounds (B), and unreacted stoichiometric mixtures (C) against Gram-positive and Gram-negative bacteria. For comparison purposes, experiments were conducted in the presence and absence of light 228

Chapter 7. Development of an automated yeast-based spectrophotometric method for toxicity screening: application to ionic liquids, GUMBOS, and deep eutectic solvents

Table 7.1. Protocol sequence for evaluation of yeast cell viability in the absence and presence of tested compounds 242
Table 7.2. Results of optimization of the automated yeast viability assay..... 243
Table S7.1. Toxicity of the studied compounds towards yeast cells expressed as IC_{50} values (μmol L^{-1}), which represents the concentration necessary to reduce cell viability by 50%. *S. cerevisiae* cells were exposed to the tested compounds for 2 h at room temperature ... 251

List of abbreviations and acronyms

Abs	Absorbance
ACN	Acetonitrile
Alb	Albumin
ANS	8-Anilino-1-naphthalenesulfonic acid
ATCC	American type culture collection
BDHA	Benzyldimethylhexadecylammonium
CA	Cellulose acetate
Cat	Catalase
CD	Cyclodextrin
α-CD	Alpha-cyclodextrin
γ-CD	Gamma-cyclodextrin
2-HP-β-CD	2-Hydroxypropyl-beta-cyclodextrin
$CDCl_3$	Deuterated chloroform
CD_3OD	Deuterated methanol
$C_{16}Py$	Cetylpyridinium
CFU	Colony-forming unit
CH	Cuvette holder
CHX	Chlorhexidine
α-ChT	α-Chymotrysin
CP-AFM	Conductive probe atomic force microscopy
Cyt c	Cytochrome c
DCM	Dichloromethane
DES	Deep eutectic solvent
DLS	Dynamic light scattering
DMPC	1,2-Dimyristoyl-*sn*-glycero-3-phosphocholine
DMSO	Dimethylsulfoxide
DMSO-d_6	Hexadeuterodimethylsulfoxide
DSC	Differential scanning calorimetry
DSM	German collection of microorganisms and cell cultures
DSSC	Dye-sensitized solar cell
EB	Erythrosin B
E. coli	*Escherichia coli*
E. faecalis	*Enterococcus faecalis*
ERD	Energy relay dye

FIL	Frozen ionic liquid
FRET	Förster resonance energy transfer
FTIR	Fourier transform infrared
GUMBOS	Group of uniform materials based on organic salts
Hb	Hemoglobin
HBA	Hydrogen bond acceptor
HBD	Hydrogen bond donor
HC	Holding coil
HePC	Hexadecylphosphocholine
HEPES	*N*-(2-hydroxyethyl)piperazine-*N*′-(2-ethanesulfonic acid)
HF-SPME	Hollow-fiber solid phase microextraction
HMBC	Heteronuclear multiple bond coherence
HR-ESI-MS	High resolution electrospray ionization mass spectrometry
HSQC	Heteronuclear single quantum coherence
IL	Ionic liquid
IPA	Isopropyl alcohol
LDA	Linear discriminant analysis
LED	Light-emitting diode
LPS	Lipopolysaccharide
LUV	Large unilamellar vesicle
LV	Latent variable
Lyz	Lysozyme
Mb	Myoglobin
MB	Methylene blue
MBC	Minimum bactericidal concentration
MHB-II	Cation-adjusted Müeller-Hinton broth
MIC	Minimum inhibitory concentration
MLV	Multilamellar vesicle
MRSA	Methicillin-resistant *Staphylococcus aureus*
MSV	Multiposition selection valve
NGMIP	NanoGUMBOS molecularly imprinted polymer
NM	Nanomaterial
NMR	Nuclear magnetic resonance
NP	Nanoparticle
N_{4444}	Tetrabutylammonium
N_{6666}	Tetrahexylammonium

OD	Optical density
OLED	Organic light-emitting diode
P. aeruginosa	*Pseudomonas aeruginosa*
PALS	Phase analysis light scattering
PCA	Principal component analysis
PDI	Polydispersity index
PLS	Partial least squares
PLSDA	Partial least squares discriminant analysis
P_{4444}	Tetrabutylphosphonium
P_{44416}	Tributylhexadecylphosphonium
QCM	Quartz crystal microbalance
RB	Rose bengal
RBC	Red blood cell
RC	Reaction coil
REACH	Registration, evaluation, authorization, and restriction of chemicals
RER	Range error ratio
RMSEC	Root mean square error of calibration
RMSECV	Root mean square error of cross-validation
RMSEP	Root mean square error of prediction
RNAse A	Ribonuclease A
ROS	Reactive oxygen species
RSD	Relative standard deviation
RTIL	Room temperature ionic liquid
R^2C	Coefficient of determination of calibration
R^2CV	Coefficient of determination of cross-validation
R^2P	Coefficient of determination of prediction
S. aureus	*Staphylococcus aureus*
S. cerevisiae	*Saccharomyces cerevisiae*
SD	Standard deviation
SDS	Sodium dodecyl sulfate
SNV	Standard normal variate
SP	Syringe pump
TEM	Transmission electron microscopy
TGA	Thermogravimetric analysis
Try	Trypsin
TSA	Tryptic soy agar

TSB	Tryptic soy broth
UV-Vis	Ultraviolet-visible
VOC	Volatile organic compound
ZP	Zeta potential

Outline of the dissertation

The present dissertation is organized into eight chapters as follows:

Chapter 1. **Theoretical background**

Chapter 1 provides an overview of the field of GUMBOS (*g*roup of *u*niform *m*aterials *b*ased on *o*rganic *s*alts). This introductory chapter also highlights the possibility of modulating properties of organic salts as well as their conversion to nanoparticles. In addition, chapter 1 describes strategies for syntheses of GUMBOS and nanoGUMBOS to obtain a variety of shapes and spectral characteristics suitable for analytical purposes, such as sensing and solid-phase extraction. The motivation and objectives for this dissertation are also presented at the end of chapter 1 as a bridge between current state-of-the-art and the original research presented herein.

Chapters 2–7. **Original research**

The next five chapters (chapters 2 to 7) describe work developed under the scope of this dissertation. Three chapters (i.e., chapters 2, 4, and 7) are published. The remaining (i.e., chapters 3, 5, and 6) have been submitted for publication in international journals with strong peer review processes. As such, each chapter is structured with the following sections: introduction, materials and methods, results and discussion, and conclusions. The limitations of the dyes selected to form GUMBOS and the deficiencies of the methodologies commonly employed for the same purpose, along with research opportunities they offer are presented in the introduction. Subsequently, the preparation of reagents, instrumentation, synthesis and characterization of GUMBOS (and nanoGUMBOS), analytical procedure, and strategies used for data analysis are provided in the experimental section. The obtained results are detailed in the next section of the manuscript, and comparisons are made with what has been described in the literature. Finally, the primary findings and improvements of these studies are highlighted in the “Conclusions” section.

Chapter 8. **Concluding remarks and future perspectives**

The final chapter of this dissertation summarizes the essential findings of all studies investigated under the scope of this dissertation. This final chapter also outlines the foremost advantages offered by these developed GUMBOS (and nanoGUMBOS), as well as provides approaches and suggestions for future research directions.

Chapter 1

Theoretical background

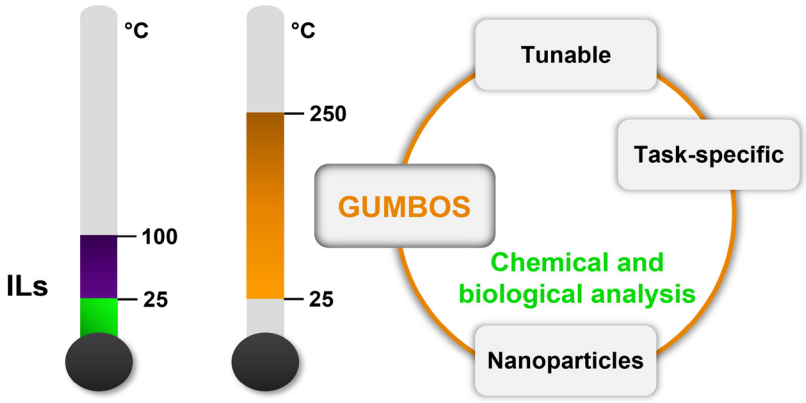

Highlights

- The tunable features of GUMBOS allow for tailoring materials for specific uses.
- NanoGUMBOS can exhibit different properties from GUMBOS.
- Methods for synthesis of nanoGUMBOS with defined characteristics are described.
- GUMBOS and nanoGUMBOS were designed for sensing and solid-phase extraction.
- NanoGUMBOS are a viable alternative to overcome potential risks of other nanoparticles.

Literature review published after international peer review as "Azevedo AMO, Santos JLM, Warner IM, Saraiva MLMFS. GUMBOS and nanoGUMBOS in chemical and biological analysis: A review. Anal Chim Acta. 2020;1133:180-98".

Abstract

GUMBOS (*g*roup of *u*niform *m*aterials *b*ased on *o*rganic *s*alts) is a novel class of materials that exhibits similar features to those of ionic liquids, but have melting points between 25 and 250 °C. GUMBOS can be easily converted into nanomaterials (nanoGUMBOS), with advantages of working at nanoscale. Due to the huge number of possible cation-anion combinations, these materials can be multifunctional and designed for a specific task.

This review highlights the possibility of fine-tuning GUMBOS physical and chemical properties in view of changing their ionic counterparts. Their outstanding potential for analytical applications is shown through recent developments in areas such as sensing, and solid-phase extraction. Available methods for synthesis of nanoGUMBOS, and their different outcomes in shapes and optical properties are described, with pros and cons being outlined. Finally, an analysis is made of opportunities and challenges faced by this class of organic ionic materials.

Keywords: Bioanalysis; GUMBOS; Ionic liquid; Nanomaterial.

1.1. Introduction

Although ionic liquids (ILs) have received increased attention recently, their history goes back to the mid-19th century when the formation of a 'red oil' was observed during the course of a Friedel-Crafts reaction (1). ILs have been defined (perhaps vaguely) as organic salts composed entirely of ions that melt below the boiling point of water (2). The choice of this maximum temperature limit is quite arbitrary, but serves the purpose of distinguishing ILs from molten salts (3). It is also worth noting that there are many synonyms for materials that meet ILs definition, namely 'room temperature molten salts', 'liquid organic salts', and 'ionic fluids' (1).

In contrast to inorganic salts that have high melting temperatures because of strong interionic electrostatic interactions, ILs exhibit much lower melting points (m.p.< 100 ºC) due to inefficient packing of the ions (4, 5). Symmetry seems to play an important role in crystal packing, with irregularly shaped cations leading to poor lattice matching and reduced melting temperatures (6, 7). For example, when Na^+ of sodium chloride (NaCl) is replaced by the asymmetric and bulky 1-ethylimidazolium (C_2im) cation, the melting point decreases from 800 to 58 °C (Fig. 1.1) (5, 8). The melting points of ILs are also influenced by the size and charge distribution of constituent ions as well as by the length of alkyl side chains (7, 9). Furthermore, it has been reported that polymorphism can lead to inhibition of crystallization, consequent depression of the melting point, and thus formation of ILs (10, 11).

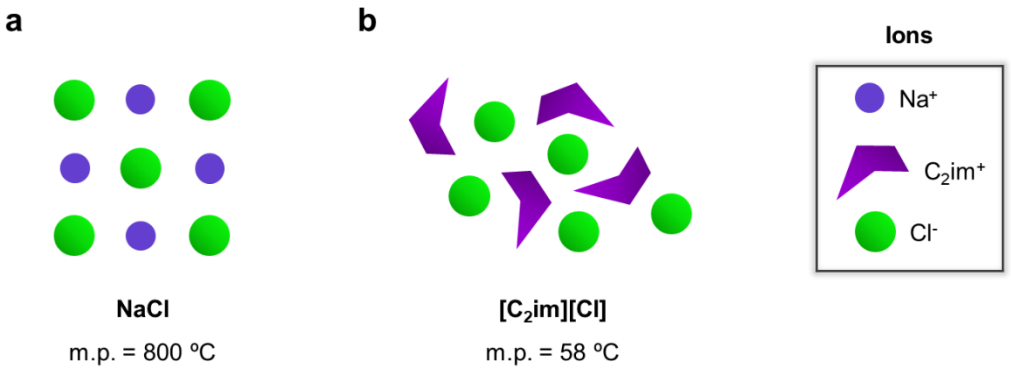

Fig. 1.1. Schematic representation of the change in ion packing from (a) NaCl to (b) [C_2im][Cl].

A growing interest in ILs as greener alternatives to conventional organic solvents is due to their peculiar features, namely unique solvation capability for a wide range of polar and nonpolar molecules, great chemical and thermal stability, high ionic conductivity, large electrochemical window, low flammability and vapor pressure. Moreover, ILs properties can

readily be tuned by varying the cation, anion, and attached substituents (12-14). For instance, the miscibility of ILs with water is primarily dictated by the hydrophilic/hydrophobic property of the anion. Hydrophilic anions such as halides and nitrate form ILs that are water miscible, whereas more hydrophobic anions, e.g., bis(trifluoromethylsulfonyl)imide and hexafluorophosphate usually hinder aqueous miscibility. Furthermore, increasing the alkyl chain length of an organic cation leads to enhanced hydrophobicity, and thus results in lower solubility (15, 16). In addition to water miscibility and hydrophobicity, the viscosity, density, and solvation behavior of ILs can also be modulated by changing their chemical structure (17-19). Similar to what happens with the aforementioned properties, toxicity and biodegradability seem to be related to the structural elements of ILs, which allows the design of less toxic and more environmentally friendly compounds (20). Ultimately, the cation and anion may have distinct and desirable functions, enabling the preparation of multifunctional materials in a simpler and more convenient way (21, 22).

Over the last two decades, tremendous progress in the field of ILs has been observed, with applications extending from analytical chemistry (23, 24) and electrochemistry (25, 26) to biotechnology (27, 28), engineering (29, 30), drug delivery, and pharmaceutics (31-33). In addition, ILs have been used at the industrial level, namely in the BASIL, Difasol, and Ionikylation processes developed by BASF, IFP (Institut Français du Pétrole), and PetroChina, respectively (34). Applications of ILs have also been proposed for the food industry, including as surfactants, lubricants, and solvents for extraction procedures (35, 36). However, it is worth noting that the use of ILs can be restricted by their relatively low maximum temperature limit. Thus, the emergence of solid-state analogues of ILs has opened many new possibilities for applications (37).

Although much attention has been paid to use of ILs in liquid-state applications, much less reference has been made to solid-phase utilization. It was only a decade ago that the first reports emerged of so-called ‘GUMBOS’ (*g*roup of *u*niform *m*aterials *b*ased on *o*rganic *s*alts) (38). These materials share similar properties to those of ILs, but can be differentiated by the melting points (< 100 °C for ILs and 25–250 °C for GUMBOS), making them suitable for analytical, biomedical, and materials application (37). In parallel, a number of studies have focused on controlled synthesis of nanomaterials derived from GUMBOS (nanoGUMBOS) as well as their characterization and potential uses (39-41).

This review updates the literature regarding GUMBOS-based materials, integrating studies conducted in this field since 2014. The versatility and tunable properties of these compounds are highlighted, with emphasis placed on applications that were not mentioned in Warner’s perspective article (37). Here, we also describe alternative strategies for synthesis of nanoGUMBOS, and discuss their pros and cons. Finally, opportunities and challenges of this novel class of materials are outlined.

A list of abbreviations, names, and chemical structures of ions typically used to form ILs and GUMBOS mentioned in this review is provided in Table 1.1.

1.2. Ionic liquids

Within ILs, two broad categories can be distinguished. These categories are based on the melting point: room temperature ILs (RTILs, m.p. < 25 °C) and frozen ILs (FILs, 25 ºC <m.p.< 100 ºC) (37).

1.2.1. Room temperature ionic liquids

After an initial report by Paul Walden (1914) on synthesis and physical properties of ethylammonium nitrate (m.p. = 13–14 ºC), RTILs began to be exploited as electrolytes for batteries (34, 69). Since then, this group of compounds has sparked interest for applications in many other fields, namely analytical chemistry (70) and nanotechnology (71).

Some researchers have devoted efforts toward development of nanosensors based on RTILs. For instance, Das and coworkers have described preparation and pH dependent properties of NMs derived from ILs containing the trihexyltetradecylphosphonium (P_{66614}) cation paired with the fluorescein (FL) anion. $[P_{66614}]_2[FL]$ nanodroplets exhibited variable sizes and colorimetric responses as a function of pH values, which supports their potential use as biosensors for early detection of cancer and bacterial infections (Fig. 1.2) (63). These same nanodroplets were employed by Galpothdeniya and colleagues for development of a selective and sensitive fluorescence sensor for detection of albumins. Spectral analysis revealed distinct fluorescent features of $[P_{66614}]_2[FL]$ nanodroplets with respect to the type and concentration of proteins. In the presence of human and bovine serum albumins, there was an enhancement of more than 19 times in the integrated fluorescence intensity. In contrast, the remaining proteins produced a less than 5-fold increase (64).

Table 1.1. Names, abbreviations, and chemical structures of the cations and anions reported in this review.

Cations			**Anions**		
[Abbreviation] Name	Chemical structure	Ref.	**[Abbreviation]** Name	Chemical structure	Ref.
[AP] 1-aminopyrene	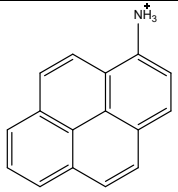	(42)	**[AOT]** Bis(2-ethyl-1-hexyl) sulfosuccinate	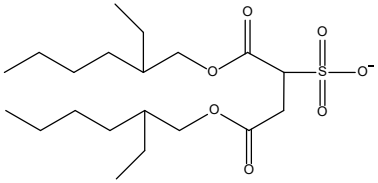	(43-47)
[BG] Brilliant green	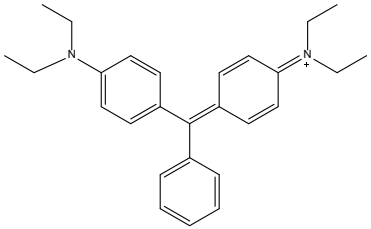	(48)	**[Asc]** Ascorbate	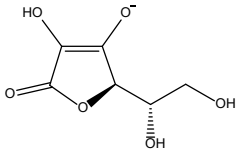	(42, 49, 50)
[C_2im] 1-ethylimidazolium	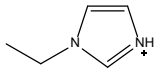	(8)	**[BETI]** Bis(pentafluoroethylsulfonyl) imide	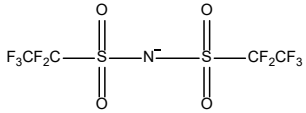	(44, 48-54)
[C_3mim] 1-methy-3-propylimidazolium	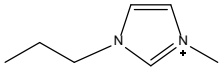	(55)	**[CuPcS_4]** Copper phthalocyanine-3,4',4'',4'''-tetrasulfonic acid	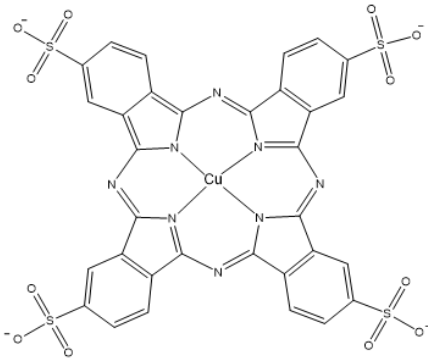	(56)
[C_4dmim] 1-butyl-2,3-dimethylimidazolium	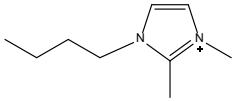	(57)			
[C_{16}mim] 1-hexadecyl-3-methylimidazolium	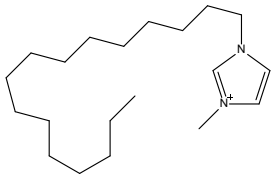	(58, 59)			

Table 1.1 *(continued)*

Cations			Anions		
[Abbreviation] Name	Chemical structure	Ref.	**[Abbreviation]** Name	Chemical structure	Ref.
[DD] 1,1'-diethyl-2,2'-dicarbocyanine	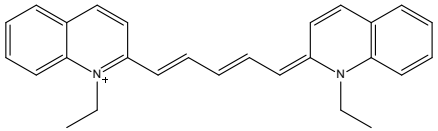	(52)			
[DDMA] 3-(dodecyldimethyl-ammonio)propanesulfonate	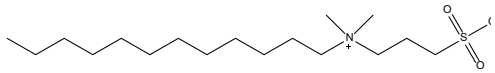	(56)			
[HMT] 1,1′,3,3,3′,3′-hexamethylindotricarbocyanine	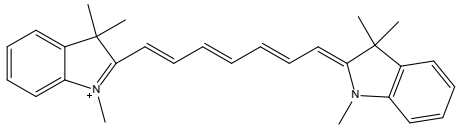	(43-46)	**[CuTCPP]** Copper (II) meso-tetra(4-carboxyphenyl)porphyrin	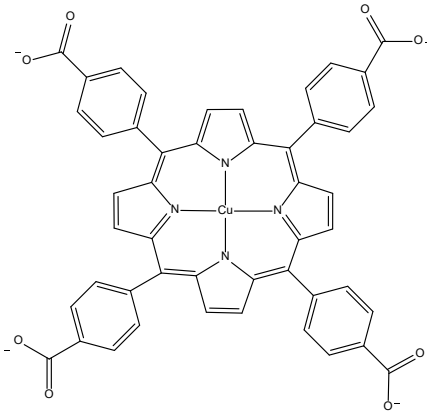	(60)
[IR780] 2-[2-[2-chloro-3-[(1,3-dihydro-3,3-dimethyl-1-propyl-2*H*-indol-2-ylidene)ethylidene]-1-cyclohexen-1-yl]ethenyl]-3,3-dimethyl-1-propylindolium	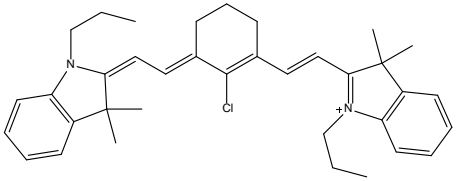	(49, 61)			
[N_{4444}] Tetrabutylammonium	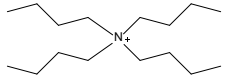	(56)			
[P_{4444}] Tetrabutylphosphonium	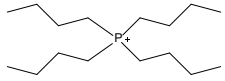	(56)	**[DC]** Deoxycholate	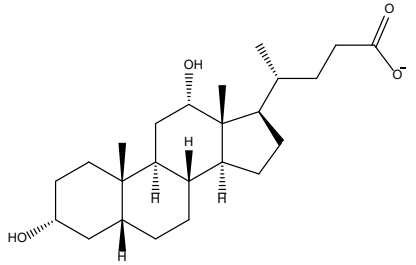	(62)

(continued on next page)

Table 1.1 *(continued)*

Cations			Anions		
[Abbreviation] Name	Chemical structure	Ref.	**[Abbreviation]** Name	Chemical structure	Ref.
[P_{4448}] Tributyl-*n*-octylphosphonium	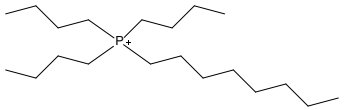	(56)	**[FL]** Fluorescein	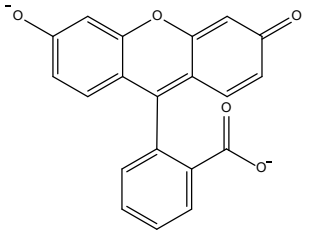	(63, 64)
[P_{66614}] Trihexyltetradecylphosphonium	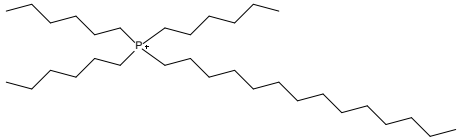	(60, 63-65)			
[PC] 1,1'-diethyl-2,2'-carbocyanine	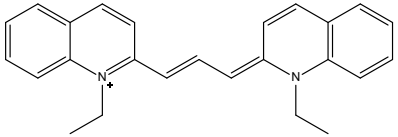	(52)	**[NTf_2]** Bis(trifluoromethylsulfonyl)imide	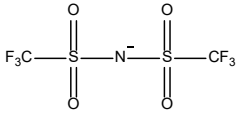	(42, 44, 46, 47, 51, 52, 54, 55, 58, 66)
[PIC] 1,1'-diethyl-2,2'-cyanine	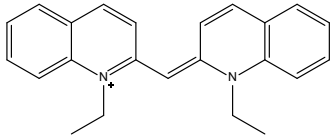	(51, 52, 54)			
[Ptc] Iron(III) phthalocyanine	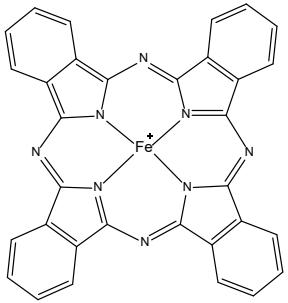	(62)	**[OTf]** Trifluoromethanesulfonate	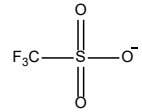	(49, 50)

(continued on next page)

Table 1.1 *(continued)*

Cations			Anions		
[Abbreviation] Name	Chemical structure	Ref.	**[Abbreviation]** Name	Chemical structure	Ref.
[R6G] Rhodamine 6G	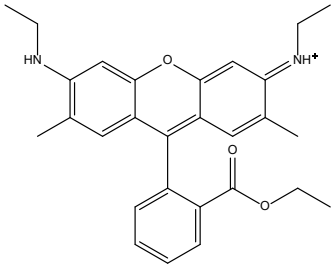	(39, 50)	**[PF_6]** Hexafluorophosphate	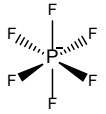	(57)
[TC0] 3,3'-diethylthiacyanine	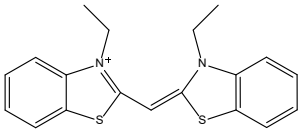	(53)	**[TFPB]** 3,5-bis (trifluoromethyl) phenyltrifluoroborate	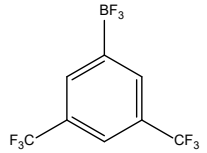	(43, 44)
[TC1] 3,3'-diethylthiacarbocyanine	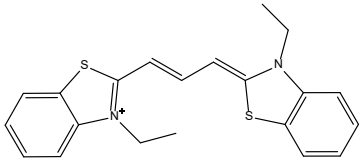	(53)	**[TFP4B]** Tetrakis[3,5-bis-(1,1,1,3,3,3-hexafluoro-2-methoxy-2-propyl)phenyl] borate	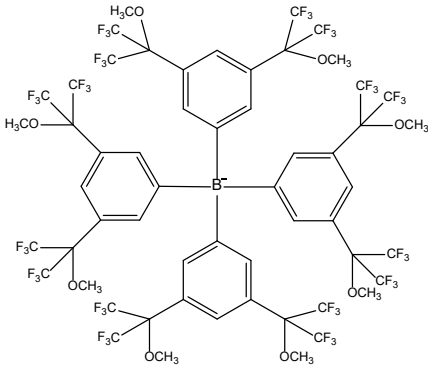	(44)

(continued on next page)

Table 1.1 *(continued)*

Cations			Anions		
[Abbreviation] Name	Chemical structure	Ref.	**[Abbreviation]** Name	Chemical structure	Ref.
[TC2] 3,3'-diethylthiadicarbocyanine	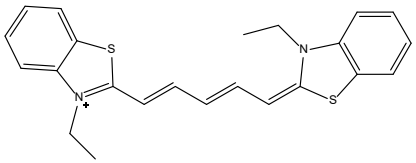	(53)	**[TPB]** Tetraphenylborate	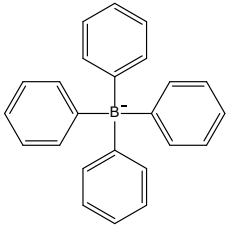	(39, 50, 55, 61)
[1048] 1-butyl-2-[2-[3-[(1-butyl-6-chlorobenz[cd]indol-2(1*H*)-ylidene)ethylidene]-2-chloro-1-cyclohexen-1-yl]ethenyl]-6-chlorobenz[cd]indolium	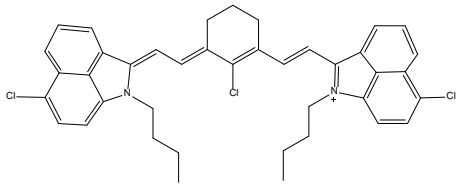	(67, 68)	**[Zn-PCS]** Zinc(II) phthalocyanine tetrasulfonate	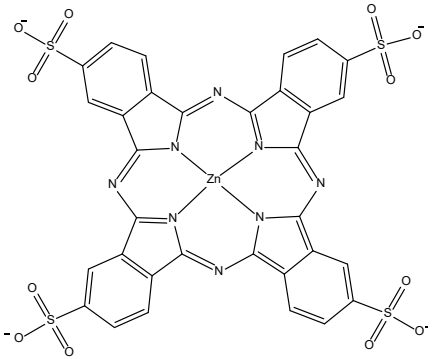	(65)
[1061] 4-[2-[2-chloro-3-[(2,6-diphenyl-4*H*-thiopyran-4-ylidene)ethylidene]-1-cyclohexen-1-yl]ethenyl]-2,6-diphenylthiopyrylium	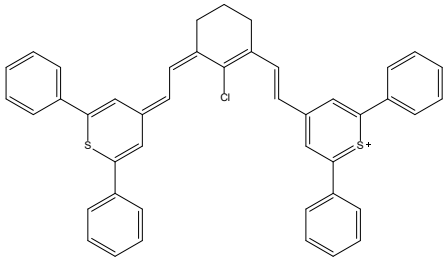	(67, 68)			

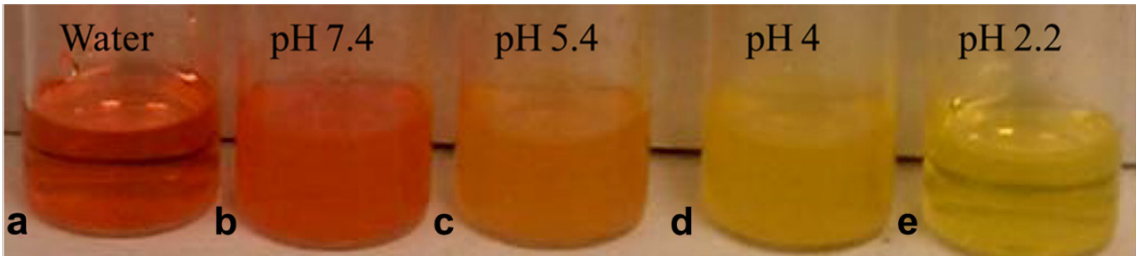

Fig. 1.2. pH dependent colorimetric response of $[P_{66614}]_2[FL]$ nanodroplets in (a) water and buffers of pH (b) 7.4, (c) 5.4, (d) 4, and (e) 2.2. The color changes from red to orange, orange green, and light green as the pH decreases. Adapted with permission from (63). Copyright (2013) Royal Society of Chemistry.

The unique properties of RTILs have also led to their use as stabilizers (72) and reaction media for the synthesis of NMs (73), allowing better control of morphology (74). A number of studies have examined the stabilizing effect of ILs on nanoparticles (NPs). For example, Safavi *et al.* reported synthesis of stable gold NPs using imidazolium-based amino acid ILs with distinct alkyl side chain lengths. It was also observed that the cation with the longest alkyl chain (dodecyl) imparted greater stability to NPs (75). More recently, Guleria and coworkers discovered that 1-ethyl-3-methylimidazolium thiocyanate slows down phase transformation of selenium NPs, imparting them with higher stability (> 2 months) (76). In addition to their role as stabilizers, ILs have been employed as solvents for synthesis of several NMs, including cobalt platinum nanorods (77), gold nanosheets (78), and nickel NPs (79). In contrast, Trewyn and colleagues demonstrated the possibility of modulating the morphology of NPs through use of RTILs as synthetic templates. Mesoporous silica NMs with morphologies ranging from spheres to ellipsoids, rods, and tubes were prepared by using four distinct RTILs (1-tetradecyl-3-methylimidazolium bromide, 1-hexadecyl-3-methylimidazolium bromide, 1-octadecyl-3-methylimidazolium bromide, and 1-tetradecyloxymethyl-3-methylimidazolium chloride) (80).

1.2.2. Frozen ionic liquids

In the past, concerted efforts to replace volatile organic solvents drove the notion that solid ILs were useless and needed modifications to depress the melting points to a room temperature range. The pursuit for RTILs has led to investigations such as using compressed carbon dioxide to decrease the melting point of FILs (81). Another example where solid ILs were regarded as unfortunate (since RTILs were desired) is in the preparation of amino acid chiral ILs as solvents for asymmetric synthesis by Bao and coworkers (82). In fact, only a few published studies have found general utility for FILs. For example, Rutten *et al.* demonstrated the use of FILs as substrates for rewritable imaging.

The authors reported the discovery of a method for producing localized charge patterns that allowed recording of a rewritable image or data set on the surface of 1-ethyl-3-methylimidazolium ethylsulfate and provided a useful probe for conductor-insulator transition (83). In contrast, Pang and coworkers developed a simple method for hollow fiber solid-phase microextraction of dichlorodiphenyltrichloroethane and its primary metabolites using the hydrophobic IL 1-hexadecyl-3-methylimidazolium bis(trifluoromethylsulfonyl) imide ([C_{16}mim][NTf_2]) as sorbent. Briefly, [C_{16}mim][NTf_2] methanolic solution was loaded into hollow fiber membrane and solvent was evaporated under vacuum at 60 ºC. This FIL was confined in hollow fiber pores via NTf_2 anion as confirmed by EDX (energy dispersive X-ray spectroscopy) and FTIR analysis. The obtained results demonstrated that the proposed method exhibits low limits of detection and comparable relative standard deviations to other methods (Table 1.2). Indeed, this FIL reinforced hollow fiber shows high extraction efficiency for dichlorodiphenyltrichloroethane and its primary metabolites with low limits of detection, good linearity, and recovery. Additionally, as it is easily functionalized, FIL based hollow fiber solid-phase microextraction (HF-SPME) is a promising approach for trace determination of various organic compounds and metal ions (58).

Table 1.2. Comparison of the FIL based hollow-fiber solid-phase microextraction with other reported methods for determination of dichlorodiphenyltrichloroethane and its primary metabolites in real samples. Reprinted with permission from (58). Copyright (2017) Wiley.

Method	Detection system	Linear range (µg L^{-1})	LOD (µg L^{-1})	LOQ (µg L^{-1})	RSD (%)	Matrix	Ref.
IL-DLLME[a]	HPLC-UV	1–100	<0.45	__	<6.7	Water	(90)
SPE	GC-MS	50–500[f]	30[f]	100[f]	13.9	Drinking water	(91)
d-SPE[b]	ELISA	0.625–25[g]	<0.4[g]	__	__	Fish	(92)
TDH-Mg-Al-LDO-GCB SPE[c]	GC-MS	10–5000[g]	<3.33[g]	<11.11[g]	<1.3	Green tea	(93)
MAME-SPME[d]	HPLC-UV	30–500[g]	<84[g]	__	<8.4	Soil	(94)
SWCNT-SPME[e]	GC-ECD	2–800[f]	<1.43[f]	__	<13.9	Water	(95)
Graphene-coated SPME	GC-MS	10–1000[f]	<0.21[f]	__	<6.6	Water	(96)
FIL reinforced HF-SPME	HPLC-UV	0.5–50	<0.38	<1.25	<6	Water	(58)

[a] Temperature-controlled IL dispersive liquid-liquid microextraction.
[b] Dispersive SPE.
[c] Three dimensionally honeycomb mg-Al layered double oxide combined with graphitized carbon black.
[d] Microwave-assisted micellar extraction coupled with SPME.

[e] Single-walled carbon nanotubes as sorbents for SPME.
[f] ng L^{-1}.
[g] µg Kg^{-1}.

A year later, 3-hydroxy-2-naphthoate based ILs were synthesized and the impact of cation's central atom (N or P) on extraction efficiency of heavy metals and leaching behavior was further investigated. Both ILs were able to extract metal ions (Ag, Cd, Cu, and Pb) from aqueous solutions, but with distinct efficiencies. The ammonium IL provided a faster extraction and showed higher selectivity toward Cu, while Pb was found to be the best extracted metal with phosphonium IL. This difference in extraction speed can be explained by the greater polarity of ammonium IL, which also proved to be more stable than the phosphonium one during extraction. Additionally, the higher hydrophobicity of the selected anion led to substantial reduction of leaching when compared to ILs containing similar cations and more hydrophilic anions. Further developments of this work will include immobilization of ILs onto solid supports for microextraction of heavy metals (84). Overall, the possibility of designing ILs to incorporate functional groups that selectively interact with analytes, together with their unique physicochemical properties, make ILs suitable for application in solid-phase extraction. It is worth noting that, because of their dual nature, ILs can also interact with either polar or nonpolar molecules (85-87). There have also been reports on synthesis and use of FIL micro- and nanoparticles (88, 89).

1.3. Group of uniform materials based on organic salts (GUMBOS)

GUMBOS have emerged primarily from interest of the Warner research group at Louisiana State University. The desire of this group is to manipulate properties of solid-phase organic ionic materials that do not fit the general definition of ILs. This group has proposed a melting point range between 25 and 250 ºC for GUMBOS (37). Therefore, many GUMBOS can also be categorized as FILs since some have melting points that fall below 100 ºC (Fig. 1.3).

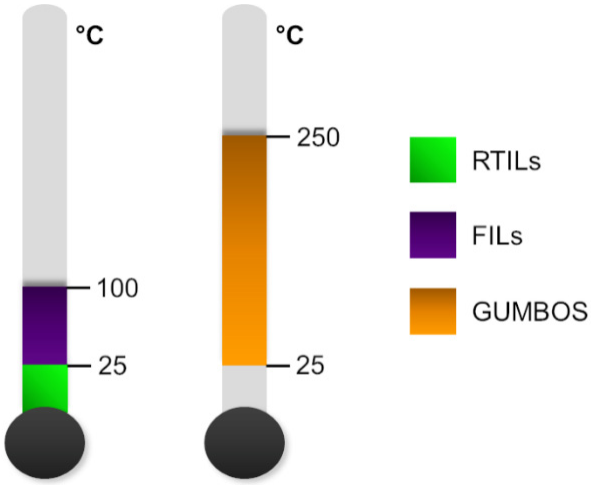

Fig. 1.3. Melting range for RTILs, FILs, and GUMBOS.

The development of solid-phase materials from organic salts has brought a new meaning to FILs, which until then had been discredited. In fact, until recently, many ILs researchers had proclaimed that you were a failure if your IL is a solid. Although solid-phase, many GUMBOS properties, including solubility, thermal stability, and fluorescence can also be tuned by varying the constituent ions (37, 97, 98). The effect of three counteranions ($BETI^-$, NTF_2^-, and OTf^-) on morphological, spectral, and physical characteristics of the propidium cation was studied by De Silva et al. It was found that the incorporation of bulkier and more hydrophobic anions ($BETI^-$ and NTF_2^-) led to lower crystallinity, higher solubility in less polar solvents (e.g. ethyl acetate, tetrahydrofuran, and dichloromethane), and greater thermal stability compared to propidium iodide. The lower stability of the parent dye is due to the nucleophilic and basic nature of the halide. Anion exchange with $BETI^-$ and NTF_2^- also resulted in an increase of quantum yield by providing a more hydrophobic environment to propidium luminophore (98). Li and coworkers from this group further demonstrated that several properties can be incorporated into a single molecule. For example, these authors synthesized four phosphonium-lanthanide compounds that simultaneously exhibited paramagnetism and luminescence, attributable to the dysprosium-containing anion, as well as tumor-targeting properties, which are assigned to the presence of the aryltriphenylphosphonium cations (99).

Due to their peculiar properties and high tunability, GUMBOS are considered promising candidates for various analytical applications, including as sensing materials for organic vapors and proteins (56, 57, 60, 100, 101) as well as MALDI matrices for analyses of peptides (42). Regmi and coworkers investigated the vapor sensing properties of composite films containing binary blends of GUMBOS and polymers using a quartz crystal microbalance (QCM) device as a sensor. They were able to demonstrate the superior potential for discrimination and molecular weight determination of various volatile analytes

using this approach (57, 100). A patent for molecular weight determination using the QCM also resulted from this research (102). Later on, this research group described preparation of two QCM sensors coated with phthalocyanine and porphyrin-based GUMBOS that displayed cross-reactive responses to different organic vapors, making this approach a promising tool for application in array-based vapor sensors (60). The estimated detection limits and sensitivities for some volatile organic compounds are compiled in Table 1.3.

Table 1.3. Summary of the concentration ranges, detection limits, and sensitivities for different volatile organic compounds.

Analyte	VOC sensor[a]	Range studied (mg L^{-1})	Detection limit (mg L^{-1})	Sensitivity (Hz/mgL^{-1})	Ref.
Acetone	$[C_4dmim][PF_6]$-CA[b]	0.19–60.8	0.0806	6.7	(57)
	$[P_{66614}]_4[CuTCPP]$	0.191–19.1	35.8[c]	__	(60)
Acetonitrile	$[C_4dmim][PF_6]$-CA[b]	0.19–15.2	0.0267	24.6	(57)
	$[P_{66614}]_4[CuTCPP]$	0.190–19.0	18.7[c]	__	(60)
Benzene	$[N_{4444}]_4[CuPcS_4]$	41–126	5.99	0.155	(56)
	$[P_{4444}]_4[CuPcS_4]$		0.951	0.165	
	$[DDMA]_4[CuPcS_4]$		3.87	0.087	
	$[P_{4448}]_4[CuPcS_4]$		3.16	0.279	
1-Butanol	$[P_{66614}]_4[CuTCPP]$	0.117–1.88	0.363[c]	__	(60)
Chloroform	$[C_4dmim][PF_6]$-CA[b]	0.36–57.0	0.1271	4.1	(57)
	$[N_{4444}]_4[CuPcS_4]$	161–405	2.57	0.362	(56)
	$[P_{4444}]_4[CuPcS_4]$		0.507	0.310	
	$[DDMA]_4[CuPcS_4]$		3.93	0.085	
	$[P_{4448}]_4[CuPcS_4]$		1.39	0.635	
	$[P_{66614}]_4[CuTCPP]$	0.357–17.9	14.3[c]	__	(60)
Dichloromethane	$[N_{4444}]_4[CuPcS_4]$	425–861	5.85	0.159	(56)
	$[P_{4444}]_4[CuPcS_4]$		1.17	0.134	
	$[DDMA]_4[CuPcS_4]$		9.07	0.037	
	$[P_{4448}]_4[CuPcS_4]$		5.45	0.162	
Ethanol	$[C_4dmim][PF_6]$-CA[b]	0.19–60.8	0.1189	5.4	(57)
	$[N_{4444}]_4[CuPcS_4]$	18–47	0.8883	1.046	(56)
	$[P_{4444}]_4[CuPcS_4]$		0.201	0.783	
	$[DDMA]_4[CuPcS_4]$		0.379	0.885	
	$[P_{4448}]_4[CuPcS_4]$		1.26	0.700	
	$[P_{66614}]_4[CuTCPP]$	0.114–11.5	2.3[c]	0.529	(60)

(continued on next page)

Table 1.3 *(continued)*

Analyte	VOC sensor[a]	Range studied (mg L^{-1})	Detection limit (mg L^{-1})	Sensitivity (Hz/mgL^{-1})	Ref.
Heptane	$[N_{4444}]_4[CuPcS_4]$	20–75	27.5	0.034	(56)
	$[P_{4444}]_4[CuPcS_4]$		2.10	0.075	
	$[DDMA]_4[CuPcS_4]$		4.72	0.071	
	$[P_{4448}]_4[CuPcS_4]$		6.89	0.128	
Hexane	$[N_{4444}]_4[CuPcS_4]$	88–258	147.5	0.006	(56)
	$[P_{4444}]_4[CuPcS_4]$		4.41	0.036	
	$[DDMA]_4[CuPcS_4]$		10.7	0.032	
	$[P_{4448}]_4[CuPcS_4]$		14.6	0.060	
Methanol	$[C_4dmim][PF_6]$-CA[b]	0.19–61.1	0.1611	3.8	(57)
	$[N_{4444}]_4[CuPcS_4]$	41–82	3.79	0.245	(56)
	$[P_{4444}]_4[CuPcS_4]$		0.237	0.662	
	$[DDMA]_4[CuPcS_4]$		5.40	0.062	
	$[P_{4448}]_4[CuPcS_4]$		6.35	0.139	
	$[P_{66614}]_4[CuTCPP]$	0.191–11.5	5.06[c]	0.167	(60)
3-Methyl-1-butanol	$[P_{66614}]_4[CuTCPP]$	0.117–1.17	0.264[c]	__	(60)
Nitromethane	$[P_{66614}]_4[CuTCPP]$	0.275–19.3	25.4[c]	__	(60)
1-Propanol	$[N_{4444}]_4[CuPcS_4]$	8–20	0.3581	2.595	(56)
	$[P_{4444}]_4[CuPcS_4]$		0.0707	2.221	
	$[DDMA]_4[CuPcS_4]$		1.33	0.252	
	$[P_{4448}]_4[CuPcS_4]$		0.324	2.724	
	$[P_{66614}]_4[CuTCPP]$	0.116–5.94	0.911[c]	__	(60)
2-Propanol	$[P_{66614}]_4[CuTCPP]$	0.114–11.5	2.39[c]	__	(60)
Toluene	$[C_4dmim][PF_6]$-CA[b]	0.21–16.7	0.0508	11.2	(57)
	$[N_{4444}]_4[CuPcS_4]$	12–41	5.50	0.169	(56)
	$[P_{4444}]_4[CuPcS_4]$		0.418	0.376	
	$[DDMA]_4[CuPcS_4]$		1.54	0.218	
	$[P_{4448}]_4[CuPcS_4]$		1.32	0.669	
	$[P_{66614}]_4[CuTCPP]$	0.209–20.9	27.3[c]	__	(60)
Xylene	$[N_{4444}]_4[CuPcS_4]$	6–15	2.17	0.428	(56)
	$[P_{4444}]_4[CuPcS_4]$		0.235	0.669	
	$[DDMA]_4[CuPcS_4]$		0.605	0.555	
	$[P_{4448}]_4[CuPcS_4]$		0.570	1.547	

[a] GUMBOS was used as the active sensing material and immobilized on the surface of a quartz crystal resonator by solvent precipitation or electrospray methods.

[b] Cellulose acetate (CA) was used to improve film's mechanical properties.

[c] μg L^{-1}.

Galpothdeniya et al. explored the potential of 6-(*p*-toluidino)-2-naphthalenesulfonate-based sensor arrays for label-free detection and differentiation of proteins and protein mixtures. The developed sensors showed distinct fluorescence responses for each of the three tested proteins and also for different concentrations of the same protein. Additionally, this sensor array approach proved suitable for distinguishing mixtures of human serum albumin and α-antitrypsin at distinct concentrations. By using principal component analysis clusters produced from various protein concentrations, data from these studies were found to follow a specific trend (101).

GUMBOS have also been evaluated as matrix materials for MALDI determination of peptides. In one study, 1-aminopyrene (AP)-based GUMBOS with different anions resulted in matrices with tailored hydrophobicity, better performance and differential interaction with hydrophobic and hydrophilic peptides. Hydrophobic matrices were found to be more selective to valinomycin and gramicidin (hydrophobic peptides). In contrast, hydrophilic matrices displayed improved signal intensity in the presence of hydrophilic (bradykinin and angiotensin II) peptides (Fig. 1.4) (42).

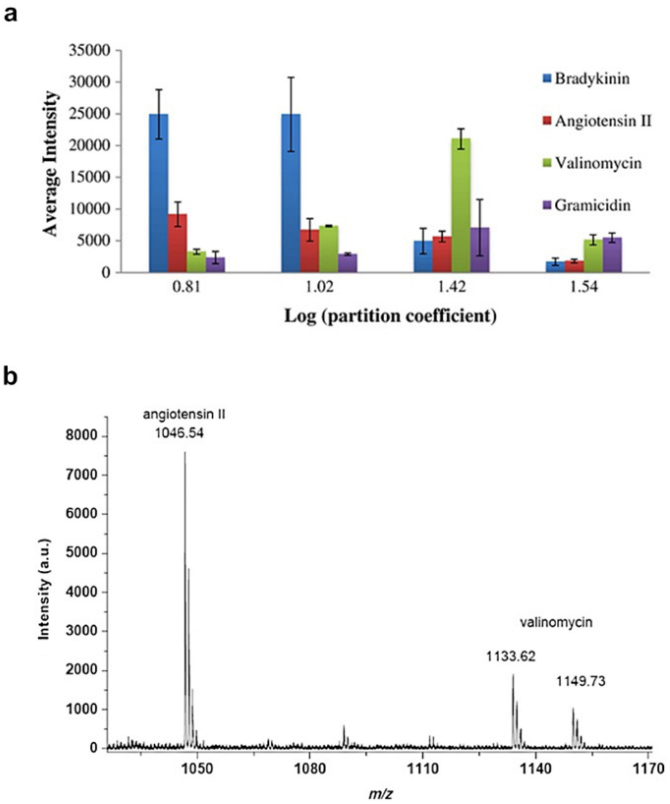

Fig. 1.4. (a) Average signal intensity plotted against the logarithm of partition coefficient of AP-derived matrices ([AP][Asc], [AP][Cl], and [AP][NTf_2], from left to right). (b) MALDI-MS spectrum in the positive ion mode of equimolar mixture of hydrophilic (angiotensin II) and hydrophobic

(valinomycin) peptides using [AP][Asc] matrix. Adapted with permission from Ref. (42). Copyright (2014) Wiley.

In the same year, Siraj and colleagues also demonstrated the ability to tune the thermal stability and fluorescence quantum yield of carbazole-derived GUMBOS through appropriate selection of the counteranion. The observed spectral and electrochemical characteristics, in combination with computed band gaps, suggest their potential use in organic light-emitting diodes (97).

The work of Kolic et al. explored the synthesis of rhodamine-, cyanine-, and porphyrin-based GUMBOS in view of their possible applications as energy relay dyes (ERDs) in dye-sensitized solar cells (DSSCs). When compared to their parent dyes, GUMBOS showed improved solubility in acetonitrile (electrolyte solvent), fluorescence quantum yield and molar extinction coefficient, making them attractive alternatives for use as ERDs. Moreover, the DSSCs fabricated from GUMBOS-derived ERDs displayed increased solar efficiencies, which seem to be dependent on anion identity (103).

The potential of GUMBOS as an alternative approach to combating bacterial infections has also been explored. In 2013, Cole et al. reported synergism and increased antibacterial activity of chlorhexidine di-ampicillin GUMBOS on seven strains of *Escherichia coli* O157:H7. Additionally, chlorhexidine di-ampicillin proved to be less toxic than its parent compounds (separately or combined), thus rationalizing its potential use in control and prevention of infections caused by enterohaemorrhagic *Escherichia coli* transmitted from ruminants (104). More recently, an extension of this work has been presented, with three more β-lactam-based chlorhexidine GUMBOS being proposed as alternatives to conventional combination drug strategy for treatment of wound infections caused by multi-drug resistant bacteria. As in the previous study, obtained results demonstrated a synergistic effect between chlorhexidine and β-lactam antibiotics when used in the form of GUMBOS. Furthermore, chlorhexidine di-carbenicillin, chlorhexidine di-cephalothin, and chlorhexidine di-oxacillin showed improved antibacterial efficacy comparable to unreacted starting materials as well as reduced toxicity against invasive cells usually present in superficial and chronic wounds (105). In subsequent work, chlorhexidine di-cephalothin and chlorhexidine di-oxacillin were loaded into hyaluronic acid/cellulose-based composites. An analysis of the results from drug release studies and Kirby-Bauer disk tests demonstrated their potential use for combating infections caused by *Staphylococcus aureus* (106).

1.4. Nanomaterials derived from GUMBOS

Materials at the nanoscale (dimensions in the 1–100 nm range) often exhibit unique properties that distinguish them from bulk counterparts, namely quantum size effects and enhanced surface area (107, 108). Compared to larger particles of the same composition, NPs possess higher surface area to volume ratio, which results, among other things, in increased solubility and allows use for the delivery of hydrophobic drugs (108-110). Additionally, the properties of NPs are dependent on particle size and shape, thus making them suitable candidates for numerous other applications in areas ranging from medicine to electronics (111).

A general overview of the synthesis methods, as well as the properties and potential applications of nanoGUMBOS is provided below.

1.4.1. Synthesis of nanoGUMBOS

Various strategies have been employed for controlled production of nanoGUMBOS with well-defined size and narrow size distribution, including both non-templated and templated synthesis methods. It has been found that size tunability can be achieved by adjusting experimental parameters such as reactants concentration, cation to anion volume ratio, and template choice. For example, when using an ultrasonication bath, the size of nanoGUMBOS decreased with reducing concentrations of reactants and ratio of cation to anion. Smaller sizes of nanoGUMBOS and increased uniformity were achieved with the use of 2-hydroxypropyl-β-cyclodextrin (HP-β-CD) and Triton X-100 micellar templates (40, 112). In addition to a soft-templating approach, a hard-template synthetic route was also described for preparation of nanoGUMBOS. One-dimensional nanostructures, e.g., nanowires, nanotubes, and nanorods were fabricated using anodic aluminum oxide membranes as templates (55, 113).

The melt-emulsion-quench (88), reprecipitation (43, 44), reverse micelle (38, 55), aerosolization (89, 114), and hydrogel-assisted (45, 46) methods have already proved useful for production of nanoGUMBOS. Nevertheless, each of these synthetic approaches has comparative pros and cons with respect to properties such as particle size and uniformity. A more detailed analysis of these methods is presented in the following subsections.

1.4.1.1. Melt-emulsion-quench approach

The first report on preparation of solid-state IL micro- and nanoparticles using a melt-emulsion-quench approach date back to 2008. In this approach, GUMBOS particles were produced from 1-butyl-2,3-dimethylimidazolium hexafluorophosphate ([C_4dmim][PF_6],

m.p.=43 ºC) via both non-surfactant and surfactant-assisted methods (57, 88). Briefly, while the first procedure begins with melting of GUMBOS, the second involves addition of the molten GUMBOS to a surfactant solution. Homogenization and probe sonication then follow, with the last step being swift quenching of the oil-in-water emulsion by immersion in ice. It was found that NPs prepared using polyoxyethylene lauryl ether (Brij® 35) were fairly uniform in size, but more irregular in shape and less spherical than those synthesized without any emulsifying agent. In addition, the surfactant-assisted method produced more monodispersed NPs due to the ability of Brij® 35 to act as a protective layer against particle coalescence (88, 89).

A melt-emulsion-quench procedure described by Tesfai et al. employs molten GUMBOS as oil phase and is advantageous for not requiring harsh conditions or use of specialized equipments or surfactants. In addition, particle shape and size can be tuned by varying various parameters, including pressure, temperature, homogenization duration, and sonication intensity (88, 89). Despite these variable parameters, control of particles size was still considered a challenge, which is why other methods have been explored for synthesis of nanoGUMBOS (40).

1.4.1.2. Reprecipitation method

The reprecipitation method commonly used in preparation of organic NPs has been adapted for synthesis of nanoGUMBOS (43, 115, 116). Similar to melt-emulsion-quench approach, this synthesis route is additive-free and does not need expensive equipment. However, this approach is more rapid and simpler to implement (43). The reprecipitation procedure starts with dissolution of GUMBOS in a ‘good’ solvent such as ethanol or tetrahydrofuran, followed by addition of an aliquot of this solution to a much larger volume of a ‘poor’ solvent (e.g., water) under sonication (43, 62). ‘Good’ and ‘poor’ solvents are those in which GUMBOS is highly and poorly soluble/insoluble, respectively. The difference in solubility of GUMBOS in the ‘good’ and ‘poor’ solvent, and the good miscibility of the two solvents play an important role in this method (117).

Although particle size can be controlled by proper selection of experimental conditions such as concentration of GUMBOS solution and volume added, this approach has proved to be a difficult task for production of NPs with diameters less than 20 nm in the absence of additives such as surfactants or polymers (Table 1.4) (40, 117). Moreover, there is a limited selection of ‘good’ and ‘poor’ solvents appropriate for reprecipitation (40, 118).

Table 1.4. Examples of nano/mesoscale GUMBOS obtained by the reprecipitation method.

Nano/mesoscale GUMBOS	Size[a]	Shape	Ref.
[BG][BETI]	[d] 30 ± 5 nm	Spherical	(48)
[HMT][AOT]	[d] 71 ± 16 nm	Spherical, slightly ovate	(43)
[HMT][TFPB]	[d] 130 ± 41 nm		
[HMT][NTf_2]	[d] 60 ± 11 nm		
[IR780][Asc]	[d] 98 ± 16 nm	Quasi-spherical, slightly ovate	(49)
[IR780][BETI]	[d] 92 ± 11 nm		
[IR780][Otf]	[d] 94 ± 12 nm		
[PEG786][NTf_2]	[d] 100–220 nm	Spherical	(47)
[PIC][BETI]	[l] 1.5 ± 0.83 μm, [w] 88 ± 26 nm	Rod-like	(51)
[PIC][BETI]–[DD][BETI]	[l] 1.5 ± 0.85 μm, [w] 101 ± 37 nm	Wire-like	(52)
[PIC][BETI]–[PC][BETI]	[l] 2.2 ± 0.75 μm, [w] 115 ± 33 nm	Rod-like network	
[PIC][NTf_2]	[l] 656 ± 139 nm, [w] 334 ± 74 nm,	Diamond-like	(51)
[PIC][NTf_2]–[DD][NTf_2]	[d] 260 ± 44 nm	Hexagonal	(52)
[PIC][NTf_2]–[PC][NTf_2]	[d] 161 ± 119 nm		
[PIC-PC][NTf_2]	[l] 189.2 ± 16.4 nm, [w] 111.4 ± 15.1 nm	Diamond-like	(66)
[Ptc][DC]	[d] 25–35 nm	Spherical	(62)
$[P_{66614}]_4$[Zn-PCS]	[d] 41.3 ± 8.7 nm	Spherical	(65)
[R6G][BETI]	101 ± 21 nm	Spherical, slightly ovate	(50)
[R6G][TPB]	92 ± 17 nm		
[TC0][BETI]	[d] 0.82 ± 0.13 μm; [l] 2.42 ± 0.20 μm	Rod-like, semi-tubular	(53)
[TC1][BETI]	[d] 153 ± 74 nm; [l] 0.53 ± 0.16 μm	Rod/wire-like	
[TC2][BETI]	[d] 137 ± 37 nm; [l] 3.16 ± 1.13 μm	Wire-like	
[1048][Folate]	[d] 121 ± 32.5 nm	Spherical	(67)
[1061][Folate]	[d] 144 ± 46.8 nm	Spherical	

[a] Particle size was determined using transmission electron microscopy (TEM).
[d] Diameter.
[l] Length.
[w] Width.

1.4.1.3. Reverse micelle strategy

Interest in using a reverse micellar template arises primarily from its ability to produce uniform and size-controlled NPs (38, 119). Unlike the melt-emulsion-quench approach, this strategy also has the advantage of providing smaller particle sizes but requires use of toxic organic solvents (119, 120). Ultimately, it may also be necessary to perform a purification step (e.g. centrifugation) (55, 121).

In a typical reverse micellar procedure, each reactant is separately solubilized within water-in-oil microemulsions of the same composition. After a microemulsions mixing step, the exchange of reacting species occurs by coalescence of reverse micelles. The reaction between solubilized reactants and splitting of fused reverse micelles into smaller droplets containing GUMBOS particles follows. It is worth mentioning that the aqueous core of reverse micelles acts as a nanoreactor for synthesis of NPs and that its size can be controlled by altering the water to surfactant molar ratio. In turn, the surfactant helps in formation of small-sized and stable particles (38, 119, 122, 123).

Similar to the aforementioned synthesis methods, the reverse micelle strategy also allows control of particles size through variations in parameters such as solvent composition, temperature, reactant, and surfactant concentrations. In fact, a direct relationship between concentration of reactant and size and uniformity of nanoGUMBOS was demonstrated. By decreasing reactant concentrations, the average diameter of NPs and the polydispersity were reduced (38, 55).

1.4.1.4. Aerosolization process

The aerosolization process begins with generation of an aerosol from GUMBOS stock solution. In order to remove humidity, the aerosolized solution passes through a silica dryer, and then sent to an electrostatic classifier. It follows the passage of size-selected nanodroplets through a tube furnace and collection of dry particles on a polytetrafluoroethylene filter (89, 114). The size and uniformity of synthesized particles are influenced by the air flow rate, concentration of GUMBOS solution, and temperature of furnace (89).

Unlike the previously described strategies for synthesis of nanoGUMBOS, the aerosol technique requires expensive and specialized equipment, and can lead to NPs aggregation because of the elevated temperatures employed in the process. However, this approach can produce high-purity NPs and has potential for industrial scalability (124, 125).

1.4.1.5. Hydrogel-assisted method

More recently, hydrogels have also been used as templates for synthesis of nanoGUMBOS. The size of NPs prepared using the hydrogel-assisted method is dependent on GUMBOS' chemical structure and hydrogel conditions (pH and concentration of tris(hydroxymethyl)aminomethane (TRIS) buffer). For instance, opposite trends were observed for 1,1′,3,3,3′,3′-hexamethylindotricarbocyanine (HMT)-derived nanoGUMBOS as a result of differences in hydrophobicity. Additionally, with increasing TRIS concentration, the average size of [HMT][NTf_2] nanoGUMBOS was found to decrease, while for [HMT][AOT] the particle size was observed to increase (45, 46).

In contrast to the aerosolization process, the hydrogel-assisted method does not involve use of specialized equipment. In fact, this procedure is easy to implement, only requiring addition of GUMBOS solution to sodium deoxycholate in TRIS buffer, followed by sonication (45, 46). This approach also allows NPs with low polydispersity, but does not easily produce nanoGUMBOS with reduced size (40).

1.4.2. Properties and applications

NMs derived from GUMBOS combine the versatility of these solid-phase compounds with the improved features obtained at nanoscale, allowing mimicry or even amelioration of characteristics of commonly used NPs (38, 113). For instance, brilliant green bis(pentafluoroethylsulfonyl)imide ([BG][BETI]) nanoGUMBOS displayed increased NIR fluorescence as compared to BG dye in water. Additionally, its second harmonic generation signal was about 7 to 23-fold greater than that of colloidal gold nanospheres of the same size and BG dye, respectively. Unlike the gold NPs and molecular dye, a clear third harmonic generation signal for [BG][BETI] nanoGUMBOS was also observed (Fig. 1.5) (48). Moreover, nanoGUMBOS with reduced toxicity can be synthesized using biological raw materials such as vitamins, thus providing a viable alternative to NPs that pose potential hazards to human health and environment (67, 126, 127).

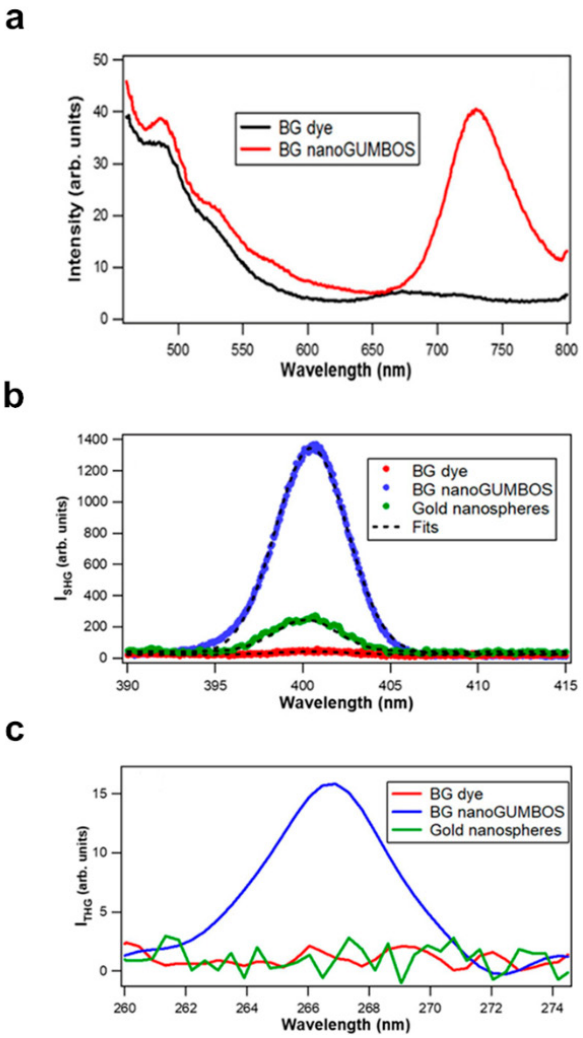

Fig. 1.5. (a) Fluorescence emission spectra of BG dye and BG-based nanoGUMBOS in water. (b) Second and (c) third harmonic generation spectra of BG dye, [BG][BETI] nanoGUMBOS, and gold nanospheres in water. Adapted with permission from Ref. (48). Copyright (2017) AIP Publishing.

The tunability of the morphological, spectral, and surface charge properties of nanoGUMBOS is associated with cation-anion combinations (41, 51). For example, Wright and colleagues showed that the morphology of gold-shelled nanostructures is dependent on GUMBOS used as core material (Fig. 1.6). Thus, spherical NPs were obtained from 1-methyl-3-propylimidazolium bis(trifluoromethylsulfonyl)imide ([C_3mim][NTf_2]), while nanorods were produced from 1-methyl-3-propylimidazolium tetraphenylborate ([C_3mim][TPB]). The optical properties of NPs were demonstrated to be related to particle size and ratio of gold hydroxide solution to gold-seeded nanoGUMBOS, whereas nanorods displayed enhanced absorption in both visible and NIR regions (55). In addition, Kolic et al. demonstrated that both size and surface charge of porphyrin-based nanoGUMBOS can be controlled by simply varying the ratio of cation to anion through ion association, eliminating the need for additives or stabilizers. Moreover, analysis of spectroscopic results revealed

that these NPs exhibit a broad absorbance spectrum as compared to the respective parent dyes. NanoGUMBOS derived from meso-tetra(4-carboxyphenyl)porphine also displayed increased fluorescence intensity (41).

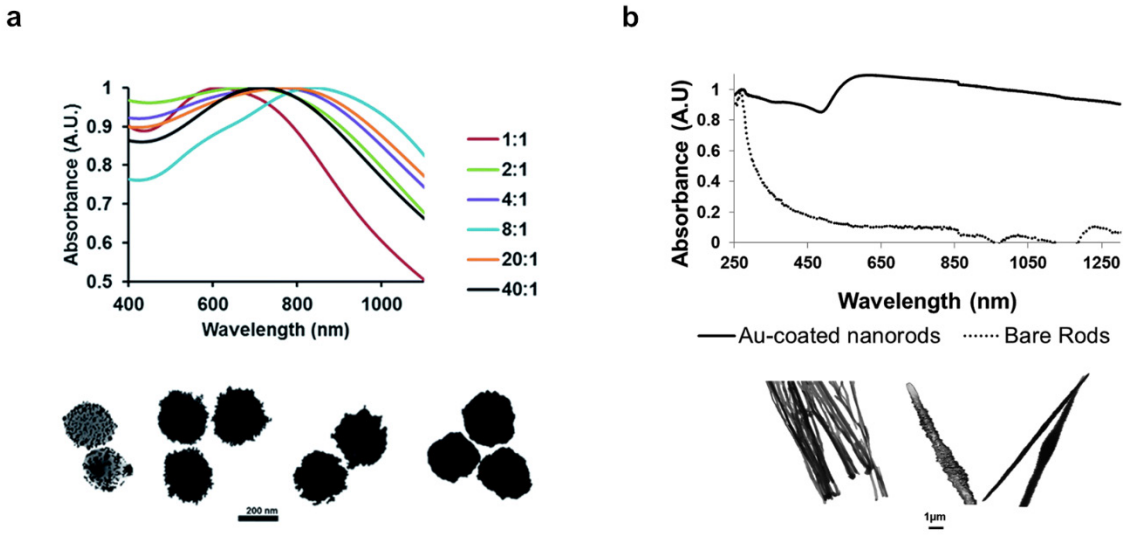

Fig. 1.6. Normalized absorbance spectra and TEM micrographs of gold-shelled nanoGUMBOS built around (a) [C_3mim][NTf_2] and (b) [C_3mim][TPB] as core materials. Adapted with permission from Ref. (55). Copyright (2014) Royal Society of Chemistry.

To date, there are already nanoGUMBOS synthesized and characterized with photothermal (61), photodynamic (128), luminescent (114), and magnetic (38) properties, among others. As a result of their tunable morphological and spectral features as well as *in vitro* behavior, these NMs are identified as promising candidates for an extended list of possible uses, including biomedical imaging (43), cancer therapy (68), sensing (66), and solid-phase extraction (59), as will be evident from discussions in the following paragraphs.

Dumke et al. evaluated the photothermal properties of NIR-absorbing nanoGUMBOS formed by the combination of two cationic dyes ([1048] and [1061]) with two biocompatible anions (deoxycholate and ascorbate). These studies were performed at distinct pH values and revealed differences in physical and spectral characteristics. Furthermore, upon exposure to NIR irradiation at 1064 nm, the temperature increased an average of 20.4 ± 2.7 ºC, and photothermal efficiency varied according to both cation and anion components (68). *In vitro* studies of folate-derived NIR-absorbing nanoGUMBOS were performed in MDA-MB-231 breast cancer cell line. The synthesized NPs ([1048][Folate] and [1061][Folate]) generated heat upon NIR laser irradiation, which led to substantial reduction of cancer cell viability. Moreover, in the absence of irradiation and at low concentrations, folate-based nanoGUMBOS exhibited little toxicity towards both cancerous and non-cancerous cells. The obtained results demonstrate the potential of this class of compounds as valuable

hyperthermal delivery systems (67). More recently, it was found that the aqueous stability, photostability, and photothermal properties of IR780 dye can be improved by counteranion exchange and subsequent conversion to nanoGUMBOS using HP-β-CD. It was postulated that when sonicated, CD would undergo crosslinking via hydrogen bonding between the hydroxyl groups. The results from *in vitro* and *in vivo* studies showed enhanced selective toxicity against cancer cells and increased photothermal efficacy upon laser irradiation, making possible its application in photothermal therapy. In addition, NIR fluorescent imaging revealed preferential accumulation and prolonged retention of CD-[IR780][TPB] nanoGUMBOS at the tumor site, allowing its use as both imaging agents and drug carriers (Fig. 1.7) (61).

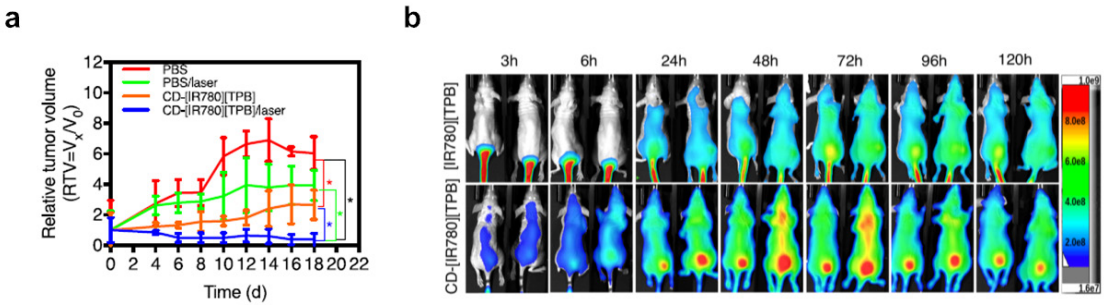

Fig. 1.7. (a) Relative tumor volume upon treatments with and without CD-based nanoGUMBOS/laser irradiation. (b) In vivo NIR fluorescent imaging of [IR780][TPB] nanoGUMBOS formed in the absence and presence of CD. Adapted with permission from Ref. (61). Copyright (2019) American Chemical Society.

Magut and colleagues assessed the effect of distinct anions on the hydrophobicity and cytotoxicity of rhodamine 6G (R6G). Hydrophilic GUMBOS ([R6G][OTf] and [R6G][Asc]) showed no selectivity for cancer cell lines. In contrast, NPs prepared from hydrophobic [R6G][TPB] and [R6G][BETI] GUMBOS revealed to be nontoxic to normal human breast fibroblasts, but inhibited proliferation of cancer cell lines in a concentration dependent manner. Moreover, MTT results showed that [R6G][TPB] and [R6G][BETI] nanoGUMBOS exhibited increased toxicity towards more invasive and aggressive breast cancer cell lines. These findings are particularly remarkable since they demonstrate the ability to reduce chemotherapeutic toxicity (50). A year later, electro-optical characterization of [R6G][TPB] nanoGUMBOS was performed by use of conductive probe atomic force microscopy (CP-AFM) and Raman spectroscopy. CP-AFM measurements showed current values between ~10^{-6} and 10^{-7} A, for voltage from 0 to +1 V, and the Raman spectra did not reveal significant differences to R6G, further confirming that the synthetic procedure did not change the chemical composition or significantly alter the dye's vibrational modes. The results also

suggest potential applications of [R6G][TPB] nanoGUMBOS in optoelectronics and sensing (39).

In recent years, the utility of nanoGUMBOS as theranostic agents has been investigated. For this purpose, Das et al. designed iron(III) phthalocyanine (Ptc)-based NPs with magnetic, pH-responsive, and fluorescent properties. After converting bulk [Ptc][DC] into nanosized particles, clear changes in magnetic characteristics were observed (from diamagnetic to paramagnetic, respectively). At the same time, these NPs proved useful as pH-responsive carriers of doxorubicin for cancer therapy. Doxorubicin loaded NPs reduced cancer cell viability in a concentration dependent manner, but did not significantly inhibit normal breast cells, even at highest concentration tested (100 μmol L^{-1}). Additionally, confocal fluorescence microscopic images of MDA-MB-231 cancer cell line, after a short incubation period of 2 h with empty NPs, evidenced their potential for simultaneous application in imaging and therapy (62). In subsequent work, it was further demonstrated that nanoGUMBOS incorporating a molecular recognition element can be synthesized and used for theranostic purposes. NanoGUMBOS molecularly imprinted polymers (NGMIPs) towards chiral recognition of L-tryptophan were prepared using four vinylimidazole IL crosslinkers. The resulting NGMIPs displayed higher binding affinity as compared to traditional molecularly imprinted polymers (~10-fold increase) and achieved good chiral differentiation of tryptophan enantiomers, with benzene-NGMIP showing the greatest enantiomeric binding ratio (13:1). These results can be explained by interactions with the imidazolium ring of the crosslinker, along with dipole interactions and/or π-stacking between the benzene spacer and aromatic region of L-tryptophan template. It is also worth noting that the use of crosslinking ILs in the synthesis of NMs enabled the imprinting process to be carried out in aqueous solutions rather than organic solvents, making this strategy a promising tool for molecular imprinting of water-soluble targets (129).

Several studies have described synthesis of nanoGUMBOS from cyanine dyes, that are known to form J- and H-type aggregates through self-assembly (43, 44, 47, 51-54, 66). Bwambok et al. noticed changes in the spectral properties of HMT-derived GUMBOS upon conversion into nanoGUMBOS. The increasing extension of absorption bands (well over two hundred nanometers in width) and slight hypsochromic shift in fluorescence emission spectra were attributed to dye aggregation within nanoGUMBOS. Additionally, the results from cellular uptake studies evidenced that [HMT][AOT] nanoGUMBOS can be efficiently internalized by Vero cells, suggesting their potential use for biomedical imaging. This strategy also mitigates dye leakage problems and avoids intense purification procedures that are necessary when using surfactants to produce dye NPs (43). In a follow-up manuscript, it was further demonstrated that spectral features of HMT-based nanoGUMBOS can be tuned by counteranion exchange (from I^- to AOT^-, NTf_2^-, $TFPB^-$, $BETI^-$

, or $TFP4B^-$) and explained by the ratio of J to H components (Fig. 1.8). For example, the predominance of J component in [HMT][AOT] nanoGUMBOS was responsible for one of the highest fluorescence signals, whereas [HMT][TFP4B] was practically nonfluorescent due to the lowest J/H ratio (<1) (44).

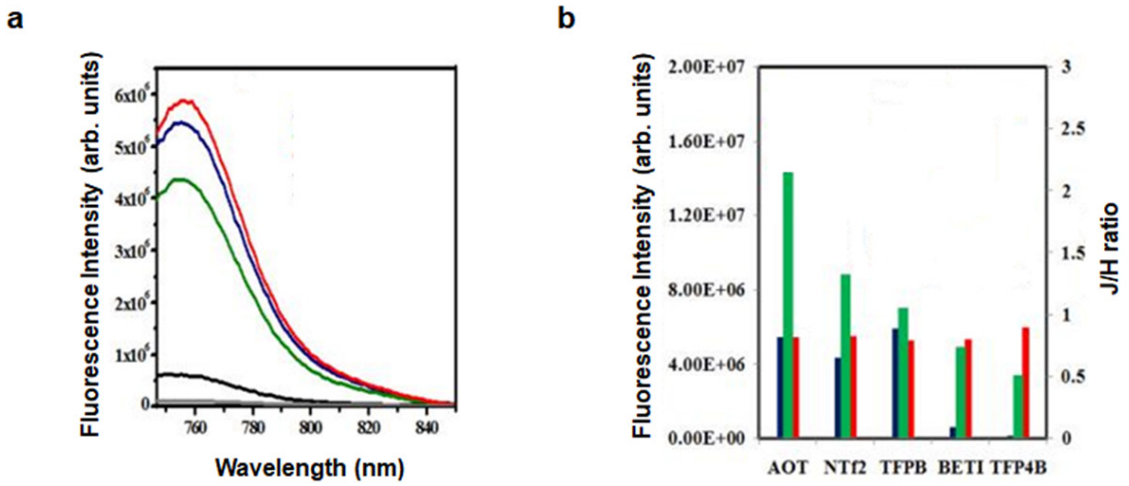

Fig. 1.8. (a) Fluorescence emission spectra of HMT-based nanoGUMBOS: [HMT][TFPB] (red); [HMT][AOT] (blue); [HMT][NTf_2] (green); [HMT][BETI] (black); and [HMT][TFP4B] (grey). (b) Fluorescence intensity of nanoGUMBOS in water (blue), ethanolic solutions of GUMBOS (red), and J/H ratio of nanoGUMBOS (green). Adapted with permission from Ref. (44). Copyright (2010) American Chemical Society.

Lu and coworkers have reported that irradiation leads to J-aggregate formation, and subsequently to increased fluorescence of the PEGylated IR786 nano- and mesoscale GUMBOS. It was found that their photostability is dependent both on the anion and concentration. [PEG786][AOT] displayed much greater photostability than [PEG786][NTf_2] and higher concentrations of either nano- and mesosized GUMBOS produced an enhancement in fluorescence intensity after irradiation for more than 500 s. Furthermore, PEG chains appear to form a protective layer around the cyanine dye, which results in reduced nonspecific protein binding and cytotoxicity (47). In the same year, a non-templated approach for controlling the morphology and spectral properties of 1,1'-diethyl-2,2'-cyanine (PIC)-based nanoGUMBOS was described for the first time. Transmission and scanning electron microscopy micrographs of these NPs revealed changes in morphology upon anion exchange with NTf_2^- and $BETI^-$. Additionally, the formation of J-aggregates within the diamond-shaped [PIC][NTf_2] nanoGUMBOS resulted in a 590-fold increase in fluorescence intensity and a 2 times enhancement in quantum yield as compared to the parent compound ([PIC][I]). In contrast, the H-aggregation of [PIC][BETI] nanorods resulted in blue-shifted absorption and reduced birefringence. The fluorescence quantum yield of [PIC][BETI]

nanoGUMBOS also exhibited an increase of one order of magnitude as compared to [PIC][I]. Ultimately, the wide absorption spectra (from visible to NIR region) justifies the use of these NMs as photosensitizers in solar cells (51). In a subsequent study, the electro-optical characterization of [PIC][NTf_2] and [PIC][BETI] nanoGUMBOS was performed by use of CP-AFM and Raman spectroscopy. The current-voltage curves of PIC-based nanoGUMBOS obtained using CP-AFM showed current values ranging from 10^{-10} to 10^{-7} A when stepping the voltage between -1 to +1 V. Additionally, J-aggregation of [PIC][NTf_2] nanoGUMBOS caused an increase of approximately 25 and 38 times in Raman signal intensity when compared to [PIC][I] raw material and [PIC][BETI] nanoGUMBOS, respectively. Overall, these results further corroborate application prospects of PIC-based nanoGUMBOS for optoelectronic applications (54).

Over the last years, some works have been devoted toward preparation of blended NMs, having explored Förster resonance energy transfer (FRET) phenomenon. In this context, binary and ternary thiacarbocyanine-derived nanostructures were found to exhibit tunable spectral characteristics that were attributed to FRET. Moreover, both morphological and spectral features were found to be dependent on the concentration of thiacarbocyanine-based species (53). In a similar study, binary nano- and mesoscale GUMBOS were synthesized using previously described PIC-based GUMBOS as donors, and longer methine chain cyanine-based GUMBOS (1,1'-diethyl-2,2'-carbocyanine, PC, and 1,1'-diethyl-2,2'-dicarbocyanine, DD) as acceptors. Unlike PC- and DD-based nanoGUMBOS, which were essentially non-fluorescent in aqueous suspension, these binary materials displayed significant fluorescence enhancement as a result of FRET. Additionally, these binary cyanine-based nanoGUMBOS exhibited broad absorption and fluorescence peaks that extend into the NIR region as a function of donor/acceptor molar ratio. The results from stability studies also evidenced higher photostability for these binary NMs as compared to the individual nanoGUMBOS with identical anions. On this basis, applications of these blended NMs for sensing and light harvesting were proposed (52). More recently, Cong and coworkers developed a ratiometric fluorescent nanoprobe based on FRET for hydroxyl radical detection. To achieve this goal, binary [PIC-PC][NTf_2] nanoGUMBOS were produced by reprecipitation of both GUMBOS and without chemical linkage. This nanoprobe showed higher selectivity for the hydroxyl radical than for other reactive oxygen species (ROS), namely superoxide anion ($O_2^{\cdot-}$), singlet oxygen ($^1O_2$), peroxynitrite anion ($ONOO^-$), and hydrogen peroxide (H_2O_2) (Fig. 1.9). The obtained results can be attributed to the difference in alkyl chain length of PIC and PC cations, which leads to distinct reduction potentials and ultimately different ROS reactivity, enabling a ratiometric fluorescence detection of ROS. Additionally, the rapid sensing response of binary nanoGUMBOS proved to overcome the

problem of reduced hydroxyl radical lifetime. This novel nanoprobe also showed utility for *in vitro* detection of hydroxyl radical in MDA-MB-231 breast cancer cells (66).

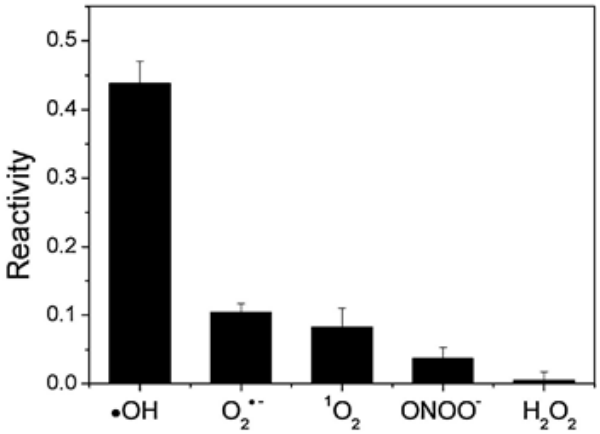

Fig. 1.9. Reactivity of the binary [PIC-PC][NTf_2] nanoprobe towards different ROS. Adapted with permission from Ref. (66). Copyright (2018) Elsevier.

A novel imidazolium-dysprosium-based magnetic nanoGUMBOS ($[C_{16}mim]_5[Dy(SCN)_8]$) was synthesized using a simple reprecipitation method for isolation of hemoglobin. The imidazolium cation was chosen because of its affinity to the heme group of hemoglobin, while dysprosium confers paramagnetic properties. The obtained results showed higher selectivity and adsorption efficiency towards hemoglobin over other proteins used in the study (Table 1.5). This can be ascribed to interactions between the nitrogen atom in the imidazolium cation and the ferrous atom in the heme group, with hydrophobic interactions also playing an important role. By using 1% (m/v) sodium dodecyl sulfate (SDS) solution, hemoglobin adsorbed on $[C_{16}mim]_5[Dy(SCN)_8]$ nanoGUMBOS could be recovered with an elution efficiency of 87%. Although circular dichroism measurements showed slight changes in hemoglobin conformation when dissolved in SDS solution, it stays mainly as α-helix. This nanoGUMBOS solid-phase extraction procedure proved also useful for selective isolation of hemoglobin from human whole blood (59). One of the advantages of nanoGUMBOS compared to other solid-phase extraction adsorbents is the simplicity of the preparation procedure, not requiring surface modification with affinity ligands to improve the selectivity of extraction or time-consuming purification steps (130, 131). Additionally, these NPs exhibit a fast adsorption rate and favorable adsorption capacity to hemoglobin (approximately 840 μg mL^{-1}). Overall, these results further support the application of nanoGUMBOS as adsorbents for selective isolation of proteins (59).

Table 1.5. Protein adsorption efficiency of $[C_{16}mim]_5[Dy(SCN)_8]$ nanoGUMBOS. Adapted with permission from Ref. (59). Copyright (2019) Elsevier.

Tested protein	Isoelectric point (pI)	Molecular weight (kDa)	Maximum adsorption efficiency (%)	Standard deviation (%)
Transferrin	5.2	80	6.8	2.72
Human serum albumin	5.3	66.5	10.0	4.53
Hemoglobin	6.9	64.5	95.4	4.27
Cytochrome c	10.7	12	12.8	7.21
Lysozyme	11.3	14.3	7.9	2.74

1.5. Other examples of solid-phase ILs chemistry

Besides the literature on GUMBOS and nanoGUMBOS, there are a few more references related to solid-phase ionic materials. Similar to what happens with ILs, there is no uniformity of terminology among these studies. For instance, 'solid ionic liquids' have been defined as salts with melting points below 120–140 ºC and have been applied as sorbents for CO_2 capture after immobilization on cellulose supports by a wet coating technique (132, 133). In addition, the terms 'ion-based organic NPs' and 'organic dye NPs' have been used to refer to NPs that appear to be identical to nanoGUMBOS (134-136). A method called 'ion-association' has also been reported for preparation of organic NPs in aqueous media, including NPs of 8-anilino-1-naphthalenesulfonate (137), cyanine (138), malachite green (139), porphyrin (140), and styryl (141) dyes. The optical properties of these type of NPs have also been investigated and appear to be related to particle size. Furthermore, the large increase observed in dye fluorescence is attributed to the synergistic effect between intermolecular H-aggregation and limited intramolecular rotation (142, 143). Another interesting example is the possibility of tuning the fluorescence color of 3,3'-diethylthiacyanine (TC0)-based NPs through FRET. Indeed, upon doping with ethidium, TC0-based NPs act as light harvesting antennae and transfer energy to the dopant acceptor, resulting in changes in color emission (144).

1.6. Motivation and goals

GUMBOS share similar traits with ILs and provide an extraordinary potential for extending applications of ILs chemistry. As they are tailored materials, they can be designed by judicious choice of the cations and anions for ion exchange to tune properties and increase the prospects of these materials for specific uses, including analytical ones. These

advantages have been extended to synthesis of nanoGUMBOS with a variety of shapes and spectral characteristics suitable for several purposes.

From a different perspective, although GUMBOS and nanoGUMBOS are potentially less toxic than other materials, toxicity and biodegradability studies are required to clarify their impact on the environment and human health. There are several works devoted to physicochemical characterization of GUMBOS and nanoGUMBOS with an objective to illustrate their applicability. However, far less attention has been paid to their biological behavior.

The amount of research on GUMBOS-based materials gives only a glance of their full potential and provides motivation for further developments in the analytical field. In this regard, the studies presented in this dissertation focus on development of novel ionic materials with properties tailored for specific applications. This work plan includes three main tasks, with the first consisting of the design, synthesis, and characterization of GUMBOS (and nanoGUMBOS) derived from selected dyes that are traditionally difficult to modify. Second, their potential use as optical probes for discrimination and quantification of proteins or as antibacterial agents is investigated. These developed approaches are expected to overcome limitations associated with the parent ions and/or the methodologies that are conventionally used for the same purpose. In addition, the studies outlined in this dissertation are intended to enhance sensitivity of such materials, while providing alternative safer strategies that avoid using toxic chemicals. With this in mind, the third objective of this dissertation is the in vitro toxicity screening of synthesized materials. This evaluation will use cell-based assays that can provide rapid and reliable results, ultimately contributing to a more sustainable development of ionic materials.

References

1. Wilkes JS. A short history of ionic liquids - from molten salts to neoteric solvents. Green Chem. 2002;4(2):73-80.

2. Hough WL, Rogers RD. Ionic liquids then and now: From solvents to materials to active pharmaceutical ingredients. Bull Chem Soc Jpn. 2007;80(12):2262-9.

3. Wilkes JS. Molten salts and ionic liquids - are they not the same thing? ECS Trans. 2007;3(35):3-7.

4. Frost DS, Nofen EM, Dai LL. Particle self-assembly at ionic liquid-based interfaces. Adv Colloid Interface Sci. 2014;206:92-105.

5. Shi R, Wang YT. Dual ionic and organic nature of ionic liquids. Sci Rep. 2016;6:19644.

6. Seddon KR. Ionic liquids for clean technology. J Chem Technol Biotechnol. 1997;68(4):351-6.

7. Lopez-Martin I, Burello E, Davey PN, Seddon KR, Rothenberg G. Anion and cation effects on imidazolium salt melting points: A descriptor modelling study. ChemPhysChem. 2007;8(5):690-5.

8. Ohno H, Yoshizawa M. Ion conductive characteristics of ionic liquids prepared by neutralization of alkylimidazoles. Solid State Ion. 2002;154:303-9.

9. Zhang H, Li MT, Yang BL. Design, Synthesis, and Analysis of Thermophysical Properties for Imidazolium-Based Geminal Dicationic Ionic Liquids. J Phys Chem C. 2018;122(5):2467-74.

10. Holbrey JD, Reichert WM, Nieuwenhuyzen M, Johnston S, Seddon KR, Rogers RD. Crystal polymorphism in 1-butyl-3-methylimidazolium halides: supporting ionic liquid formation by inhibition of crystallization. Chem Commun. 2003(14):1636-7.

11. Endo T, Morita T, Nishikawa K. Crystal polymorphism of a room-temperature ionic liquid, 1,3-dimethylimidazolium hexafluorophosphate: calorimetric and structural studies of two crystal phases having melting points of ~50K difference. Chem Phys Lett. 2011;517(4-6):162-5.

12. MacFarlane DR, Forsyth M, Howlett PC, Kar M, Passerini S, Pringle JM, et al. Ionic liquids and their solid-state analogues as materials for energy generation and storage. Nat Rev Mater. 2016;1(2):15005.

13. Vekariya RL. A review of ionic liquids: applications towards catalytic organic transformations. J Mol Liq. 2017;227:44-60.

14. Lopes JNC, Gomes MFC, Padua AAH. Nonpolar, polar, and associating solutes in ionic liquids. J Phys Chem B. 2006;110(34):16816-8.

15. Huddleston JG, Visser AE, Reichert WM, Willauer HD, Broker GA, Rogers RD. Characterization and comparison of hydrophilic and hydrophobic room temperature ionic liquids incorporating the imidazolium cation. Green Chem. 2001;3(4):156-64.
16. Klähn M, Stüber C, Seduraman A, Wu P. What determines the miscibility of ionic liquids with water? Identification of the underlying factors to enable a straightforward prediction. J Phys Chem B. 2010;114:2856-68.
17. Seki S, Kobayashi T, Kobayashi Y, Takei K, Miyashiro H, Hayamizu K, et al. Effects of cation and anion on physical properties of room-temperature ionic liquids. J Mol Liq. 2010;152(1-3):9-13.
18. Vogl T, Goodrich P, Jacquemin J, Passerini S, Balducci A. The influence of cation structure on the chemical–physical properties of protic ionic liquids. J Phys Chem C. 2016;120(16):8525-33.
19. Vaz ICM, Bastos M, Bernardes CES, Lopes JNC, Santos L. Solvation of alcohols in ionic liquids - understanding the effect of the anion and cation. Phys Chem Chem Phys. 2018;20(4):2536-48.
20. Costa SPF, Azevedo AMO, Pinto PCAG, Saraiva MLMFS. Environmental impact of ionic liquids: recent advances in (eco)toxicology and (bio)degradability. ChemSusChem. 2017;10(11):2321-47.
21. Hough-Troutman WL, Smiglak M, Griffin S, Reichert WM, Mirska I, Jodynis-Liebert J, et al. Ionic liquids with dual biological function: sweet and anti-microbial, hydrophobic quaternary ammonium-based salts. New J Chem. 2009;33(1):26-33.
22. Pernak J, Niemczak M, Zakrocka K, Praczyk T. Herbicidal ionic liquid with dual-function. Tetrahedron. 2013;69(38):8132-6.
23. Nawala J, Dawidziuk B, Dziedzic D, Gordon D, Popiel S. Applications of ionic liquids in analytical chemistry with a particular emphasis on their use in solid-phase microextraction. Trac-Trends Anal Chem. 2018;105:18-36.
24. Trujillo-Rodriguez MJ, Nan H, Varona M, Emaus MN, Souza ID, Anderson JL. Advances of Ionic Liquids in Analytical Chemistry. Anal Chem. 2019;91(1):505-31.
25. Liu HT, Liu Y, Li JH. Ionic liquids in surface electrochemistry. Phys Chem Chem Phys. 2010;12(8):1685-97.
26. Lu XY, Burrell G, Separovic F, Zhao C. Electrochemistry of room temperature protic ionic liquids: a critical assessment for use as electrolytes in electrochemical applications. J Phys Chem B. 2012;116(30):9160-70.
27. Roosen C, Muller P, Greiner L. Ionic liquids in biotechnology: applications and perspectives for biotransformations. Appl Microbiol Biotechnol. 2008;81(4):607-14.
28. Claus J, Sommer FO, Kragl U. Ionic liquids in biotechnology and beyond. Solid State Ion. 2018;314:119-28.

29. Werner S, Haumann M, Wasserscheid P. Ionic liquids in chemical engineering. Annu Rev Chem Biomol Eng. 2010;1:203-30.
30. Amiril SAS, Rahim EA, Syahrullail S. A review on ionic liquids as sustainable lubricants in manufacturing and engineering: recent research, performance, and applications. J Clean Prod. 2017;168:1571-89.
31. Azevedo AMO, Ribeiro DMG, Pinto PCAG, Lucio M, Reis S, Saraiva MLMFS. Imidazolium ionic liquids as solvents of pharmaceuticals: influence on HSA binding and partition coefficient of nimesulide. Int J Pharm. 2013;443(1-2):273-8.
32. Pinto PCAG, Ribeiro DMGP, Azevedo AMO, Dela Justina V, Cunha E, Bica K, et al. Active pharmaceutical ingredients based on salicylate ionic liquids: insights into the evaluation of pharmaceutical profiles. New J Chem. 2013;37(12):4095-102.
33. Egorova KS, Gordeev EG, Ananikov VP. Biological activity of ionic liquids and their application in pharmaceutics and medicine. Chem Rev. 2017;117(10):7132-89.
34. Plechkova NV, Seddon KR. Applications of ionic liquids in the chemical industry. Chem Soc Rev. 2008;37(1):123-50.
35. Hijo AACT, Maximo GJ, Costa MC, Batista EAC, Meirelles AJA. Applications of ionic liquids in the food and bioproducts industries. ACS Sustain Chem Eng. 2016;4(10):5347-69
36. Martins PLG, Braga AR, de Rosso VV. Can ionic liquid solvents be applied in the food industry? Trends Food Sci Technol. 2017;66:117-24.
37. Warner IM, El-Zahab B, Siraj N. Perspectives on Moving Ionic Liquid Chemistry into the Solid Phase. Anal Chem. 2014;86(15):7184-91.
38. Tesfai A, El-Zahab B, Kelley AT, Li M, Garno JC, Baker GA, et al. Magnetic and nonmagnetic nanoparticles from a group of uniform materials based on organic salts. ACS Nano. 2009;3(10):3244-50.
39. Sarkar A, Kanakamedala K, Rajathadripura MD, Jagadish NN, Magut PKS, de Rooy S, et al. Electro-Optical Characterization of nanoGUMBOS. Electron Mater Lett. 2014;10(4):775-81.
40. Hamdan S, Dumke JC, El-Zahab B, Das S, Boldor D, Baker GA, et al. Strategies for controlled synthesis of nanoparticles derived from a group of uniform materials based on organic salts. J Colloid Interface Sci. 2015;446:163-9.
41. Kolic PE, Siraj N, Hamdan S, Regmi BP, Warner IM. Synthesis and characterization of porphyrin-based GUMBOS and nanoGUMBOS as improved photosensitizers. J Phys Chem C. 2016;120(9):5155-63.
42. Al Ghafly H, Siraj N, Das S, Regmi BP, Magut PK, Galpothdeniya WI, et al. GUMBOS matrices of variable hydrophobicity for matrix-assisted laser desorption/ionization mass spectrometry. Rapid Commun Mass Spectrom. 2014;28(21):2307-14.

43. Bwambok DK, El-Zahab B, Challa SK, Li M, Chandler L, Baker GA, et al. Near-infrared fluorescent nanoGUMBOS for biomedical imaging. ACS Nano. 2009;3(12):3854-60.

44. Das S, Bwambok D, El-Zahab B, Monk J, de Rooy SL, Challa S, et al. Nontemplated approach to tuning the spectral properties of cyanine-based fluorescent nanoGUMBOS. Langmuir. 2010;26(15):12867-76.

45. Das S, de Rooy SL, Jordan AN, Chandler L, Negulescu II, El-Zahab B, et al. Tunable size and spectral properties of fluorescent nanoGUMBOS in modified sodium deoxycholate hydrogels. Langmuir. 2012;28(1):757-65.

46. McNeel KE, Das S, Siraj N, Negulescu II, Warner IM. Sodium deoxycholate hydrogels: effects of modifications on gelation, drug release, and nanotemplating. J Phys Chem B. 2015;119(27):8651-9.

47. Lu C, Das S, Magut PK, Li M, El-Zahab B, Warner IM. Irradiation induced fluorescence enhancement in PEGylated cyanine-based NIR nano- and mesoscale GUMBOS. Langmuir. 2012;28(40):14415-23.

48. Karam TE, Siraj N, Zhang Z, Ezzir AF, Warner IM, Haber LH. Ultrafast and nonlinear spectroscopy of brilliant green-based nanoGUMBOS with enhanced near-infrared emission. J Chem Phys. 2017;147(14):144701-7.

49. Chen M, Bhattarai N, Cong MY, Perez RL, McDonough KC, Warner IM. Mitochondria targeting IR780-based nanoGUMBOS for enhanced selective toxicity towards cancer cells. RSC Adv. 2018;8(55):31700-9.

50. Magut PK, Das S, Fernand VE, Losso J, McDonough K, Naylor BM, et al. Tunable cytotoxicity of rhodamine 6G via anion variations. J Am Chem Soc. 2013;135(42):15873-9.

51. Jordan AN, Das S, Siraj N, de Rooy SL, Li M, El-Zahab B, et al. Anion-controlled morphologies and spectral features of cyanine-based nanoGUMBOS - an improved photosensitizer. Nanoscale. 2012;4(16):5031-8.

52. Jordan AN, Siraj N, Das S, Warner IM. Tunable near-infrared emission of binary nano- and mesoscale GUMBOS. RSC Adv. 2014;4(54):28471-80.

53. de Rooy SL, Das S, Li M, El-Zahab B, Jordan A, Lodes R, et al. Ionically Self-Assembled, Multi-Luminophore One-Dimensional Micro- and Nanoscale Aggregates of Thiacarbocyanine GUMBOS. J Phys Chem C. 2012;116(14):8251-60.

54. Sarkar A, Kanakamedala K, Jagadish NN, Jordan A, Das S, Siraj N, et al. Electro-optical characterization of cyanine-based GUMBOS and nanoGUMBOS. Electron Mater Lett. 2014;10(5):879-85.

55. Wright AR, Li M, Ravula S, Cadigan M, El-Zahab B, Das S, et al. Soft- and hard-templated organic salt nanoparticles with the Midas touch: gold-shelled nanoGUMBOS. J Mater Chem C. 2014;2(42):8996-9003.

56. Vaughan SR, Speller NC, Chhotaray P, McCarter KS, Siraj N, Perez RL, et al. Class specific discrimination of volatile organic compounds using a quartz crystal microbalance based multisensor array. Talanta. 2018;188:423-8.

57. Regmi BP, Monk J, El-Zahab B, Das S, Hung FR, Hayes DJ, et al. A novel composite film for detection and molecular weight determination of organic vapors. J Mater Chem. 2012;22(27):13732–41.

58. Pang L, Yang P, Pang R, Li S. Bis(trifluoromethylsulfonyl)imide-based frozen ionic liquid for the hollow-fiber solid-phase microextraction of dichlorodiphenyltrichloroethane and its main metabolites. J Sep Sci. 2017;40(16):3311-7.

59. Cong MY, Perez RL, Chen M, Chapai R, Jin RY, Vidanapathirana P, et al. Imidazolium-dysprosium-based magnetic NanoGUMBOS for isolation of hemoglobin. Talanta. 2019;205:8.

60. Regmi BP, Galpothdeniya WIS, Siraj N, Webb MH, Speller NC, Warner IM. Phthalocyanine- and porphyrin-based GUMBOS for rapid and sensitive detection of organic vapors. Sens Actuator B-Chem. 2015;209:172-9.

61. Chen M, Perez RL, Du P, Bhattarai N, McDonough KC, Ravula S, et al. Tumor-Targeting NIRF NanoGUMBOS with Cyclodextrin-Enhanced Chemo/Photothermal Antitumor Activities. ACS Appl Mater Interfaces. 2019;11(31):27548-57.

62. Das S, Magut PKS, Zhao L, Hasan F, Karki AB, Jin R, et al. Multimodal theranostic nanomaterials derived from phthalocyanine-based organic salt. RSC Adv. 2015;5(38):30227-33.

63. Das S, Magut PK, de Rooy SL, Hasan F, Warner IM. Ionic liquid-based fluorescein colorimetric pH nanosensors. RSC Adv. 2013;3(43):21054-61.

64. Galpothdeniya WIS, Das S, de Rooy SL, Regmi BP, Hamdan S, Warner IM. Fluorescein-based ionic liquid sensor for label-free detection of serum albumins. RSC Adv. 2014;4(34):17533-40.

65. Siraj N, Kolic PE, Regmi BP, Warner IM. Strategy for tuning the photophysical properties of photosensitizers for use in photodynamic therapy. Chem-Eur J. 2015;21(41):14440-6.

66. Cong M, Siraj N, Bhattarai N, Kolic PE, McCarter KS, Chhotaray PK, et al. Ratiometric fluorescence detection of hydroxyl radical using cyanine-based binary nanoGUMBOS. Sens Actuator B-Chem. 2018;257:993-1000.

67. Dumke JC, Qureshi A, Hamdan S, Rupnik K, El-Zahab B, Hayes DJ, et al. In vitro activity studies of hyperthermal near-infrared nanoGUMBOS in MDA-MB-231 breast cancer cells. Photochem Photobiol Sci. 2014;13(9):1270-80.

68. Dumke JC, Oureshi A, Hamden S, El-Zaha B, Das S, Hayes DJ, et al. Photothermal response of near-infrared-absorbing nanoGUMBOS. Appl Spectrosc. 2014;68(3):340-52.

69. Angell CA, Ansari Y, Zhao ZF. Ionic Liquids: past, present and future. Faraday Discuss. 2012;154:9-27.

70. Pandey S. Analytical applications of room-temperature ionic liquids: a review of recent efforts. Anal Chim Acta. 2006;556(1):38-45.

71. de Almeida TS, Julio A, Mota JP, Rijo P, Reis CP. An emerging integration between ionic liquids and nanotechnology: general uses and future prospects in drug delivery. Ther Deliv. 2017;8(6):461-73.

72. Meyer H, Meischein M, Ludwig A. Rapid assessment of sputtered nanoparticle ionic liquid combinations. ACS Comb Sci. 2018;20(4):243-50.

73. Bhatt AI, Mechler A, Martina LL, Bond AM. Synthesis of Ag and Au nanostructures in an ionic liquid: thermodynamic and kinetic effects underlying nanoparticle, cluster and nanowire formation. J Mater Chem. 2007;17:2241-50.

74. Zhou S, Ma Z, Baker GA, Rondinone AJ, Zhu Q, Luo H, et al. Self-assembly of metal oxide nanoparticles into hierarchically patterned porous architectures using ionic liquid/oil emulsions. Langmuir. 2009;25(13):7229-33.

75. Safavi A, Zeinali S, Yazdani M. Synthesis of biologically stable gold nanoparticles using imidazolium-based amino acid ionic liquids. Amino Acids. 2012;43(3):1323-30.

76. Guleria A, Neogy S, Adhikari S. Room temperature ionic liquid assisted synthesis of highly stable amorphous Se nanoparticles: a rapid and facile methodology. Mater Lett. 2018;217:198-201.

77. Wang Y, Yang H. Synthesis of CoPt nanorods in ionic liquids. J Am Chem Soc. 2005;127:5316-7.

78. Li Z, Liu Z, Zhang J, Han B, Du J, Gao Y, et al. Synthesis of single-crystal gold nanosheets of large size in ionic liquids. J Phys Chem B. 2005;109:14445-8.

79. Wegner S, Rutz C, Schutte K, Barthel J, Bushmelev A, Schmidt A, et al. Soft, wet-chemical synthesis of metastable superparamagnetic hexagonal close-packed nickel nanoparticles in different ionic liquids. Chem-Eur J. 2017;23(26):6330-40.

80. Trewyn BG, Whitman CM, Lin VSY. Morphological control of room-temperature ionic liquid templated mesoporous silica nanoparticles for controlled release of antibacterial agents. Nano Lett. 2004;4(11):2139-43.

81. Scurto AM, Newton E, Weikel RR, Draucker L, Hallett J, Liotta CL, et al. Melting point depression of ionic liquids with CO2: phase equilibria. Ind Eng Chem Res. 2008;47(3):493-501.

82. Bao WL, Wang ZM, Li YX. Synthesis of chiral ionic liquids from natural amino acids. J Org Chem. 2003;68(2):591-3.

83. Rutten FJ, Tadesse H, Licence P. Rewritable imaging on the surface of frozen ionic liquids. Angew Chem-Int Edit. 2007;46(22):4163-5.

84. Pirkwieser P, Lopez-Lopez JA, Kandioller W, Keppler BK, Moreno C, Jirsa F. Novel 3-Hydroxy-2-Naphthoate-Based Task-Specific Ionic Liquids for an Efficient Extraction of Heavy Metals. Front Chem. 2018;6:11.

85. Clark KD, Emaus MN, Varona M, Bowers AN, Anderson JL. Ionic liquids: solvents and sorbents in sample preparation. J Sep Sci. 2018;41(1):209-35

86. Ho TD, Canestraro AJ, Anderson JL. Ionic liquids in solid-phase microextraction: A review. Anal Chim Acta. 2011;695(1-2):18-43.

87. Rebelo LPN, Lopes JNC, Esperanca JMSS, Guedes HJR, Lachwa J, Najdanovic-Visak V, et al. Accounting for the unique, doubly dual nature of ionic liquids from a molecular thermodynamic, and modeling standpoint. Accounts Chem Res. 2007;40(11):1114-21.

88. Tesfai A, El-Zahab B, Bwambok DK, Baker GA, Fakayode SO, Lowry M, et al. Controllable formation of ionic liquid micro- and nanoparticles via a melt-emulsion-quench approach. Nano Lett. 2008;8(3):897-901.

89. Warner IM, Tesfai A, El-Zahab BM, Bwambok D, Baker GA, Fakayode SO, et al., inventorsFrozen ionic liquid microparticles and nanoparticles, and methods for their synthesis and use, 2011. United States.

90. Bai HH, Zhou QX, Xie GH, Xiao JP. Enrichment and sensitive determination of dichlorodiphenyltrichloroethane and its metabolites with temperature controlled ionic liquid dispersive liquid phase microextraction prior to high performance liquid phase chromatography. Anal Chim Acta. 2009;651(1):64-8.

91. Brondi SHG, Spoljaric FC, Lancas FM. Ultratraces analysis of organochlorine pesticides in drinking water by solid phase extraction coupled with large volume injection/gas chromatography/mass spectrometry. J Sep Sci. 2005;28(17):2243-6.

92. Sapozhnikova Y, Simons T, Lehotay SJ. Evaluation of a Fast and Simple Sample Preparation Method for Polybrominated Diphenyl Ether (PBDE) Flame Retardants and Dichlorodiphenyltrichloroethane (DDT) Pesticides in Fish for Analysis by ELISA Compared with GC-MS/MS. J Agric Food Chem. 2015;63(18):4429-34

93. Huo FF, Tang H, Wu X, Chen DZ, Zhao T, Liu P, et al. Utilizing a novel sorbent in the solid phase extraction for simultaneous determination of 15 pesticide residues in green tea by GC/MS. J Chromatogr B. 2016;1023:44-54.

94. Vega Moreno D, Sosa Ferrera Z, Santana Rodiguez JJ. Microwave assisted micellar extraction coupled with solid phase microextraction for the determination of organochlorine pesticides in soil samples. Anal Chim Acta. 2006;571(1):51-7

95. Lu JX, Liu JF, Wei Y, Jiang KL, Fan SS, Liu JY, et al. Preparation of single-walled carbon nanotube fiber coating for solid-phase microextraction of organochlorine pesticides in lake water and wastewater. J Sep Sci. 2007;30(13):2138-43

96. Ke YY, Zhu F, Zeng F, Luan TG, Su CY, Ouyang GF. Preparation of graphene-coated solid-phase microextraction fiber and its application on organochlorine pesticides determination. J Chromatogr A. 2013;1300:187-92.
97. Siraj N, Hasan F, Das S, Kiruri LW, Steege Gall KE, Baker GA, et al. Carbazole-derived group of uniform materials based on organic salts: solid state fluorescent analogues of ionic liquids for potential applications in organic-based blue light-emitting diodes. J Phys Chem C. 2014;118(5):2312-20.
98. De Silva TPD, Sahasrabudhe G, Yang BQ, Wang CH, Chhotaray PK, Nesterov EE, et al. Influence of Anion Variations on Morphological, Spectral, and Physical Properties of the Propidium Luminophore. J Phys Chem A. 2019;123(1):111-9
99. Li M, Ganea GM, Lu C, de Rooy SL, El-Zahab B, Fernand VE, et al. Lipophilic phosphonium-lanthanide compounds with magnetic, luminescent, and tumor targeting properties. J Inorg Biochem. 2012;107(1):40-6.
100. Regmi BP, Speller NC, Anderson MJ, Brutus JO, Merid Y, Das S, et al. Molecular weight sensing properties of ionic liquid-polymer composite films: theory and experiment. J Mater Chem C. 2014;2(24):4867-78.
101. Galpothdeniya WIS, Fronczek FR, Cong M, Bhattarai N, Siraj N, Warner IM. Tunable GUMBOS-based sensor array for label-free detection and discrimination of proteins. J Mat Chem B. 2016;4(8):1414-22.
102. Warner IM, Regmi BP, El-Zahab BM, Hayes DJ, inventorsDetection and molecular weight determination of organic vapors, 2017. United States.
103. Kolic PE, Siraj N, Cong MY, Regmi BP, Luan XN, Wang Y, et al. Improving energy relay dyes for dye-sensitized solar cells by use of a group of uniform materials based on organic salts (GUMBOS). RSC Adv. 2016;6(97):95273-82.
104. Cole MR, Li M, Jadeja R, El-Zahab B, Hayes D, Hobden JA, et al. Minimizing human infection from Escherichia coli O157:H7 using GUMBOS. J Antimicrob Chemother. 2013;68(6):1312-8.
105. Cole MR, Hobden JA, Warner IM. Recycling antibiotics into GUMBOS: a new combination strategy to combat multi-drug-resistant bacteria. Molecules. 2015;20(4):6466-87.
106. Lopez KM, Ravula S, Perez RL, Ayala CE, Losso JN, Janes ME, et al. Hyaluronic Acid-Cellulose Composites as Patches for Minimizing Bacterial Infections. ACS Omega. 2020;5(8):4125-32.
107. Boverhof DR, Bramante CM, Butala JH, Clancy SF, Lafranconi M, West J, et al. Comparative assessment of nanomaterial definitions and safety evaluation considerations. Regul Toxicol Pharmacol. 2015;73(1):137-50.

108. Buzea C, Pacheco II, Robbie K. Nanomaterials and nanoparticles: sources and toxicity. Biointerphases. 2007;2(4):MR17-71.

109. Liu YX, Qi Q, Li XM, Liu J, Wang LY, He J, et al. Self-assembled pectin-conjugated eight-arm polyethylene glycol-dihydroartemisinin nanoparticles for anticancer combination therapy. ACS Sustain Chem Eng. 2017;5(9):8097-107.

110. Li JX, Jiang F, Chi Z, Han D, Yu LJ, Liu CG. Development of Enteromorpha prolifera polysaccharide-based nanoparticles for delivery of curcumin to cancer cells. Int J Biol Macromol. 2018;112:413-21.

111. Khan I, Saeed K, Khan I. Nanoparticles: properties, applications and toxicities. Arab J Chem. 2017;12 (7):908-31

112. Bhattarai N, Chen M, Perez RL, Ravula S, Chhotaray P, Hamdan S, et al. Enhanced chemotherapeutic toxicity of cyclodextrin templated size-tunable rhodamine 6G nanoGUMBOS. J Mat Chem B. 2018;6(34):5451-9.

113. de Rooy SL, El-Zahab B, Li M, Das S, Broering E, Chandler L, et al. Fluorescent one-dimensional nanostructures from a group of uniform materials based on organic salts. Chem Commun. 2011;47(31):8916-8.

114. Dumke JC, El-Zahab B, Challa S, Das S, Chandler L, Tolocka M, et al. Lanthanide-based luminescent nanoGUMBOS. Langmuir. 2010;26(19):15599-603.

115. Gesquiere AJ, Uwada T, Asahi T, Masuhara H, Barbara PF. Single molecule spectroscopy of organic dye nanoparticles. Nano Lett. 2005;5(7):1321-5.

116. Peng AD, Xiao DB, Ma Y, Yang WS, Yao JN. Tunable emission from doped 1,3,5-triphenyl-2-pyrazoline organic nanoparticles. Adv Mater. 2005;17(17):2070-3.

117. Suk J, Bard AJ. Electrochemistry and electrogenerated chemiluminescence of organic nanoparticles. J Solid State Electrochem. 2011;15(11-12):2279-91.

118. Kwon E, Oikawa H, Kasai H, Nakanishi H. A fabrication method of organic nanocrystals using stabilizer-free emulsion. Cryst Growth Des. 2007;7(4):600-2.

119. Zhang W, Qiao X, Chen J. Synthesis of nanosilver colloidal particles in water/oil microemulsion. Colloid Surf A-Physicochem Eng Asp. 2007;299(1-3):22-8.

120. Chin SF, Azman A, Pang SC. Size controlled synthesis of starch nanoparticles by a microemulsion method. J Nanomater. 2014;2014:1-7.

121. Dahl JA, Maddux BLS, Hutchison JE. Toward greener nanosynthesis. Chem Rev. 2007;107(6):2228-69.

122. Uskokovic V, Drofenik M. Synthesis of materials within reverse micelles. Surf Rev Lett. 2005;12(2):239-77.

123. Ganguli AK, Ahmad T, Vaidya S, Ahmed J. Microemulsion route to the synthesis of nanoparticles. Pure Appl Chem. 2008;80(11):2451-77.

124. Buesser B, Pratsinis SE. Design of nanomaterial synthesis by aerosol processes. Annu Rev Chem Biomol Eng. 2012;3:103-27.

125. Kastrinaki G, Lorentzou S, Karagiannakis G, Rattenbury M, Woodhead J, Konstandopoulos AG. Parametric synthesis study of iron based nanoparticles via aerosol spray pyrolysis route. J Aerosol Sci. 2018;115:96-107.

126. Han Z, Yan Q, Ge W, Liu ZG, Gurunathan S, de Felici M, et al. Cytotoxic effects of ZnO nanoparticles on mouse testicular cells. Int J Nanomed. 2016;11:5187–203.

127. Zhang WC, Xiao BD, Fang T. Chemical transformation of silver nanoparticles in aquatic environments: mechanism, morphology and toxicity. Chemosphere. 2018;191:324-34.

128. Karam TE, Siraj N, Warner IM, Haber LH. Anomalous size-dependent excited-state relaxation dynamics of nanoGUMBOS. J Phys Chem C. 2015;119(50):28206-13

129. Hamdan S, Moore L, Lejeune J, Hasan F, Carlisle TK, Bara JE, et al. Ionic liquid crosslinkers for chiral imprinted nanoGUMBOS. J Colloid Interface Sci. 2016;463:29-36.

130. Yu XL, Liu H, Diao JX, Sun Y, Wang YC. Magnetic molecularly imprinted polymer nanoparticles for separating aromatic amines from azo dyes - Synthesis, characterization and application. Sep Purif Technol. 2018;204:213-9.

131. Mahmoud ME, Amira MF, Zaghloul AA, Ibrahim GAA. High performance microwave-enforced solid phase extraction of heavy metals from aqueous solutions using magnetic iron oxide nanoparticles-protected-nanosilica. Sep Purif Technol. 2016;163:169-72.

132. Reed DG, Dowson GRM, Styring P. Cellulose-Supported Ionic Liquids for Low-Cost Pressure Swing CO2 Capture. Front Energy Res. 2017;5:12.

133. Garcia-Gutierrez P, Cuellar-Franca RM, Reed D, Dowson G, Styring P, Azapagic A. Environmental sustainability of cellulose-supported solid ionic liquids for CO2 capture. Green Chem. 2019;21(15):4100-14.

134. Yao H, Ou Z, Kimura K. Ion-based organic nanoparticles: synthesis, characterization, and optical properties of pseudoisocyanine dye nanoparticles. Chem Lett. 2005;34(8):1108-9.

135. Yao H, Yamashita M, Kimura K. Organic styryl dye nanoparticles: synthesis and unique spectroscopic properties. Langmuir. 2009;25:1131-7.

136. Alifu N, Yan LL, Zhang HQ, Zebibula A, Zhu ZG, Xi W, et al. Organic dye doped nanoparticles with NIR emission and biocompatibility for ultra-deep in vivo two-photon microscopy under 1040 nm femtosecond excitation. Dyes Pigment. 2017;143:76-85.

137. Yokoi Y, Yao H. Organic nanoparticles of anion-based fluorophore 8-anilino-1-naphthalenesulfonate (ANS): Effects of ion-association and post-dilution. J Mol Struct. 2020;1200:6.

138. Ou Z, Yao H, Kimura K. Organic nanoparticles of cyanine dye in aqueous solution. Bull Chem Soc Jpn. 2007;80(2):295-302.
139. Funada T, Hirose T, Tamai N, Yao H. Organic nanoparticles of malachite green with enhanced far-red emission: size-dependence of particle rigidity. Phys Chem Chem Phys. 2015;17(16):11006-13.
140. Ou Z, Yao H, Kimura K. Organic nanoparticles of porphyrin without self-aggregation. Chem Lett. 2006;35(7):782-3.
141. Yao H, Funada T. Organic nanoparticles of an extended π-conjugated styryl dye: modulation of fluorescence peak energy and intensity in the near-infrared (NIR) region. J Photochem Photobiol A-Chem. 2016;330:140-9.
142. Yao H, Ashiba K. Highly fluorescent organic nanoparticles of thiacyanine dye: a synergetic effect of intermolecular H-aggregation and restricted intramolecular rotation. RSC Adv. 2011;1(5):834-8.
143. Enseki T, Yao H. Controlled formation of fluorescent organic nanoparticles of carbocyanine dye via ion-association approach. Chem Lett. 2012;41(10):1119-21.
144. Yao H, Ashiba K. Efficient excitation-energy transfer in ion-based organic nanoparticles with versatile tunability of the fluorescence colours. ChemPhysChem. 2012;13(11):2703-10.

Chapter 2

Protein discrimination using erythrosin B-based GUMBOS in combination with UV–Vis spectroscopy and chemometrics

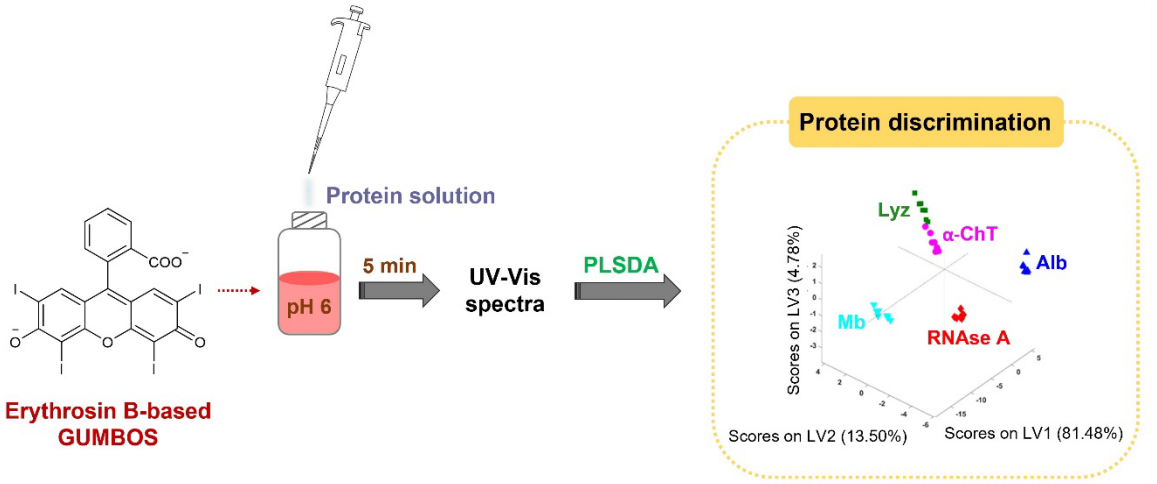

Highlights

- Erythrosin B-based GUMBOS were synthesized and characterized for the first time.
- In contrast to pH, the equilibration time did not affect protein discrimination.
- Percentages of correct protein assignments ranged from 86.5 to 100.0% (pH 3.0–6.0).
- $[P_{4444}]_2[EB]$ and $[N_{4444}]_2[EB]$ were able to discriminate among four Alb/Mb mixtures.

Manuscript published after international peer review as "Azevedo AMO, Sousa C, Chen M, Ayala CE, Perez RL, Santos JLM, Warner IM, Saraiva MLMFS. Protein discrimination using erythrosin B-based GUMBOS in combination with UV–Vis spectroscopy and chemometrics. Talanta. 2022;240:123164".

Abstract

GUMBOS (*g*roup of *u*niform *m*aterials *b*ased on *o*rganic *s*alts) have recently emerged as interesting materials for protein analysis due to their unique features and high tunability. In this regard, four novel erythrosin B (EB)-based GUMBOS were synthesized and their potential to discriminate among proteins with distinct properties (e.g., size, charge, and hydrophobicity) was assessed. These solid-phase materials were prepared using a single-step metathesis reaction between EB and various phosphonium and ammonium cations, namely tetrabutylphosphonium (P_{4444}^+), tributylhexadecylphosphonium (P_{44416}^+), tetrabutylammonium (N_{4444}^+), and benzyldimethylhexadecylammonium ($BDHA^+$). Subsequently, the effect of pH (3.0, 4.5, and 6.0) and reaction time (5, 10, and 15 min) on the discriminatory power of synthesized GUMBOS was evaluated. Absorption spectra resulting from the interaction between EB-based GUMBOS and proteins were analyzed using partial least squares discriminant analysis (PLSDA). Unlike time, the pH value was determined to have influence over GUMBOS discrimination potential. Correct protein assignments varied from 86.5% to 100.0%, and the best discriminatory results were observed for $[P_{4444}]_2[EB]$ and $[N_{4444}]_2[EB]$ at pH 6.0. Additionally, these two GUMBOS allowed discrimination of protein mixtures containing different ratios of albumin and myoglobin, which appeared as individualized clusters in the PLSDA scores plots. Overall, this study showcases EB-based GUMBOS as simple synthetic targets to provide a label-free, cost-effective, rapid, and successful approach for discrimination of single proteins and their mixtures.

Keywords: Erythrosin B; GUMBOS; PLSDA; Protein discrimination.

2.1. Introduction

Proteins have been used as biomarkers for early diagnosis of various diseases, customization of treatment plans, and prognostic stratification of patients. For example, elevated levels of serum myoglobin (Mb) and troponin I play an important role in the acute coronary syndrome diagnosis and are predictive of a higher 5-year mortality risk (1, 2). High concentrations of biliary calprotectin and serum interleukin-8 are associated with disease severity in primary sclerosing cholangitis and transplant-free survival (3, 4). In fact, a combined analysis of multiple biomarkers has better accuracy for assessing diagnoses, providing disease progression predictions, or evaluating therapeutic responses when compared to analysis of individual proteins (5, 6). Moreover, a single biomarker can be associated with numerous diseases and various proteins can be indicative of the same medical condition (7, 8).

Enzyme-linked immunosorbent assay (ELISA) is the most commonly used method for protein detection in biomedical research and clinical diagnosis owing to its high sensitivity and specificity (9, 10). However, the high cost, laborious and time-consuming processes, along with the need for specific antibodies have hindered its widespread application (11, 12). Mass spectrometry-based approaches offer several advantages over conventional immunoassay formats, including identification of proteoforms, as well as detection and quantification of protein biomarkers in a multiplexed manner. Nevertheless, this method requires expensive instrumentation and well-trained personnel (13, 14). Due to cost-effectiveness, simplicity, and the ability to obtain rapid responses, optical sensor arrays provide a reliable alternative to detect and discriminate structurally related proteins as well as complex protein mixtures (15, 16). In contrast to a “lock-and-key” approach, this sensing system comprises multiple receptors that interact differently with each protein or protein mixture and generate unique response patterns (17, 18). The acquired data can then be processed using chemometric tools such as hierarchical cluster analysis (HCA), linear discriminant analysis (LDA), principal component analysis (PCA), and partial least squares discriminant analysis (PLSDA) (19, 20). Despite the great potential of a sensor array strategy, its large-scale application has been hampered by need for a large number of sensing elements (sometimes even higher than the number of proteins), which increases the time required for data acquisition, processing, and analyses (16, 21). Furthermore, sensing materials often demand laborious chemical modifications to achieve the desired performance (22). GUMBOS (*g*roup of *u*niform *m*aterials *b*ased on *o*rganic *s*alts) have recently emerged as alternative materials for detection and discrimination of proteins because of their facile synthesis and high tunability (23, 24). The physicochemical properties of these solid-state materials can be easily modulated by varying the cation-anion

combination similar to ionic liquids (ILs) chemistry, thus avoiding complicated synthetic procedures (25, 26).

Erythrosin B (EB) is an anionic xanthene dye that has been used for various purposes, such as a colorant in food products (27), a vital stain (28), and a flaviviruses inhibitor (29). It has also been applied as a sensor for oxygen (30), heavy metals and halide ions (31), as well as proteins (32). To date, there are only a few spectrophotometric methods for protein determination using EB and they present several operational disadvantages, such as high temperature, long reaction time, and necessary additives (32-34). In this context, there is a growing interest in the development of viable alternative strategies to both detect and discriminate multiple proteins.

In this study, we describe the synthesis of four novel EB-based GUMBOS and evaluate their ability to discriminate single and binary mixtures of proteins. Ultraviolet-visible (UV-Vis) spectra resulting from the binding of GUMBOS to proteins were later analyzed using PLSDA. Percentages of correct protein assignments were equal to or greater than 86.5% and mixtures with different ratios of albumin (Alb) and Mb appeared as well-defined clusters in two-dimensional partial least squares discriminant analysis (2D-PLSDA) scores plots. These findings support potential use of EB-derived GUMBOS as alternative sensing materials for protein identification.

2.2. Material and methods

2.2.1. Reagents and solvents

$[Na]_2[EB]$ (2',4',5',7'-tetraiodofluorescein disodium salt), tetrabutylphosphonium bromide ($[P_{4444}][Br]$), tetrabutylammonium bromide ($[N_{4444}][Br]$), sodium phosphate dibasic (Na_2HPO_4), sodium phosphate monobasic (NaH_2PO_4), Alb (from human serum), α-chymotrysin (α-ChT, from bovine pancreas), lysozyme (Lyz, from chicken egg white), Mb (from equine heart), and ribonuclease A (RNAse A, from bovine pancreas) were all purchased from Sigma-Aldrich (St. Louis, MO) and used as received. Tributylhexadecylphosphonium bromide ($[P_{44416}][Br]$) was obtained from Tokyo Chemical Industries, Co. (TCI–America, Portland, OR) and benzyldimethylhexadecylammonium chloride ([BDHA][Cl]) from Alfa Aesar (Haverhill, MA). Citric acid, sodium hydroxide, and 1-octanol were purchased from Honeywell (Charlotte, NC). Dimethylsulfoxide (DMSO) was acquired from Merck (Darmstadt, Germany) and deuterated chloroform ($CDCl_3$, 99.8%) with 0.03% tetramethylsilane was obtained from Beantown Chemical (BTC, Hudson, NH).

A series of citrate buffers (0.1 mol L^{-1}) were prepared from citric acid and adjusted to pH 3.0, 4.5, or 6.0 by adding sodium hydroxide. Phosphate buffer (0.01 mol L^{-1}, pH 7.4) was used for the preparation of protein stock solutions (1 mg mL^{-1}) and obtained by mixing Na_2HPO_4 and NaH_2PO_4. All buffer solutions were prepared using high purity water (Milli-Q®, 18.2 MΩ cm). EB-based GUMBOS were dissolved in DMSO and protected from light degradation.

2.2.2. Instrumentation

Proton (^1H, 400MHz) and carbon (^{13}C, 125MHz) nuclear magnetic resonance (NMR) spectra were recorded using a Bruker Avance III NanoBay 400 and a Bruker AV-500. NMR samples were prepared by dissolving GUMBOS in $CDCl_3$. Coupling constants (*J*) were reported in Hz and chemical shifts (δ) in ppm. Abbreviations used to explain multiplicities were as follows: singlet (s), doublet (d), triplet (t), and multiplet (m).

An Agilent 6230 B-TOF LC/MS was used for high-resolution mass spectrometry (HRMS) measurements at the Louisiana State University Mass Spectrometry facility. Differential scanning calorimetry (DSC) thermograms were acquired using a TA DSC Q200 instrument. Approximately 2–5 mg of GUMBOS were crimped in an aluminum pan and heated from 25 to 150 ºC at a rate of 10 ºC min^{-1} under a nitrogen purge (50 mL min^{-1}). An empty pan was used as a reference during DSC measurements.

Fourier transform infrared (FTIR) measurements were performed on a Bruker Tensor 27 spectrometer, equipped with a Pike Miracle ATR cell. Spectra were collected from 4000 to 650 cm^{-1} by averaging 32 scans at a resolution of 4 cm^{-1}. Opus 8.0 software was used for data collection and initial processing.

Absorption studies were performed, at room temperature, on a Jasco V-660 spectrophotometer, equipped with a 1 cm path length quartz cuvette. Spectra were collected in the range of 250–800 nm using a slit width of 5 nm. The whole spectral data were subjected to PLSDA in order to discriminate aqueous protein samples.

2.2.3. Synthesis and structural characterization of GUMBOS

EB-derived GUMBOS were synthesized using a simple metathesis reaction (23). Sodium cations of EB dye were exchanged with several bulky organic cations (P_{4444}^+, P_{44416}^+, N_{4444}^+, and $BDHA^+$). Briefly, both cation and anion (2:1.1 molar ratio) were dissolved in phosphate buffer pH 7.4 and stirred for 24 h in the dark at room temperature (Fig. 2.1). GUMBOS precipitated after the allotted reaction time, were washed several times with water to eliminate sodium halide by-products, and freeze-dried. Ultimately, GUMBOS formation was

confirmed using NMR and FTIR spectroscopy as well as HRMS. Structural characterization data can be found in Supplementary Material (Figs. S2.1–S2.9 and Table S2.1).

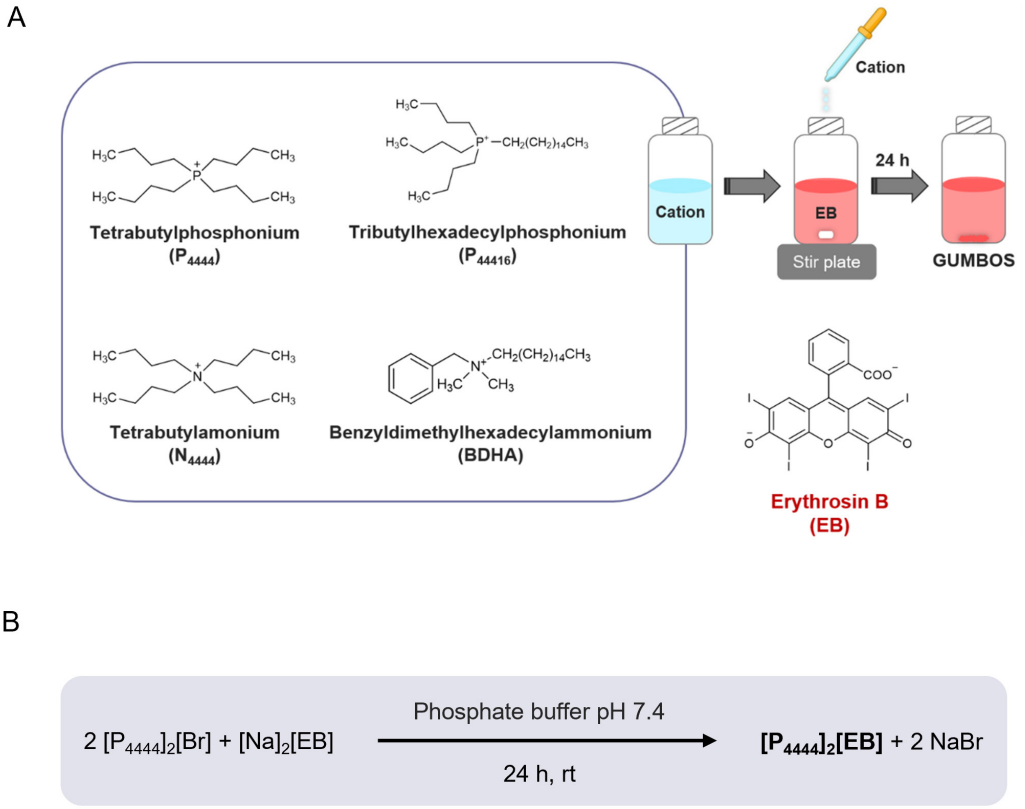

Fig. 2.1. (A) Chemical structures of the cations used in the synthesis of EB-based GUMBOS. (B) Synthetic diagram of $[P_{4444}]_2[EB]$ GUMBOS.

2.2.4. Octanol/water partitioning

Following synthesis of EB-based GUMBOS, octanol/water partition coefficient ($K_{O/W}$) values were determined using a modified shake-flask method (35). Before experiments, 1-octanol and water were mutually saturated by stirring for 24 h, and then phases were separated. Each compound was dissolved in 5 mL of 1-octanol saturated with water (C_i), to which an equal volume of water-saturated with octanol was added. After stirring the mixture for 24 h at room temperature, the absorbance of upper organic layer was measured at 540 nm. GUMBOS concentration (C_O) was calculated from the respective calibration curve, which was previously established using 1-octanol standard solutions (range of 2–8 μmol L^{-1}). The aqueous concentration (C_W) was obtained by subtracting GUMBOS concentration in the octanol layer (C_O) from its initial concentration (C_i). Finally, $K_{O/W}$ was calculated using the equation:

$$K_{O/W} = C_O/C_W \qquad (1)$$

Three independent experiments were performed for each compound.

2.2.5. Protein discrimination using the synthesized GUMBOS

Discrimination capabilities of EB-based GUMBOS ($[P_{4444}]_2[EB]$, $[P_{44416}]_2[EB]$, $[N_{4444}]_2[EB]$, and $[BDHA]_2[EB]$) were tested using five proteins, e.g., RNAse A, Lyz, Alb, Mb, and α-ChT. The assays were performed at three different pH values (3.0, 4.5, and 6.0), and absorption spectra were acquired after 5, 10, and 15 min. GUMBOS and protein concentrations were held constant at 1 μmol L^{-1} and 20 μg mL^{-1}, respectively.

The ability of $[P_{4444}]_2[EB]$ and $[N_{4444}]_2[EB]$ to discriminate between mixtures of Alb and Mb at different proportions (20% Alb + 80% Mb, 40% Alb + 60% Mb, 60% Alb + 40% Mb, and 80% Alb + 20% Mb) was also examined. Studies were conducted only with GUMBOS mentioned above at pH 6.0 and after a reaction period of 5 min since these were the conditions that led to best discrimination results. Total protein concentration was maintained constant at 4 μg mL^{-1}. For all assays, seven replicate samples were obtained from independent experiments on two different days.

2.2.6. Data analysis

UV-Vis spectra were preprocessed using standard normal variate (SNV) (36), and then mean-centered before PLSDA application. PLSDA is a supervised model based on the PLS2 algorithm, which requires previous knowledge of the data set (37, 38). In PLSDA, to each known sample (x_i, GUMBOS spectra in the presence of a single protein) is assigned a vector of zeros with value one at the position corresponding to its class (y_i, in this study to each protein). The structure of the PLSDA model is described by Eqs. 2 and 3. Model loadings (P and Q) and corresponding scores (T and U) are obtained by sequentially extracting the components or latent variables (LVs) from matrices X (spectra) and Y (matrix codifying the proteins).

$$X = TP^t + E \qquad (2)$$

$$Y = UQ^t + F \qquad (3)$$

The algorithm correlates the scores of each block (T and U), yielding an internal regression matrix. This internal regression can be transformed on a regression matrix B. In this case, the regression matrix is composed of three vectors: one regression vector corresponding to each protein. E and F are the residual matrices and depend on the number of LVs selected. Predictions for new samples are obtained by multiplying a new spectrum (x_{new}) by the regression matrix B:

$$y_{new} = x_{new} B \qquad (4)$$

The prediction (y_{new} = [$y_{new,1}$, $y_{new,2}$,…,$y_{new,n}$]) is then converted into a class assignment (protein) from which confusion matrices are obtained. During the development of PLSDA model, 70% of the samples are randomly selected to obtain the regression matrix B and 30% are used as new samples for prediction. This procedure is repeated 100 times per PLSDA model and confusion matrices present the mean values of correct protein assignments for the prediction samples.

Chemometric data analysis was performed in MATLAB version 7.4 Release 2018b (MathWorks, Natick, MA) and PLS Toolbox version 8.7 (2019) for MATLAB (Eigenvector Research, Manson, WA).

2.2.7. Rationale of the study

Four EB-based materials ([P_{4444}]$_2$[EB], [P_{44416}]$_2$[EB], [N_{4444}]$_2$[EB], and [BDHA]$_2$[EB]) were synthesized for the first time and structurally characterized using several traditional techniques as previously described in section 2.2.3. In order to confirm if they could be categorized as GUMBOS, their melting points were determined by DSC. Relative hydrophobicities were measured as $K_{O/W}$ to better understand GUMBOS-protein binding.

Absorption spectra were used to evaluate the potential of synthesized materials to discriminate among five proteins with different features at three pH values (3.0, 4.5, and 6.0) and reaction times (5, 10, and 15 min). Acidic pH conditions were studied as they are known to promote the formation of complexes between EB dye and proteins (32-34). For each EB-derived GUMBOS and experimental condition, a single PLSDA model was developed, in which a total of 36 PLSDA models: 4 GUMBOS x 3 pH values x 3 reaction times were combined, and the corresponding confusion matrix was generated (further details in section 2.2.6). The highest percentages of correct predictions obtained from confusion matrices were observed at pH 6.0 and 5 min of reaction for [P_{4444}]$_2$[EB] and [N_{4444}]$_2$[EB]. These two GUMBOS were subsequently used to discriminate between four binary mixtures of Alb and Mb under the conditions previously established (pH 6.0, 5 min).

2.3. Results

2.3.1. Structural characterization of EB-based GUMBOS

Structures of the resulting GUMBOS were determined by NMR (^{1}H and ^{13}C), FTIR, and HRMS spectra analysis. A 2:1 stoichiometric ratio of cation to anion was confirmed through

integration of proton NMR signals (Figs. S2.1, S2.3, S2.5, and S2.7). It is worth noting that FTIR peaks attributable to starting materials were also observed in the spectra of final products (Fig. S2.9). Analysis of HRMS results further evidenced successful synthesis of EB-based GUMBOS. In the positive ion mode, peaks with *m/z* values of 259.2557, 427.4432, 242.2841, and 360.3630 were assigned to P_{4444}, P_{44416}, N_{4444}, and BDHA cations. The negative ion mode HRMS spectra showed presence of EB anion in all synthesized compounds. Moreover, experimental results were in good agreement with expected *m/z* values (Table S2.1).

2.3.2. UV-Vis properties of EB-derived GUMBOS

Absorption spectra of synthesized compounds were measured at a concentration of 1 µmol L^{-1} in DMSO. The UV-Vis profile of all EB-based GUMBOS is similar to the parent dye (Fig. 2.2) and shows an intense band at 540 nm, a shoulder at approximately 500 nm, corresponding to $S_0 \rightarrow S_1$ transitions, as well as a lower intensity band near 330 nm associated with transitions $S_0 \rightarrow S_2$ (39, 40). Differences in absorbance values of EB-based GUMBOS are most likely the result of cation variations.

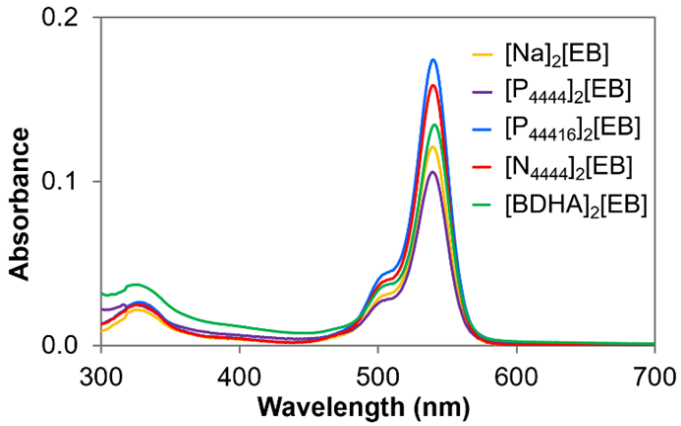

Fig. 2.2. UV-Vis spectra of $[Na]_2[EB]$ and EB-based GUMBOS (1 µmol L^{-1}) in DMSO.

2.3.3. Melting point and hydrophobicity of the synthesized materials

Similar to ILs, the physicochemical properties of GUMBOS can be fine-tuned through use of different ion exchange. In order to demonstrate this effect, the melting point and hydrophobicity of synthesized GUMBOS were determined. DSC thermograms (Fig. S2.10) show a broad endothermic peak for all compounds, which can be associated with either dehydration of adsorbed water or the amorphous property of GUMBOS (41, 42). Variation in melting points of synthesized compounds (from approximately 55.1 to 81.4 ºC) can be explained by differences in size and symmetry of cations. In fact, the reduced melting points of GUMBOS as compared to $[Na]_2[EB]$ (m.p. = 315 ºC, Sigma-Aldrich) can be attributed to

replacement of Na^+ by relatively large phosphonium and ammonium cations (43). Furthermore, the higher melting points of $[P_{4444}]_2[EB]$ and $[N_{4444}]_2[EB]$ in relation to the other GUMBOS studied can be justified by symmetry of these cations, which could lead to a more efficient crystal packing and stronger ionic interactions (44, 45). The melting point of $[P_{44416}]_2[EB]$ was not determined by DSC since it remained a sticky solid at room temperature.

The relative hydrophobicity of GUMBOS was assessed through determination of octanol/water partition coefficients. Table S2.2 lists $\log K_{O/W}$ values for all synthesized compounds. Data analysis shows that hydrophobicity follows the order of $[N_{4444}]_2[EB] < [P_{4444}]_2[EB] < [P_{44416}]_2[EB] < [BDHA]_2[EB]$; thus demonstrating the cation's influence on GUMBOS hydrophobicity (23). Moreover, and in line with previous reports (46, 47), the elongation of alkyl side chain from four (P_{4444}^+) to sixteen (P_{44416}^+) carbons leads to an increase in $\log K_{O/W}$.

2.3.4. Protein discrimination using the synthesized GUMBOS

In order to evaluate the discrimination potential of EB-based GUMBOS, five proteins with distinct molecular weights (13.7–66.5 KDa), isoelectric points (4.7–11.4), and abundance levels were chosen as target analytes (Table S2.3). For example, Alb constitutes about 50% of the total protein content in plasma, while cardiac Mb is released after myocardial infarction (48, 49). UV-Vis spectra of the four synthesized materials in the presence of each protein were then recorded at three pH values (3.0, 4.5, and 6.0) and time points (5, 10, and 15 min) (Fig. S2.11). Spectral data were subjected to PLSDA to find differences among protein samples. Thirty-six PLSDA models were developed (Figs. 2.3–2.6), and the corresponding confusion matrices were generated. The total percentages of correct protein identifications obtained with the four GUMBOS at three pH values and reaction times are summarized in Table 2.1.

Table 2.1. Total percentages of correct predictions (%) obtained from the confusion matrices of PLSDA models (4 LVs), which were developed for protein discrimination using the synthesized EB-based GUMBOS.

pH	Time (min)	Total percentage of correct protein predictions			
		$[P_{4444}]_2[EB]$	$[P_{44416}]_2[EB]$	$[N_{4444}]_2[EB]$	$[BDHA]_2[EB]$
3.0	5	87.9	97.8	90.6	99.5
	10	86.5	95.5	90.1	99.7
	15	88.2	95.0	88.4	99.6
4.5	5	98.4	94.2	95.2	93.9
	10	99.6	91.9	93.1	93.2
	15	100.0	93.3	93.5	93.0
6.0	5	100.0	94.5	100.0	98.3
	10	100.0	96.2	99.9	98.7
	15	100.0	97.7	100.0	98.8

2.3.4.1. $[P_{4444}]_2[EB]$

For $[P_{4444}]_2[EB]$, the scores plots corresponding to the first three LVs of PLSDA regression models obtained at pH 3.0 for 5, 10, and 15 min of reaction time are presented in Fig. 2.3 (panels IA–IC), which also globally encompass approximately 95% of spectral variability. The scores plots showed five clusters, each corresponding to a single protein. Alb, Mb, and RNAse A clusters were perfectly separated, while some degree of overlap was found between α-ChT and Lyz clusters. It should be noted that the obtained results are quite similar for all time points. The first LV (LV1) encompasses around 60% of spectral variability being mostly responsible for discrimination between Alb and Mb. LV2 mainly accounts for discrimination between RNAse A and Lyz + α-ChT (32–35% of spectral variability), whereas Lyz and α-ChT were mainly discriminated in the third LV. Table S2.4 presents confusion matrices obtained from the corresponding PLSDA regression models (at pH 3.0 for 5, 10, and 15 min of reaction). Global percentages of correct discrimination of proteins were calculated by sum of diagonals at nearly 90% for the three reaction times, which can be considered quite satisfactory. Alb and Mb were correctly predicted for the three allotted times and were determined to be in good agreement with the clusters observed in scores plots. With respect to RNAse A, the great majority were correctly predicted (95.5%–5 min, 96.0%–10 min, 98.5%–15 min); although a few were predicted as α-ChT (4.5%–5 min, 4.0%–10 min, 1.5%–15 min). Around 80% of Lyz spectra (79.5%–5 min, 80.5%–10 min, 77.0%–15 min) were correctly predicted, with the remaining 20% misidentified solely as α-ChT spectra. Concerning the latter, the percentage of correct identifications varied from

56.0% (10 min) to 65.5% (15 min). After 5 and 10 min of reaction, α-ChT spectra were misidentified only as Lyz spectra (35.5% and 44.0%, respectively), whereas upon 15 min 0.5% were misidentified as being RNAse A and 34.0% as Lyz spectra.

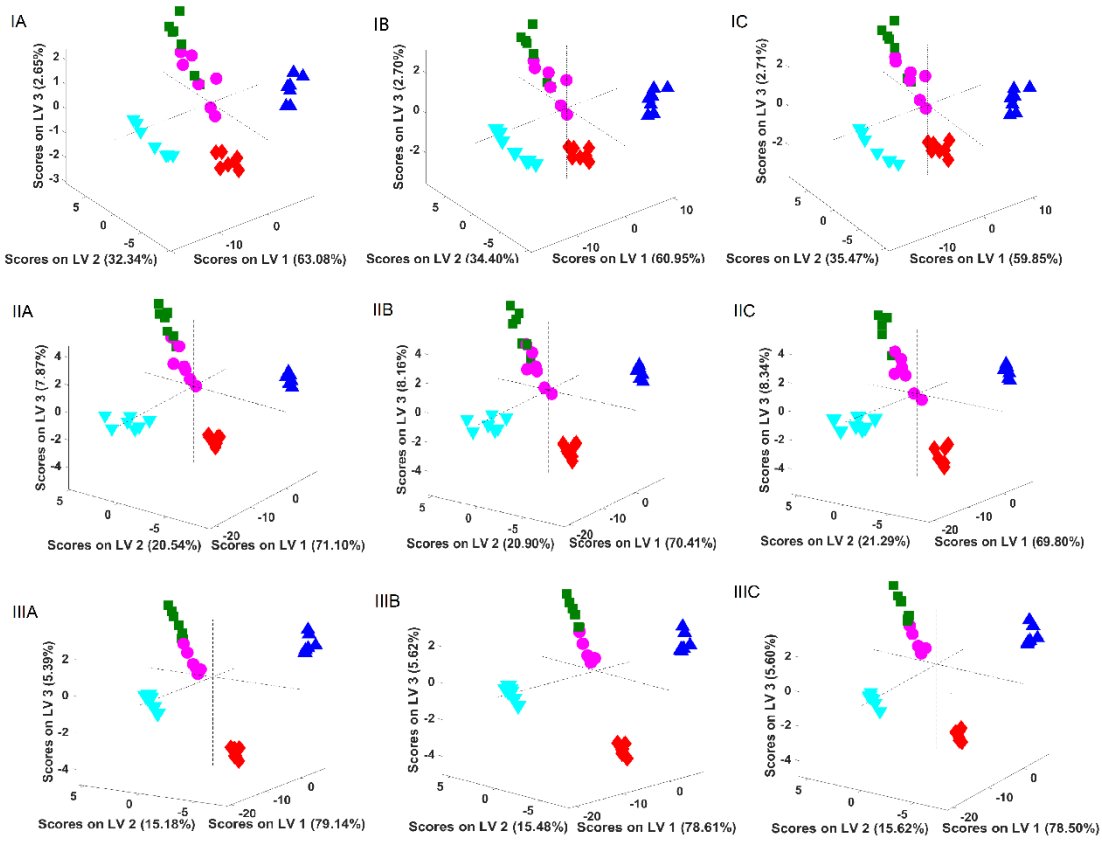

Fig. 2.3. Scores plots corresponding to the first three LVs of PLSDA regression models obtained using UV-Vis spectra at pH 3.0 (IA–IC), pH 4.5 (IIA–IIC), and pH 6.0 (IIIA–IIIC) for protein discrimination. $[P_{4444}]_2$[EB] GUMBOS + RNAse A (◆), Lyz (■), Alb (▲), Mb (▼), and α-ChT (●). Models A, B, and C correspond to 5, 10, and 15 min of reaction.

Regarding pH 4.5 and 6.0, the scores plots (panels IIA–IIC and IIIA–IIIC from Fig. 2.3) revealed similar clusters to those observed at pH 3.0, with the first three LVs encompassing around 98% (LV1 approximately 70%, LV2 approximately 20%, LV3 approximately 8%) and 99% (LV1 approximately 79%, LV2 approximately 15%, LV3 approximately 5%) of spectral variability, respectively. Protein discrimination was also observed among the same LVs (LV1–Alb/Mb, LV2–RNAse A/Lyz + α-ChT, LV3–Lyz/α-ChT). These findings were consistently noticed for the three reaction times. Regarding the confusion matrices obtained from PLSDA models at pH 4.5 and 6.0 (Tables S2.5 and S2.6, respectively), a very satisfactory percentage of correct discrimination of proteins was also achieved (98.4%–5 min, 99.6%–10 min, 100.0%–15 min at pH 4.5 and 100.0%–5, 10, 15 min at pH 6.0). Similar to what was observed for pH 3.0, it appears that reaction time did not influence protein

discrimination. On the contrary, pH value impacted the results. Correct protein discrimination was nearly 90% for pH 3.0, 99% for pH 4.5, and 100% for pH 6.0 (Table 2.1). Regarding misidentifications at pH 4.5, all were related to α-ChT spectra and were erroneously identified as Lyz spectra.

2.3.4.2. $[P_{44416}]_2$[EB]

For $[P_{44416}]_2$[EB] at pH 3.0, the scores plots of PLSDA regression models (first three LVs encompassing about 99% of spectral variability) presented five individualized clusters, each containing a single protein, for all times studied (Fig. 2.4, panels IA–IC). In contrast to data observed for $[P_{4444}]_2$[EB] GUMBOS, no overlapping clusters were visible to the naked eye. The clusters obtained for Alb, Mb, and RNAse A were more scattered, which could lead to some misidentifications. LV1 mainly contributed to discrimination between Alb and Mb, while LV2 and LV3 seemed to be a cause for the remaining discriminations. As seen in Table 2.1, the percentages of correct protein discrimination range from 95.0% (15 min) to 97.8% (5 min). Similar to what was observed for $[P_{4444}]_2$[EB], Alb and Mb were correctly predicted consistently (Table S2.7), whereas some RNAse A was predicted as α-ChT (1.5%–5 min, 15.0%–10 min, 9.0%–15 min). It should also be noted that, when using the $[P_{44416}]_2$[EB] GUMBOS, the percentage of RNAse A incorrectly predicted after 10 and 15 min was higher than that for $[P_{4444}]_2$[EB]. This result was consistent with the widest scatter of clusters. Regarding Lyz spectra, they were all correctly predicted upon 10 min, being the wrong predictions related to α-ChT spectra (3.0%–5 min, 7.5%–15 min). In fact, α-ChT showed the worst predictions (93.5%–5 min, 92.5%–10 min, 91.5%–15 min), being misidentified as Lyz.

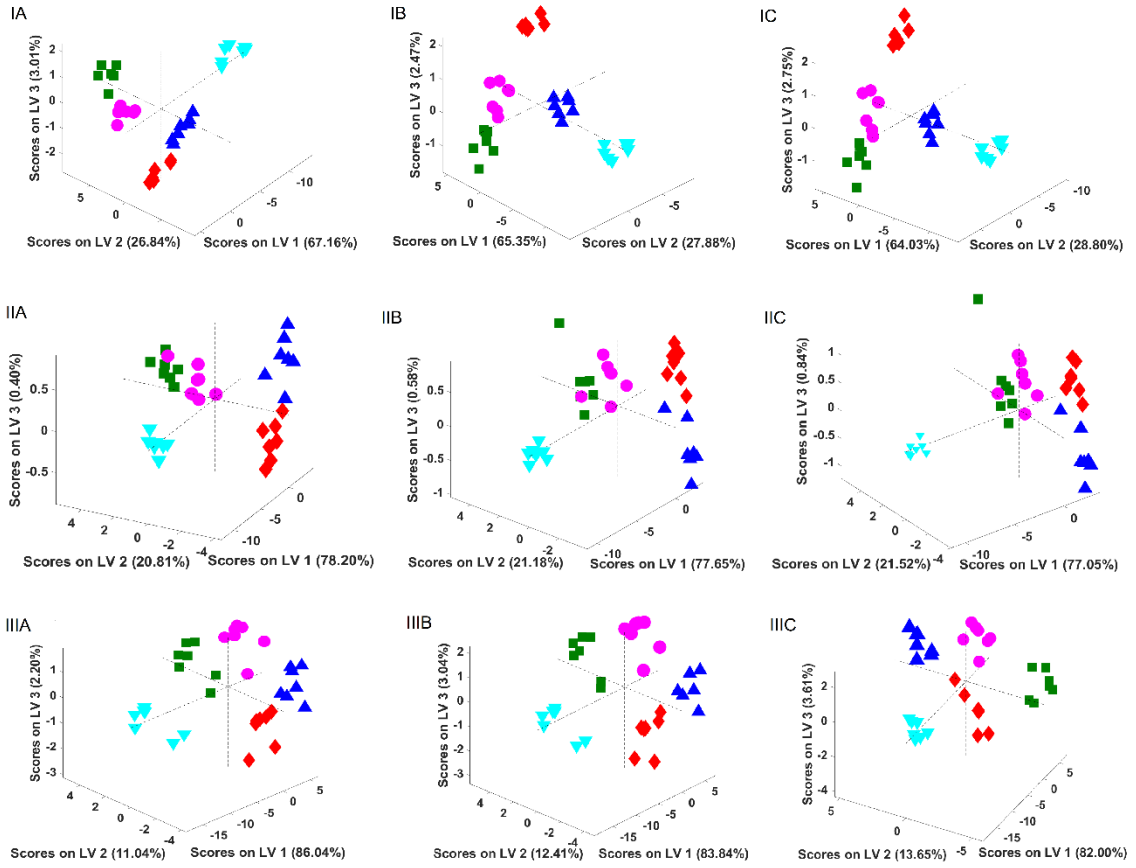

Fig. 2.4. Scores plots corresponding to the first three LVs of PLSDA regression models obtained using UV-Vis spectra at pH 3.0 (IA–IC), pH 4.5 (IIA–IIC), and pH 6.0 (IIIA–IIIC) for protein discrimination. $[P_{44416}]_2$[EB] GUMBOS + RNAse A (◆), Lyz (■), Alb (▲), Mb (▼), and α-ChT (●). Models (A) 5, (B) 10, and (C) 15 min of reaction.

Concerning pH 4.5, the scores plots obtained for all time points (first three LVs encompassing around 98% of spectral variability) showed one well-individualized cluster belonging to Mb, two somehow contiguous clusters corresponding to Alb and RNAse A as well as a fourth cluster containing Lyz and α-ChT proteins (Fig. 2.4, panels IIA–IIC). At pH 6.0, the scores plots (first three LVs accounting for 98% of spectral variability) were quite similar to those achieved at pH 3.0 (Fig. 2.4, panels IIIA–IIIC). In these cases, no visible overlapping was observed, but clusters remained scattered. Overall, the percentage of correct protein identifications varied from 91.9% (10 min) to 94.2% (5 min) at pH 4.5, and from 94.5% (5 min) to 97.7% (15 min) at pH 6.0 (Tables S2.8 and S2.9, respectively). The lower percentages observed at pH 4.5, as compared with the corresponding values at pH 3.0 and 6.0, were in agreement with the overlapping clusters observed in PLSDA scores plots (Fig. 2.4, panels IIA–IIC). When regarding each protein individually, with both pH values and the three reaction times, only Mb spectra had a consistently correct prediction of 100.0%. The great majority of Alb spectra were also correctly predicted (97.0%–5 min,

84.0%–10 min, 86.0%–15 min at pH 4.5, and 92.5%–5 min, 98.0%–10 min, 98.5%–15 min at pH 6.0), while the remaining were erroneously identified as RNAse A or RNAse A and α-ChT spectra. Additionally, RNAse A was also correctly predicted in general for both pH values. It was, however, misidentified as Alb (5.5%–5 min), Lyz (1.5%–15 min), and Lyz + Alb (2.5% + 1.5%–10 min) at pH 4.5, or as Alb (1.0%–5 min and 0.5%–15 min) at pH 6.0. Lyz spectra were 100.0% correctly predicted at 5 and 10 min for pH 4.5 and were misidentified only as α-ChT spectra after 15 min of reaction (3.0% of wrong predictions). With respect to pH 6.0, Lyz was globally well predicted (91.5%–5 min, 94.5%–10 min, 98.0–15 min), being misidentified only as RNAse A at 5 and 10 min as well as RNAse A (1.0%) and α-ChT (1.0%) at 15 min. Overall, α-ChT spectra were the worst predicted (87.5%–5 min, 76.5%–10 min, 85.0%–15 min at pH 4.5, and 89.5%–5 min, 88.5%–10 min, 92.5%–15 min at pH 6.0), being misidentified with several proteins depending on the pH and reaction period.

2.3.4.3. $[N_{4444}]_2$[EB]

The scores plots obtained from PLSDA models (three LVs encompassing around 97% of spectral variability for the three reaction times) presented in Fig. 2.5 (panels IA–IC) showed three well-individualized clusters. Two of them contain spectra of a single protein (Alb or Mb) and the third one spectra of RNAse A, Lyz, and α-ChT. It should also be noted that spectra of these three proteins appeared in the scores plots contiguously, with minimal cluster overlapping. The worst discrimination was observed at 5 and 10 min with responses to Lyz and α-ChT analytes. LV1 seemed to be the principal cause for the discrimination of Alb and Mb, while other proteins fell into the third cluster and were partially discriminated in LV2 and LV3. No relevant differences were observed in the scores plots obtained for the three reaction periods, which was in accordance with the percentage of correct predictions acquired through the confusion matrices (around 90% for the times studied, Table 2.1). Alb, Mb, and RNAse A were almost always correctly predicted (100.0%), with exception of RNAse A at 15 min (0.5% misidentified as α-ChT). In contrast, Lyz and α-ChT spectra presented lower percentages of correct identifications and were misidentified as each other. The percentages of Lyz misidentifications were 17.0% at 5 min, 18.5% at 10 min, 21.5% at 15 min, while in relation to α-ChT were 30.0% at 5 min, 31.0% at 10 min, and 36.0% at 15 min (Table S2.10).

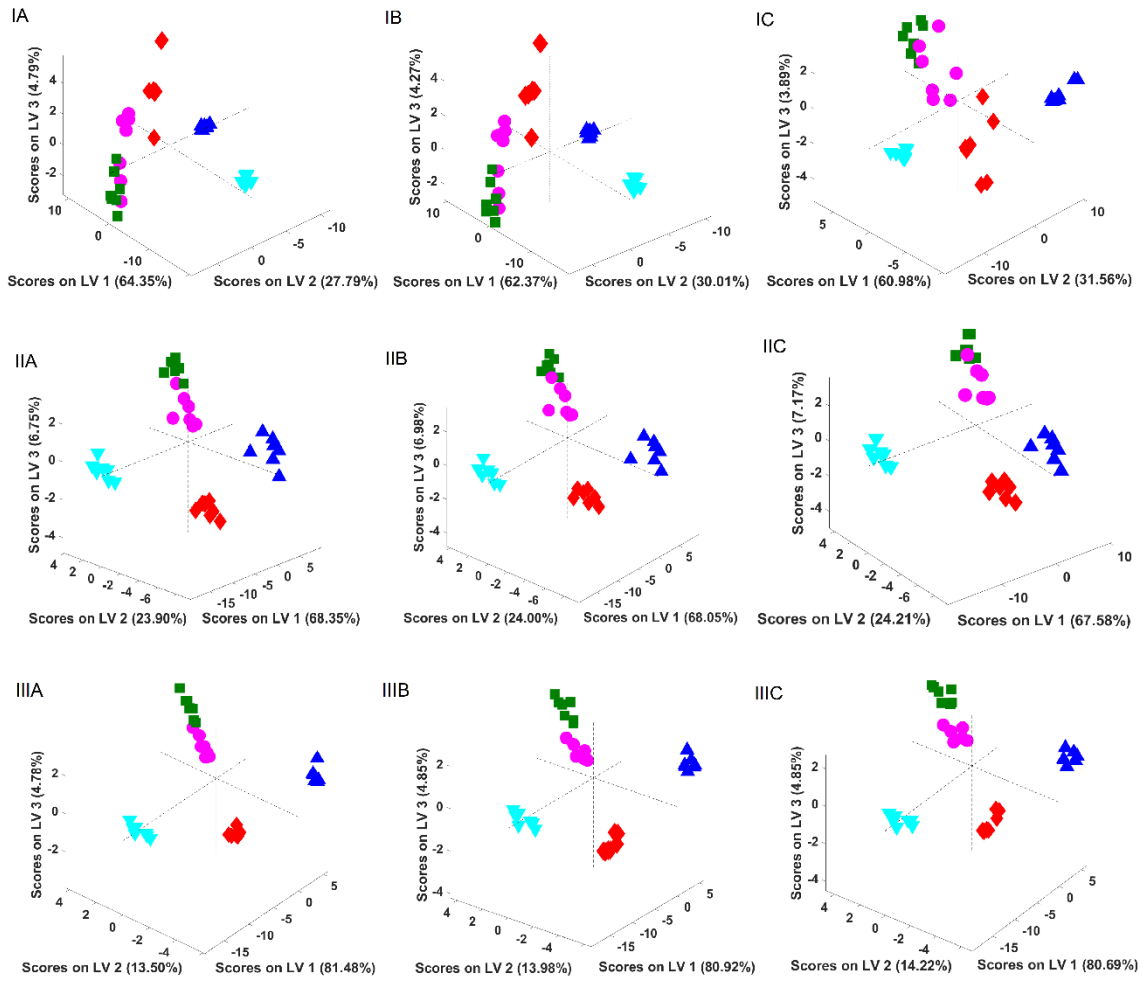

Fig. 2.5. Scores plots corresponding to the first three LVs of PLSDA regression models obtained using UV-Vis spectra at pH 3.0 (IA–IC), pH 4.5 (IIA–IIC), and pH 6.0 (IIIA–IIIC) for protein discrimination. $[N_{4444}]_2$[EB] GUMBOS + RNAse A (♦), Lyz (■), Alb (▲), Mb (▼), and α-ChT (●). Models A, B, and C correspond to 5, 10, and 15 min of reaction.

With respect to both pH 4.5 (Fig. 2.5, panels IIA–IIC) and pH 6.0 (Fig. 2.5, panels IIIA–IIIC), the scores maps showed more clearly defined clusters than those obtained at pH 3.0. For the $[N_{4444}]_2$[EB] GUMBOS, time did not seem to be an influential factor for protein discrimination, which is in contrast to what was observed for pH value. Spectral variability captured on the first three LVs was around 99% for all reaction times and both pH values. The percentages of correct discrimination of proteins were consistent with such findings, at approximately 93 to 95% for pH 4.5 and 100% for pH 6.0 (Tables S2.11–pH 4.5 and S2.12–pH 6.0). At pH 4.5, Alb and Mb spectra were correctly identified as well as RNAse A spectra at 15 min. After 5 and 10 min, however, RNAse A was predicted as α-ChT (0.5%–5 min and 1.0%–10 min). Similar to what was observed for pH 3.0, Lyz and α-ChT were misidentified as each other (Lyz as α-ChT: 11.5%–5 min, 18.0%–10 min, 15.0%–15 min, and α-ChT as Lyz: 12.0%–5 min, 15.5%–10 min, 17.5%–15 min). At pH 6.0, the only misidentification was

related to 0.5% of α-ChT spectra, which were predicted as Lyz upon 10 min of reaction.

2.3.4.4. $[BDHA]_2[EB]$

The scores plots obtained for protein discrimination using $[BDHA]_2[EB]$ were similar to those acquired for the $[P_{4444}]_2[EB]$ GUMBOS, but with a slightly lower overlap between Lyz and α-ChT spectra (Fig. 2.6, panels IA–IC). Five well-individualized clusters (each one corresponding to a single protein) were discriminated among LV1 (Alb from Mb from RNAse A + Lyz + α-ChT), LV2 (RNAse A from Lyz + α-ChT), and LV3 (Lyz from α-ChT). Spectral variability captured on the first three LVs was around 99% for all times studied. The total percentages of correct protein assignments (> 99%) were in agreement with the well-individualized clusters obtained for the three reaction periods (Table S2.13). Alb, Mb, RNAse A, and Lyz spectra were 100% correctly predicted, with erroneous identifications related to a few α-ChT spectra identified as Lyz (2.5%–5 min, 1.5%–10 min, 2.0%–15 min) (Table S2.13).

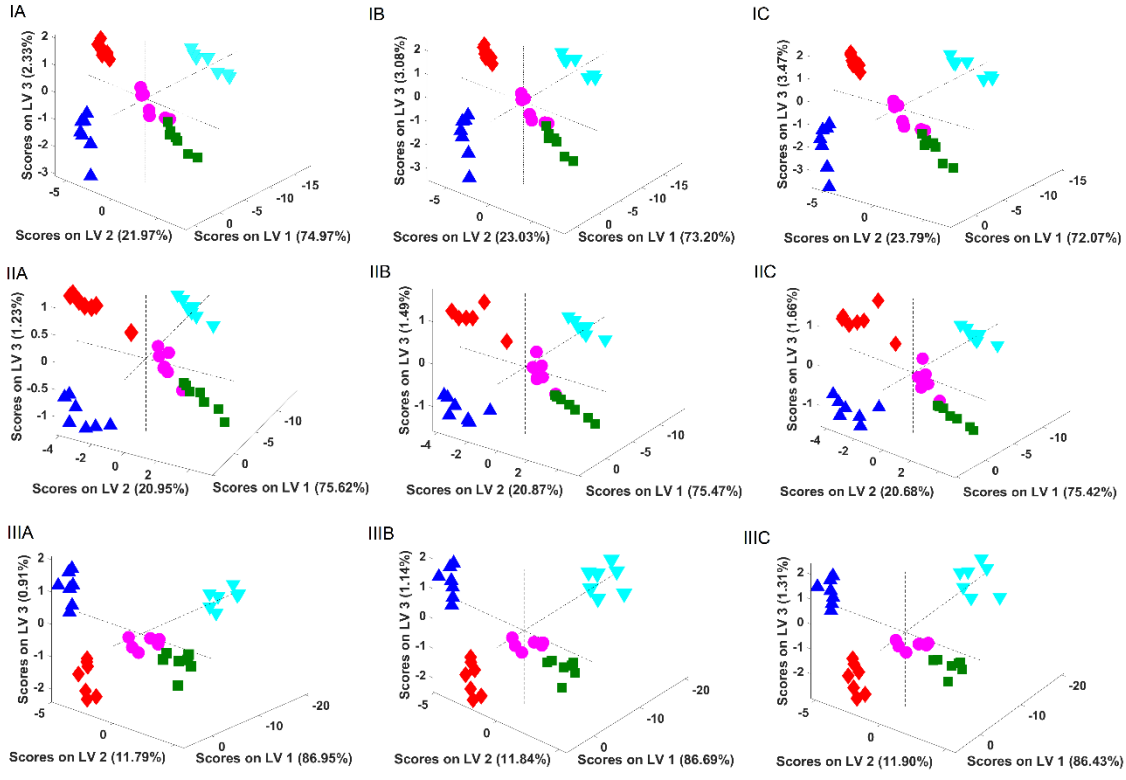

Fig. 2.6. Scores plots corresponding to the first three LVs of PLSDA regression models obtained using UV-Vis spectra at pH 3.0 (IA–IC), pH 4.5 (IIA–IIC), and pH 6.0 (IIIA–IIIC) for protein discrimination. $[BDHA]_2[EB]$ GUMBOS + RNAse A (◆), Lyz (■), Alb (▲), Mb (▼), and α-ChT (●). Models (A) 5, (B) 10, and (C) 15 min of reaction.

Regarding pH 4.5 and 6.0, the scores maps presented similar clusters to those observed at pH 3.0, with 98% of spectral variability captured on the first three LVs for all reaction times (panels IIA–IIC and IIIA–IIIC from Fig. 2.6). The percentages of correct identifications of proteins were nearly 93 and 99% for pH 4.5 and 6.0, respectively (Tables S2.14 and S2.15). As noted previously, GUMBOS-protein reaction times do not seem to affect these percentages, but pH value does. At pH 4.5 (Table S2.14), only Mb spectra were correctly identified for the three times studied. Regarding Alb spectra, 97.5%–5 min, 91.0%–10 min, and 88.5%–15 min were correctly predicted, as these responses were misidentified as α-ChT (2.5%–5 min, 6.0%–10 min, 8.0%–15 min), RNAse A (2.5%–10 min, 1.0%–15 min), and Lyz spectra (1.0%–10 min, 1.5%–15 min). RNAse A spectra correct identifications varied from 86.5% (15 min) to 88.0% (10 min), as it was misidentified as α-ChT (11.0%–5 min, 11.5%–10 min, 12.5%–15 min), Mb (1.5%–5 min), Alb (0.5%–10 min), and Lyz spectra (1.0%–15 min). With respect to Lyz spectra, the incorrect identifications were solely predicted as α-ChT spectra (6.5%–5 min, 3.5%–10 min, 2.0%–15 min). Similarly, α-ChT spectra were misidentified as Lyz (9.0%–5 min, 9.5%–10 min, 7.5%–15 min) and as RNAse A spectra (0.5%) at 15 min. At pH 6.0, higher percentages of correct protein assignments were observed (Table S3.15), with Alb, Mb, and RNAse A correctly predicted in a consistent fashion. In contrast, Lyz was relatively poorly predicted as RNAse A (4.5%–5 min, 2.5%–10 min, 2.5%–15 min) and α-ChT (4.0%–5 min, 1.5%–10 min, 1.5%–15 min). α-ChT spectra were correctly predicted consistently at 5 min and poorly predicted solely as Lyz spectra (2.5%–10 min, 2.0%–15 min).

2.3.5. Discrimination of binary mixtures containing Alb and Mb

Among the synthesized GUMBOS, $[P_{4444}]_2[EB]$ and $[N_{4444}]_2[EB]$ were those that showed better ability to discriminate proteins at pH 6.0. Moreover, Alb and Mb were the proteins that consistently exhibited higher percentages of correct assignments. With this in mind, the $[P_{4444}]_2[EB]$ and $[N_{4444}]_2[EB]$ GUMBOS were used to discriminate between four protein mixtures of Alb and Mb (20% Alb + 80% Mb, 40% Alb + 60% Mb, 60% Alb + 40% Mb, and 80% Alb + 20% Mb). Scores plots of the developed PLSDA models for $[P_{4444}]_2[EB]$ and $[N_{4444}]_2[EB]$ are provided in Fig. 2.7. In both cases, discrimination of protein mixtures clearly occurs in LV1, which encompassed almost 90% of spectral variability and where more well-defined clusters were found. GUMBOS spectra in the presence of a single protein (100% Alb or Mb) appeared on opposite sides of the scores map. It is interesting to note that on the positive side of the LV1 axis, where 100% Alb samples are located, all samples containing more than 50% of Alb were also observed. In contrast, spectra with less than 50% of Alb and more than 50% of Mb appeared on the negative side of LV1, which contains

100% Mb spectra. Separation of spectra along LV1 in two groups (> 50% Alb and < 50% Mb or < 50% Alb and > 50% Mb) was clear evidence that both GUMBOS possess the ability for discrimination of protein mixtures.

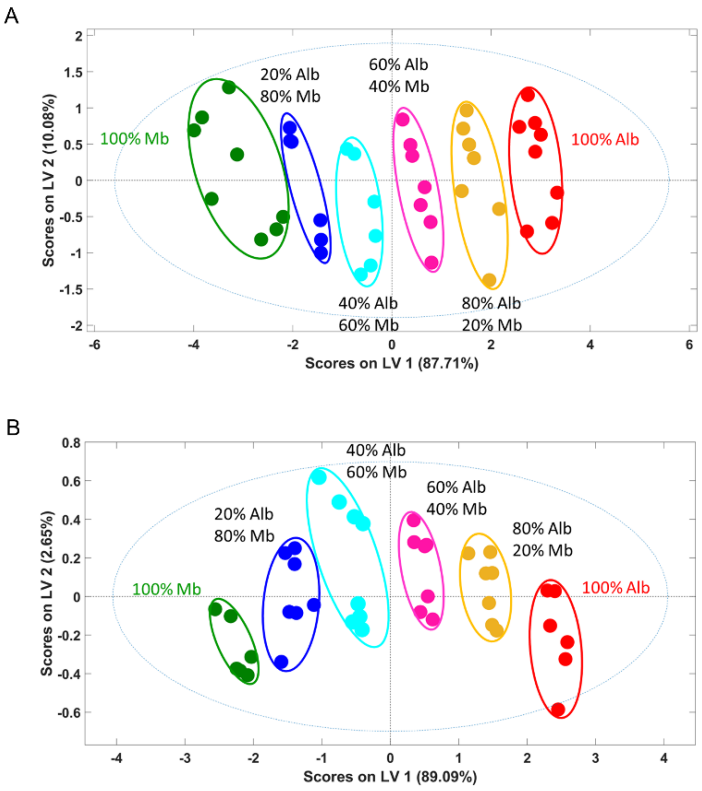

Fig. 2.7. Scores plots corresponding to the first two LVs of PLSDA regression models developed using the UV-Vis spectra of (A) $[P_{4444}]_2[EB]$ and (B) $[N_{4444}]_2[EB]$ after incubation with binary mixtures of Alb + Mb.

2.4. Discussion

In this work, it was demonstrated that EB-based GUMBOS in combination with UV-Vis spectroscopy and PLSDA can successfully discriminate not only single proteins, but also binary mixtures of Alb and Mb. This study also investigated whether pH and reaction time affect GUMBOS discrimination performance.

Although numerous methods have been developed to discriminate proteins, most of them are laborious and time-consuming. Synthesis of sensing materials often involves multi-step reactions and purification procedures, which has limited their widespread use and has motivated the search for viable alternatives (50-52). As a result of simplicity of their design and synthetic process, along with the possibility to tune their properties, GUMBOS appear to be promising candidates for discrimination of proteins (23, 24, 26). In this work, it was

shown that melting point and hydrophobicity of EB-based GUMBOS as well as their ability to discriminate proteins can be modulated through simple cation exchange (Na^+ by P_{4444}^+, P_{44416}^+, N_{4444}^+, and $BDHA^+$). A single by-product is formed during this reaction, which is easily removed simply by washing with water.

It is worth noting that, because of its relatively large, planar, and rigid structure, EB can strongly bind to hydrophobic protein surface residues. Although van der Waals and π-stacking interactions can also occur, the primary driving forces are hydrophobic interactions (53-55). EB-based GUMBOS were found to display varying degrees of hydrophobicity that were attributed to cation exchange and have led to changes in protein binding affinity. The absorbance response patterns were then used to discriminate each protein by applying PLSDA models. Chemometric analyses revealed that $[P_{4444}]_2$[EB] and $[N_{4444}]_2$[EB] show higher discriminatory power than $[P_{44416}]_2$[EB] and $[BDHA]_2$[EB] GUMBOS. Moreover, similarities in their ability to discriminate proteins can be explained using the chemical resemblance between phosphorus and nitrogen atoms and shorter alkyl side chain length, which reduces steric hindrance and improves GUMBOS accessibility to proteins (56).

Results demonstrated that the size, surface charge, and hydrophobic properties of proteins may also affect the extent of interaction with sensing materials, thus corroborating previous studies (23, 50, 57). Overall, Alb and Mb were determined to have the highest percentages of correct predictions as seen from the confusion matrices of PLSDA models (Tables S2.4–S2.15). These findings can be explained by the fourfold difference in molecular weight between the two proteins (66.5 vs 16.7 kDa), opposite surface charges at pH 7.4, and great variation in their hydrophobicity (58). In contrast, Lyz and α-ChT were the most misclassified and appeared as overlapping clusters in the scores plots. The same tendency was reported by Hewitt and Wilson (59).

The impact of pH and reaction time on the discriminatory power of EB-based GUMBOS was further examined. After 5, 10, and 15 min, the PLSDA scores plots did not show major differences in clustering patterns (Figs. 2.3–2.6), which suggests a rapid binding between GUMBOS and proteins. Moreover, the percentages of correct predictions were similar for all time points (Table 2.1), and thus, a period of 5 min was selected. In contrast, Soedjak reported that binding of EB dye to proteins is slow at room temperature and requires about 2 h to be completed (24 times more than the corresponding GUMBOS) (32). That study also showed that an acidic environment tends to promote formation of EB-protein complexes, which was later confirmed by other studies (33, 34). In an attempt to determine if the same procedures apply to EB-derived GUMBOS, experiments were conducted at pH 3.0, 4.5, and 6.0. As seen in Table 2.1, the percentages of correct assignments varied from 86.5 to 100.0% depending on the pH of citrate buffer and GUMBOS chemical structure. The

best results were obtained at pH 6.0 and can be assigned to the dianionic form of EB in the GUMBOS (pK_{COOH} = 2.35 and pK_{OH} = 3.79) (60). Overall, it was found that time does not affect the discriminatory power of synthesized GUMBOS, while pH does.

Discrimination of protein binary mixtures is far more challenging as the two proteins can interact with each other and compete for binding to the sensing material (50). Both $[P_{4444}]_2$[EB] and $[N_{4444}]_2$[EB] GUMBOS were able to discriminate between mixtures containing different proportions of Alb and Mb. 2D-PLSDA scores plots showed clearly defined and separate clusters of mixtures and allowed discrimination of pure and mixed proteins, similar to what has been reported in the literature for sensor arrays and other chemometric models (24, 61, 62). However, in this work, an assembly of sensors was not required, with protein discrimination being achieved by use of single GUMBOS.

Finally, it is important to highlight the ability of chemometric tools to extract useful analytical information from complex datasets. Both unsupervised (PCA and HCA) and supervised (LDA) models have been used to analyze the response patterns generated from GUMBOS-based sensor arrays (23, 24). In this work, PLSDA models were developed to discriminate not only single but also binary mixtures of proteins by using the entire spectral wavelength range of data collected. The first LV seemed to be the main factor responsible for discrimination of Alb from Mb and then from RNAse A + Lyz + α-ChT. Such results were obtained for all EB-based GUMBOS, independent of the reaction time and pH, and can be attributed to the nature of proteins as previously discussed.

2.5. Conclusions

In this study, four novel EB-based GUMBOS were synthesized and used to discriminate single and binary protein mixtures. The pH and reaction time were also investigated for their effect on discrimination performance of synthesized materials. It was found that changes in pH value (3.0–6.0) affected discrimination ability of EB-based GUMBOS, while the reaction period (5–15 min) did not seem to affect the results. The percentages of correct protein assignments ranged from 86.5 to 100.0%, being the best results achieved with $[P_{4444}]_2$[EB] and $[N_{4444}]_2$[EB] at pH 6.0 and 5 min of reaction time. Under these conditions, it was possible to discriminate between protein mixtures containing four different ratios of Alb and Mb since they appeared as well individualized clusters in the 2D-PLSDA scores plots. Although the underlying mechanism still necessitates further clarification, it is reasonable to infer that the results are derived from changes in the absorption spectra of GUMBOS due to protein binding. Thus, the obtained results demonstrate the potential of using these and other GUMBOS in combination with UV-Vis spectroscopy and chemometric tools to discriminate

individual proteins and their mixtures. Moreover, this GUMBOS approach offers many advantages as compared to traditional analytical methods, including simplicity, rapidity, and cost-effectiveness. This alternative strategy is label-free, requires only five min of reaction time, and avoids the use of expensive instrumentation and complicated synthesis of probes. As part of future studies, it is planned to extend the application of this approach to more complex proteins and matrices (e.g., urine and blood).

SUPPLEMENTARY MATERIAL

Characterization of EB-based GUMBOS

$[P_{4444}]_2[EB]$

^{1}H NMR (400 MHz, $CDCl_3$, ppm): δ 8.29-8.34 (m, 1H); 7.49-7.53 (m, 3H); 7.41-7.48 (m, 1H); 7.01-7.03 (m, 1H); 2.17 (bs, 16H); 1.42 (bs, 24H); 0.87-0.94 (m, 24H). ^{13}C NMR (125 MHz, $CDCl_3$, ppm): δ = 172.20, 172.17, 168.76, 157.93, 138.37, 133.30, 131.10, 129.02, 128.66, 112.97, 112.95, 95.44, 75.17, 24.06, 23.96, 23.79, 18.88, 18.51, 13.58.

$[P_{44416}]_2[EB]$

^{1}H NMR (400 MHz, $CDCl_3$, ppm): δ 8.28-8.40 (m, 1H); 7.46-7.56 (m, 3H); 7.40-7.46 (m, 1H); 7.00-7.04 (m, 1H); 2.19 (bs, 16H); 1.42 (bs, 33H); 1.26 (bs, 50H); 0.87-0.93 (m, 21H). ^{13}C NMR (125 MHz, $CDCl_3$, ppm): δ = 172.20, 168.72, 157.79, 156.49, 138.26, 133.13, 130.98, 128.82, 128.50, 128.25, 112.81, 95.32, 75.04, 31.77, 30.74, 30.63, 29.56, 29.53, 29.50, 29.43, 29.21, 28.90, 23.96, 23.84, 23.71, 23.68, 22.53, 21.77, 21.73, 18.96, 18.76, 18.59, 18.38, 13.98, 13.48.

$[N_{4444}]_2[EB]$

^{1}H NMR (400 MHz, $CDCl_3$, ppm): δ 8.30-8.36 (m, 1H); 7.47-7.56 (m, 3H); 7.38-7.45 (m, 1H); 7.00-7.04 (m, 1H); 3.10 (bs, 16H); 1.48-1.61 (m, 16H); 1.29-1.38 (m, 16H); 0.92-0.95 (m, 24H). ^{13}C NMR (125 MHz, $CDCl_3$, ppm): δ = 171.74, 168.34, 157.72, 156.94, 141.45, 138.33, 133.01, 128.60, 128.38, 127.91, 112.67, 95.23, 74.82, 58.39, 23.83, 19.61, 13.62.

$[BDHA]_2[EB]$

^{1}H NMR (400 MHz, $CDCl_3$, ppm): δ 8.29-8.33 (m, 1H); 7.58-7.62 (m, 2H); 7.51-7.57 (m, 1H); 7.36-7.48 (m, 10H); 7.05-7.10 (m, 1H); 4.48-4.55 (bs, 4H); 3.12-3.22 (bs, 4H); 2.96 (s, 12H); 1.21-1.35 (bs, 50H); 0.85-0.93 (m, 6H). ^{13}C NMR (125 MHz, $CDCl_3$, ppm): δ = 172.32, 169.84, 157.85, 156.65, 138.39, 133.09, 132.66, 130.81, 129.20, 128.97, 128.39, 127.23, 113.04, 95.60, 75.36, 67.60, 63.57, 49.63, 31.90, 29.70, 29.67, 29.65, 29.62, 29.50, 29.43, 29.34, 29.24, 26.34, 22.86, 22.66, 14.11.

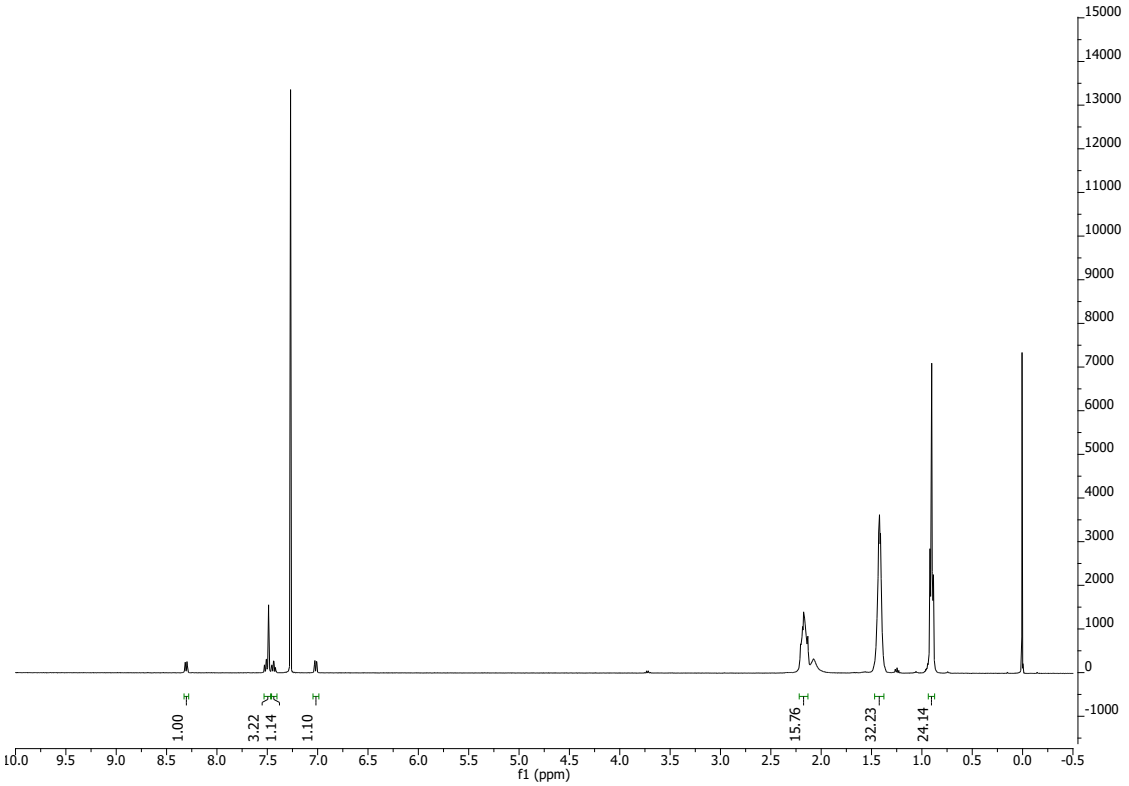

Fig. S2.1. ^{1}H NMR spectrum of $[P_{4444}]_2$[EB] GUMBOS.

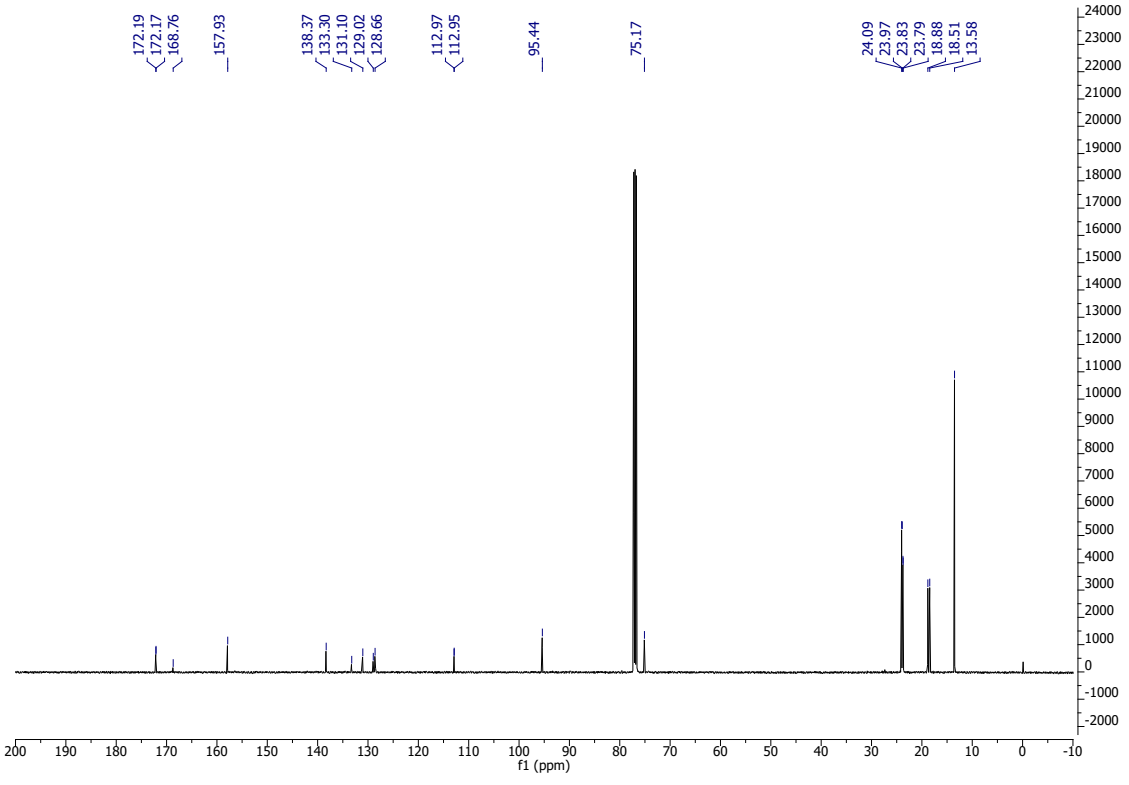

Fig. S2.2. ^{13}C NMR spectrum of $[P_{4444}]_2$[EB].

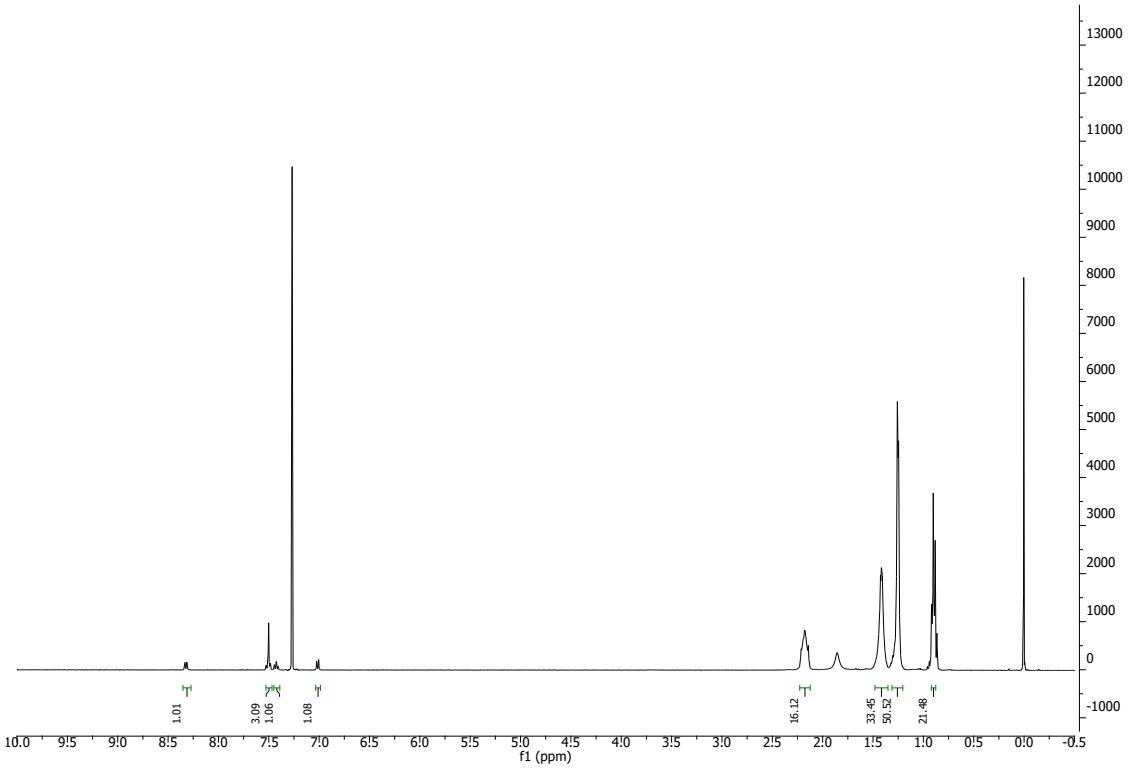

Fig. S2.3. ^{1}H NMR spectrum of $[P_{44416}]_2[EB]$.

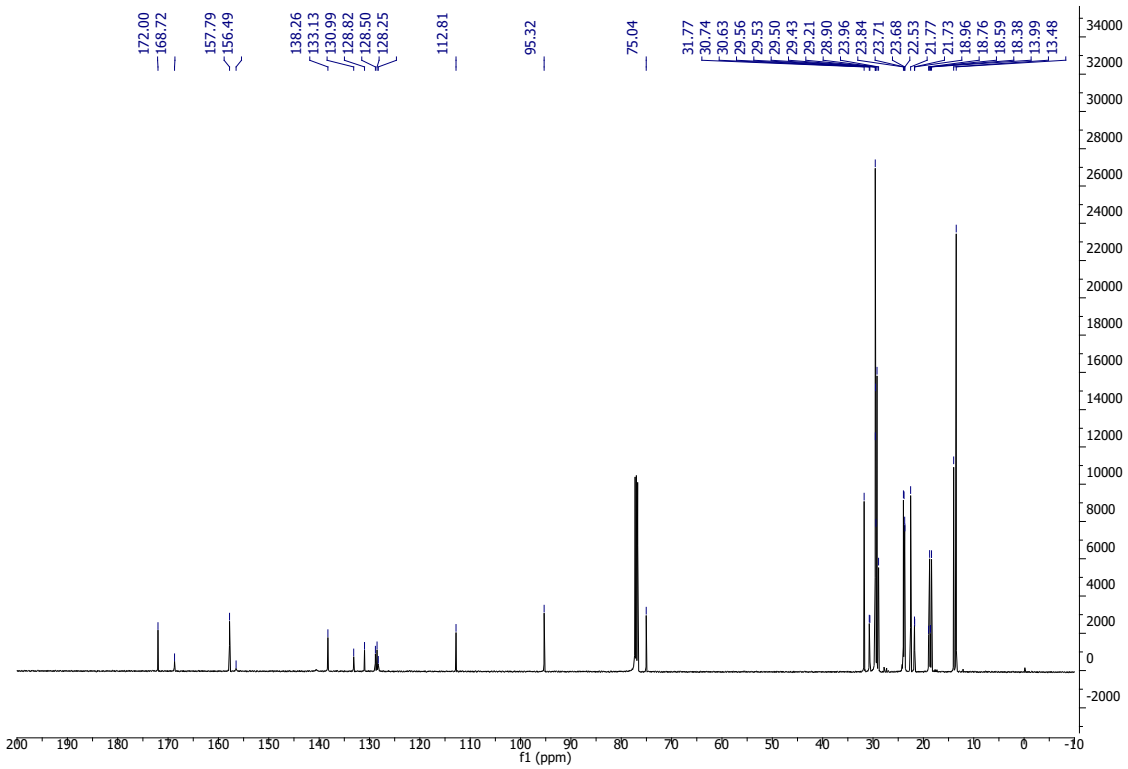

Fig. S2.4. ^{13}C NMR spectrum of $[P_{44416}]_2[EB]$ GUMBOS.

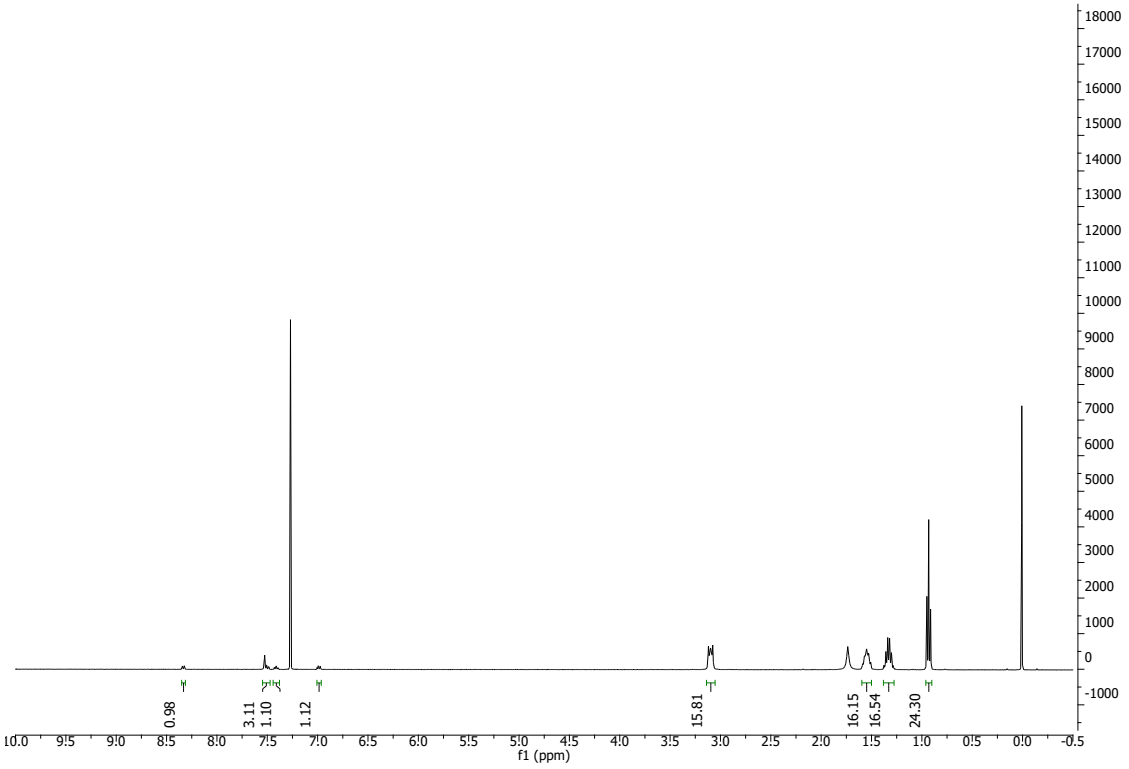

Fig. S2.5. ^{1}H spectrum of $[N_{4444}]_2[EB]$.

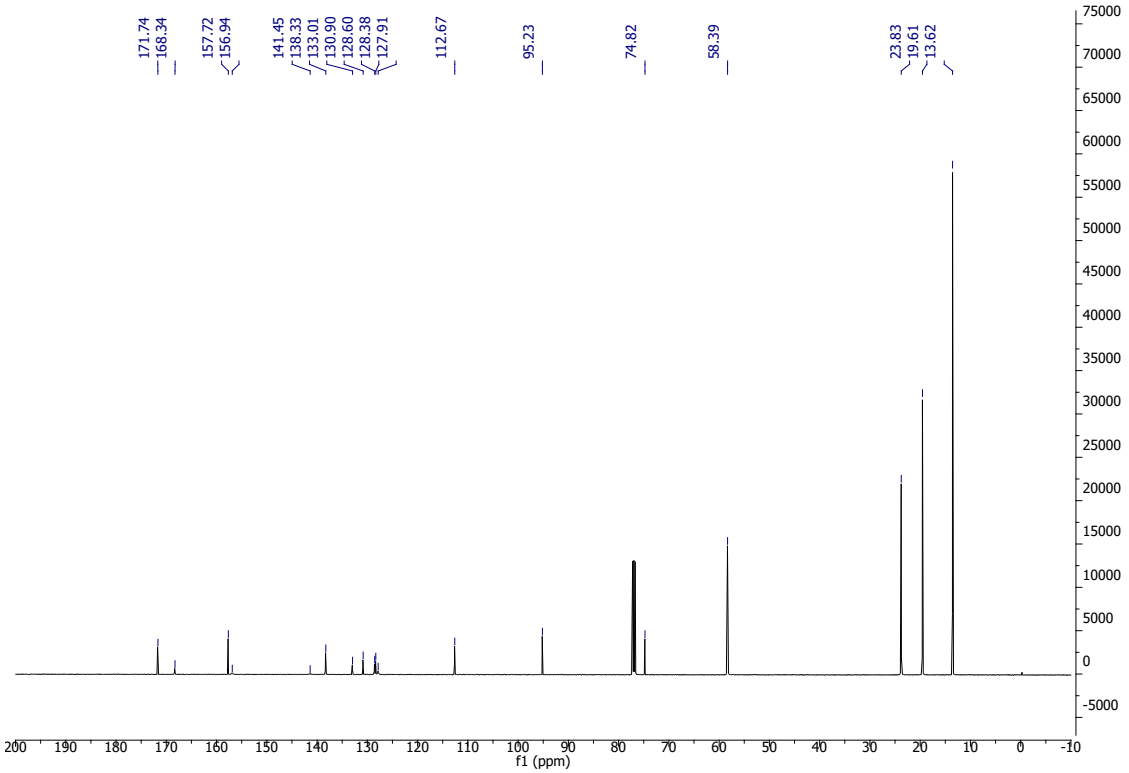

Fig. S2.6. ^{13}C spectrum of $[N_{4444}]_2[EB]$ in $CDCl_3$.

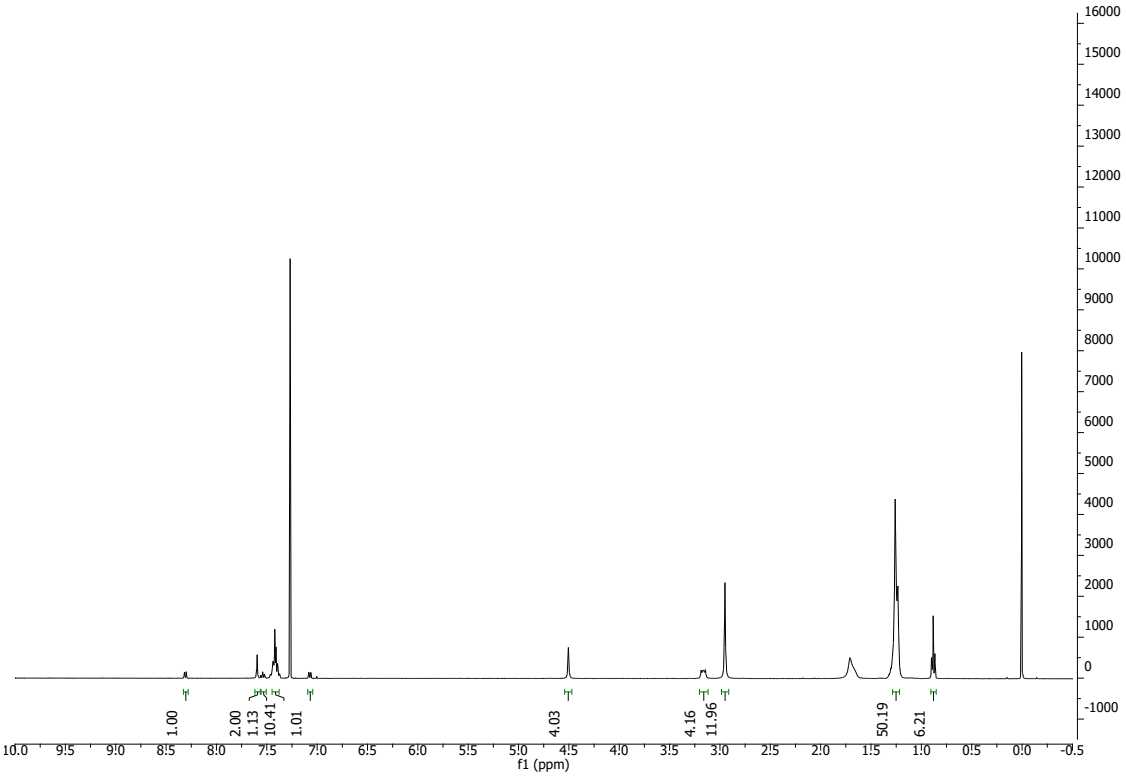

Fig. S2.7. ^{1}H NMR spectrum of $[BDHA]_2[EB]$ GUMBOS.

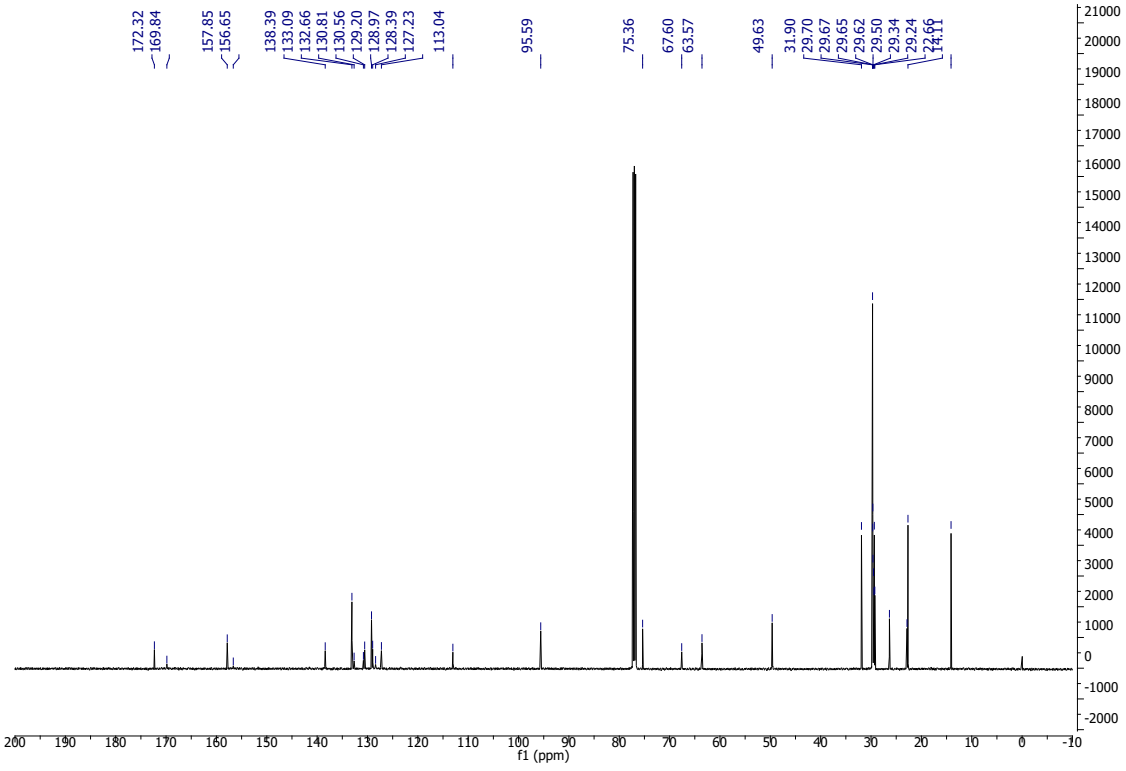

Fig. S2.8. ^{13}C NMR spectrum of $[BDHA]_2[EB]$.

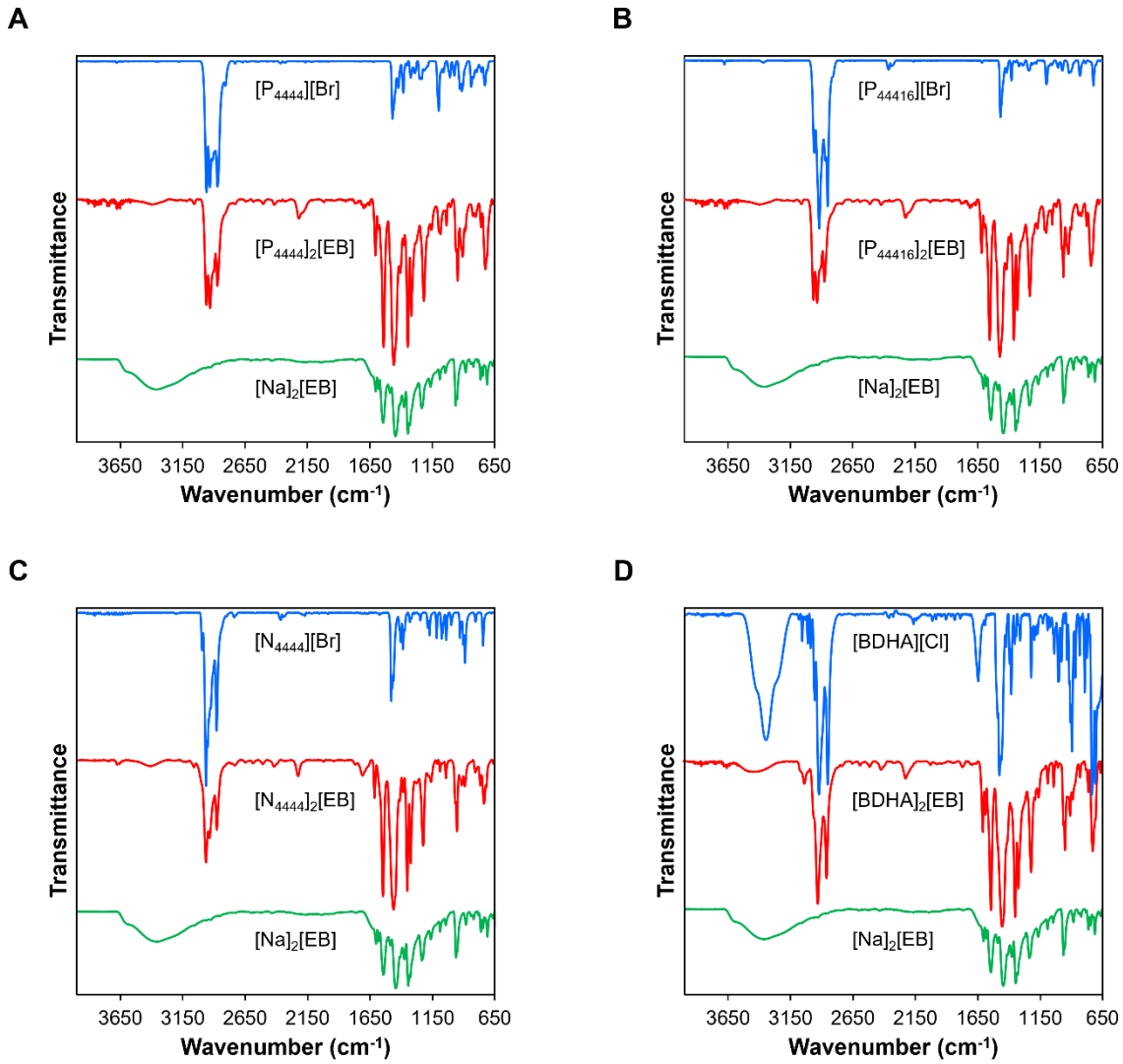

Fig. S2.9. Overlay of FTIR spectra of starting materials (blue and green) and resulting products (red): (A) $[P_{4444}]_2[EB]$, (B) $[P_{44416}]_2[EB]$, (C) $[N_{4444}]_2[EB]$, and (D) $[BDHA]_2[EB]$.

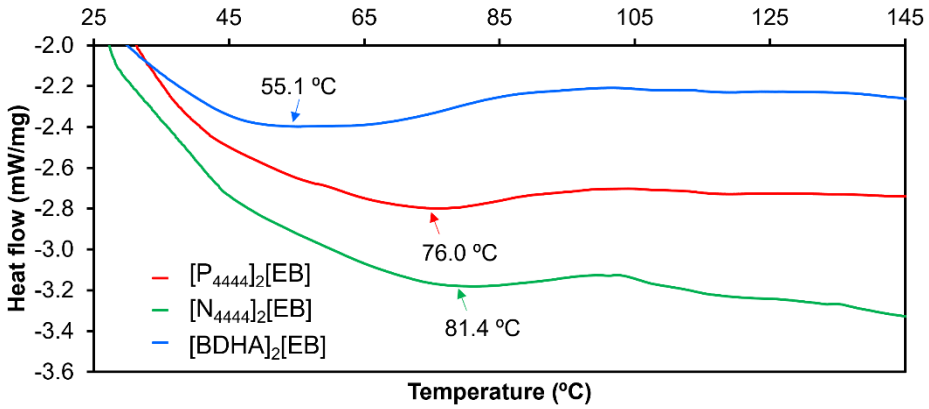

Fig. S2.10. DSC thermograms of EB-based GUMBOS.

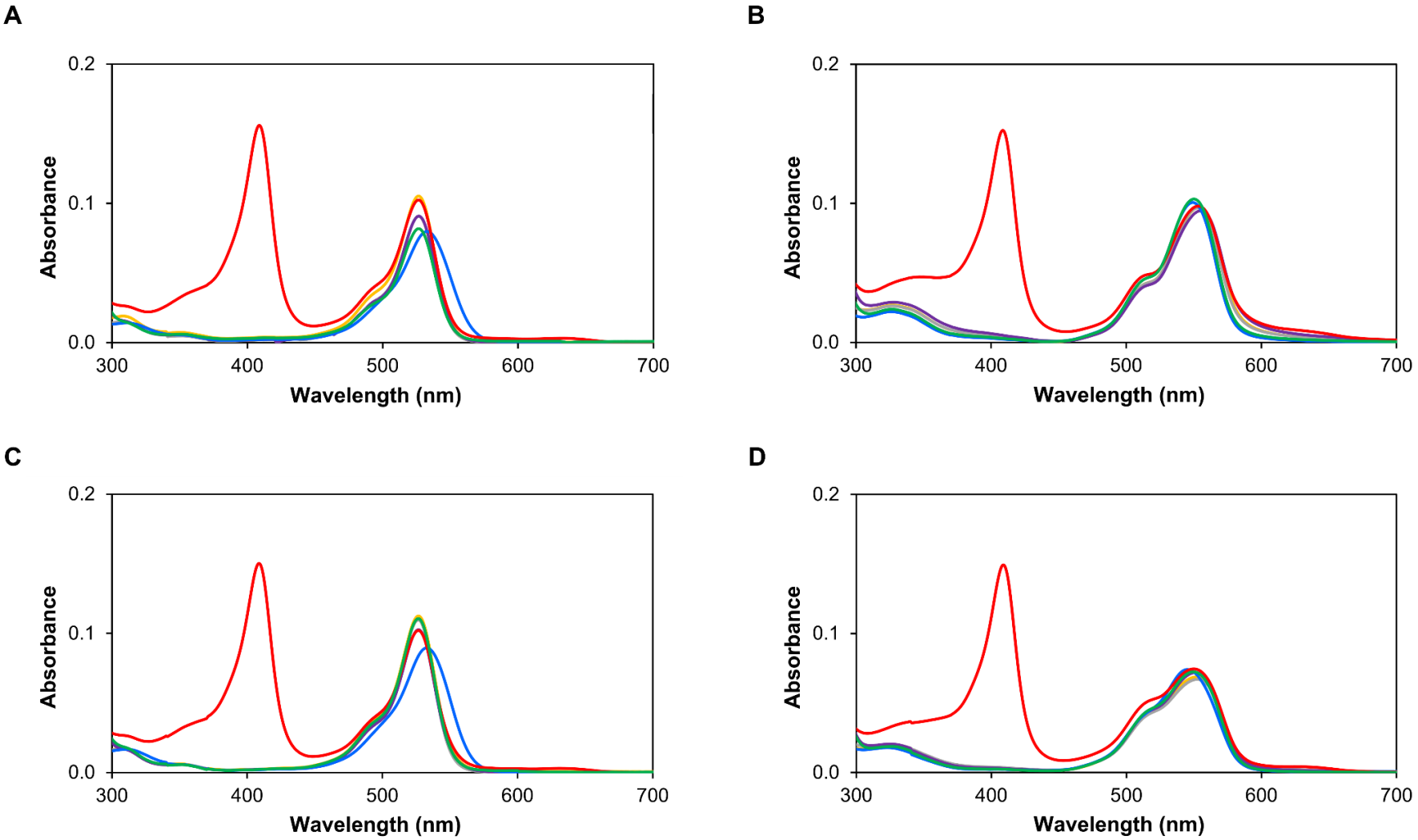

Fig. S2.11. Absorbance spectra of (A) $[P_{4444}]_2[EB]$, (B) $[P_{44416}]_2[EB]$, (C) $[N_{4444}]_2[EB]$, and (D) $[BDHA]_2[EB]$: alone (–) and in the presence of RNAse A (–), Lyz (–), Alb (–), Mb (–), and α-ChT (–). Spectra were recorded at pH 6.0 after 5 min of reaction time.

Table S2.1. Yield and ESI-MS analysis of synthesized materials.

GUMBOS	Yield (%)	Ionic formula		ESI-MS (positive mode)		ESI-MS (negative mode)	
		Cation	Anion	Expected mass (*m/z*)	Experimental mass (*m/z*)	Expected mass (*m/z*)	Experimental mass (*m/z*)
$[P_{4444}]_2[EB]$	97	$C_{16}H_{36}P^+$	$C_{20}H_7I_4O_5^-$	259.2549	259.2557	834.6478	834.6460
$[P_{44416}]_2[EB]$	92	$C_{28}H_{60}P^+$		427.4427	427.4432		834.6461
$[N_{4444}]_2[EB]$	74	$C_{16}H_{36}N^+$		242.2842	242.2841		834.6463
$[BDHA]_2[EB]$	81	$C_{25}H_{46}N^+$		360.3625	360.3630		834.6464

Table S2.2. Logarithm of the octanol/water partition coefficients ($\log K_{O/W}$) of EB-based GUMBOS.

GUMBOS	$\log K_{O/W}$ ± SD [a]
$[P_{4444}]_2[EB]$	1.10 ± 0.02
$[P_{44416}]_2[EB]$	1.73 ± 0.03
$[N_{4444}]_2[EB]$	0.77 ± 0.06
$[BDHA]_2[EB]$	1.87 ± 0.06

[a] Data presented as mean ± standard deviation of three independent experiments.
For $[Na]_2[EB]$, $\log K_{O/W}$ = -0.15 (63).

Table S2.3. Molecular weights and isoelectric points of target proteins.

Protein	Molecular weight (kDa)	Isoelectric point	Ref.
RNase A	13.7	9.6	(64)
Lyz	14.3	11.4	(65)
Alb	66.5	4.7	(66)
Mb	16.7	7.0	(67)
α-ChT	25.0	8.8	(64)

Protein discrimination using the synthesized GUMBOS

Table S2.4. Confusion matrices obtained from the PLSDA models developed for protein discrimination at pH 3.0 using the $[P_{4444}]_2$[EB] GUMBOS. Models A, B, and C correspond to 5, 10, and 15 min of reaction.

Model A	RNAse A	Lyz	Alb	Mb	α-ChT	
RNAse A	19.10	0	0	0	0.90	–
Lyz	0	15.90	0	0	4.10	–
Alb	0	0	20.00	0	0	–
Mb	0	0	0	20.00	0	–
α-ChT	0	7.10	0	0	12.90	–
				Correct protein discrimination (%)		**87.9**
Model B	RNAse A	Lyz	Alb	Mb	α-ChT	
RNAse A	19.20	0	0	0	0.80	–
Lyz	0	16.10	0	0	3.90	–
Alb	0	0	20.00	0	0	–
Mb	0	0	0	20.00	0	–
α-ChT	0	8.80	0	0	11.20	–
				Correct protein discrimination (%)		**86.5**
Model C	RNAse A	Lyz	Alb	Mb	α-ChT	
RNAse A	19.70	0	0	0	0.30	–
Lyz	0	15.40	0	0	4.60	–
Alb	0	0	20.00	0	0	–
Mb	0	0	0	20.00	0	–
α-ChT	0.10	6.80	0	0	13.10	–
				Correct protein discrimination (%)		**88.2**

Table S2.5. Confusion matrices for protein discrimination at pH 4.5 using the $[P_{4444}]_2$[EB] GUMBOS and acquired from the PLSDA models. (A) 5, (B) 10, and (C) 15 min of reaction.

Model A	RNAse A	Lyz	Alb	Mb	α-ChT	
RNAse A	20.00	0	0	0	0	–
Lyz	0	20.00	0	0	0	–
Alb	0	0	20.00	0	0	–
Mb	0	0	0	20.00	0	–
α-ChT	0	1.60	0	0	18.40	–
				Correct protein discrimination (%)		**98.4**
Model B	RNAse A	Lyz	Alb	Mb	α-ChT	
RNAse A	20.00	0	0	0	0	–
Lyz	0	20.00	0	0	0	–
Alb	0	0	20.00	0	0	–
Mb	0	0	0	20.00	0	–
α-ChT	0	0.40	0	0	19.60	–
				Correct protein discrimination (%)		**99.6**
Model C	RNAse A	Lyz	Alb	Mb	α-ChT	
RNAse A	20.00	0	0	0	0	–
Lyz	0	20.00	0	0	0	–
Alb	0	0	20.00	0	0	–
Mb	0	0	0	20.00	0	–
α-ChT	0	0	0	0	20.00	–
				Correct protein discrimination (%)		**100.0**

Table S2.6. Confusion matrices acquired from the PLSDA models developed for discrimination of proteins at pH 6.0 using the $[P_{4444}]_2$[EB] GUMBOS. Models A, B, and C correspond to 5, 10, and 15 min of reaction time.

Model A	RNAse A	Lyz	Alb	Mb	α-ChT	
RNAse A	20.00	0	0	0	0	–
Lyz	0	20.00	0	0	0	–
Alb	0	0	20.00	0	0	–
Mb	0	0	0	20.00	0	–
α-ChT	0	0	0	0	20.00	–
					Correct protein discrimination (%)	**100.0**
Model B	RNAse A	Lyz	Alb	Mb	α-ChT	
RNAse A	20.00	0	0	0	0	–
Lyz	0	20.00	0	0	0	–
Alb	0	0	20.00	0	0	–
Mb	0	0	0	20.00	0	–
α-ChT	0	0	0	0	20.00	–
					Correct protein discrimination (%)	**100.0**
Model C	RNAse A	Lyz	Alb	Mb	α-ChT	
RNAse A	20.00	0	0	0	0	–
Lyz	0	20.00	0	0	0	–
Alb	0	0	20.00	0	0	–
Mb	0	0	0	20.00	0	–
α-ChT	0	0	0	0	20.00	–
					Correct protein discrimination (%)	**100.0**

Table S2.7. Confusion matrices for discrimination of proteins at pH 3.0 using the $[P_{44416}]_2[EB]$ GUMBOS and acquired from PLSDA models: (A) 5, (B) 10, and (C) 15 min of reaction.

Model A	RNAse A	Lyz	Alb	Mb	α-ChT	
RNAse A	19.70	0	0	0	0.30	–
Lyz	0	19.40	0	0	0.60	–
Alb	0	0	20.00	0	0	–
Mb	0	0	0	20.00	0	–
α-ChT	0	1.30	0	0	18.70	–
				Correct protein discrimination (%)		**97.8**
Model B	RNAse A	Lyz	Alb	Mb	α-ChT	
RNAse A	17.00	0	0	0	3.00	–
Lyz	0	20.00	0	0	0	–
Alb	0	0	20.00	0	0	–
Mb	0	0	0	20.00	0	–
α-ChT	0	1.50	0	0	18.50	–
				Correct protein discrimination (%)		**95.5**
Model C	RNAse A	Lyz	Alb	Mb	α-ChT	
RNAse A	18.20	0	0	0	1.80	–
Lyz	0	18.50	0	0	1.50	–
Alb	0	0	20.00	0	0	–
Mb	0	0	0	20.00	0	–
α-ChT	0	1.70	0	0	18.30	–
				Correct protein discrimination (%)		**95.0**

Table S2.8. Confusion matrices obtained from the PLSDA models for protein discrimination at pH 4.5 using the $[P_{44416}]_2$[EB] GUMBOS. Models A, B, and C correspond to 5, 10, and 15 min of reaction period.

Model A	RNAse A	Lyz	Alb	Mb	α-ChT	
RNAse A	18.90	0	1.10	0	0	–
Lyz	0	20.00	0	0	0	–
Alb	0.50	0	19.40	0	0.10	–
Mb	0	0	0	20.00	0	–
α-ChT	0	2.30	0.10	0	17.50	–
				Correct protein discrimination (%)		**95.8**
Model B	RNAse A	Lyz	Alb	Mb	α-ChT	
RNAse A	19.20	0.50	0.30	0	0	–
Lyz	0	20.00	0	0	0	–
Alb	1.40	0	16.80	0	1.80	–
Mb	0	0	0	20.00	0	–
α-ChT	0	3.60	1.10	0	15.30	–
				Correct protein discrimination (%)		**91.3**
Model C	RNAse A	Lyz	Alb	Mb	α-ChT	
RNAse A	19.70	0.30	0	0	0	–
Lyz	0	19.40	0	0	0.60	–
Alb	0.90	0	17.20	0	1.90	–
Mb	0	0	0	20.00	0	–
α-ChT	0	2.10	0.90	0	17.00	–
				Correct protein discrimination (%)		**93.3**

Table S2.9. Confusion matrices for discrimination of proteins at pH 6.0 using $[P_{44416}]_2$[EB] GUMBOS and acquired from the PLSDA models: (A) 5, (B) 10, and (C) 15 min of reaction.

Model A	RNAse A	Lyz	Alb	Mb	α-ChT	
RNAse A	19.80	0	0.20	0	0	–
Lyz	0.80	18.30	0	0	0.90	–
Alb	1.30	0	18.50	0	0.20	–
Mb	0	0	0	20.00	0	–
α-ChT	0.20	0.60	1.30	0	17.90	–
				Correct protein discrimination (%)		**94.5**
Model B	RNAse A	Lyz	Alb	Mb	α-ChT	
RNAse A	20.00	0	0	0	0	–
Lyz	0.70	18.90	0	0	0.40	–
Alb	0.40	0	19.60	0	0	–
Mb	0	0	0	20.00	0	–
α-ChT	0.40	0.50	1.40	0	17.70	–
				Correct protein discrimination (%)		**96.2**
Model C	RNAse A	Lyz	Alb	Mb	α-ChT	
RNAse A	19.90	0	0.10	0	0	–
Lyz	0.20	19.60	0	0	0.20	–
Alb	0.10	0	19.70	0	0.20	–
Mb	0	0	0	20.00	0	–
α-ChT	0	0.60	0.90	0	18.50	–
				Correct protein discrimination (%)		**97.7**

Table S2.10. Confusion matrices obtained from PLSDA models developed for discrimination of proteins at pH 3.0 using the $[N_{4444}]_2$[EB] GUMBOS. Models A, B, and C correspond to 5, 10, and 15 min of reaction time.

Model A	RNAse A	Lyz	Alb	Mb	α-ChT	
RNAse A	20.00	0	0	0	0	–
Lyz	0	16.60	0	0	3.40	–
Alb	0	0	20.00	0	0	–
Mb	0	0	0	20.00	0	–
α-ChT	0	6.00	0	0	14.00	–
				Correct protein discrimination (%)		**90.6**
Model B	RNAse A	Lyz	Alb	Mb	α-ChT	
RNAse A	20.00	0	0	0	0	–
Lyz	0	16.30	0	0	3.70	–
Alb	0	0	20.00	0	0	–
Mb	0	0	0	20.00	0	–
α-ChT	0	6.20	0	0	13.80	–
				Correct protein discrimination (%)		**90.1**
Model C	RNAse A	Lyz	Alb	Mb	α-ChT	
RNAse A	19.90	0	0	0	0.10	–
Lyz	0	15.70	0	0	4.30	–
Alb	0	0	20.00	0	0	–
Mb	0	0	0	20.00	0	–
α-ChT	0	7.20	0	0	12.80	–
				Correct protein discrimination (%)		**88.4**

Table S2.11. Confusion matrices obtained from the PLSDA models developed for discrimination of proteins at pH 4.5 using the GUMBOS $[N_{4444}]_2[EB]$. Models A, B, and C correspond to 5, 10, and 15 min of reaction period.

Model A	RNAse A	Lyz	Alb	Mb	α-ChT	
RNAse A	19.90	0	0	0	0.10	–
Lyz	0	17.70	0	0	2.30	–
Alb	0	0	20.00	0	0	–
Mb	0	0	0	20.00	0	–
α-ChT	0	2.40	0	0	17.60	–
				Correct protein discrimination (%)		**95.2**
Model B	RNAse A	Lyz	Alb	Mb	α-ChT	
RNAse A	19.80	0	0	0	0.20	–
Lyz	0	16.40	0	0	3.60	–
Alb	0	0	20.00	0	0	–
Mb	0	0	0	20.00	0	–
α-ChT	0	3.10	0	0	16.90	–
				Correct protein discrimination (%)		**93.1**
Model C	RNAse A	Lyz	Alb	Mb	α-ChT	
RNAse A	20.00	0	0	0	0	–
Lyz	0	17.00	0	0	3.00	–
Alb	0	0	20.00	0	0	–
Mb	0	0	0	20.00	0	–
α-ChT	0	3.50	0	0	16.50	–
				Correct protein discrimination (%)		**93.5**

Table S2.12. Confusion matrices obtained from the PLSDA models developed for protein discrimination at pH 6.0 using the $[N_{4444}]_2$[EB] GUMBOS. Models A, B, and C: 5, 10, and 15 min of reaction.

Model A	RNAse A	Lyz	Alb	Mb	α-ChT	
RNAse A	20.00	0	0	0	0	–
Lyz	0	20.00	0	0	0	–
Alb	0	0	20.00	0	0	–
Mb	0	0	0	20.00	0	–
α-ChT	0	0	0	0	20.00	–
				Correct protein discrimination (%)		**100.0**
Model B	RNAse A	Lyz	Alb	Mb	α-ChT	
RNAse A	20.00	0	0	0	0	–
Lyz	0	20.00	0	0	0	–
Alb	0	0	20.00	0	0	–
Mb	0	0	0	20.00	0	–
α-ChT	0	0.10	0	0	19.90	–
				Correct protein discrimination (%)		**99.9**
Model C	RNAse A	Lyz	Alb	Mb	α-ChT	
RNAse A	20.00	0	0	0	0	–
Lyz	0	20.00	0	0	0	–
Alb	0	0	20.00	0	0	–
Mb	0	0	0	20.00	0	–
α-ChT	0	0	0	0	20.00	–
				Correct protein discrimination (%)		**100.0**

Table S2.13. Confusion matrices generated from the PLSDA models used for protein discrimination at pH 3.0 with the GUMBOS $[BDHA]_2[EB]$. Models A, B, and C correspond to 5, 10, and 15 min of reaction period.

Model A	RNAse A	Lyz	Alb	Mb	α-ChT	
RNAse A	20.00	0	0	0	0	–
Lyz	0	20.00	0	0	0	–
Alb	0	0	20.00	0	0	–
Mb	0	0	0	20.00	0	–
α-ChT	0	0.50	0	0	19.50	–
				Correct protein discrimination (%)		**99.5**
Model B	RNAse A	Lyz	Alb	Mb	α-ChT	
RNAse A	20.00	0	0	0	0	–
Lyz	0	20.00	0	0	0	–
Alb	0	0	20.00	0	0	–
Mb	0	0	0	20.00	0	–
α-ChT	0	0.30	0	0	19.70	–
				Correct protein discrimination (%)		**99.7**
Model C	RNAse A	Lyz	Alb	Mb	α-ChT	
RNAse A	20.00	0	0	0	0	–
Lyz	0	20.00	0	0	0	–
Alb	0	0	20.00	0	0	–
Mb	0	0	0	20.00	0	–
α-ChT	0	0.40	0	0	19.60	–
				Correct protein discrimination (%)		**99.6**

Table S2.14. Confusion matrices for discrimination of proteins at pH 4.5 using the GUMBOS $[BDHA]_2[EB]$ and acquired from PLSDA models: A, B, and C correspond to 5, 10, and 15 min of reaction.

Model A	RNAse A	Lyz	Alb	Mb	α-ChT	
RNAse A	17.50	0	0	0.30	2.20	–
Lyz	0	18.70	0	0	1.30	–
Alb	0	0	19.50	0	0.50	–
Mb	0	0	0	20.00	0	–
α-ChT	0	1.80	0	0	18.20	–
					Correct protein discrimination (%)	**93.9**
Model B	RNAse A	Lyz	Alb	Mb	α-ChT	
RNAse A	17.60	0.00	0.10	0	2.30	–
Lyz	0	19.30	0	0	0.70	–
Alb	0.50	0.20	18.20	0	1.10	–
Mb	0	0	0	20.00	0	–
α-ChT	0	1.90	0	0	18.10	–
					Correct protein discrimination (%)	**93.2**
Model C	RNAse A	Lyz	Alb	Mb	α-ChT	
RNAse A	17.30	0.20	0	0	2.50	–
Lyz	0	19.60	0	0	0.40	–
Alb	0.20	0.30	17.70	0	1.60	–
Mb	0	0	0	20.00	0	–
α-ChT	0.10	1.50	0	0	18.40	–
					Correct protein discrimination (%)	**93.0**

Table S2.15. Confusion matrices obtained from the PLSDA models developed for protein discrimination at pH 6.0 using the $[BDHA]_2[EB]$ GUMBOS. Models A, B, and C: 5, 10, and 15 min of reaction.

Model A	RNAse A	Lyz	Alb	Mb	α-ChT	
RNAse A	20.00	0	0	0	0	–
Lyz	0.90	18.30	0	0	0.80	–
Alb	0	0	20.00	0	0	–
Mb	0	0	0	20.00	0	–
α-ChT	0	0	0	0	20.00	–
				Correct protein discrimination (%)		**98.3**
Model B	RNAse A	Lyz	Alb	Mb	α-ChT	
RNAse A	20.00	0	0	0	0	–
Lyz	0.50	19.20	0	0	0.30	–
Alb	0	0	20.00	0	0	–
Mb	0	0	0	20.00	0	–
α-ChT	0	0.50	0	0	19.50	–
				Correct protein discrimination (%)		**98.7**
Model C	RNAse A	Lyz	Alb	Mb	α-ChT	
RNAse A	20.00	0	0	0	0	–
Lyz	0.50	19.20	0	0	0.30	–
Alb	0	0	20.00	0	0	–
Mb	0	0	0	20.00	0	–
α-ChT	0	0.40	0	0	19.60	–
				Correct protein discrimination (%)		**98.8**

References

1. Jaffery Z, Nowak R, Khoury N, Tokarski G, Lanfear DE, Jacobsen G, et al. Myoglobin and troponin I elevation predict 5-year mortality in patients with undifferentiated chest pain in the emergency department. Am Heart J. 2008;156(5):939-45.

2. Kumar V, Brent JR, Shorie M, Kaur H, Chadha G, Thomas AG, et al. Nanostructured Aptamer-Functionalized Black Phosphorus Sensing Platform for Label-Free Detection of Myoglobin, a Cardiovascular Disease Biomarker. ACS Appl Mater Interfaces. 2016;8(35):22860-8.

3. Vesterhus M, Holm A, Hov JR, Nygard S, Schrumpf E, Melum E, et al. Novel serum and bile protein markers predict primary sclerosing cholangitis disease severity and prognosis. J Hepatol. 2017;66(6):1214-22.

4. Vesterhus M, Karlsen TH. Emerging therapies in primary sclerosing cholangitis: pathophysiological basis and clinical opportunities. J Gastroenterol. 2020;55(6):588-614.

5. Xu T, Fang YX, Rong AA, Wang JH. Flexible combination of multiple diagnostic biomarkers to improve diagnostic accuracy. BMC Med Res Methodol. 2015;15:7.

6. Pena MJ, Mischak H, Heerspink HJL. Proteomics for prediction of disease progression and response to therapy in diabetic kidney disease. Diabetologia. 2016;59(9):1819-31.

7. Uryu K, Chen XH, Martinez D, Browne KD, Johnson VE, Graham DI, et al. Multiple proteins implicated in neurodegenerative diseases accumulate in axons after brain trauma in humans. Exp Neurol. 2007;208(2):185-92.

8. Spindel S, Sapsford KE. Evaluation of Optical Detection Platforms for Multiplexed Detection of Proteins and the Need for Point-of-Care Biosensors for Clinical Use. Sensors. 2014;14(12):22313-41.

9. Rusling JF. Multiplexed Electrochemical Protein Detection and Translation to Personalized Cancer Diagnostics. Anal Chem. 2013;85(11):5304-10.

10. Van Gool A, Corrales F, Colovic M, Krstic D, Oliver-Martos B, Martinez-Caceres E, et al. Analytical techniques for multiplex analysis of protein biomarkers. Expert Rev Proteomics. 2020;17(4):257-73.

11. Stahl-Zeng J, Lange V, Ossola R, Eckhardt K, Krek W, Aebersold R, et al. High sensitivity detection of plasma proteins by multiple reaction monitoring of N-glycosites. Mol Cell Proteomics. 2007;6(10):1809-17.

12. Dzimianski JV, Lorig-Roach N, O'Rourke SM, Alexander DL, Kimmey JM, DuBois RM. Rapid and sensitive detection of SARS-CoV-2 antibodies by biolayer interferometry. Sci Rep. 2020;10(1):12.

13. Donnelly DP, Rawlins CM, DeHart CJ, Fornelli L, Schachner LF, Lin ZQ, et al. Best practices and benchmarks for intact protein analysis for top-down mass spectrometry. Nat Methods. 2019;16(7):587-94.
14. Smit NPM, Ruhaak LR, Romijn FPHTM, Pieterse MM, van der Burgt YEM, Cobbaert CM. The Time Has Come for Quantitative Protein Mass Spectrometry Tests That Target Unmet Clinical Needs. J Am Soc Mass Spectrom. 2021;32(3):636-47.
15. Li Z, Askim JR, Suslick KS. The Optoelectronic Nose: Colorimetric and Fluorometric Sensor Arrays. Chem Rev. 2019;119(1):231-92.
16. Fan JM, Qi L, Han HF, Ding LP. Array-Based Discriminative Optical Biosensors for Identifying Multiple Proteins in Aqueous Solution and Biofluids. Front Chem. 2020;8:18.
17. Hou CJ, Dong JL, Zhang GP, Lei Y, Yang M, Zhang YC, et al. Colorimetric artificial tongue for protein identification. Biosens Bioelectron. 2011;26(10):3981-6.
18. Bigdeli A, Ghasemi F, Golmohammadi H, Abbasi-Moayed S, Nejad MAF, Fahimi-Kashani N, et al. Nanoparticle-based optical sensor arrays. Nanoscale. 2017;9(43):16546-63.
19. Umali AP, Anslyn EV. A general approach to differential sensing using synthetic molecular receptors. Curr Opin Chem Biol. 2010;14(6):685-92.
20. Nielsen JE, Pedersen KS, Vestergard K, Maltesen RG, Christiansen G, Lundbye-Christensen S, et al. Novel Blood-Derived Extracellular Vesicle-Based Biomarkers in Alzheimer's Disease Identified by Proximity Extension Assay. Biomedicines. 2020;8(7):21.
21. De M, Rana S, Akpinar H, Miranda OR, Arvizo RR, Bunz UHF, et al. Sensing of proteins in human serum using conjugates of nanoparticles and green fluorescent protein. Nat Chem. 2009;1(6):461-5.
22. Xi HY, Li X, Liu QY, Chen ZB. Cationic polymer-based plasmonic sensor array that discriminates proteins. Analyst. 2018;143(22):5578-82.
23. Galpothdeniya WIS, Fronczek FR, Cong M, Bhattarai N, Siraj N, Warner IM. Tunable GUMBOS-based sensor array for label-free detection and discrimination of proteins. J Mat Chem B. 2016;4(8):1414-22.
24. Perez RL, Cong M, Vaughan SR, Ayala CE, Galpothdeniya WIS, Mathaga JK, et al. Protein Discrimination Using a Fluorescence-Based Sensor Array of Thiacarbocyanine-GUMBOS. ACS Sensors. 2020;5(8):2422-9.
25. Warner IM, El-Zahab B, Siraj N. Perspectives on Moving Ionic Liquid Chemistry into the Solid Phase. Anal Chem. 2014;86(15):7184-91.
26. Azevedo AMO, Santos JLM, Warner IM, Saraiva MLMFS. GUMBOS and nanoGUMBOS in chemical and biological analysis: A review. Anal Chim Acta. 2020;1133:180-98.

27. Lehto S, Buchweitz M, Klimm A, Strassburger R, Bechtold C, Ulberth F. Comparison of food colour regulations in the EU and the US: a review of current provisions. Food Addit Contam Part A-Chem. 2017;34(3):335-55.

28. Franke JD, Braverman AL, Cunningham AM, Eberhard EE, Perry GA. Erythrosin B: a versatile colorimetric and fluorescent vital dye for bacteria. Biotechniques. 2020;68(1):7-13.

29. Li Z, Sakamuru S, Huang RL, Brecher M, Koetzner CA, Zhang J, et al. Erythrosin B is a potent and broad-spectrum orthosteric inhibitor of the flavivirus NS2B-NS3 protease. Antiviral Res. 2018;150:217-25.

30. Lam SK, Chan MA, Lo D. Characterization of phosphorescence oxygen sensor based on erythrosin B in sol-gel silica in wide pressure and temperature ranges. Sens Actuator B-Chem. 2001;73(2-3):135-41.

31. Wang ML, Meng GW, Huang Q. Iodeosin-based fluorescent and colorimetric sensing for Ag^{+}, Hg^{2+}, Fe^{3+}, and further for halide ions in aqueous solution. RSC Adv. 2014;4(16):8055-8.

32. Soedjak HS. Colorimetric micromethod for protein determination with erythrosin B. Anal Biochem. 1994;220(1):142-8.

33. Isoe J, Kaneko E. A new spectrophotometric method for determination of urinary protein using Erythrosin B. Chem Lett. 2006;35(8):922-3.

34. Kaneko E, Yasuda H, Higurashi A, Yoshimura H. Spot test of urinary protein using Erythrosin B and a membrane film. Analyst. 2010;135(7):1564-8.

35. OECD. Guideline No. 107, Partition Coefficient (n-octanol/water): Shake Flask Method 1995.

36. Naes T, Isaksson T, Fearn T, Davies T. A user-friendly guide to multivariate calibration and classification. Chichester, UK: NIR Publications; 2002.

37. Geladi P, Kowalski BR. Partial least-squares regression: A tutorial. Anal Chim Acta. 1986;185:1-17.

38. Alsberg BK, Kell DB, Goodacre R. Variable selection in discriminant partial least-squares analysis. Anal Chem. 1998;70(19):4126-33.

39. Fleming GR, Knight AWE, Morris JM, Morrison RJS, Robinson GW. Picosecond Fluorescence Studies of Xanthene Dyes. J Am Chem Soc. 1977;99(13):4306-11.

40. Montero E, Garcia MA, Villegas MA, Llopis J. Spectral pH dependence of erythrosin B in sol-gel silica coatings and buffered solutions. Bol Soc Esp Ceram Vidr. 2008;47(1):1-6.

41. Tobyn M, Brown J, Dennis AB, Fakes M, Gao Q, Gamble J, et al. Amorphous Drug-PVP Dispersions: Application of Theoretical, Thermal and Spectroscopic Analytical

Techniques to the Study of a Molecule With Intermolecular Bonds in Both the Crystalline and Pure Amorphous State. J Pharm Sci. 2009;98(9):3456-68.

42. Chen M, Perez RL, Du P, Bhattarai N, McDonough KC, Ravula S, et al. Tumor-Targeting NIRF NanoGUMBOS with Cyclodextrin-Enhanced Chemo/Photothermal Antitumor Activities. ACS Appl Mater Interfaces. 2019;11(31):27548-57.

43. Wasserscheid P, Welton T. Ionic Liquids in Synthesis. 2nd ed. Weinheim: Wiley-VCH; 2008.

44. Lopez-Martin I, Burello E, Davey PN, Seddon KR, Rothenberg G. Anion and cation effects on imidazolium salt melting points: A descriptor modelling study. ChemPhysChem. 2007;8(5):690-5.

45. Zhang H, Li MT, Yang BL. Design, Synthesis, and Analysis of Thermophysical Properties for Imidazolium-Based Geminal Dicationic Ionic Liquids. J Phys Chem C. 2018;122(5):2467-74.

46. Freire MG, Neves CMSS, Carvalho PJ, Gardas RL, Fernandes AM, Marrucho IM, et al. Mutual Solubilities of water and hydrophobic ionic liquids. J Phys Chem B. 2007;111(45):13082-9.

47. Yamamoto E, Yamaguchi S, Nagamune T. Protein Refolding by N-Alkylpyridinium and N-Alkyl-N-methylpyrrolidinium Ionic Liquids. Appl Biochem Biotechnol. 2011;164(6):957-67.

48. Anderson NL, Anderson NG. The human plasma proteome - History, character, and diagnostic prospects. Mol Cell Proteomics. 2002;1(11):845-67.

49. Issaq HJ, Xiao Z, Veenstra TD. Serum and plasma proteomics. Chem Rev. 2007;107(8):3601-20.

50. Zhou HC, Baldini L, Hong J, Wilson AJ, Hamilton AD. Pattern recognition of proteins based on an array of functionalized porphyrins. J Am Chem Soc. 2006;128(7):2421-5.

51. Fang Z, Liu LP, Wang Y, Xi DM, Zhang SS. Unambiguous Discrimination of Multiple Protein Biomarkers by Nanopore Sensing with Double-Stranded DNA-Based Probes. Anal Chem. 2020;92(2):1730-7.

52. Zhou W, Hou JZ, Li YX, Zhou HP, Huang H, Zhang L, et al. Protein discrimination based on DNA induced perylene probe self-assembly. Talanta. 2021;224:10.

53. Egbaria K, Friedman M. Adsorption of Fluorescein Dyes on Albumin Microspheres. Pharm Res. 1992;9(5):629-35.

54. Ganesan L, Margolles-Clark E, Song Y, Buchwald P. The food colorant erythrosine is a promiscuous protein-protein interaction inhibitor. Biochem Pharmacol. 2011;81(6):810-8.

55. Ganesan L, Buchwald P. The promiscuous protein binding ability of erythrosine B studied by metachromasy (metachromasia). J Mol Recognit. 2013;26(4):181-9.

56. Vaughan SR, Speller NC, Chhotaray P, McCarter KS, Siraj N, Perez RL, et al. Class specific discrimination of volatile organic compounds using a quartz crystal microbalance based multisensor array. Talanta. 2018;188:423-8.

57. Xi HY, He WW, Liu QY, Chen ZB. Protein Discrimination Using a Colorimetric Sensor Array Based on Gold Nanoparticle Aggregation Induced by Cationic Polymer. ACS Sustain Chem Eng 2018;6(8):10751-7.

58. Ranjan S, Chung WK, Zhu M, Robbins D, Cranner SM. Implementation of an experimental and computational tool set to study protein-mAb interactions. Biotechnol Prog. 2019;35(4):12.

59. Hewitt SH, Wilson AJ. Protein sensing and discrimination using highly functionalised ruthenium(II) tris(bipyridyl) protein surface mimetics in an array format. Chem Commun. 2017;53(91):12278-81.

60. Batistela VR, Pellosi DS, de Souza FD, da Costa WF, Santin SMD, de Souza VR, et al. pK_a determinations of xanthene derivates in aqueous solutions by multivariate analysis applied to UV-Vis spectrophotometric data. Spectroc Acta Pt A-Molec Biomolec Spectr. 2011;79(5):889-97.

61. Wei XC, Wang YX, Zhao YX, Chen ZB. Colorimetric sensor array for protein discrimination based on different DNA chain length-dependent gold nanoparticles aggregation. Biosens Bioelectron. 2017;97:332-7.

62. Yan P, Li XZ, Dong YH, Li BY, Wu YY. A pH-based sensor array for the detection and identification of proteins using CdSe/ZnS quantum dots as an indicator. Analyst. 2019;144(9):2891-7.

63. Levitan H. Food, drug, and cosmetic dyes: Biological effects related to lipid solubility. Proc Natl Acad Sci USA. 1977;74(7):2914-8.

64. Ferreira LA, Fedotoff O, Uversky VN, Zaslavsky BY. Effects of osmolytes on protein-solvent interactions in crowded environments: study of sucrose and trehalose effects on different proteins by solvent interaction analysis. RSC Adv. 2015;5(34):27154-62.

65. Martinez-Sernandez V, Orbegozo-Medina RA, Romaris F, Paniagua E, Ubeira FM. Usefulness of ELISA Methods for Assessing LPS Interactions with Proteins and Peptides. PLoS One. 2016;11(6):17.

66. Vicente FA, Bairos J, Roque M, Coutinho JAP, Ventura SPM, Freire MG. Use of Ionic Liquids as Cosurfactants in Mixed Aqueous Micellar Two-Phase Systems to Improve the Simultaneous Separation of Immunoglobulin G and Human Serum Albumin from Expired Human Plasma. ACS Sustain Chem Eng. 2019;7(17):15102-13.

67. Li DY, Wang YZ, Zhao XL, He XW, Li WY, Zhang YK. Facile synthesis of ionic liquid functionalized silica-capped CdTe quantum dots for selective recognition and detection of hemoproteins. J Mat Chem B. 2014;2(34):5659-65.

Chapter 3

Exploring the potential of erythrosin B-based GUMBOS for qualitative and quantitative analyses of proteins

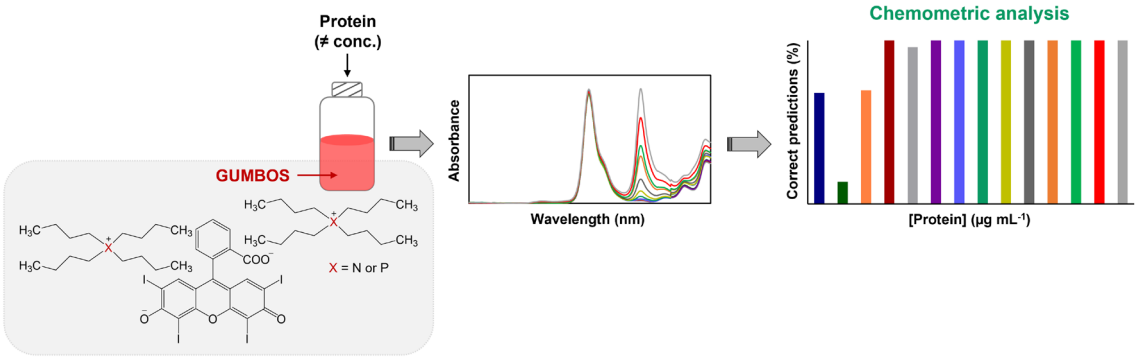

Highlights

- $[N_{4444}]_2[EB]$ showed better discrimination performance than $[P_{4444}]_2[EB]$.
- Higher percentages of correct predictions were obtained for [Protein] ≥ 0.50 μg mL^{-1}.
- GUMBOS were determined to have a wider linear range than that reported for EB dye.
- Alb, Mb, Lyz, and α-ChT were successfully quantified using both GUMBOS.

Manuscript submitted as "Azevedo AMO, Sousa C, Ayala CE, Perez RL, Santos JLM, Warner IM, Saraiva MLMFS. Exploring the potential of erythrosin B-based GUMBOS for qualitative and quantitative analyses of proteins".

Abstract

Detection of protein biomarkers and changes in their concentrations plays an important role in disease diagnosis and treatment strategy. The present study investigated erythrosin B (EB)-based GUMBOS (*g*roup of *u*niform *m*aterials *b*ased on *o*rganic *s*alts) as optical probes for the potential discrimination and quantification of proteins. Albumin (Alb), ribonuclease A (RNAse A), myoglobin (Mb), lysozyme (Lyz), and α-chymotrypsin (α-ChT) were selected as target analytes primarily due to their distinct levels in biofluids and surface hydrophobicity. Ultraviolet-visible spectra of tetrabutylammonium- and tetrabutylphosphonium-erythrosin B GUMBOS (i.e., $[N_{4444}]_2$[EB] and $[P_{4444}]_2$[EB]) in the presence of each protein at different concentrations (0.05–20 μg mL^{-1}) were analyzed using partial least squares discriminant analysis. The highest percentages of correct assignments were achieved using $[N_{4444}]_2$[EB] for protein concentrations greater than 0.50 μg mL^{-1} and Mb was the best identified using both GUMBOS. Notably, $[N_{4444}]_2$[EB] and $[P_{4444}]_2$[EB] were determined to discriminate proteins at concentrations lower than those reported for other sensing systems. Partial least squares models were further developed for quantification purposes. It was found that EB-based GUMBOS allow estimation of concentrations of Mb, Alb, Lyz, and α-ChT from 0.50 to 20 μg mL^{-1}. Mb, Alb, and Lyz concentrations were best predicted using $[N_{4444}]_2$[EB] (errors ≤ 5.2%), while $[P_{4444}]_2$[EB] was best for estimating concentrations of α-ChT and RNAse A (errors ≤ 5.2% and 13.4%, respectively). The results described above clearly indicate the potential of EB-based GUMBOS to discriminate as well as quantify several protein analytes in a rapid and non-laborious manner.

Keywords: Erythrosin B; GUMBOS; Chemometrics; Protein analysis.

3.1. Introduction

Various analytical methods have been reported for detection and quantification of protein biomarkers. Immunoassays are among the most commonly used in research and clinical practice due to their high selectivity and sensitivity, which arise from strong antibody-protein interactions (1, 2). However, this approach relies on availability of high-affinity antibodies and is difficult to multiplex (3, 4). In contrast, sensor arrays, including fluorometric ones, usually comprise a set of non-specific and cross-reactive elements that produce distinct response patterns for each analyte (5, 6). Although fluorometric sensor arrays provide high discriminatory power and sensitivity, fluorescent sensing materials often require tedious multistep synthetic procedures and can suffer from photobleaching. In turn, colorimetric detection offers a simple, rapid, and low-cost alternative for protein analysis (7, 8). The interaction between dyes and proteins can result in noticeable color changes and/or variations in ultraviolet-visible (UV-Vis) spectra, which usually require minimal preprocessing (9, 10). Moreover, application of chemometric tools such as linear discriminant analysis (LDA), partial least squares discriminant analysis (PLSDA), and partial least squares (PLS) allows extraction of relevant information from overlapped data, improving selectivity, and minimizing interference effects (9, 11). Despite these significant advantages, multi-element sensor arrays often exhibit high detection limits, and their construction process can be complex, time-consuming, and costly (6, 12, 13).

More recently, several research groups have explored the potential of GUMBOS (*g*roup of *u*niform *m*aterials *b*ased on *o*rganic *s*alts)-based sensing approach to detect and discriminate proteins (14-16). In contrast to other sensing materials, GUMBOS can be synthesized using a simple metathesis reaction and do not require extensive purification (14, 17). Additionally, their physicochemical properties are easily tuned by varying the cation, alkyl side chain length, and anion (18, 19). Despite the great promise of GUMBOS for protein analysis, these materials remain largely unexplored (14-16).

In previous work, tetrabutylammonium- and tetrabutylphosphonium-erythrosin B GUMBOS (i.e., $[N_{4444}]_2[EB]$ and $[P_{4444}]_2[EB]$) were determined to successfully discriminate proteins at a standardized concentration of 20 μg mL^{-1} and pH 6.0, achieving a percentage of correct assignments of 100% (16). In this study, the ability of $[N_{4444}]_2[EB]$ and $[P_{4444}]_2[EB]$ to distinguish serum and non-serum proteins at concentrations as low as 0.05 μg mL^{-1} were investigated. A range of detection limits is necessary to evaluate the detection and discrimination potential of these EB-based GUMBOS as fluctuations in protein levels can aid in early disease diagnosis and allow prompt treatment, which can improve patient outcomes and reduce healthcare costs (20, 21). Due to their distinct levels in biological fluids and physicochemical properties (e.g., surface hydrophobicity and size), albumin (Alb),

ribonuclease A (RNAse A), myoglobin (Mb), lysozyme (Lyz), and α-chymotrypsin (α-ChT) were selected as target analytes to assess GUMBOS discrimination performance. UV-Vis spectra of $[N_{4444}]_2[EB]$ and $[P_{4444}]_2[EB]$ in the presence of each protein and protein concentration were analyzed using PLSDA. Subsequently, PLS models were developed for quantification purposes, which indicated that the EB-based GUMBOS studied herein have the potential to expand the detection range of various protein analytes.

3.2. Material and methods

3.2.1. Reagents and solvents

Tetrabutylammonium bromide ($[N_{4444}][Br]$, 98%); tetrabutylphosphonium bromide ($[P_{4444}][Br]$, 98%); 2',4',5',7'-tetraiodofluorescein disodium salt ($[Na]_2[EB]$, 90%); Alb from human serum; RNAse A from bovine pancreas; Mb from equine heart; Lyz from chicken egg white; α-ChT from bovine pancreas; sodium phosphate dibasic (Na_2HPO_4); and sodium phosphate monobasic (NaH_2PO_4) were all purchased from Sigma-Aldrich (St. Louis, MO) and used as supplied. Citric acid and sodium hydroxide (NaOH) were acquired from Honeywell (Charlotte, NC). Dimethylsulfoxide (DMSO) was obtained from Merck KGaA (Darmstadt, Germany).

A 0.1 mol L^{-1} citrate buffer solution was prepared by dissolving citric acid in ultrapure water (Milli-Q®, 18.2 MΩ cm) and adjusting pH to 6.0 with NaOH. Phosphate buffer (0.01 mol L^{-1}, pH 7.4) was obtained by mixing aqueous solutions of Na_2HPO_4 and NaH_2PO_4 and further used for the preparation of protein stock solutions (1 mg mL^{-1}). Both GUMBOS were dissolved in DMSO and protected from light.

3.2.2. Synthesis and characterization of GUMBOS

EB-based GUMBOS were synthesized using a single-step metathesis reaction as previously described (16). The sodium cations of EB dye were replaced by two relatively large and symmetrical cations (N_{4444}^+ and P_{4444}^+). Both cation and anion (the latter in slight excess) were dissolved in phosphate buffer pH 7.4 and stirred for 24 h at room temperature (Fig. 3.1). The resulting precipitate was washed several times with water to remove sodium bromide by-product, and subsequently freeze-dried. Structural characterization was performed using nuclear magnetic resonance, Fourier transform infrared, and mass spectrometry.

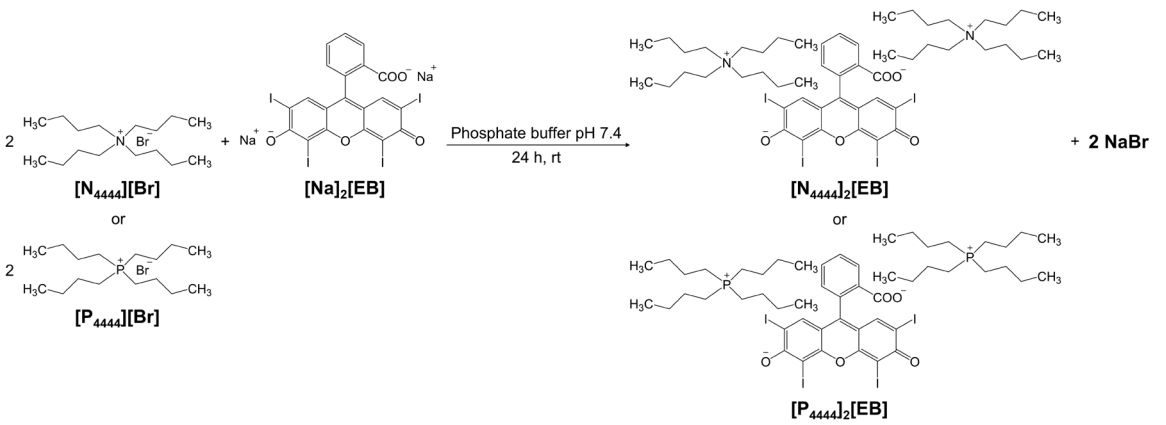

Fig. 3.1. Synthetic diagram of $[N_{4444}]_2[EB]$ and $[P_{4444}]_2[EB]$ GUMBOS.

3.2.3. Spectra acquisition

UV-Vis spectra of EB-based GUMBOS, in the absence and presence of protein analytes, were acquired using a Jasco V-660 spectrophotometer and a 1 cm quartz cuvette. Briefly, increasing volumes of each protein solution were added to a vial containing phosphate buffer pH 6.0 and $[N_{4444}]_2[EB]$ or $[P_{4444}]_2[EB]$ GUMBOS (final volume = 5 mL). After a 5 min reaction period, absorption spectra were collected in the range of 800–250 nm. The concentration of GUMBOS solution was maintained at 1 μmol L^{-1}, while protein concentrations varied from 0.05 to 20 μg mL^{-1} (0.05, 0.10, 0.15, 0.20, 0.30, 0.40, 0.50, 1, 2, 4, 8, 10, 15, and 20 μg mL^{-1}). For each protein, seven replicates were obtained from independent experiments on two different days.

3.2.4. Multivariate data analysis

Spectral data were modeled using PLSDA (22) to evaluate discrimination ability of synthesized GUMBOS and PLS (23) to predict protein concentrations. Before chemometric analysis, collected UV-Vis spectral data were preprocessed using standard normal variate (SNV) (24), and then mean-centered. During development of PLSDA and PLS models, the number of latent variables (LVs) was optimized based on the root mean square error of cross-validation (RMSECV). RMSECV values were also used to select an optimal spectral region for PLS analysis. PLSDA models were developed using the entire range of spectral wavelength (800–250 nm). For a detailed description of how chemometric models were built, please see our previous manuscript (16).

Spectra preprocessing and modeling were performed in MATLAB R2018b, version 9.5 (MathWorks, Natick, MA) and PLS Toolbox 8.7 (Eigenvector Research, Manson, WA).

3.3. Results and discussion

3.3.1. Discrimination of proteins at different concentrations

In order to evaluate the ability of $[N_{4444}]_2$[EB] and $[P_{4444}]_2$[EB] to discriminate protein samples at different concentrations, 1400 (2 GUMBOS x 5 proteins x 14 concentrations x 10 LVs) independent PLSDA models were developed. The optimum number of LVs was set to six since, for the majority of PLSDA models, it led to the lowest RMSECV values. The percentages of correct protein assignments obtained with $[N_{4444}]_2$[EB] and $[P_{4444}]_2$[EB] GUMBOS for each protein concentration are presented in Figs. 3.2 and 3.3, respectively. Regarding the total percentages of correct assignments, they seemed to have a decreasing trend for lower concentrations of proteins using both GUMBOS (Figs. 3.2A and 3.3A). Nevertheless, $[N_{4444}]_2$[EB] showed overall better performance, reaching total percentages of correct assignments higher than 80 and 95% for concentrations equal to or greater than 0.20 and 1 μg mL^{-1}, respectively. The $[P_{4444}]_2$[EB] GUMBOS only achieved a total percentage of correct assignments ≥ 90% for protein concentrations equal to or greater than 4 μg mL^{-1}. These results demonstrate the impact of the cation's central atom on discrimination performance of synthesized GUMBOS and can be attributed to differences in electron density. Nitrogen is less positively charged than phosphorus and its charge is more delocalized, which can promote formation of hydrogen bonds between $[N_{4444}]_2$[EB] and proteins (N^+-C-H···O), and contribute to increased binding affinity (25, 26). Other studies have shown that GUMBOS sensing properties are influenced by cation's heteroatoms and alkyl side chain length (16, 27).

With respect to each protein individually, higher percentages of correct predictions were also obtained for the highest protein concentrations tested, but some fluctuations were observed. Alb was predicted quite well using $[N_{4444}]_2$[EB] GUMBOS (Fig. 3.2B) for protein concentrations equal to or greater than 1 μg mL^{-1} (96.5% for [Protein] = 1 μg mL^{-1} and 100.0% for concentrations ranging from 2 to 20 μg mL^{-1}). However, below this concentration, large fluctuations were randomly detected (correct predictions varied from 55.5% to 100.0%). When using $[P_{4444}]_2$[EB] (Fig. 3.3B), such fluctuations were observed for even higher concentrations of Alb (up to 2 μg mL^{-1}). Satisfactory percentages of correct identifications were obtained only for protein concentrations equal to or greater than 4 μg mL^{-1} (94.7–100.0%).

RNAse A followed a quite similar tendency to that observed for Alb (Figs. 3.2C and 3.3C for $[N_{4444}]_2$[EB] and $[P_{4444}]_2$[EB], respectively). The percentages of correct assignments varied from 90.0 to 100.0% for 20 ≥ [Protein] ≥ 2 μg mL^{-1} using $[N_{4444}]_2$[EB], while for $[P_{4444}]_2$[EB] GUMBOS they were in the range of 97.3–100.0% for 20 ≥ [Protein] ≥ 8 μg mL^{-1}. Random

fluctuations were observed in the percentages of correct assignments for concentrations of RNAse A below 2 and 8 μg mL^{-1} with $[N_{4444}]_2$[EB] and $[P_{4444}]_2$[EB] GUMBOS, respectively.

Mb appeared to be the best predicted among all proteins using both GUMBOS (Figs. 3.2D and 3.3D for $[N_{4444}]_2$[EB] and $[P_{4444}]_2$[EB], respectively), which is in line with previously observed results at a concentration of 20 μg mL^{-1} (16). In fact, the percentages of correct assignments obtained with the $[N_{4444}]_2$[EB] GUMBOS were from 96.0 to 100.0% for concentrations between 0.20 and 20 μg mL^{-1}. Similarly, with $[P_{4444}]_2$[EB], the percentages of correct protein assignments varied from 91.3 to 100.0% for a concentration range of 0.30–20 μg mL^{-1}. The only exception was an unexpected and inexplicable result (13.5%) obtained with $[N_{4444}]_2$[EB] GUMBOS at a protein concentration of 0.10 μg mL^{-1}.

Regarding Lyz (Figs. 3.2E and 3.3E for $[N_{4444}]_2$[EB] and $[P_{4444}]_2$[EB], respectively), it was found that from 0.50 to 20 μg mL^{-1} both GUMBOS present a good prediction ability (> 90%), with a single poor result (80.7%) obtained at 1 μg mL^{-1} using $[P_{4444}]_2$[EB]. Below this concentration, random fluctuations in the percentages of correct assignments (similar to those observed for other proteins) were observed.

With respect to α-ChT (Figs. 3.2F and 3.3F for $[N_{4444}]_2$[EB] and $[P_{4444}]_2$[EB], respectively), the percentages of correct protein assignments obtained using $[N_{4444}]_2$[EB] showed a very inconsistent pattern, splitting from 14.0 (0.10 μg mL^{-1}) to 100.0% (2 μg mL^{-1}). However, these percentages varied only from 82.0 to 93.0% for concentrations in the range of 4–20 μg mL^{-1}. A more defined trend was observed for $[P_{4444}]_2$[EB] GUMBOS, which allowed percentages of correct assignments between 85.3 and 100.0% for concentrations of α-ChT equal to or greater than 0.50 μg mL^{-1}. Below this concentration, large fluctuations in the results were noticed. The best discrimination performance of $[P_{4444}]_2$[EB] can be attributed to its higher hydrophobicity (16), which may lead to increased protein binding affinity. In fact, hydrophobic interactions are known to play an important role in formation of EB-protein complexes and α-ChT has a large accessible surface area (28-30). Previous studies also showed that α-ChT can be inhibited by compounds containing phosphorus, suggesting the involvement of this atom in the binding process (31, 32). Additionally, α-ChT was found to be one of the worst predicted in our last work (16).

Finally, it is worth noting that this GUMBOS strategy reached satisfactory percentages of correct protein assignments for concentrations lower than those described for several other sensing systems (≥ 5 μg mL^{-1}) and did not require the use of an assembly of multiple EB-based probes (33-35).

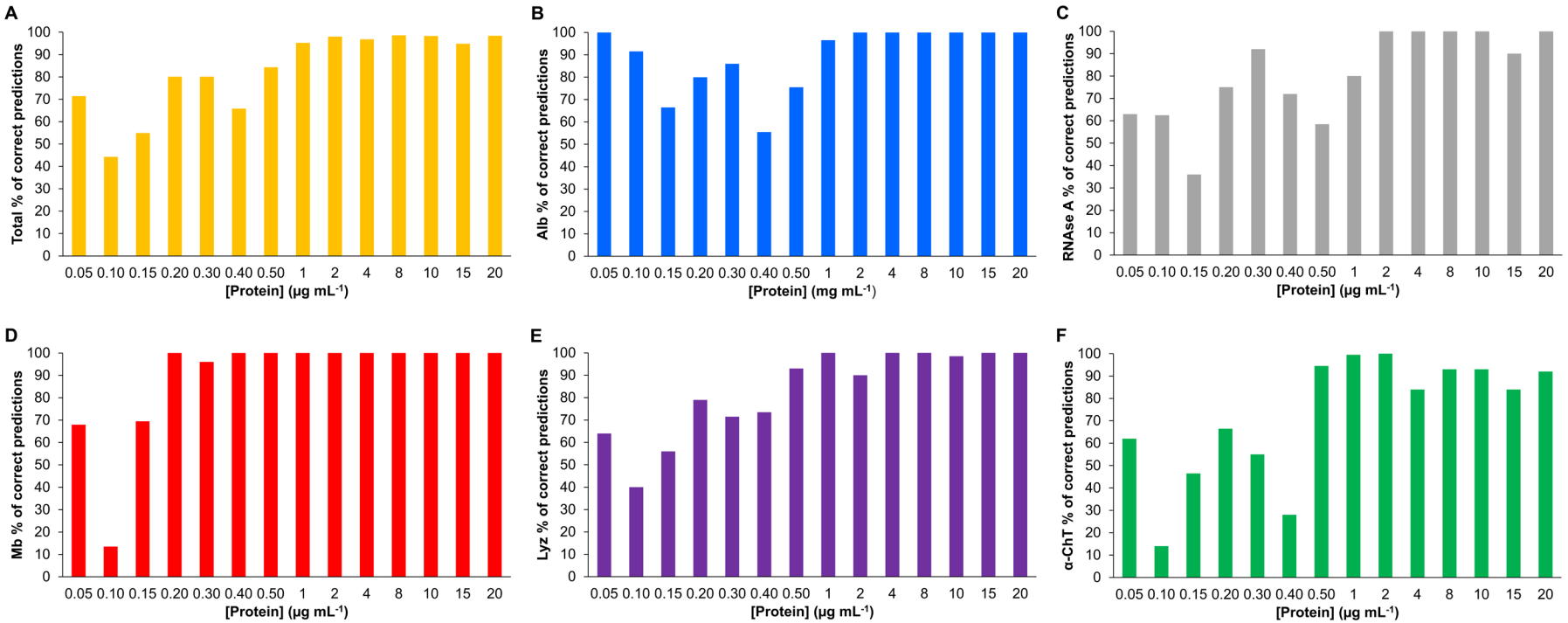

Fig. 3.2. Total percentages (%) of correct protein assignments (A) and percentage (%) of correct assignments of Alb (B), RNAse A (C), Mb (D), Lyz (E), and α-ChT (F) at different concentrations, obtained from the confusion matrices of PLSDA regression models (6 LVs) developed using the $[N_{4444}]_2$[EB] GUMBOS.

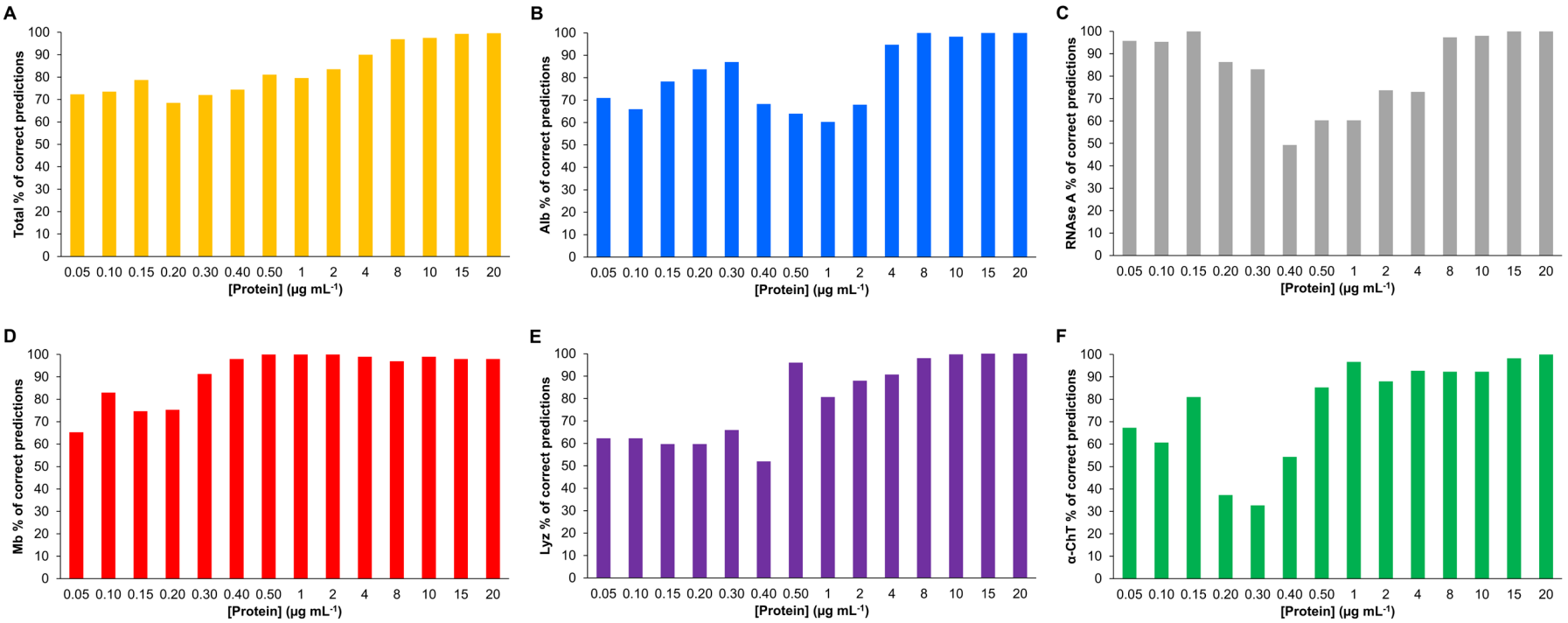

Fig. 3.3. Total percentages (%) of correct assignments (A) and percentage (%) of correct assignments of Alb (B), RNAse A (C), Mb (D), Lyz (E), and α-ChT (F) at different concentrations obtained from the confusion matrices of PLSDA regression models, which were developed using 6 LVs and $[P_{4444}]_2[EB]$ GUMBOS.

3.3.2. Quantitative analysis of proteins

The capability of synthesized GUMBOS to predict protein concentration was further assessed using PLS. Models were developed using UV-Vis spectra of $[N_{4444}]_2[EB]$ and $[P_{4444}]_2[EB]$ GUMBOS in the presence of various concentrations (0.05–20 μg mL^{-1}) of each protein. Deviation from linearity was observed below 0.50 μg mL^{-1} (data not shown). Thus, the models presented herein were further developed using a protein concentration range of 0.50–20 μg mL^{-1}. It is worth noting that this GUMBOS approach has a wider linear range than that described for other spectrophotometric methods using EB. For example, Soedjak reported a linear relationship between absorbance at 545 nm and protein concentration ranging from 2 to 14 μg mL^{-1} (36), while the method proposed by Isoe and Kaneko showed a linear range up to 1.5 μg mL^{-1} (37). Additionally, the present method requires only a 5 min incubation period at room temperature and eliminates the need for additives such as Triton X-100 (16, 36, 37).

In this study, PLS models were optimized by selecting the appropriate number of LVs (1–10) and spectral region (R1, R2, R3, and R4; Fig. 3.4) from the RMSECV plots. Variation in RMSECV with the number of LVs and spectral region is shown in Figs. S3.1 and S3.2 (A–E) for $[N_{4444}]_2[EB]$ and $[P_{4444}]_2[EB]$ GUMBOS, respectively. Four LVs were selected as an optimum number since a plateau was observed in RMSECV values from 5 to 10 LVs. Additionally, region R4 (Fig. 3.4) was chosen for analysis as it led to lower cross-validation errors (RMSECV).

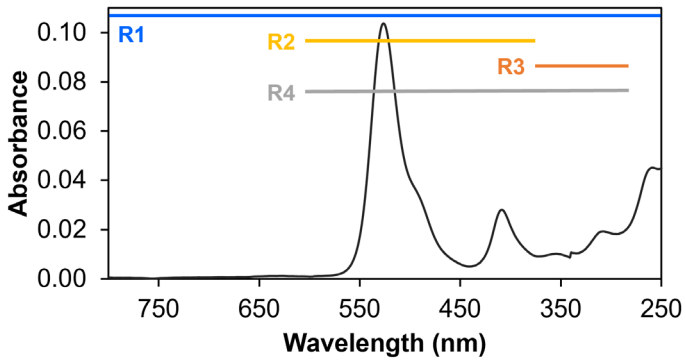

Fig. 3.4. UV-Vis spectrum of $[P_{4444}]_2[EB]$ GUMBOS + Mb (4 μg mL^{-1}) illustrating the four spectral regions (R1, R2, R3, and R4) considered during optimization of PLS models.

The figures of merit obtained from optimum PLS models are presented in Table 3.1. Overall, determination coefficients calculated for the highest protein concentration range (0.50–20 μg·mL^{-1}) were very satisfactory, most being greater than 0.97. The exceptions were RNAse A for both GUMBOS and Mb for $[P_{4444}]_2[EB]$, with the coefficient of determination of cross-

validation of the latter having the lowest score (R^2CV = 0.84). Additionally, the $[N_{4444}]_2$[EB] GUMBOS generally showed higher coefficients than $[P_{4444}]_2$[EB] for all proteins. These findings were in good agreement with obtained errors for concentration estimates.

When compared to other proteins, RNAse A and Mb presented higher errors in percentage (Table 3.2) for the three sample sets (C, calibration; CV, cross-validation; and P, prediction). Errors associated with the estimates were also determined to be lower for $[N_{4444}]_2$[EB] than for $[P_{4444}]_2$[EB]. The best performance regarding protein concentration prediction was achieved with $[N_{4444}]_2$[EB] GUMBOS for Alb, Mb, and Lyz, and with $[P_{4444}]_2$[EB] for α-ChT. RNAse A was the only protein poorly predicted using $[N_{4444}]_2$[EB] (errors from 14.0 to 17.9% for calibration and prediction sets, respectively). This result can be explained by the lower surface hydrophobicity and smaller size of RNAse A (16, 30, 38). In fact, significantly higher concentrations are often required to detect small-sized proteins as compared to larger ones due to the lower signal-to-noise ratio (39, 40). The results of quantitative analysis corroborate previous findings regarding protein discrimination, with the best performance achieved using $[N_{4444}]_2$[EB] and the highest percentages of correct assignments observed for protein concentrations above 0.50 μg mL^{-1}.

Table 3.1. Figures of merit corresponding to the optimum PLS models (4 LVs and spectral range from 600 to 290 nm) developed to estimate protein concentrations (0.50–20 μg·mL^{-1}) using EB-based GUMBOS.

GUMBOS	Protein	RMSEC	R^2C	RMSECV	R^2CV	RMSEP	R^2P
$[N_{4444}]_2$[EB]	Alb	0.20	0.999	0.27	0.997	0.39	0.998
	RNAse A	1.06	0.970	1.34	0.953	1.35	0.959
	Mb	0.24	0.996	0.44	0.992	0.35	0.990
	Lyz	0.21	0.999	0.33	0.996	0.37	0.996
	α-ChT	0.47	0.993	0.70	0.971	0.73	0.991
$[P_{4444}]_2$[EB]	Alb	0.49	0.990	0.64	0.986	0.69	0.988
	RNAse A	0.61	0.977	0.82	0.960	1.01	0.977
	Mb	1.26	0.957	1.68	0.841	1.81	0.913
	Lyz	0.30	0.998	0.39	0.997	0.50	0.997
	α-ChT	0.20	0.998	0.31	0.997	0.39	0.996

Root mean square error of calibration (RMSEC), cross-validation (RMSECV), and prediction (RMSEP); Coefficient of determination of calibration (R^2C), cross-validation (R^2CV), and prediction (R^2P).

Table 3.2. Errors (%) obtained for the calibration (C), cross-validation (CV), and prediction (P) sets used to develop the PLS models for protein quantification.

GUMBOS	Protein	C error (%)	CV error (%)	P error (%)
$[N_{4444}]_2[EB]$	Alb	2.6	3.6	5.2
	RNAse A	14.0	17.7	17.9
	Mb	3.2	5.8	4.6
	Lyz	2.8	4.4	4.9
	α-ChT	6.2	9.3	9.7
$[P_{4444}]_2[EB]$	Alb	6.5	8.5	9.1
	RNAse A	8.1	10.8	13.4
	Mb	16.7	22.2	23.9
	Lyz	4.0	5.2	6.6
	α-ChT	2.6	4.1	5.2

3.4. Conclusions

In this study, the ability of $[N_{4444}]_2[EB]$ and $[P_{4444}]_2[EB]$ GUMBOS to discriminate and quantify several proteins was evaluated. The highest percentages of correct protein assignments were observed for concentrations greater than 0.50 μg mL^{-1}, with Mb being the best identified among all proteins. It was also found that both GUMBOS can successfully estimate the concentration of four out of five proteins (e.g., Alb, Mb, Lyz, and α-ChT) in the range of 0.50–20 μg mL^{-1}. The $[N_{4444}]_2[EB]$ GUMBOS was best for predicting Alb, Mb, and Lyz concentrations (errors ≤ 5.2%), while the concentration of α-ChT was better estimated using $[P_{4444}]_2[EB]$ (errors ≤ 5.2%). RNAse A was the worst predicted and, similar to what was observed for α-ChT, the best estimate was obtained with $[P_{4444}]_2[EB]$ (errors between 8.1 and 17.9%). Overall, the obtained results demonstrated the great potential of using EB-based GUMBOS as probes for rapid and sensitive analyses of various proteins.

SUPPLEMENTARY MATERIAL

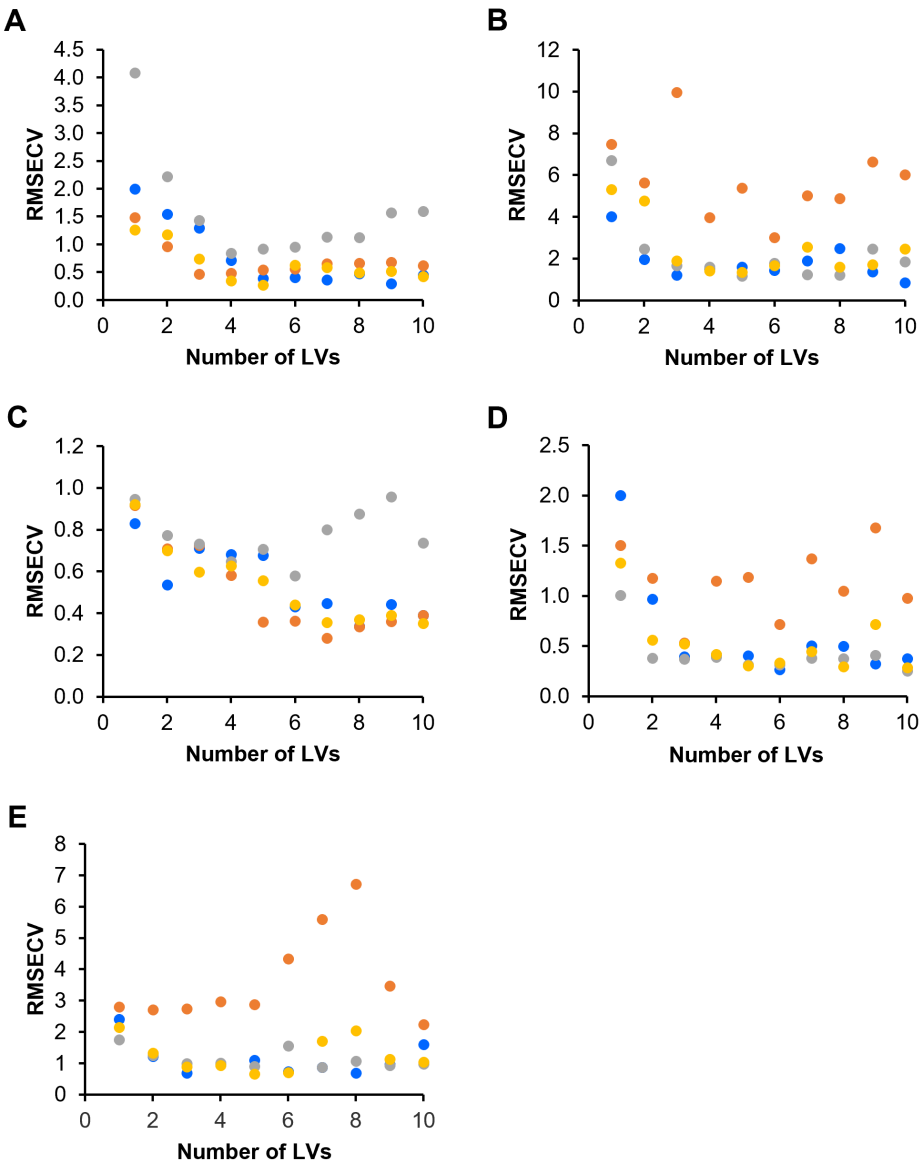

Fig. S3.1. Root mean square error of cross-validation (RMSECV) obtained from the PLS models developed to predict protein concentration using UV-Vis spectra of $[N_{4444}]_2[EB]$ GUMBOS in the presence of Alb (A); RNAse A (B); Mb (C); Lyz (D); and α-ChT (E). Legend: ● R1; ● R2; ● R3; ● R4.

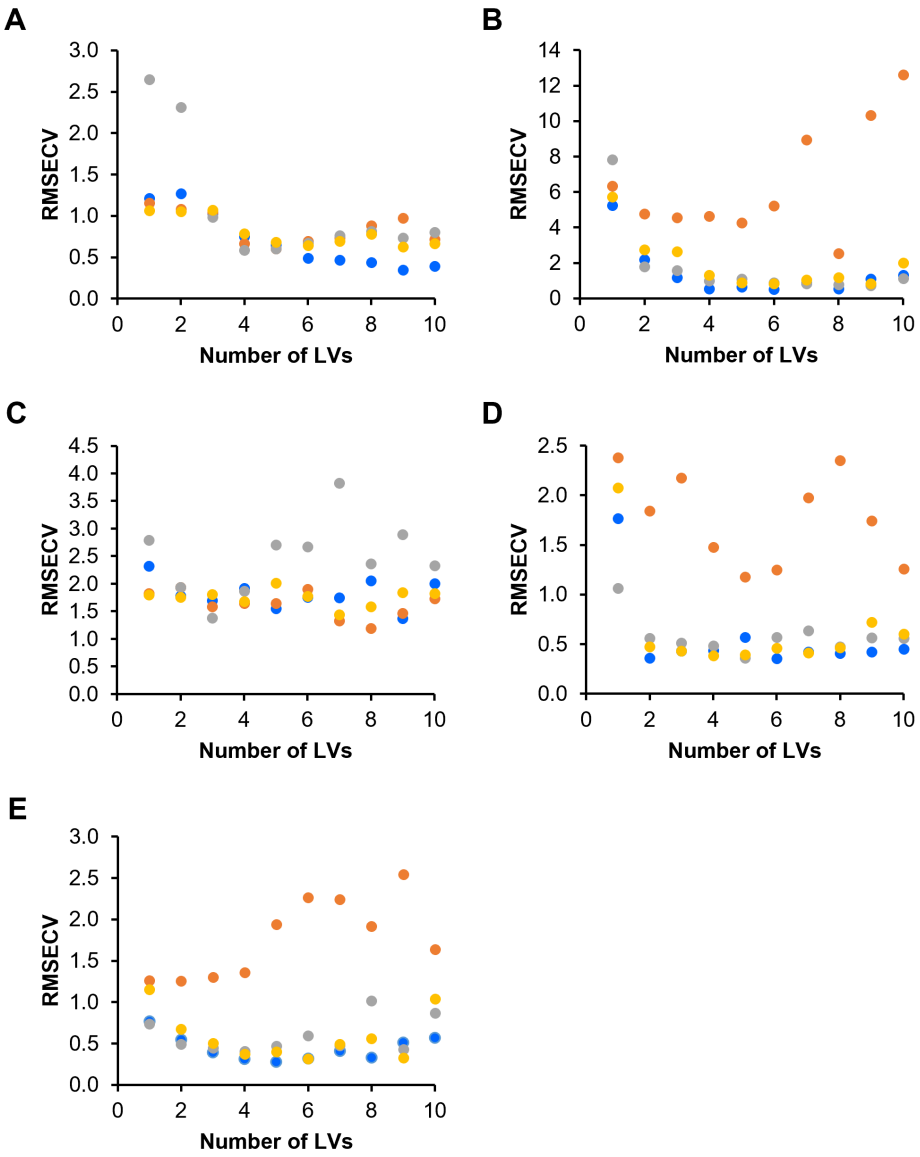

Fig. S3.2. Root mean square error of cross-validation (RMSECV) obtained from the PLS models developed to estimate the concentration of proteins using UV-Vis spectra of $[P_{4444}]_2[EB]$ GUMBOS in the presence of Alb (A); RNAse A (B); Mb (C); Lyz (D); and α-ChT (E). Legend: ● R1; ● R2; ● R3; ● R4.

References

1. Van Gool A, Corrales F, Colovic M, Krstic D, Oliver-Martos B, Martinez-Caceres E, et al. Analytical techniques for multiplex analysis of protein biomarkers. Expert Rev Proteomics. 2020;17(4):257-73.
2. Aitekenov S, Gaipov A, Bukasov R. Review: Detection and quantification of proteins in human urine. Talanta. 2021;223:20.
3. Albert KJ, Lewis NS, Schauer CL, Sotzing GA, Stitzel SE, Vaid TP, et al. Cross-reactive chemical sensor arrays. Chem Rev. 2000;100(7):2595-626.
4. Goetze S, Schuffler P, Athanasiou A, Koetemann A, Poyet C, Fankhauser CD, et al. Use of MS-GUIDE for identification of protein biomarkers for risk stratification of patients with prostate cancer. Clin Proteom. 2022;19(1):13.
5. Hou CJ, Dong JL, Zhang GP, Lei Y, Yang M, Zhang YC, et al. Colorimetric artificial tongue for protein identification. Biosens Bioelectron. 2011;26(10):3981-6.
6. Fan JM, Qi L, Han HF, Ding LP. Array-Based Discriminative Optical Biosensors for Identifying Multiple Proteins in Aqueous Solution and Biofluids. Front Chem. 2020;8:18.
7. Qiang H, Wei XC, Liu QY, Chen ZB. Iodide-Responsive Cu-Au Nanoparticle-Based Colorimetric Sensor Array for Protein Discrimination. ACS Sustain Chem Eng. 2018;6(11):15720-6.
8. Li Z, Askim JR, Suslick KS. The Optoelectronic Nose: Colorimetric and Fluorometric Sensor Arrays. Chem Rev. 2019;119(1):231-92.
9. Rios-Reina R, Azcarate SM. How Chemometrics Revives the UV-Vis Spectroscopy Applications as an Analytical Sensor for Spectralprint (Nontargeted) Analysis. Chemosensors. 2023;11(1):22.
10. Li T, Zhu X, Hai X, Bi S, Zhang X. Recent Progress in Sensor Arrays: From Construction Principles of Sensing Elements to Applications. ACS Sens. 2023.
11. Martynko E, Kirsanov D. Application of Chemometrics in Biosensing: A Brief Review. Biosensors-Basel. 2020;10(8):20.
12. De M, Rana S, Akpinar H, Miranda OR, Arvizo RR, Bunz UHF, et al. Sensing of proteins in human serum using conjugates of nanoparticles and green fluorescent protein. Nat Chem. 2009;1(6):461-5.
13. Zhou W, Hou JZ, Li YX, Zhou HP, Huang H, Zhang L, et al. Protein discrimination based on DNA induced perylene probe self-assembly. Talanta. 2021;224:10.
14. Galpothdeniya WIS, Fronczek FR, Cong MY, Bhattarai N, Siraj N, Warner IM. Tunable GUMBOS-based sensor array for label-free detection and discrimination of proteins. J Mat Chem B. 2016;4(8):1414-22.

15. Perez RL, Cong MY, Vaughan SR, Ayala CE, Galpothdeniya WIS, Mathaga JK, et al. Protein Discrimination Using a Fluorescence-Based Sensor Array of Thiacarbocyanine-GUMBOS. ACS Sens. 2020;5(8):2422-9.
16. Azevedo AMO, Sousa C, Chen M, Ayala CE, Perez RL, Santos JLM, et al. Protein discrimination using erythrosin B-based GUMBOS in combination with UV–Vis spectroscopy and chemometrics. Talanta. 2022;240:123164.
17. Perez RL, Ayala CE, Warner IM. Group of Uniform Materials Based on Organic Salts (GUMBOS): A Review of Their Solid State Properties and Applications. In: Sohel Murshed SM, editor. Ionic Liquids - Thermophysical Properties and Applications: IntechOpen; 2021.
18. Warner IM, El-Zahab B, Siraj N. Perspectives on Moving Ionic Liquid Chemistry into the Solid Phase. Anal Chem. 2014;86(15):7184-91.
19. Azevedo AMO, Santos JLM, Warner IM, Saraiva MLMFS. GUMBOS and nanoGUMBOS in chemical and biological analysis: A review. Anal Chim Acta. 2020;1133:180-98.
20. Schneider JE, Dick K, Cooper JT, Chami N. Pancreatic stone protein point-of-care testing can reduce healthcare expenditure in sepsis. Health Econ Rev. 2022;12(1):11.
21. Huang ML, Ding ZY, Li WS, Chen WB, Du YD, Jia HY, et al. Identification of protein biomarkers in host cerebrospinal fluid for differential diagnosis of tuberculous meningitis and other meningitis. Front Neurol. 2022;13:12.
22. Alsberg BK, Kell DB, Goodacre R. Variable selection in discriminant partial least-squares analysis. Anal Chem. 1998;70(19):4126-33.
23. Geladi P, Kowalski BR. Partial least-squares regression: A tutorial. Anal Chim Acta. 1986;185:1-17.
24. Naes T, Isaksson T, Fearn T, Davies T. A user-friendly guide to multivariate calibration and classification. Chichester, UK: NIR Publications; 2002.
25. Carvalho PJ, Ventura SPM, Batista MLS, Schroder B, Goncalves F, Esperanca J, et al. Understanding the impact of the central atom on the ionic liquid behavior: Phosphonium vs ammonium cations. J Chem Phys. 2014;140(6):12.
26. Itoh Y, Nakashima Y, Tsukamoto S, Kurohara T, Suzuki M, Sakae Y, et al. N+-C-H center dot center dot center dot O Hydrogen bonds in protein-ligand complexes. Sci Rep. 2019;9:12.
27. Vaughan SR, Speller NC, Chhotaray P, McCarter KS, Siraj N, Perez RL, et al. Class specific discrimination of volatile organic compounds using a quartz crystal microbalance based multisensor array. Talanta. 2018;188:423-8.
28. Egbaria K, Friedman M. Adsorption of fluorescein dyes on albumin microspheres. Pharm Res. 1992;9(5):629-35.

29. Ganesan L, Margolles-Clark E, Song Y, Buchwald P. The food colorant erythrosine is a promiscuous protein-protein interaction inhibitor. Biochem Pharmacol. 2011;81(6):810-8.
30. Bakk A, Hoye JS, Hansen A. Apolar and polar solvation thermodynamics related to the protein unfolding process. Biophys J. 2002;82(2):713-9.
31. Jansen EF, Nutting MDF, Balls AK. Mode of inhibition of chymotrypsin by diisopropyl fluorophosphate. 1. Introduction of phosphorus. J Biol Chem. 1949;179(1):201-4.
32. Kilby BA, Youatt G. The inhibition of trypsin and chymotrypsin by certain organic phosphorus esters. Biochem J. 1954;57(2):303-9.
33. Kong H, Liu D, Zhang SC, Zhang XR. Protein Sensing and Cell Discrimination Using a Sensor Array Based on Nanomaterial-Assisted Chemiluminescence. Anal Chem. 2011;83(6):1867-70.
34. Xu SH, Lu X, Yao CX, Huang F, Jiang H, Hua WH, et al. A Visual Sensor Array for Pattern Recognition Analysis of Proteins Using Novel Blue-Emitting Fluorescent Gold Nanoclusters. Anal Chem. 2014;86(23):11634-9.
35. Shen YS, Huang YF, Zhang PMM, Guo BC, Jiang HT, Tan CY, et al. Fluorescence Sensor Array for Discrimination of Urine Proteins and Differentiation Diagnosis of Urinary System Diseases. ACS Appl Bio Mater. 2020;3(9):5639-43.
36. Soedjak HS. Colorimetric micromethod for protein determination with erythrosin-B. Anal Biochem. 1994;220(1):142-8.
37. Isoe J, Kaneko E. A new spectrophotometric method for determination of urinary protein using Erythrosin B. Chem Lett. 2006;35(8):922-3.
38. Ferreira LA, Fedotoff O, Uversky VN, Zaslavsky BY. Effects of osmolytes on protein-solvent interactions in crowded environments: study of sucrose and trehalose effects on different proteins by solvent interaction analysis. RSC Adv. 2015;5(34):27154-62.
39. Lin XY, Ivanov AP, Edel JB. Selective single molecule nanopore sensing of proteins using DNA aptamer-functionalised gold nanoparticles. Chem Sci. 2017;8(5):3905-12.
40. Cardoch S, Timneanu N, Caleman C, Scheicher RH. Distinguishing between Similar Miniproteins with Single-Molecule Nanopore Sensing: A Computational Study. ACS Nanosci Au. 2022;2(2):119–27.

Chapter 4

Combined use of phosphonium-erythrosin B-based nanoGUMBOS, UV-Vis spectroscopy, and chemometrics for discrimination and quantification of proteins

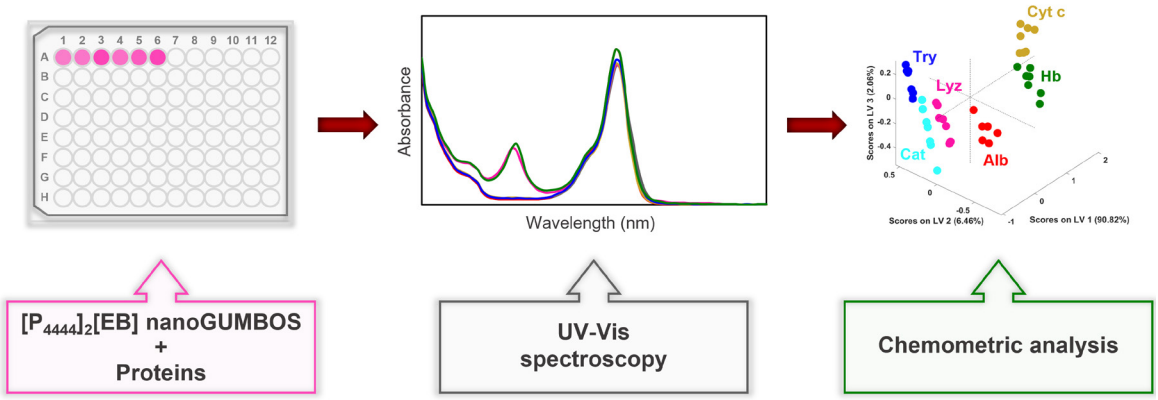

Highlights

- A novel phosphonium-erythrosin B-based nanoGUMBOS ($[P_{4444}]_2[EB]$) was synthesized.
- The best discrimination result (99.6%) was obtained for 5 min sonication without CD.
- The nanoGUMBOS was able to distinguish proteins at concentrations ≥ 2 μg mL^{-1}.
- Binary and ternary mixtures of Lyz, Cyt c, and Hb were successfully discriminated.
- The PLS model developed for Alb proved to be suitable for quantification purposes.

Manuscript published after international peer review as "Azevedo AMO, Sousa C, Rodrigues SSM, Chen M, Ayala CE, Perez RL, Santos JLM, Warner IM, Saraiva MLMFS. Combined use of phosphonium-erythrosin B-based nanoGUMBOS, UV-Vis spectroscopy, and chemometrics for discrimination and quantification of proteins. Dyes Pigment. 2022;207:8".

Abstract

Nanoparticles derived from a *g*roup of *u*niform *m*aterials *b*ased on *o*rganic *s*alts (nanoGUMBOS) are considered promising candidates for protein analysis due to their facile synthesis in aqueous media and high tunability. In this study, a phosphonium-erythrosin B-based nanoGUMBOS (i.e., $[P_{4444}]_2$[EB]) was prepared using an ultrasound-assisted reprecipitation method, and its ability to discriminate and quantify proteins was evaluated. Sonication time (30 s, 5 min, and 15 min) and cyclodextrin templating (α-, 2-HP-β-, and γ-CD) were investigated for their effects on discrimination performance of synthesized nanomaterial. Six proteins (albumin, hemoglobin, trypsin, catalase, lysozyme, and cytochrome c) with different abundance levels and physicochemical properties were selected as target analytes. Absorbance response patterns generated from interactions between $[P_{4444}]_2$[EB] nanoGUMBOS and proteins were analyzed using partial least squares discriminant analysis. Percentages of correct protein discrimination ranged from 94.6 to 99.6%, with the latter being the best result obtained using non-templated nanoGUMBOS formed after 5 min sonication. Under optimized conditions, it was possible to discriminate all protein samples with percentages of correct assignments greater than 90% for concentrations as low as 2.0 μg mL^{-1}. The discrimination capability of synthesized nanoGUMBOS was further evaluated using mixtures of different ratios of lysozyme, cytochrome c, and hemoglobin. Finally, partial least squares models were developed for protein quantification and the best performance was observed for albumin. Results support potential use of $[P_{4444}]_2$[EB] nanoGUMBOS in combination with ultraviolet-visible spectroscopy and chemometrics for qualitative and quantitative analyses of individual proteins and mixtures of proteins.

Keywords: Chemometrics; NanoGUMBOS; Proteins; Ultraviolet-visible spectroscopy.

4.1. Introduction

Simultaneous analyses of multiple protein biomarkers has been recognized as a valuable tool for improving diagnostic accuracy, predicting long-term outcomes, and guiding treatment decisions (1, 2). Thus, considerable efforts have been made to develop rapid and sensitive methods for detection and quantification of proteins using a multiplexed approach. Mass spectrometry is one of the most widely used analytical tools due to the ability to measure hundreds of proteins and proteoforms in a small sample volume. Nevertheless, this method requires specialized equipment, extensive sample preparation, and highly trained technicians (3-5). Due to simplicity of operation, rapidity, and cost-effectiveness, optical sensor arrays have emerged as promising alternatives for discrimination of chemically or structurally similar proteins, quantification of their levels, and identification of complex mixtures (6, 7). These sensing platforms usually consist of a set of chemical sensors that interact differently with protein analytes, generating unique response patterns for each. Chemometric tools such as principal component analysis (PCA), partial least squares discriminant analysis (PLSDA), and partial least squares (PLS), may then be applied to extract relevant information from datasets (8, 9). However, widespread use of sensor arrays has been limited by the need for a large number of recognition elements as compared to proteins, which leads to high sample consumption as well as long acquisition and processing times (7, 10). There is a growing demand for simple sensor arrays composed of only a few sensing elements and/or single sensor systems, such as those that use multiple wavelengths to provide cross-reactive responses to proteins (11, 12).

Various sensing scaffolds have been employed for protein analyses, including fluorescent dyes, conjugated polymers, and functionalized porphyrins (13-15). More recently, nanoparticles have attracted considerable attention due to their unique optical properties, improved photochemical stability, and possibility of surface modification (16, 17). Despite these advantages, conventional nanoparticles often involve complex synthetic procedures, time-consuming purification steps, as well as expensive and hazardous chemicals (18, 19). The simplicity of preparation and high tunability of nanoparticles derived from a *g*roup of *u*niform *m*aterials *b*ased on *o*rganic *s*alts (nanoGUMBOS) make them suitable candidates for detection and discrimination of proteins. Modulation of nanoGUMBOS properties may be achieved by changing the cation, anion, and alkyl chain length, thus eliminating the need for selective ligands while minimizing toxicity (20, 21). Furthermore, particle size may be controlled by simply adjusting experimental parameters such as concentration of GUMBOS solution, sonication time, and presence of template (22, 23). This is particularly relevant since it is known that size can affect nanoparticle-protein interactions (24, 25).

In the study reported here, a phosphonium-erythrosin B-based nanoGUMBOS (i.e.,

$[P_{4444}]_2$[EB]) was synthesized using a simple ultrasound-assisted reprecipitation method, and its potential to discriminate and quantify various protein analytes was examined. The impact of sonication time and template choice on nanoGUMBOS size and, consequently, on its discriminatory power was assessed by PLSDA. Under optimized synthesis conditions, the ability of $[P_{4444}]_2$[EB] nanoGUMBOS to discriminate individual proteins at different concentrations (20.0–0.5 μg mL^{-1}) and protein mixtures was also examined. Moreover, PLS models were developed for protein quantification.

4.2. Experimental

4.2.1. Reagents and solvents

Tetrabutylphosphonium bromide ($[P_{4444}][Br]$, 98%); 2',4',5',7'-tetraiodofluorescein disodium salt ($[Na]_2$[EB], 90%); alpha (α), 2-hydroxypropyl-beta (2-HP-β), and gamma (γ) CDs (≥ 98%); albumin (Alb) from human serum; human hemoglobin (Hb); trypsin (Try) from porcine pancreas; catalase (Cat) from bovine liver; lysozyme (Lyz) from chicken egg white; cytochrome c (Cyt c) from bovine heart; sodium phosphate dibasic (Na_2HPO_4); and sodium phosphate monobasic (NaH_2PO_4) were all obtained from Sigma-Aldrich (St. Louis, MO) and used as supplied. Dimethylsulfoxide (DMSO) was purchased from Merck KGaA (Darmstadt, Germany).

Phosphate buffer (10 mmol L^{-1}, pH 7.4) was obtained by dissolving Na_2HPO_4 and NaH_2PO_4 in ultrapure water (Milli-Q, 18.2 MΩ cm), and used for preparation of protein stock solutions. These solutions (300 μg mL^{-1}) were further diluted in phosphate buffer to obtain concentrations ranging from 20.0 to 0.5 μg mL^{-1}. Details of the synthesis and characterization of EB-based GUMBOS can be found in our previous study (26).

4.2.2. Synthesis of nanoGUMBOS

$[P_{4444}]_2$[EB] nanoGUMBOS were synthesized using an ultrasonication-assisted reprecipitation method (Fig. S4.1) (27). Briefly, 200 μL of an 8 mmol L^{-1} solution of GUMBOS in DMSO were added to 9800 μL of ultrapure water with and without CD (1:1 molar ratio). The mixture was then sonicated using an amplitude of 20% for 30 s, 5 min, and 15 min using a Vibra-Cell VCX 130 (Sonics & Materials, Inc., Newtown, CT) with a 6 mm diameter tip. Vials were kept in an ice bath during the procedure to avoid overheating.

4.2.3. Characterization of the synthesized nanoGUMBOS

Optical properties of $[P_{4444}]_2$[EB] nanoGUMBOS were investigated using UV-Vis spectroscopy. Absorbance measurements (300–700 nm) were performed on a Jasco V-660 spectrophotometer using a 1 cm quartz cuvette.

The hydrodynamic diameter, polydispersity index (PDI), and zeta potential (ZP) of synthesized nanoGUMBOS were determined using dynamic and phase analysis light scattering (DLS and PALS, respectively) with a ZetaPALS analyzer (Brookhaven Instruments, Holtsville, NY). Particle size and ZP measurements were performed at 25 ºC with a detection angle of 90º and 15º, respectively. The number of runs per measurement was set to six (each with a duration of 2 min and 10 cycles, respectively), and the count rate was kept in the range of 300–500 kcps. Results were expressed as the mean ± standard deviation (SD) of three batches of nanoGUMBOS.

Transmission electron microscopy (TEM) analysis was performed to further examine the size and shape of $[P_{4444}]_2$[EB] nanoGUMBOS. Briefly, an aliquot of 10 µL of nanoGUMBOS dispersion was placed on a formvar/carbon film-coated mesh nickel grid (Electron Microscopy Sciences, Hatfield, PA) and left standing for 2 min, after which excess liquid was removed using filter paper. Images were recorded using a JEM-1400 microscope (JEOL Ltd., Tokyo, Japan) operated at 120 kV and equipped with a CCD camera Orious 1100 W. Subsequently, the diameters of 100 randomly selected nanoGUMBOS were measured using ImageJ 1.53e (National Institutes of Health, Bethesda, MD), and data were fitted to a Gaussian function for determination of average particle size.

4.2.4. Evaluation of storage stability

The stability of $[P_{4444}]_2$[EB] nanoGUMBOS was assessed by monitoring changes in hydrodynamic diameter and PDI over eight weeks. For this study, nanoGUMBOS were stored in the dark at room temperature and DLS measurements were performed as described above.

4.2.5. Discrimination and quantification of proteins using nanoGUMBOS

In order to obtain maximum discrimination among proteins, the effect of sonication time and CD template on the discrimination performance of $[P_{4444}]_2$[EB] nanoGUMBOS was evaluated. Briefly, 20 µL of each protein sample (e.g., Alb, Hb, Try, Cat, Lyz, and Cyt c) were added to a 96-well microplate containing 80 µL of nanoGUMBOS dispersion and 200 µL of phosphate buffer pH 7.4. After a 5 min reaction period, UV-Vis spectra (Fig. 4.1) were recorded from 300 to 700 nm using a Cytation 3 imaging reader (BioTek Instruments, Winooski, VT). Protein and nanoGUMBOS concentrations were fixed at 20 µg mL^{-1} and 4

μmol L^{-1}, respectively.

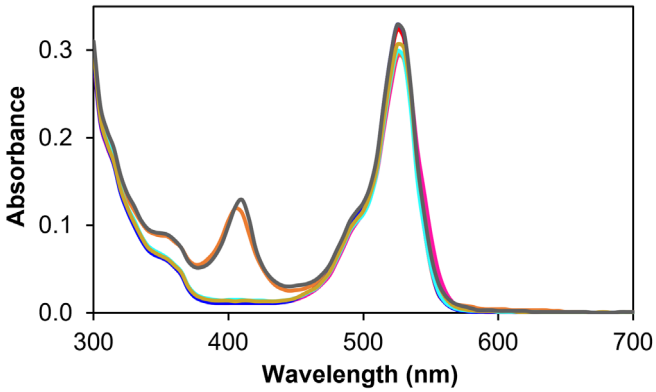

Fig. 4.1. Absorbance spectra of $[P_{4444}]_2$[EB] nanoGUMBOS (–) and $[P_{4444}]_2$[EB] nanoGUMBOS in the presence of Alb (–), Hb (–), Try (–), Cat (–), Lyz (–), and Cyt c (–). NanoGUMBOS were obtained after 5 min of sonication without CD.

Additional studies were performed to investigate the discrimination power of synthesized nanoGUMBOS at lower protein concentrations (15.0–0.5 μg mL^{-1}) as well as binary and ternary mixtures of Lyz, Cyt c, and Hb (total protein concentration = 6 μg mL^{-1}). Only $[P_{4444}]_2$[EB] nanoGUMBOS formed upon 5 min of sonication and in the absence of CD was used since these conditions resulted in better discrimination. The experimental procedure used for protein quantification was similar to that described above. For each protein, seven replicates were obtained.

4.2.6. Data analysis

Before modeling, all spectra were preprocessed using standard normal variate (SNV) (28), and then mean-centered. PLSDA was used to discriminate proteins and their mixtures at different concentrations/ratios, while PLS was used for predicting protein concentrations. The entire spectral wavelength range (300–700 nm) was considered in the analysis.

PLSDA is a supervised classification method based on the PLS2 algorithm, which relies on prior knowledge of the data set (29, 30). In PLSDA, to each known sample (x_i, nanoGUMBOS spectra in the presence of a single protein) is assigned a vector of zeros with value one at the position corresponding to its class (y_i, in this study to each protein). The structure of the PLSDA model is described by Eqs. 1 and 2. Model loadings (P and Q) and corresponding scores (T and U) are obtained by sequentially extracting the components or latent variables (LVs) from matrices X (spectra) and Y (matrix codifying the proteins).

$$X = TP^t + E \qquad (1)$$

$$Y = UQ^t + F \qquad (2)$$

The algorithm correlates the scores of each block (T and U), yielding an internal regression matrix. This internal regression can be transformed on a regression matrix B. In this case, the regression matrix is composed of three vectors: one regression vector corresponding to each protein. E and F are the residual matrices and depend on the number of LVs selected. Predictions for new samples are obtained by multiplying a new spectrum (x_{new}) by the regression matrix B:

$$y_{new} = x_{new} B \qquad (3)$$

The prediction ($y_{new} = [y_{new,1}, y_{new,2},\ldots,y_{new,n}]$) is then converted into a class assignment (protein) from which confusion matrices are obtained. Before applying PLSDA, 70% of the samples are randomly selected to obtain the regression matrix B and 30% are used as new samples for prediction. This procedure is repeated 100 times per PLSDA model and confusion matrices present the mean values of correct protein assignments for the prediction samples.

During development of PLS models, samples were randomly separated into two sets: one for calibration + cross-validation (70%) and another for prediction (30%). The first set was further divided into a 70:30 ratio as described for PLSDA models. It is noted that the prediction set was totally independent, and never included in the calibration step (neither for calibration nor for cross-validation). The accuracy of PLS models was evaluated by calculating the coefficient of determination of calibration, cross-validation, and prediction (R^2C, R^2CV, and R^2P); the root mean square error of calibration, cross-validation, and prediction (RMSEC, RMSECV, and RMSEP); and the range error ratio (RER).

Data preprocessing and modeling were performed in MATLAB R2018b (MathWorks, Natick, MA) and PLS Toolbox 8.7 (Eigenvector Research, Manson, WA).

4.3. Results and discussion

4.3.1. Characterization of the synthesized nanoGUMBOS

Following synthesis, nanoGUMBOS properties were studied using UV-Vis spectroscopy, DLS/PALS, and TEM. As shown in Fig. S4.2, the synthesized nanoGUMBOS displayed similar absorption spectra to that of $[Na]_2[EB]$ (parent dye) with an intense band at 527 nm, a shoulder at approximately 487 nm, and a lower intensity band around 310 nm (31, 32).

Increased absorbance and spectral broadening is attributed to dye aggregation within nanoGUMBOS (33, 34).

The results of particle size and ZP measurements are presented in Tables S4.1 and S4.2. Hydrodynamic diameters varied from 133 to 238 nm depending on sonication time and template choice. For example, templating with 2-HP-β-CD led to a reduction in particle size from 159 to 139 nm. PDI values were found to be lower than 0.2 for all synthesized nanoGUMBOS, indicating that particles are moderately polydisperse (35). Examination of ZP data confirmed formation of highly stable nanoparticle dispersions (ZP ≥ -30 mV) (35). The negative charge can be ascribed to adsorption of EB anion on the surface of nanoGUMBOS (22, 23). It is also worth noting that changes in sonication time and CD template did not significantly affect ZP, contrary to what was observed for particle size.

TEM analysis revealed formation of quasi-spherical nanoparticles with an average diameter of 119 nm (Fig. S4.3). As expected, this value is lower than that obtained by DLS since it represents the size of nanoparticles in dry form (35, 36). It was also found that $[P_{4444}]_2[EB]$ nanoGUMBOS remain stable for at least three weeks when stored in the dark at room temperature (Fig. S4.4).

4.3.2. Experimental optimization

4.3.2.1. Sonication time

The impact of sonication time on the discriminatory power of $[P_{4444}]_2[EB]$ nanoGUMBOS was evaluated using six proteins, e.g., Alb, Hb, Try, Cat, Lyz, and Cyt c at the concentration of 20.0 μg mL^{-1}. These proteins were chosen as target analytes because they differ in abundance, hydrophobicity, isoelectric point, and molecular weight (Table S4.3). For example, Alb is the most abundant serum protein (normal concentration range = 35–50 mg mL^{-1}), displays higher surface hydrophobicity than Lyz, and has a molecular weight four times smaller as compared to Cat (37, 38). However, within this set of proteins, several pairs possess similar isoelectric points and molecular weights, which constitutes an additional challenge for discrimination of proteins using synthesized nanoGUMBOS.

Three PLSDA models, each corresponding to a single sonication time (30 s, 5 min, and 15 min), were developed as previously described in section 4.2.6. All scores maps showed six clusters, each related to a single protein, with varying degrees of overlap (Fig. 4.2). The first three latent variables (LVs) of PLSDA models encompassed around 99% of spectral variability and LV1 (≈ 90%) seemed to be responsible for discrimination between Hb + Cyt c and the remaining proteins. Alb was discriminated from Try, Cat, and Lyz on the second LV (LV2: 6–8% of spectral variability), being the last three proteins discriminated in different

degrees along LV2 and LV3. The total percentages of correct protein assignments obtained from confusion matrices were: 96.4%–30 s, 99.6%–5 min, and 95.5%–15 min (Table 4.1). Alb, Hb, and Cyt c were 100% correctly predicted for the three sonication times. Try, Cat, and Lyz were misidentified mostly among each other, with the worst results obtained for 15 min of sonication. These findings demonstrate the impact of sonication time on discrimination performance of synthesized nanoGUMBOS. Moreover, surface charge, hydrophobicity, and size seem to affect the extent of interaction between $[P_{4444}]_2$[EB] nanoGUMBOS and protein analytes. Other studies confirm the role that these physicochemical properties play in discrimination of proteins (39, 40). The higher affinity of synthesized nanoGUMBOS for positively charged proteins (e.g., Alb and Hb) can be explained by its negative surface charge. Although hydrophobic and van der Waals interactions may also be involved, electrostatic interactions are thought to be the primary parameter responsible for protein discrimination (41, 42). Try and Lyz misidentifications can be attributed to similarity of their isoelectric points (10.5 *versus* 11.4). Additionally, the large molecular weight of Cat (250.0 kDa) can explain its reduced binding efficiency as compared to other positively charged proteins (Alb and Hb), and consequently, the lower percentages of correct predictions that were obtained (43).

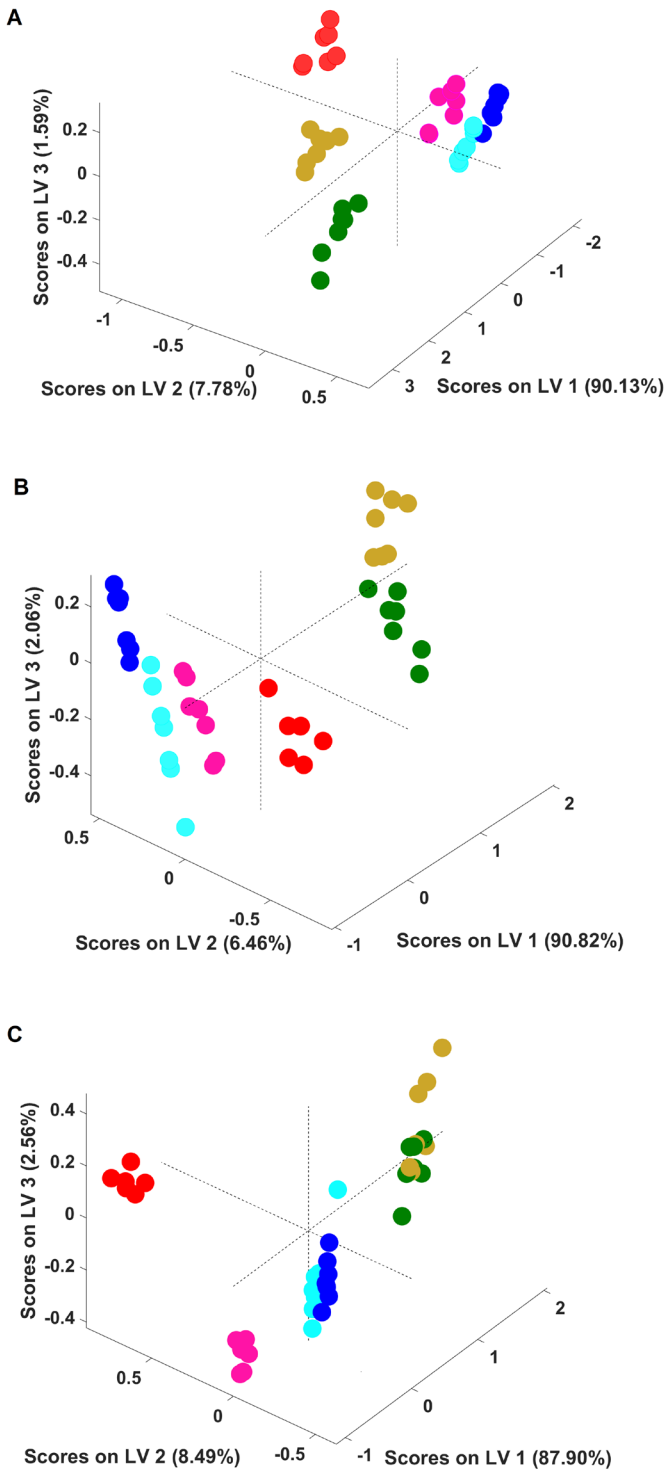

Fig. 4.2. Scores plots corresponding to the first three LVs of PLSDA regression models developed with UV-Vis spectra for protein discrimination: • Alb, • Hb, • Try, • Cat, • Lyz, and • Cyt c. $[P_{4444}]_2$[EB] nanoGUMBOS obtained after 30 s (A), 5 min (B), and 15 min (C) of sonication.

Table 4.1. Confusion matrices obtained from the PLSDA regression models developed for protein discrimination using the $[P_{4444}]_2[EB]$ nanoGUMBOS. Models A, B, and C correspond to 30 s, 5 min, and 15 min of sonication.

Model A	Alb	Hb	Try	Cat	Lyz	Cyt c	
Alb	16.67	0	0	0	0	0	–
Hb	0	16.67	0	0	0	0	–
Try	0	0	14.50	0.56	1.61	0	–
Cat	0	0	0.72	15.94	0	0	–
Lyz	0	0	0.11	0.56	16.00	0	–
Cyt c	0	0	0	0	0	16.67	–
					Correct protein discrimination (%)		**96.4**
Model B	Alb	Hb	Try	Cat	Lyz	Cyt c	
Alb	16.67	0	0	0	0	0	–
Hb	0	16.67	0	0	0	0	–
Try	0	0	16.61	0.06	0	0	–
Cat	0.11	0	0.06	16.50	0	0	–
Lyz	0.11	0	0	0.06	16.50	0	–
Cyt c	0	0	0	0	0	16.67	–
					Correct protein discrimination (%)		**99.6**
Model C	Alb	Hb	Try	Cat	Lyz	Cyt c	
Alb	16.67	0	0	0	0	0	–
Hb	0	16.67	0	0	0	0	–
Try	0	0	15.56	0.61	0.50	0	–
Cat	0	0	3.22	13.39	0.06	0	–
Lyz	0	0	0.06	0.06	16.56	0	–
Cyt c	0	0	0	0	0	16.67	–
					Correct protein discrimination (%)		**95.5**

4.3.2.2. CD templating

After fixing sonication time at 5 min, the ability of $[P_{4444}]_2$[EB] nanoGUMBOS to discriminate among proteins was evaluated in the presence of three CDs (α, 2-HP-β, and γ). The developed PLSDA models (Fig. S4.5) were quite similar to those obtained during optimization of sonication time, with six moderately separated clusters being observed (around 99% of spectral variability captured on the first three LVs). The corresponding confusion matrices were generated (Table S4.4) and the total percentages of correct protein assignments were shown in Fig. 4.3. Despite the high percentages of correct predictions obtained for all CD-templated nanoGUMBOS, the best result was achieved in the absence of CDs. Thus, it was decided to proceed with this study using non-templated nanoGUMBOS.

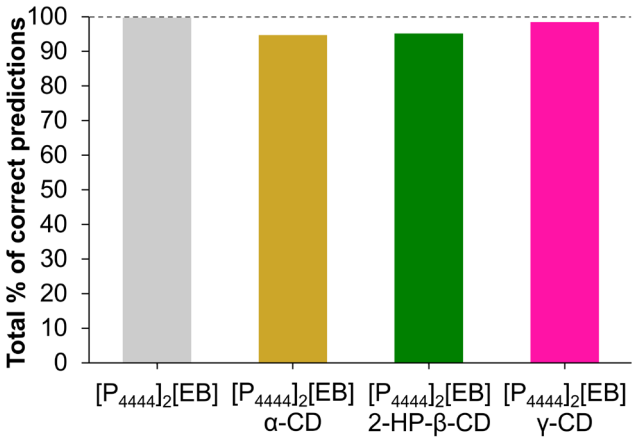

Fig. 4.3. Total percentages of correct protein discrimination obtained with the $[P_{4444}]_2$[EB] nanoGUMBOS synthesized in the absence and presence of three CDs (α, 2-HP-β, and γ).

4.3.3. Discrimination of proteins and their concentrations

Optimization of sonication time and assessment of impact of CDs on discrimination success was performed at a protein concentration of 20.0 μg mL^{-1}. Additional studies were performed to evaluate the ability of $[P_{4444}]_2$[EB] nanoGUMBOS to distinguish lower concentrations of proteins (15.0–0.5 μg mL^{-1}). For each concentration, a PLSDA model was developed (data not shown) and a corresponding confusion matrix was obtained (more details in section 4.2.6). Despite encompassing high spectral variability in the first three LVs (≈ 96–99%), the degree of clusters overlapping increased for lower concentrations of proteins. This finding was consistent with smaller percentages of correct protein assignments obtained from confusion matrices (Fig. 4.4). $[P_{4444}]_2$[EB] nanoGUMBOS was able to discriminate between 70–80% of the protein samples with concentrations of 0.5 and 1.0 μg mL^{-1}. Additionally, there was an improvement in discrimination performance of nanoGUMBOS for

concentrations higher than 1.0 μg mL^{-1} (percentage of correct discriminations > 90%). Only small fluctuations occurred in total percentages of correct protein predictions from 2.0 to 20.0 μg mL^{-1}, with maximum (99.6%) being obtained for the highest concentration tested. In fact, this nanoGUMBOS approach produces a very satisfactory percentage of correct identifications for lower concentrations of proteins as compared to those reported for other sensing systems (44-47). Moreover, it requires only 5 min of reaction time and one probe to discriminate among all protein samples.

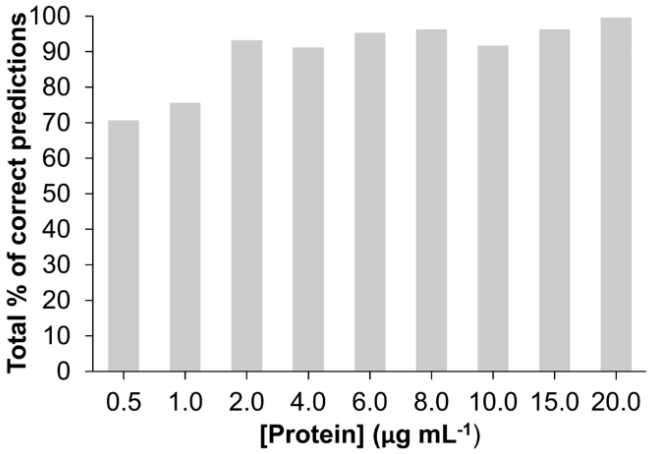

Fig. 4.4. Total percentages of correct protein assignments obtained with the $[P_{4444}]_2[EB]$ nanoGUMBOS at various protein concentrations.

Regarding each protein individually (Table 4.2), Hb and Cyt c seemed to be the best predicted in the whole concentration range (percentage of correct predictions ≥ 99% for [Protein] ≥ 2.0 μg mL^{-1}). Cat was the worst predicted (75.3–91.7%), reaching 99.0% of correct prediction only for [Protein] = 20.0 μg mL^{-1}. Alb, Try, and Lyz presented random fluctuations in the percentages of correct discriminations across the concentration range, being the worst result obtained for Lyz at 1.0 μg mL^{-1} (52.0%) and the best result found for Alb at the concentration of 20.0 μg mL^{-1} (100% of correct predictions).

Table 4.2. Percentages of correct predictions (%) for different concentrations of proteins obtained from the confusion matrices of PLSDA regression models.

[Protein] ($\mu g\ mL^{-1}$)	Correct protein predictions (%)					
	Alb	Hb	Try	Cat	Lyz	Cyt c
0.5	62.0	70.0	76.3	76.7	65.3	74.0
1.0	70.7	83.0	99.0	75.3	52.0	73.7
2.0	91.3	98.7	99.0	80.7	89.7	100.0
4.0	97.0	100.0	74.3	79.3	96.7	100.0
6.0	99.0	100.0	93.7	79.0	100.0	100.0
8.0	100.0	100.0	90.3	88.0	99.3	100.0
10.0	66.7	100.0	79.3	87.0	86.3	100.0
15.0	100.0	100.0	93.0	91.7	93.3	100.0
20.0	100.0	100.0	99.7	99.0	99.0	100.0

4.3.4. Discrimination of binary and ternary mixtures of Lyz, Cyt c, and Hb

The ability of $[P_{4444}]_2[EB]$ nanoGUMBOS to discriminate between mixtures of Lyz + Cyt c, Lyz + Hb, Cyt c + Hb, and Lyz + Cyt c + Hb was also evaluated. For each protein mixture, a PLSDA model was developed and scores maps were obtained (Fig. 4.5). Regarding Lyz + Cyt c, the first two LVs of the PLSDA model (Fig. 4.5A) encompassed 99% of spectral variability, being the samples discriminated across LV1. Pure Lyz and Cyt c samples were located on opposite sides of the scores map (positive and negative, respectively), while mixed samples appeared between them. It is noted that samples possessing 50% of each protein were precisely located in the middle of the scores map (0 of the LV1 axis) and that those containing 75% + 25% were closer to the corresponding pure protein. This clear separation of samples corroborates previous results concerning discrimination of single proteins. Lyz and Cyt c were also easily discriminated between each other, appearing on opposite sides of the first LV of scores map. Regarding the mixture of Lyz and Hb (Fig. 4.5B), a quite similar result was obtained. Pure samples of Lyz and Hb appeared on opposite sides of LV1, with mixed samples located between them according to protein ratio. Hb was located near Cyt c in the scores map when the six proteins were discriminated simultaneously (Fig. 4.2B), which somehow justifies the similar results of Lyz + Cyt c and Lyz + Hb mixtures. In this context, it was decided to evaluate the ability of $[P_{4444}]_2[EB]$ nanoGUMBOS to discriminate between protein mixtures of Hb and Cyt c. The scores plot obtained from the corresponding PLSDA model (Fig. 4.5C) showed considerably overlapped clusters when only the first two LVs were used (data not shown). In contrast to

previously studied mixtures, use of the third LV was mandatory for clusters separation. Considering the three LVs, it was possible to observe five individualized clusters, which were located in the scores map according to the ratio of proteins in the mixture. Results obtained for this mixture were in good agreement with the already mentioned closeness of Hb and Cyt c when the six proteins were discriminated simultaneously. An additional study was performed to evaluate the behavior of $[P_{4444}]_2$[EB] nanoGUMBOS towards a ternary mixture of Lyz, Cyt c, and Hb (1:1:1, Fig. 4.5D). The scores map of the PLSDA model confirmed conclusions noted above. Separation of pure samples of Lyz, Cyt c, and Hb was observed in the first LV, confirming the high structural similarity between Cyt c and Hb previously reported in the literature (48). Moreover, 50:50 mixtures of these proteins were located in the scores map near the middle of pure samples. Regarding the ternary mixture (Lyz:Cyt c:Hb), samples were not in a central position between pure proteins (Fig. 4.5D). They seemed to be quite closer to pure Hb and Cyt c samples, and more separate from Lyz. However, this location in the scores map was expected since two pure samples (Hb and Cyt c) appeared on the negative side of LV1, while only one (Lyz) was located on the positive side.

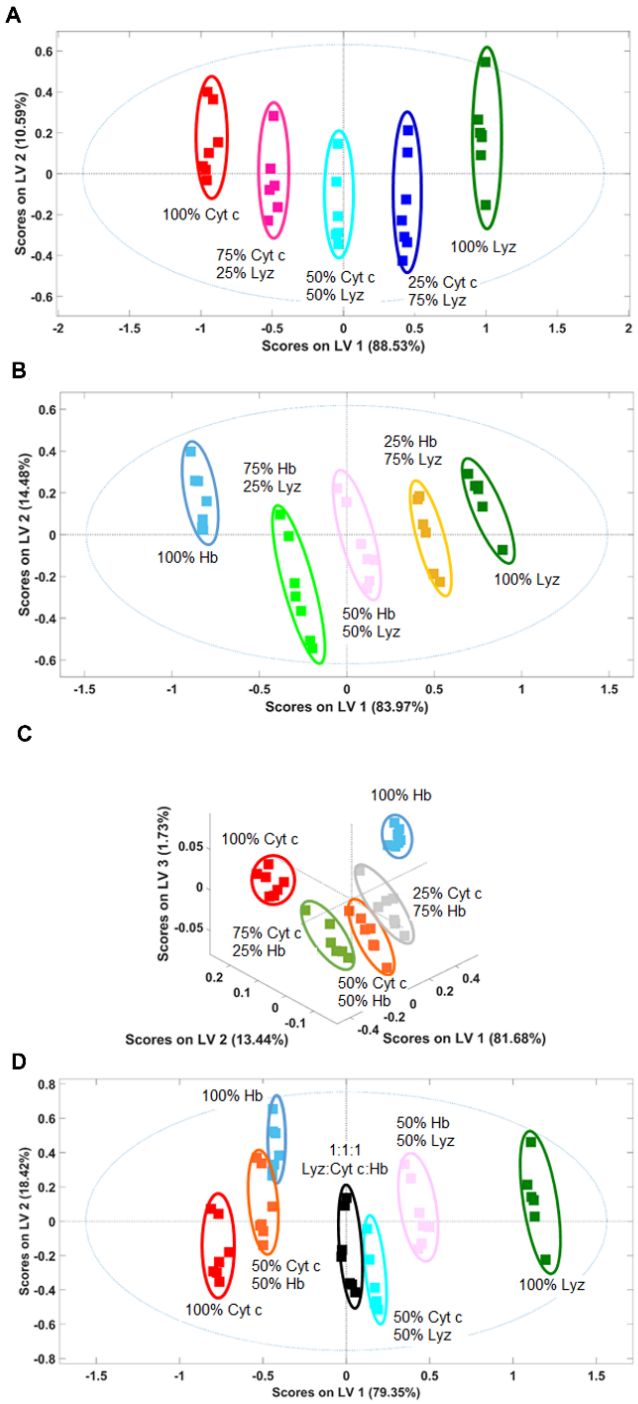

Fig. 4.5. Scores plots of PLSDA regression models developed with UV-Vis spectra of $[P_{4444}]_2$[EB] nanoGUMBOS incubated with mixtures of (A) Lyz and Cyt c; (B) Lyz and Hb; (C) Cyt c and Hb; and (D) Lyz, Cyt c, and Hb. Legend: ■ 100% Lyz; ■ 100% Cyt c; ■ 100% Hb; ■ 75% Lyz + 25% Cyt c; ■ 50% Lyz + 50% Cyt c; ■ 25% Lyz + 75% Cyt c; ■ 25% Lyz + 75% Hb; ■ 50% Lyz + 50% Hb; ■ 75% Lyz + 25% Hb; ■ 50% Cyt c + 50% Hb; ■ 75% Cyt c + 25% Hb; ■ 75% Cyt c + 25% Hb; ■ 1:1:1, Lyz:Cyt c:Hb.

4.3.5. Protein quantitative analysis

Regarding protein discrimination using $[P_{4444}]_2[EB]$ nanoGUMBOS, a very satisfactory percentage of correct assignments (> 90%) was achieved for concentrations ranging from 2.0 to 20.0 μg mL^{-1}. Therefore, it was decided to evaluate the ability of this nanoGUMBOS to quantify each protein separately in the mentioned concentration range. Six PLS models (one for each protein) were developed, being the number of LVs selected from the RMSECV plots (Fig. S4.6, A–F). The figures of merit obtained are presented in Table 4.3. Overall, the PLS model developed for Alb quantification provided the best performance. Despite having a slightly higher RMSEC than Try (6.5 *versus* 4.5%), the corresponding RMSECV was the lowest in this study (7.8%). The R^2C and R^2CV obtained for Alb were also the highest ones (0.99 for both). In contrast, the PLS model developed for Cat quantification showed the worst performance with a RMSEC of 10.4% (R^2C = 0.97) and a RMSECV of 26.8% (R^2CV = 0.83). The remaining four proteins presented intermediate RMSEC values (Hb = 9.8%, Try = 4.5%, Lyz = 7.3%, and Cyt c = 8.2%) and very good calibration coefficients of determination (0.98–0.99). Additionally, the errors of cross-validation set (RMSECV) were lower than those obtained for calibration (Hb = 18.5%, Try = 16.0%, Lyz = 14.3%, and Cyt c = 19.3%), with R^2CV ranging from 0.91 to 0.94. All PLS models developed were validated using an independent set of samples (the prediction set P), which was randomly selected from initial data and never used in the calibration or cross-validation steps. This set of samples further allowed testing of the robustness of the PLS models. Although coefficients of determination obtained for the prediction set were quite good (0.88–0.97); for Cat, the value was only 0.78. Root mean square errors were quite variable and followed a similar trend to that observed for the cross-validation set (8.9–28.1%), being the best performance achieved for quantification of Alb. Regarding RER, the worst results were obtained for Hb and Cat (below 10). For Try, Lyz, and Cyt c, 15 > RER ≥ 10, suggesting that the developed models are suitable for calibration and quality control. The RER value obtained for Alb was 21.6, indicating that the model is appropriate for quantification (RER ≥ 15) (49).

Table 4.3. Figures of merit obtained from the PLS models developed to predict protein concentration (20.0 ≥ [Protein] ≥ 2.0 μg mL^{-1}) using the $[P_{4444}]_2[EB]$ nanoGUMBOS.

Protein	LVs	RMSEC	R^2C	RMSECV	R^2CV	RMSEP	R^2P	RER
Alb	4	0.60	0.99	0.72	0.99	0.83	0.97	21.6
Hb	6	0.91	0.98	1.72	0.93	1.92	0.88	9.4
Try	6	0.42	0.99	1.49	0.94	1.46	0.95	12.3
Cat	6	0.97	0.97	2.49	0.83	2.61	0.78	6.9
Lyz	5	0.68	0.99	1.33	0.94	1.15	0.97	15.7
Cyt c	6	0.76	0.98	1.79	0.91	1.37	0.95	13.1

Latent variable (LV); Root mean square error of calibration (RMSEC), cross-validation (RMSECV), and prediction (RMSEP); Coefficient of determination of calibration (R^2C), cross-validation (R^2CV), and prediction (R^2P); RER = Δy/RMSEP.

4.4. Conclusions

This study focused on development of an alternative strategy to discriminate and quantify proteins. A phosphonium-erythrosin B-based nanoGUMBOS was synthesized using a simple reprecipitation method and its discrimination performance was optimized by varying sonication time (30 s–15 min) and CD template (α, 2-HP-β, or γ). The percentages of correct protein assignments varied from 94.6 to 99.6%, with best results obtained when sonication time was set to 5 min and using no template. Under these conditions, it was possible to discriminate proteins at various concentrations (from 20.0 to 2.0 μg mL^{-1}) and distinguish between mixtures of Lyz, Cyt c, and Hb at different proportions (25% + 50%, 50% + 50%, 75% + 25%, and 1:1:1). Regarding protein quantification, the models developed for Alb and Cat showed the best and worst performance, respectively. The PLS model obtained for Alb (RER = 21.6) proved also to be suitable for quantification purposes, while those developed for Try, Lyz, and Cyt c seemed to be appropriate for calibration and quality control (15 > RER ≥ 10). Overall, the obtained results demonstrated that the proposed strategy holds great promise for rapid discrimination of single proteins and their mixtures at different concentrations/ratios as well as quantification of Alb. Moreover, this approach is label-free, requires only one probe to discriminate all protein samples, and involves use of small volumes of reagents, which make this strategy attractive for high-throughput applications. Future studies include analysis of other proteins of interest and biofluids such as blood and urine.

SUPPLEMENTARY MATERIAL

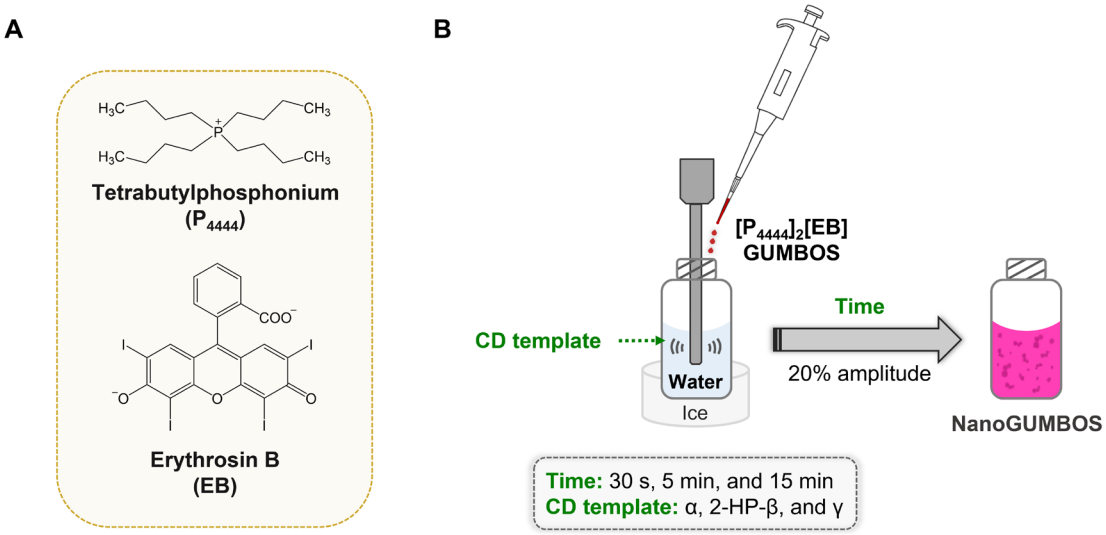

Fig. S4.1. (A) Chemical structures of the ions used to form $[P_{4444}]_2$[EB] GUMBOS. (B) Scheme of the reprecipitation procedure used for the synthesis of nanoGUMBOS.

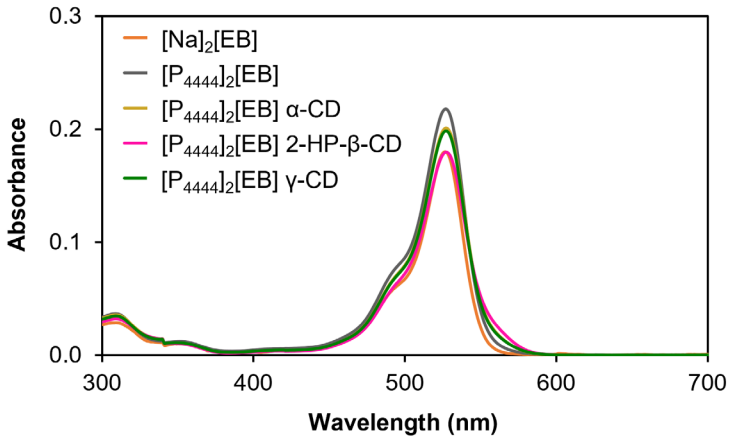

Fig. S4.2. UV–Vis spectra of $[Na]_2$[EB] and $[P_{4444}]_2$[EB] nanoGUMBOS (4 μmol L^{-1}) in water. Both non-templated and CD-templated nanoGUMBOS were obtained after 5 min of sonication.

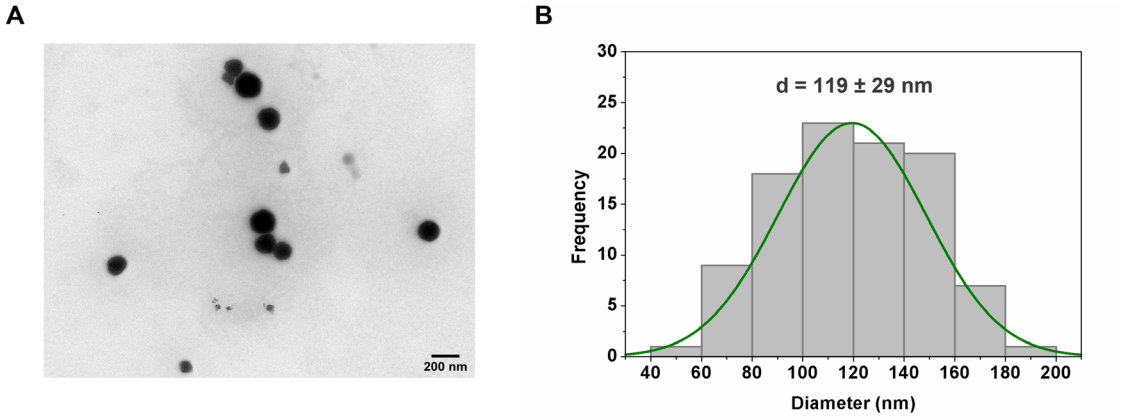

Fig. S4.3. TEM image of $[P_{4444}]_2[EB]$ nanoGUMBOS (A) and the corresponding particle size distribution histogram with Gaussian fitting (B).

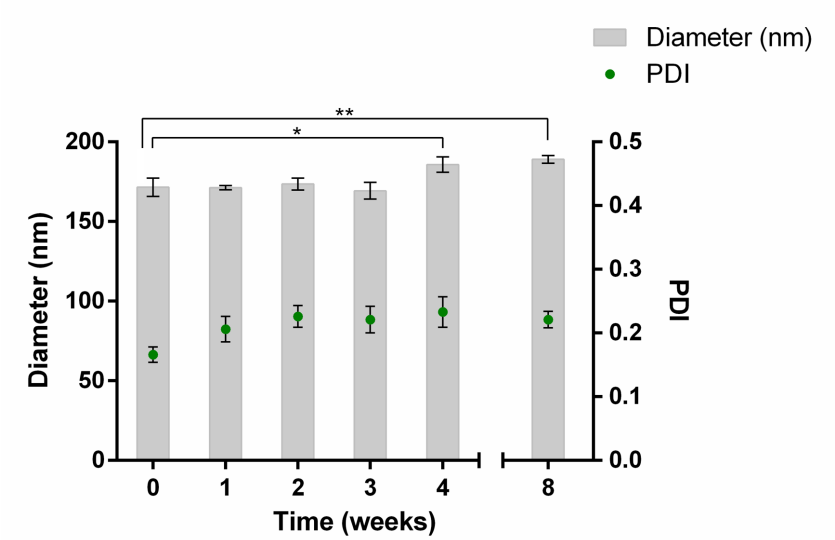

Fig. S4.4. Effect of storage time on the hydrodynamic diameter and PDI of $[P_{4444}]_2[EB]$ nanoGUMBOS. Statistical analysis was performed using the non-parametric Kruskal-Wallis test (*P < 0.05 and **P < 0.01).

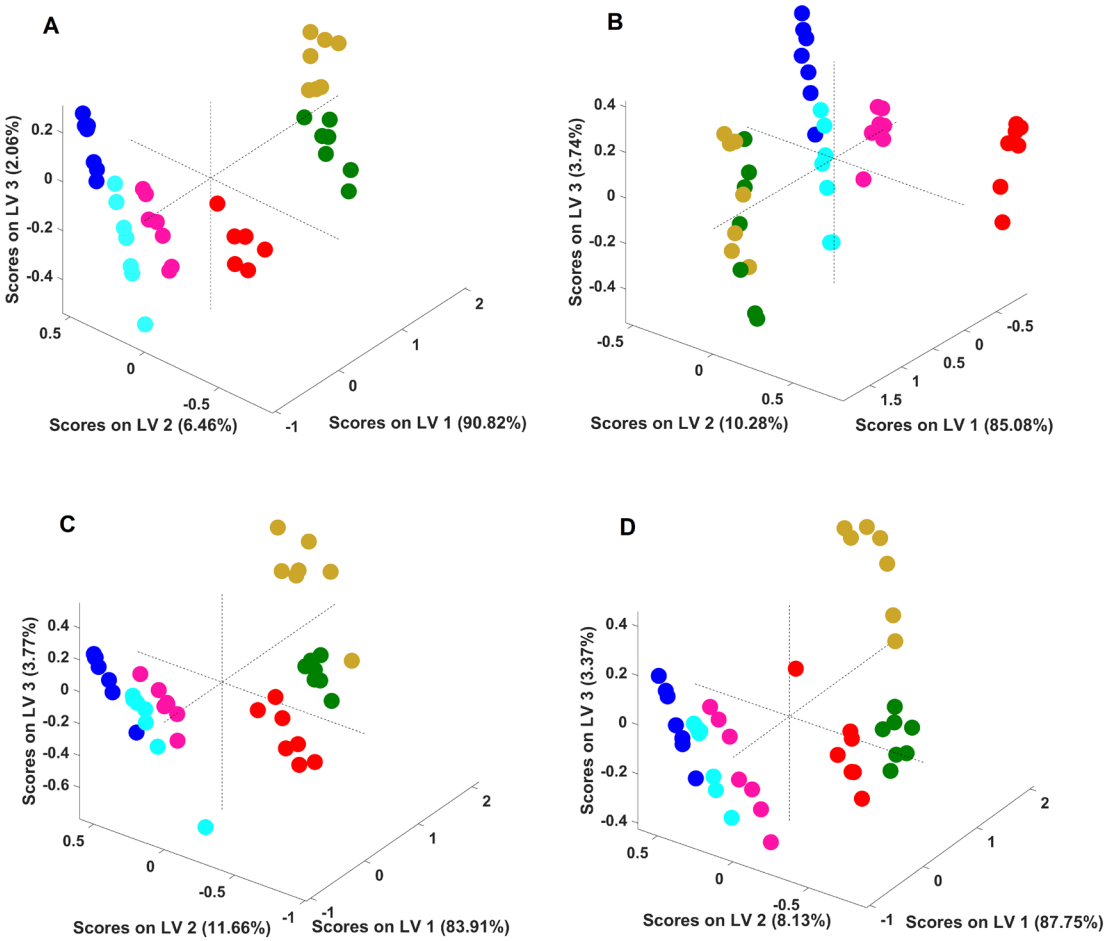

Fig. S4.5. Scores plots corresponding to the first three LVs of PLSDA regression models developed using UV-Vis spectra of $[P_{4444}]_2[EB]$ nanoGUMBOS for protein discrimination: • Alb, • Hb, • Try, • Cat, • Lyz, and • Cyt c. Models A, B, C, and D correspond to nanoGUMBOS synthesized in the absence and presence of α-, 2-HP-β-, and γ-CD, respectively.

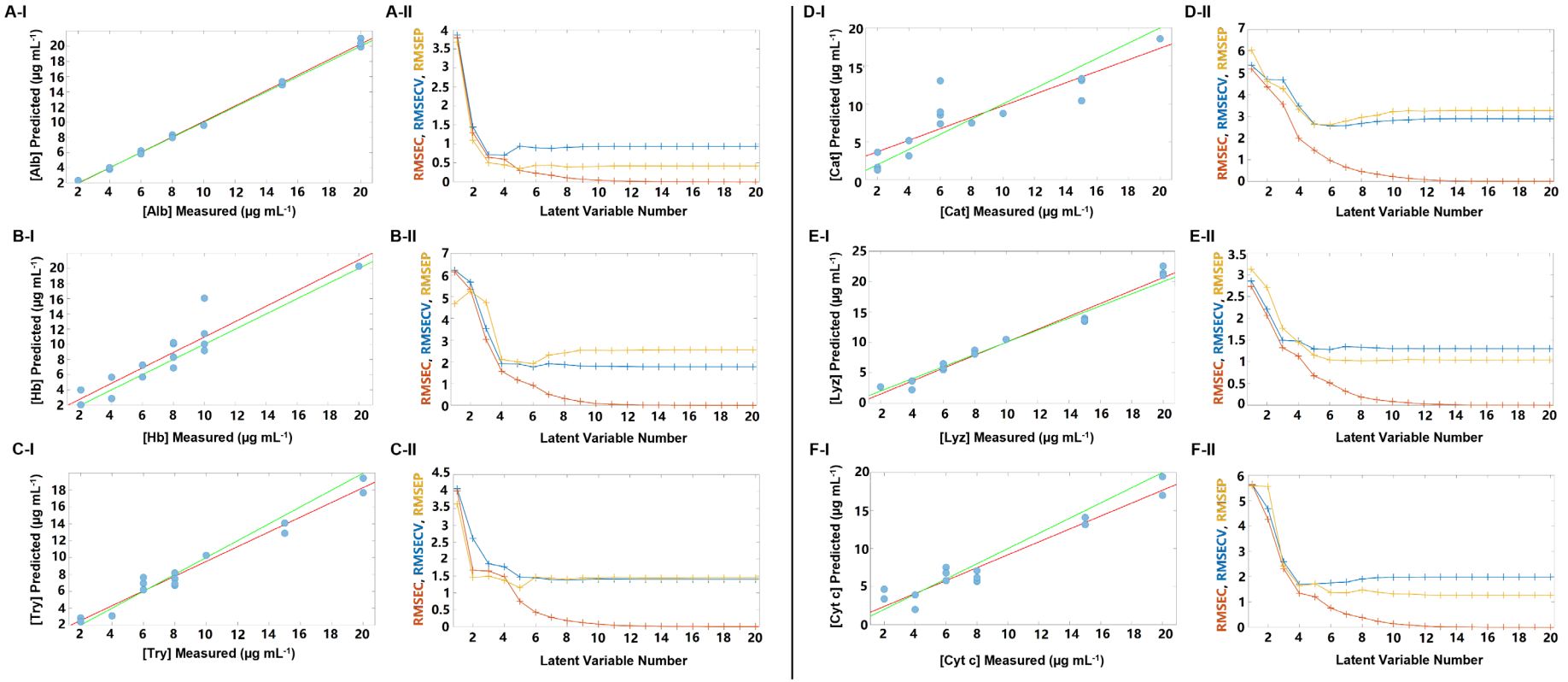

Fig. S4.6. PLS regression results obtained for (A) Alb, Albumin; (B) Hb, Hemoglobin; (C) Try, Trypsin; (D) Cat, Catalase; (E) Lyz, Lysozyme; and (F) Cyt c, Cytochrome c. Panels I refer to the PLS regression model developed for each protein: true protein concentration (measured) *versus* protein concentration predicted by the UV-Vis spectra (predicted). The red and green lines correspond to calibration and cross-validation data, respectively. Panels II show the root mean square error of calibration (RMSEC), cross-validation (RMSECV), and prediction (RMSEP) variation *versus* number of latent variables (LVs) used in the PLS models. Although using a larger number of LVs can lead to lower errors, no significant decrease was observed for LVs > 4.

Table S4.1. Hydrodynamic diameter, polydispersity index (PDI), and zeta potential (ZP) of $[P_{4444}]_2$[EB] nanoGUMBOS obtained after 30 s, 5 min, and 15 min of sonication. Values represent the mean and standard deviation of three batches of nanoGUMBOS.

Time	Diameter (nm)	PDI	ZP (mV)
30 s	133 ± 9	0.133 ± 0.011	-44 ± 5
5 min	159 ± 9	0.165 ± 0.013	-43 ± 3
15 min	172 ± 11	0.129 ± 0.010	-38 ± 2

Table S4.2. Characterization of CD-templated nanoGUMBOS in terms of hydrodynamic diameter, polydispersity index (PDI), and zeta potential (ZP). Data expressed as mean ± standard deviation (n = 3).

NanoGUMBOS	Diameter (nm)	PDI	ZP (mV)
$[P_{4444}]_2$[EB]	159 ± 9	0.165 ± 0.013	-43 ± 3
$[P_{4444}]_2$[EB] α-CD	238 ± 2	0.170 ± 0.013	-41 ± 4
$[P_{4444}]_2$[EB] 2-HP-β-CD	139 ± 11	0.180 ± 0.012	-42 ± 1
$[P_{4444}]_2$[EB] γ-CD	191 ± 6	0.165 ± 0.012	-39 ± 2

Table S4.3. Molecular weights and isoelectric points of target proteins.

Protein	Isoelectric point	Molecular weight (kDa)	Ref.
Alb	4.7	66.5	(50)
Hb	6.8	64.5	(51)
Try	10.5	23.8	(52)
Cat	5.4	250.0	(53)
Lyz	11.4	14.3	(51)
Cyt c	10.0–10.5	12.3	(54)

Table S4.4. Confusion matrices obtained from the PLSDA regression models developed for protein discrimination using the $[P_{4444}]_2$[EB] nanoGUMBOS synthesized in the absence (A) and presence of three CDs: α (B), 2-HP-β (C), and γ (D).

Model A	Alb	Hb	Try	Cat	Lyz	Cyt c	
Alb	16.67	0	0	0	0	0	–
Hb	0	16.67	0	0	0	0	–
Try	0	0	16.61	0.06	0	0	–
Cat	0.11	0	0.06	16.50	0	0	–
Lyz	0.11	0	0	0.06	16.50	0	–
Cyt c	0	0	0	0	0	16.67	–
				Correct protein discrimination (%)			**99.6**
Model B	Alb	Hb	Try	Cat	Lyz	Cyt c	
Alb	16.67	0	0	0	0	0	–
Hb	0	16.67	0	0	0	0	–
Try	0	0	14.11	1.89	0.67	0	–
Cat	0	0	0.33	15.28	1.06	0	–
Lyz	0	0	1.17	0.33	15.17	0	–
Cyt c	0	0	0	0	0	16.67	–
				Correct protein discrimination (%)			**94.6**
Model C	Alb	Hb	Try	Cat	Lyz	Cyt c	
Alb	16.67	0	0	0	0	0	–
Hb	0	16.67	0	0	0	0	–
Try	0	0	14.56	0.61	1.50	0	–
Cat	0	0	0.06	13.89	2.72	0	–
Lyz	0	0	0.06	0	16.61	0	–
Cyt c	0	0	0	0	0	16.67	–
				Correct protein discrimination (%)			**95.1**
Model D	Alb	Hb	Try	Cat	Lyz	Cyt c	
Alb	16.67	0	0	0	0	0	–
Hb	0	16.67	0	0	0	0	–
Try	0	0	16.22	0	0.44	0	–
Cat	0	0	0	16.11	0.56	0	–
Lyz	0.1	0	0.44	0	16.11	0	–
Cyt c	0	0	0	0	0	16.67	–
				Correct protein discrimination (%)			**98.4**

References

1. Motiei L, Pode Z, Koganitsky A, Margulies D. Targeted Protein Surface Sensors as a Tool for Analyzing Small Populations of Proteins in Biological Mixtures. Angew Chem-Int Edit. 2014;53(35):9289-93.

2. Fang Z, Liu LP, Wang Y, Xi DM, Zhang SS. Unambiguous Discrimination of Multiple Protein Biomarkers by Nanopore Sensing with Double-Stranded DNA-Based Probes. Anal Chem. 2020;92(2):1730-7.

3. Kingsmore SF. Multiplexed protein measurement: technologies and applications of protein and antibody arrays. Nat Rev Drug Discov. 2006;5(4):310-20.

4. Donnelly DP, Rawlins CM, DeHart CJ, Fornelli L, Schachner LF, Lin ZQ, et al. Best practices and benchmarks for intact protein analysis for top-down mass spectrometry. Nat Methods. 2019;16(7):587-94.

5. Smit NPM, Ruhaak LR, Romijn FPHTM, Pieterse MM, van der Burgt YEM, Cobbaert CM. The Time Has Come for Quantitative Protein Mass Spectrometry Tests That Target Unmet Clinical Needs. J Am Soc Mass Spectrom. 2021;32(3):636-47.

6. Hou CJ, Dong JL, Zhang GP, Lei Y, Yang M, Zhang YC, et al. Colorimetric artificial tongue for protein identification. Biosens Bioelectron. 2011;26(10):3981-6.

7. Fan JM, Qi L, Han HF, Ding LP. Array-Based Discriminative Optical Biosensors for Identifying Multiple Proteins in Aqueous Solution and Biofluids. Front Chem. 2020;8:18.

8. Umali AP, Anslyn EV. A general approach to differential sensing using synthetic molecular receptors. Curr Opin Chem Biol. 2010;14(6):685-92.

9. Martynko E, Kirsanov D. Application of Chemometrics in Biosensing: A Brief Review. Biosensors-Basel. 2020;10(8):20.

10. Fan JM, Ding LP. Single-system based discriminative optical sensors: different strategies and versatile applications. Analyst. 2018;143(16):3775-88.

11. Zheng DM, Fan JM, Huang XY, Ding LP, Xin YH. Fluorescent binary ensemble with pattern recognition ability for identifying multiple metalloproteins with applications in serum and urine. RSC Adv. 2017;7(79):50097-105.

12. Fan JM, Zheng DM, Huang XY, Ding LP, Xin YH, Fang Y. A single discriminative sensor based on supramolecular self-assemblies of an amphiphilic cholic acid-modified fluorophore for identifying multiple proteins. Sens Actuator B-Chem. 2018;263:336-46.

13. Perez RL, Cong MY, Vaughan SR, Ayala CE, Galpothdeniya WIS, Mathaga JK, et al. Protein Discrimination Using a Fluorescence-Based Sensor Array of Thiacarbocyanine-GUMBOS. ACS Sens. 2020;5(8):2422-9.

14. Miranda OR, You CC, Phillips R, Kim IB, Ghosh PS, Bunz UHF, et al. Array-based sensing of proteins using conjugated polymers. J Am Chem Soc. 2007;129(32):9856-7.

15. Zhou HC, Baldini L, Hong J, Wilson AJ, Hamilton AD. Pattern recognition of proteins based on an array of functionalized porphyrins. J Am Chem Soc. 2006;128(7):2421-5.
16. Miranda OR, Creran B, Rotello VM. Array-based sensing with nanoparticles: 'Chemical noses' for sensing biomolecules and cell surfaces. Curr Opin Chem Biol. 2010;14(6):728-36.
17. Bigdeli A, Ghasemi F, Golmohammadi H, Abbasi-Moayed S, Nejad MAF, Fahimi-Kashani N, et al. Nanoparticle-based optical sensor arrays. Nanoscale. 2017;9(43):16546-63.
18. Ravichandran V, Vasanthi S, Shalini S, Shah SAA, Tripathy M, Paliwal N. Green synthesis, characterization, antibacterial, antioxidant and photocatalytic activity of Parkia speciosa leaves extract mediated silver nanoparticles. Results Phys. 2019;15:8.
19. Cao Y, Dhahad HA, El-Shorbagy MA, Alijani HQ, Zakeri M, Heydari A, et al. Green synthesis of bimetallic ZnO-CuO nanoparticles and their cytotoxicity properties. Sci Rep. 2021;11(1):8.
20. Bhattarai N, Chen M, Perez RL, Ravula S, Strongin RM, McDonough K, et al. Comparison of Chemotherapeutic Activities of Rhodamine-Based GUMBOS and NanoGUMBOS. Molecules. 2020;25(14):13.
21. Azevedo AMO, Santos JLM, Warner IM, Saraiva MLMFS. GUMBOS and nanoGUMBOS in chemical and biological analysis: A review. Anal Chim Acta. 2020;1133:180-98.
22. Hamdan S, Dumke JC, El-Zahab B, Das S, Boldor D, Baker GA, et al. Strategies for controlled synthesis of nanoparticles derived from a group of uniform materials based on organic salts. J Colloid Interface Sci. 2015;446:163-9.
23. Chen M, Bhattarai N, Cong MY, Perez RL, McDonough KC, Warner IM. Mitochondria targeting IR780-based nanoGUMBOS for enhanced selective toxicity towards cancer cells. RSC Adv. 2018;8(55):31700-9.
24. Deng ZJ, Liang MT, Toth I, Monteiro MJ, Minchin RF. Molecular Interaction of Poly(acrylic acid) Gold Nanoparticles with Human Fibrinogen. ACS Nano. 2012;6(10):8962-9.
25. Saptarshi SR, Duschl A, Lopata AL. Interaction of nanoparticles with proteins: relation to bio-reactivity of the nanoparticle. J Nanobiotechnol. 2013;11:12.
26. Azevedo AMO, Sousa C, Chen M, Ayala CE, Perez RL, Santos JLM, et al. Protein discrimination using erythrosin B-based GUMBOS in combination with UV–Vis spectroscopy and chemometrics. Talanta. 2022;240:123164.
27. Cong MY, Perez RL, Chen M, Chapai R, Jin RY, Vidanapathirana P, et al. Imidazolium-dysprosium-based magnetic NanoGUMBOS for isolation of hemoglobin. Talanta. 2019;205:120078.

28. Naes T, Isaksson T, Fearn T, Davies T. A user-friendly guide to multivariate calibration and classification. Chichester, UK: NIR Publications; 2002.
29. Geladi P, Kowalski BR. Partial least-squares regression: A tutorial. Anal Chim Acta. 1986;185:1-17.
30. Alsberg BK, Kell DB, Goodacre R. Variable selection in discriminant partial least-squares analysis. Anal Chem. 1998;70(19):4126-33.
31. Fleming GR, Knight AWE, Morris JM, Morrison RJS, Robinson GW. Picosecond Fluorescence Studies of Xanthene Dyes. J Am Chem Soc. 1977;99(13):4306-11.
32. Montero E, Garcia MA, Villegas MA, Llopis J. Spectral pH dependence of erythrosin B in sol-gel silica coatings and buffered solutions. Bol Soc Esp Ceram Vidr. 2008;47(1):1-6.
33. Dahne L. Self-organization of polymethine dyes in thin solid layers. J Am Chem Soc. 1995;117(51):12855-60.
34. Das S, Bwambok D, El-Zahab B, Monk J, de Rooy SL, Challa S, et al. Nontemplated Approach to Tuning the Spectral Properties of Cyanine-Based Fluorescent NanoGUMBOS. Langmuir. 2010;26(15):12867-76.
35. Bhattacharjee S. DLS and zeta potential - What they are and what they are not? J Control Release. 2016;235:337-51.
36. Mourdikoudis S, Pallares RM, Thanh NTK. Characterization techniques for nanoparticles: comparison and complementarity upon studying nanoparticle properties. Nanoscale. 2018;10(27):12871-934.
37. Anderson NL, Anderson NG. The human plasma proteome - History, character, and diagnostic prospects. Mol Cell Proteomics. 2002;1(11):845-67.
38. Nicolau DV, Paszek E, Fulga F, Nicolau DV. Mapping Hydrophobicity on the Protein Molecular Surface at Atom-Level Resolution. PLoS One. 2014;9(12):28.
39. You CC, Miranda OR, Gider B, Ghosh PS, Kim IB, Erdogan B, et al. Detection and identification of proteins using nanoparticle-fluorescent polymer 'chemical nose' sensors. Nat Nanotechnol. 2007;2(5):318-23.
40. Li XN, Wen F, Creran B, Jeong YD, Zhang XR, Rotello VM. Colorimetric Protein Sensing Using Catalytically Amplified Sensor Arrays. Small. 2012;8(23):3589-92.
41. Ganesan L, Margolles-Clark E, Song Y, Buchwald P. The food colorant erythrosine is a promiscuous protein-protein interaction inhibitor. Biochem Pharmacol. 2011;81(6):810-8.
42. Wang FY, Lu YX, Yang JC, Chen Y, Jing WJ, He LY, et al. A smartphone readable colorimetric sensing platform for rapid multiple protein detection. Analyst. 2017;142(17):3177-82.

43. Joseph A, Nyambura CW, Bondurant D, Corry K, Beebout D, Wood TR, et al. Formulation and Efficacy of Catalase-Loaded Nanoparticles for the Treatment of Neonatal Hypoxic-Ischemic Encephalopathy. Pharmaceutics. 2021;13(8):17.
44. Kong H, Liu D, Zhang SC, Zhang XR. Protein Sensing and Cell Discrimination Using a Sensor Array Based on Nanomaterial-Assisted Chemiluminescence. Anal Chem. 2011;83(6):1867-70.
45. Xu SH, Lu X, Yao CX, Huang F, Jiang H, Hua WH, et al. A Visual Sensor Array for Pattern Recognition Analysis of Proteins Using Novel Blue-Emitting Fluorescent Gold Nanoclusters. Anal Chem. 2014;86(23):11634-9.
46. Xu SH, Wu YF, Sun XM, Wang ZQ, Luo XL. A multicoloured Au NCs based cross-reactive sensor array for discrimination of multiple proteins. J Mat Chem B. 2017;5(22):4207-13.
47. Shen YS, Huang YF, Zhang PMM, Guo BC, Jiang HT, Tan CY, et al. Fluorescence Sensor Array for Discrimination of Urine Proteins and Differentiation Diagnosis of Urinary System Diseases. ACS Appl Bio Mater. 2020;3(9):5639-43.
48. Chertkova RV, Brazhe NA, Bryantseva TV, Nekrasov AN, Dolgikh DA, Yusipovich AI, et al. New insight into the mechanism of mitochondrial cytochrome c function. PLoS One. 2017;12(5):20.
49. AACC. Near-infrared methods – Guidelines for model development and maintenance. St. Paul, MN: AACC Press; 1999.
50. Vicente FA, Bairos J, Roque M, Coutinho JAP, Ventura SPM, Freire MG. Use of Ionic Liquids as Cosurfactants in Mixed Aqueous Micellar Two-Phase Systems to Improve the Simultaneous Separation of Immunoglobulin G and Human Serum Albumin from Expired Human Plasma. ACS Sustain Chem Eng. 2019;7(17):15102-13.
51. Martinez-Sernandez V, Orbegozo-Medina RA, Romaris F, Paniagua E, Ubeira FM. Usefulness of ELISA Methods for Assessing LPS Interactions with Proteins and Peptides. PLoS One. 2016;11(6):17.
52. Craig M, Bordes R, Holmberg K. Polypeptide multilayer self-assembly and enzymatic degradation on tailored gold surfaces studied by QCM-D. Soft Matter. 2012;8(17):4788-94.
53. Feoktistova NA, Balabushevich NG, Skirtach AG, Volodkin D, Vikulina AS. Inter-protein interactions govern protein loading into porous vaterite CaCO3 crystals. Phys Chem Chem Phys. 2020;22(17):9713-22.
54. Baghdady YZ, Schug KA. Online Comprehensive High pH Reversed Phase x Low pH Reversed Phase Approach for Two-Dimensional Separations of Intact Proteins in Top-Down Proteomics. Anal Chem. 2019;91(17):11085-91.

Chapter 5

Studies of protein binding to biomimetic membranes using ANS-based GUMBOS

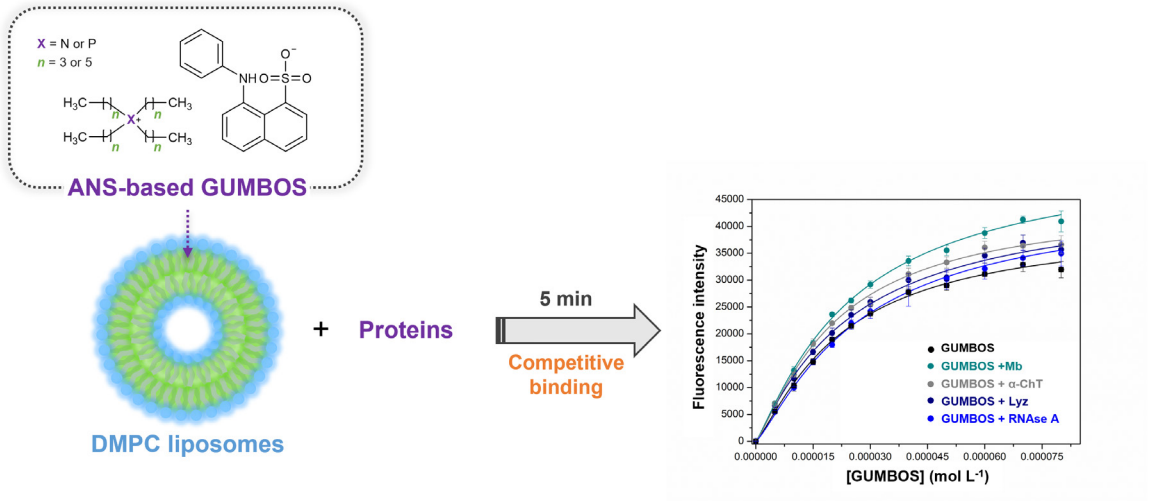

Highlights

- ANS-based GUMBOS were synthesized and characterized using different techniques.
- The synthesized GUMBOS showed improved optical properties and lipophilicity.
- Proteins produced different fluorescence responses with each of the probes tested.
- Results suggest competition between proteins and GUMBOS for membrane binding sites.

Manuscript submitted as "Azevedo AMO, Nunes C, Moniz T, Perez RL, Ayala CE, Rangel M, Reis S, Santos JLM, Warner IM, Saraiva MLMFS. Studies of protein binding to biomimetic membranes using ANS-based GUMBOS".

Abstract

Tuning the ANS (8-anilino-1-naphthalenesulfonic acid) structure usually requires harsh conditions and long reaction times, which can result in low yields. Herein, ANS was modified to form ANS GUMBOS (*g*roup of *u*niform *m*aterials *b*ased on *o*rganic *s*alts), prepared with simple ion metathesis reactions and distinct cations, namely tetrabutylammonium (N_{4444}), tetrahexylammonium (N_{6666}), and tetrabutylphosphonium (P_{4444}). These ANS-based GUMBOS were investigated as fluorescent probes for membrane binding studies with four proteins having distinct physicochemical properties. Liposomes of dimyristoyl-*sn*-glycero-phosphocholine (DMPC) were employed as membrane models as a result of their ability to mimic the structure and chemical composition of cell membranes. Changes in fluorescence intensity were used to monitor protein binding to liposomes, and adsorption data were fitted to a Freundlich-like isotherm. It was determined that [N_{4444}][ANS] and [P_{4444}][ANS] GUMBOS have enhanced optical properties and lipophilicity as compared to parent ANS. As a result, these two GUMBOS were selected for subsequent protein-membrane binding studies. Both [N_{4444}][ANS] and [P_{4444}][ANS] GUMBOS and parent ANS independently reached membrane saturation within the same concentration range. Furthermore, distinct fluorescence responses were observed upon addition of proteins to each probe, which demonstrates the impact of lipophilic properties of such probes on the binding process. The relative maintenance of binding cooperativity and maximum fluorescence intensity suggests that proteins compete with ANS-based probes for the same membrane binding sites. Finally, this GUMBOS-based approach is simple, rapid, and involves relatively small amounts of reagents, making it attractive for high-throughput purposes. These results presented herein can also provide relevant information for designing GUMBOS with ameliorated properties.

Keywords: ANS; GUMBOS; Liposome; Protein; Protein-membrane binding.

5.1. Introduction

The binding of proteins to biological membranes plays an important role in a multitude of cellular processes, including signal transduction, lipid metabolism, and vesicle trafficking (1, 2). Additionally, protein-lipid interactions are understood to be involved in pathological conditions ranging from inflammation to cancer (3, 4). For example, it has been proposed that oligomeric beta-amyloid binds to GM1 ganglioside and decreases membrane fluidity, thereby stimulating proteolytic cleavage of the amyloid precursor protein. This effect can result in beta-amyloid accumulation and formation of neuritic plaques, which are characteristic hallmarks of Alzheimer's disease (5, 6).

Various membrane model systems have been employed to study interactions between proteins and lipids, including liposomes, lipid monolayers, and supported lipid bilayers (7, 8). Liposomes are among the most commonly used models as a result of their ability to closely resemble the structure and properties of cell membranes. In fact, these model systems are composed of a phospholipid bilayer enclosing an aqueous compartment that can mimic the anisotropic environment of biological membranes (9-11). Phosphatidylcholine accounts for 39% of plasma membrane phospholipids and is predominant in eukaryotic cells. As such, 1,2-dimyristoyl-*sn*-glycero-3-phosphocholine (DMPC) was chosen for preparation of liposomes in the present study (12, 13).

ANS (i.e., 8-Anilino-1-naphthalenesulfonic acid) is an anionic dye that has been widely employed as a fluorescent probe for protein analyses. Several research groups have demonstrated the ability of this probe to determine surface hydrophobicity of proteins, detect conformational changes, and characterize protein binding sites (14-16). ANS has also been used to study protein interactions with lipid membranes (17, 18). However, it is worth noting that this probe is mostly located at the membrane surface since its naphthalene moiety only partially enters the hydrophobic core (19, 20). Tuning the ANS structure can include extensive resource investment, harsh conditions, and long reaction times, which can result in low yields (21, 22). In contrast, we hypothesized that ANS GUMBOS (*g*roup of *u*niform *m*aterials *b*ased on *o*rganic *s*alts) can be used to tune ANS and can be prepared using a simple ion-exchange metathesis reaction, without need for extensive resource input and time consuming purification steps (23, 24). GUMBOS properties including, but not limited to, lipophilicity can also be readily tuned by changing the cation-anion combination, thereby avoiding complicated chemical modifications. Moreover, this approach constitutes a cost-effective tool for designing ANS derivatives with enhanced and targetted properties (25, 26). In this study, ANS was converted into GUMBOS via simple metathesis reactions using distinct cations, namely tetrabutylammonium (N_{4444}), tetrahexylammonium (N_{6666}), and tetrabutylphosphonium (P_{4444}). The properties of ANS-based GUMBOS were examined and

their potential applications as fluorescent probes for membrane binding studies were investigated. For this purpose and due to differences in surface hydrophobicity, lysozyme (Lyz), myoglobin (Mb), α-chymotrypsin (α-ChT), and ribonuclease A (RNAse A) were selected as model proteins. Changes in fluorescence intensities were used to study protein binding to DMPC liposomes. Experiments were also conducted with the parent ANS dye to further confirm the potential of this GUMBOS approach.

5.2. Material and methods

5.2.1. Reagents and solvents

Tetrabutylammonium bromide ([N_{4444}][Br]), tetrahexylammonium bromide ([N_{6666}][Br]), Lyz from chicken egg white, Mb from equine heart, α-ChT from bovine pancreas, RNAse A from bovine pancreas, *N*-(2-hydroxyethyl)piperazine-*N*′-(2-ethanesulfonic acid) (HEPES) hemisodium salt, hexadecylphosphocholine (HePC), and dichloromethane (DCM) were all purchased from Sigma-Aldrich (St. Louis, MO). Tetrabutylphosphonium bromide ([P_{4444}][Br]) was acquired from Fluka (Charlotte, NC) and DMPC was obtained from Avanti Polar Lipids (Alabaster, AL). ANS ammonium salt ([NH_4][ANS]) was purchased from Tokyo Chemical Industry (TCI America, Portland, OR) and ANS from Invitrogen (Waltham, MA). Sodium chloride (NaCl) was obtained from PanReac AppliChem (Darmstadt, Germany). Chloroform and methanol were purchased from VWR International (Radnor, PA), and acetonitrile (ACN) from Riedel-de Haën (Seelze, Germany). Deuterated methanol (CD_3OH, 99.8%) with 0.03% (v/v) tetramethylsilane was acquired from Eurisotop (Saarbrücken, Germany).

HEPES buffer 0.01 mol L^{-1} (pH 7.4, I = 0.1 mol L^{-1}) was obtained by dissolving HEPES and NaCl in high-purity water (Milli-Q, 18.2 MΩ cm), and used for preparation of HePC stock suspension. This suspension (600 μmol L^{-1}) was further diluted in HEPES buffer to a concentration of 100 μmol L^{-1}. Protein stock and working solutions (2 mg mL^{-1} and 300 μg mL^{-1}, respectively) were prepared in the same buffer. ANS-based GUMBOS were dissolved in ACN, protected from light, and used immediately after preparation. Before membrane partition and protein-lipid binding studies, these stock solutions were further diluted in HEPES buffer to obtain a concentration of 450 μmol L^{-1} and 100 μmol L^{-1}, respectively.

5.2.2. Instrumentation

Nuclear magnetic resonance (NMR) spectra were recorded using a Bruker Avance III 400 operating at 400.15 MHz for proton (^1H) and 100.62 MHz for carbon (^{13}C). The spectrometer was equipped with a pulse gradient unit, capable of producing a z-gradient of 50.0 G cm^{-1}.

Two-dimensional (2D) $^{1}H–^{13}C$ heteronuclear single quantum coherence (HSQC) and $^{1}H–^{13}C$ heteronuclear multiple bond coherence (HMBC) spectra were acquired and processed using Bruker's TopSpin software version 4.0.1. NMR samples were prepared by dissolving synthesized GUMBOS in CD_3OH. Coupling constants (*J*) and chemical shifts (δ) were reported in Hz and ppm, respectively. Peak multiplicities were abbreviated as follows: bs, broad singlet; dd, double doublet; t, triplet; q, quartet; quint, quintet; and m, multiplet. NMR analyses were conducted at "Laboratório de Análise Estrutural, Centro de Materiais da Universidade do Porto (CEMUP), Portugal".

High-resolution mass spectrometry (HRMS) measurements were performed at the Louisiana State University Mass Spectrometry facility using an Agilent 6230 B-TOF LC/MS system, operated in both positive and negative ionization modes. A Bruker Tensor 27 spectrometer, equipped with a PIKE MIRacle ATR accessory, was used to obtain Fourier transform infrared (FTIR) spectra in the range of 4000 to 400 cm^{-1}. Resolution was set to 4 cm^{-1} and the number of scans to 32.

Ultraviolet-visible (UV-Vis) and fluorescence spectroscopic studies were performed using a Jasco V-660 spectrophotometer and a Jasco FP-6500 spectrofluorometer, both equipped with a 1 cm quartz cuvette. UV-Vis spectra were recorded in the range of 250–500 nm, and fluorescence emission spectra from 390 to 650 nm upon excitation at 370 nm.

Thermal stability of $[N_{4444}][ANS]$ and $[P_{4444}][ANS]$ was investigated using a TA Discovery TGA 550 instrument. GUMBOS were heated from 25 to 595 ºC using a ramp rate of 10 ºC min^{-1}. The melting points of these compounds were also determined using a MEL-TEMP® apparatus. Membrane partition and competitive binding assays were performed on a BioTek® Cytation 3 imaging reader.

5.2.3. Synthesis and characterization of GUMBOS

ANS-based GUMBOS were synthesized using simple ion-exchange metathesis reactions, where the ammonium cation of ANS parent dye was replaced with N_{4444}^{+}, N_{6666}^{+}, and P_{4444}^{+} (Fig. 5.1A). Following a previously described procedure, 5 mL of water containing the desired cation were added to 10 mL of a DCM solution of $[NH_4][ANS]$ (1.1:1 molar ratio) (27, 28). The biphasic mixture was stirred for 48 h in the dark at room temperature, after which the top layer (aqueous phase) was discarded (Fig. 5.1B). The DCM phase was then washed several times with water to minimize any remaining halogenated byproduct (i.e., NH_4Br). Subsequently, DCM was evaporated and residual water was removed by freeze-drying. The resulting GUMBOS were structurally characterized using NMR, HRMS, and FTIR. Additionally, spectral properties were investigated using UV-Vis and fluorescence spectroscopies. Physical characteristics such as lipophilicity, thermal stability, and melting

point, were also examined using derivative UV-Vis spectrophotometry, thermogravimetric analysis (TGA), and melting point determination, respectively.

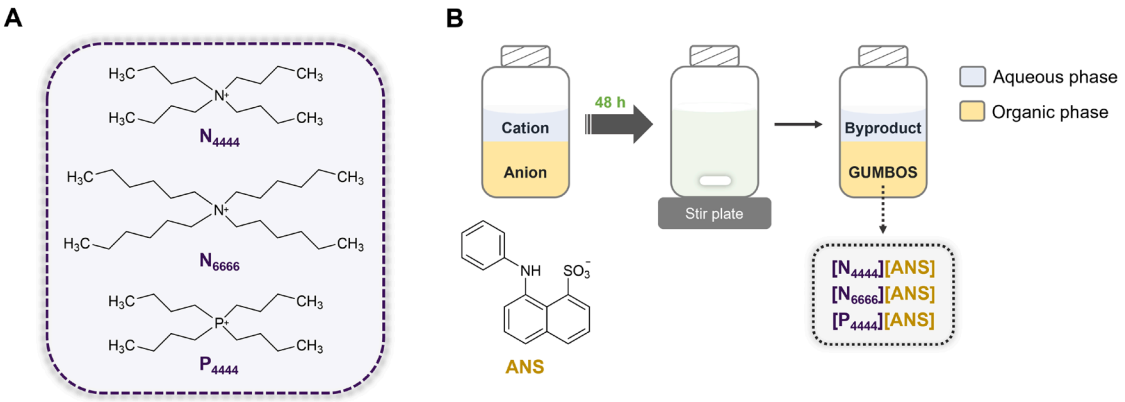

Fig. 5.1. (A) Chemical structures of the cations used to form ANS-based GUMBOS. (B) Schematic representation of GUMBOS syntheses.

5.2.4. GUMBOS partitioning

HePC micelle/buffer partition coefficients (K_p) of synthesized GUMBOS and parent ANS dye were assessed using a derivative UV-Vis spectrophotometry protocol as previously described (29, 30). Samples were prepared by adding 50 µL of each probe solution (final concentration = 75 µmol L^{-1}) to increasing volumes of HePC suspension to obtain concentrations ranging from 0 to 200 µmol L^{-1}. In parallel, references were obtained by replacing GUMBOS and ANS with HEPES buffer containing the same percentage of ACN as samples (< 3%). Both samples and references were incubated at 37 ºC for 30 min, after which absorption spectra were recorded in the spectral range of 300–600 nm. Experimental results were analyzed using the Excel spreadsheet (K_p calculator) developed by Magalhaes et al., which first subtracts each reference spectrum from the corresponding sample spectrum, and then generates the spectrum of derivatives (29). Second derivative values, measured at the wavelength where light scattering was negligible (λ = 348 nm), were plotted against the concentrations of HePC. The value of K_p (mol L^{-1}) was determined by fitting Eq. 1 to experimental data using a nonlinear least-squares regression method (29):

$$D_T = D_W + \frac{(D_L - D_W)K_p[L]}{1 + K_p[L]} \qquad (1)$$

where D_T, D_W, and D_L represent the second derivative intensities obtained from absorbance values of the total amount of GUMBOS, and from GUMBOS in the aqueous and lipid phases, respectively. The parameter [L] is the HePC concentration and K_p the partition

coefficient (both expressed in mol L^{-1}). The dimensionless value (logD) was calculated by dividing the molar partition coefficient by HePC molar volume (0.406 L mol^{-1}) (29).

5.2.5. Preparation of DMPC liposomes

Liposomes were prepared using a thin-film hydration method in combination with extrusion (31, 32). First, DMPC was dissolved into a mixture of chloroform and methanol (9:1, v/v), and then the organic solvent mixture was evaporated using a nitrogen stream and vacuum. The resulting lipid film was dispersed in HEPES buffer at 40 ºC (i.e., above DMPC main phase transition temperature) and vortexed to form multilamellar vesicles (MLVs) (33, 34). Subsequently, the MLVs suspension was extruded ten times through a polycarbonate filter with a pore size of 100 nm to obtain large unilamellar vesicles (LUVs).

5.2.6. Protein-membrane binding studies

Binding of proteins to liposomes was studied using fluorescence titration with ANS-based GUMBOS and the parent dye. Briefly, 20 µL of each protein sample (i.e., Lyz, Mb, α-ChT, and RNAse A) were mixed with 30 µL of DMPC LUVs and increasing volumes of ANS-based GUMBOS or parent ANS (final concentration = 0–80 µmol L^{-1}). HEPES buffer was added to achieve a final volume of 300 µL. Protein and lipid concentrations were fixed at 20 µg mL^{-1} and 10 µmol L^{-1}, respectively. References were prepared in the absence of GUMBOS or parent dye, which were replaced with HEPES buffer using the same percentage of organic solvent (ACN) as the corresponding samples. Following a 5 min incubation period at 37 ºC, fluorescence emission spectra were recorded from 380 to 650 nm, using 350 nm excitation. Absorbance values were measured at the excitation wavelength to correct fluorescence intensities using Eq. 2, minimizing inner filter effects (35). This effect results from protein absorption at the fluorophore's excitation wavelength and decreases the effective intensity of the exciting light beam, which ultimately leads to a reduction in the overall fluorescence intensity. Thus,

$$I_{corr} = I \frac{A_T}{A_F} \frac{1-10^{-A_F}}{1-10^{-A_T}} \qquad (2)$$

where I_{corr} is the corrected fluorescence intensity and I the experimental fluorescence. The parameters A_T and A_F represent the absorbance of the sample with and without protein, respectively.

Finally, the impact of proteins on the membrane binding of ANS-based GUMBOS was investigated by fitting corrected adsorption data to an equation derived from the Freundlich isotherm (Eq. 3) (36):

$$[\mathrm{GUMBOS}]_{\mathrm{B}} = \mathrm{C}_{\max}\frac{(\mathrm{K}_b[\mathrm{GUMBOS}]_{\infty})^{\mathrm{b}}}{1+(\mathrm{K}_b[\mathrm{GUMBOS}]_{\infty})^{\mathrm{b}}} \qquad (3)$$

where K_b is the binding constant, C_{max} is the maximum fluorescence intensity, b is the cooperativity of the binding process, and B and ∞ represent the concentrations of the bound and free forms of GUMBOS. This same equation was applied to experimental data obtained using the parent ANS dye.

5.3. Results and discussion

5.3.1. Structural characterization of the synthesized GUMBOS

The structures of ANS-based GUMBOS were determined using combined analysis of NMR (1D and 2D), HRMS, and FTIR data. Integration of peaks in ^{1}H NMR spectra confirmed the desired 1:1 stoichiometric ratio of cation to anion (Figs. S5.1, S5.5, and S5.9). Carbon signals (Figs. S5.2, S5.6, and S5.10) were assigned based on the results of ^{13}C spectra, HSQC, and HMBC experiments, which showed the expected ^{1}H–^{13}C single and multiple bond correlations (Figs. S5.3, S5.4, S5.7, S5.8, S5.11, and S5.12). Detailed NMR analysis can be found in Supplementary Material.

Mass peaks corresponding to N_{4444}^{+}, N_{6666}^{+}, and P_{4444}^{+} were observed in the positive ion mode at *m/z* values of 242.2848, 354.4109, and 259.2562, respectively. Analyses of the negative ion mode spectra confirmed the presence of ANS anion in all synthesized compounds. Moreover, there is good agreement between experimental and theoretical *m/z* values (Table S5.1). Peaks attributable to starting materials were found in the FTIR spectra of final products (Fig. S5.13), thus providing additional evidence of successful synthesis of ANS-based GUMBOS.

5.3.2. Optical properties of ANS-based GUMBOS

UV-Vis and fluorescence spectroscopies were used to investigate the optical properties of synthesized compounds. The absorption profile of ANS-based GUMBOS (Fig. 5.2A) shows two bands at 370 and 270 nm, with the band centered at 270 nm being blue-shifted by about 10 nm as compared to the parent ANS dye (37). Fluorescence maxima were observed around 470 nm (Fig. 5.2B). Changes in absorbance and fluorescence intensities are likely the result of structural differences between the cations used in GUMBOS syntheses. For

example, an increase in alkyl chain length of the ammonium cation from four to six carbons (N_{4444}^+ *versus* N_{6666}^+) led to a decrease in signal intensity. On the contrary, [N_{4444}][ANS] and [P_{4444}][ANS] exhibited similar absorbance and fluorescence values, thus suggesting that the cation's central atom (N or P) does not significantly affect the optical properties of synthesized GUMBOS (38).

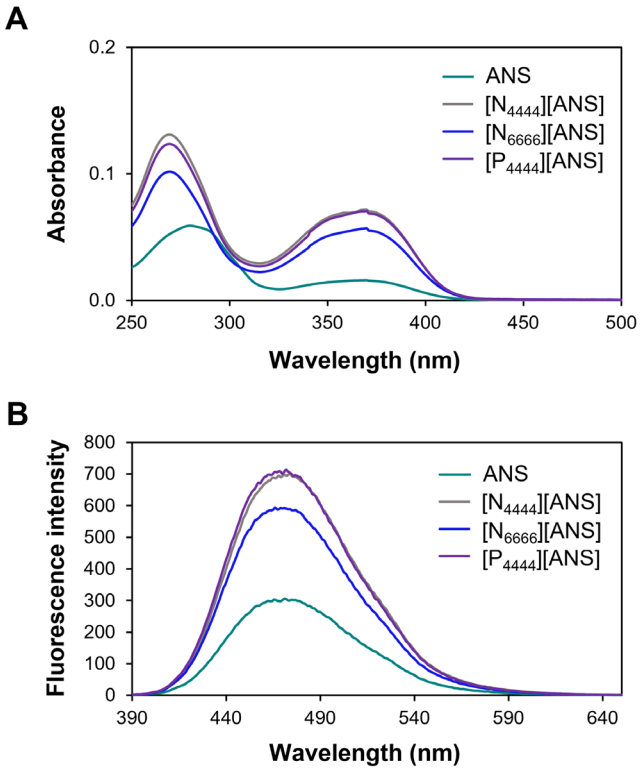

Fig. 5.2. (A) UV-Vis and (B) fluorescence spectra (λ_{exc} = 370 nm) of parent ANS dye and ANS-based GUMBOS at the concentration of 10 μmol L^{-1} in ACN.

5.3.3. Lipophilicity of the synthesized materials

The lipophilicity of ANS-based GUMBOS was evaluated through determination of micelle/buffer partition coefficients using derivative UV-Vis spectrophotometry. HePC micelles were chosen as membrane models due to simplicity and rapidity of their preparation, which further eliminates the need for potentially toxic organic solvents (e.g., octanol) (29, 39). In contrast to traditional octanol/water system, these biomimetic models not only consider hydrophobic interactions, but also hydrogen bonding, electrostatic, and dipole-dipole interactions (40-42). Moreover, this method does not require separation of lipid and aqueous phases, thus leading to better reproducibility. Application of derivative spectrophotometry helps to minimize effects of light scattering from HePC micelles and improves resolution of absorption bands (43, 44). Partition coefficients estimated for parent

ANS dye and ANS-based GUMBOS are provided in Table 5.1. Analyses of data shows that lipophilicity can be tuned using cation exchange, with increasing order of ANS < $[P_{4444}][ANS]$ < $[N_{4444}][ANS]$. Other studies have demonstrated the impact of cations on GUMBOS lipophilicity (24, 45). It is also worth noting that these differences in lipophilicity may affect probes' location within liposomes. The lipophilicity of $[N_{6666}][ANS]$ could not be determined due to solubility problems. For this reason, $[N_{6666}][ANS]$ GUMBOS was excluded from further analyses.

Table 5.1. Partition coefficients (expressed as K_p and logD) of parent ANS and ANS-based GUMBOS in micelles of HePC (pH 7.4, 37 ºC). Results are presented as the mean ± standard deviation of three replicates.

Compound	K_p (L mol^{-1})	logD (dimensionless)
ANS	3877 ± 572	3.98 ± 0.06
$[N_{4444}][ANS]$	95398 ± 12397	5.37 ± 0.06
$[P_{4444}][ANS]$	36967 ± 4112	4.96 ± 0.05

5.3.4. Thermal stability and melting point of ANS-based GUMBOS

Thermal behaviors of $[N_{4444}][ANS]$ and $[P_{4444}][ANS]$ GUMBOS were further investigated using TGA. Fig. S5.14 and Table S5.2 present the weight loss curves and temperatures at which GUMBOS weight was reduced by 50% ($T_{50\%}$), respectively. Similar to what has been reported for other ionic compounds, the thermal stability of ANS-based GUMBOS was found to be dependent on the cation employed, with $[P_{4444}][ANS]$ being the most stable (38, 46, 47).

Finally, melting points were determined using a capillary tube method. The lower melting points of GUMBOS as compared to parent ANS dye (Table S5.2) can be attributed to the relatively large size of N_{4444} and P_{4444} cations. Additionally, similarity of the results obtained for these two GUMBOS can be explained by the length of the cations' pendant alkyl side chains (e.g., *n* = 4) (26, 48, 49).

5.3.5. Protein-membrane binding studies

In order to study protein binding to biomimetic membranes (i.e., DMPC liposomes), a fluorescence titration with parent ANS dye and ANS-based GUMBOS was performed. Fluorescence changes have been used to investigate competition for the same membrane binding sites between proteins and parent ANS dye as the ANS dye is known to fluoresce when electrostatically bound to phospholipid headgroups (36, 50). However, it is tempting

to hypothesize that the synthesized GUMBOS could form additional interactions with membranes as a result of their tuned features (e.g., lipophilicity and hydrogen-bonding ability), leading to more distinguishable responses upon addition of proteins (45). Binding isotherms were obtained by plotting corrected fluorescence intensity, in the absence (Fig. 5.3A) and presence (Figs. 5.3B–5.3D) of proteins, as a function of increasing concentrations of parent ANS and ANS-based GUMBOS. The resulting curves were then fitted to Eq. 3, thus allowing calculation of binding constant (K_b), binding process cooperativity (b), and maximum fluorescence intensity (C_{max}). The estimated values for these parameters are presented in embedded tables of Fig. 5.3.

As shown in Fig. 5.3A, parent ANS dye and ANS-based GUMBOS independently reach saturation within the same concentration range. Despite such findings, GUMBOS exhibited slightly higher fluorescence signals than ANS dye, which could be the result of different interactions with liposomes, differences in GUMBOS structures, or even a combination of both. These results further suggest that it is possible to tune sensitivity by converting ANS into GUMBOS, similar to what has been found in previous works (38, 51). It is recognized that the present study was not an exhaustive investigation, and thus, as part of future work, a wider range of cations will be used to form ANS GUMBOS to investigate cation effects on tuning properties.

It is also worth noting that each protein (i.e., Lyz, Mb, α-ChT, and RNAse A) produced distinct fluorescence responses with parent ANS, $[N_{4444}][ANS]$, and $[P_{4444}][ANS]$ (Figs. 5.3B to 5.3D). Moreover, different fluorescence signals were obtained for the same protein when using these three probes. These findings suggest that membrane binding is affected by protein properties, such as surface hydrophobicity, which further corroborates previous reports (52, 53). For example, there was a decrease in the K_b value determined for $[N_{4444}][ANS]$ in the presence of RNAse A (the most hydrophilic among selected proteins), revealing low affinity of this protein for GUMBOS binding sites (14, 54). In turn, an observed increase in K_b when proteins are present suggests higher dissociation of fluorescent probes and, consequently, weaker membrane binding. The relative maintenance of values for b and C_{max} further indicates that proteins do not change binding rates of parent ANS or ANS-based GUMBOS, but rather hinders their access to membranes through a competitive mechanism (36).

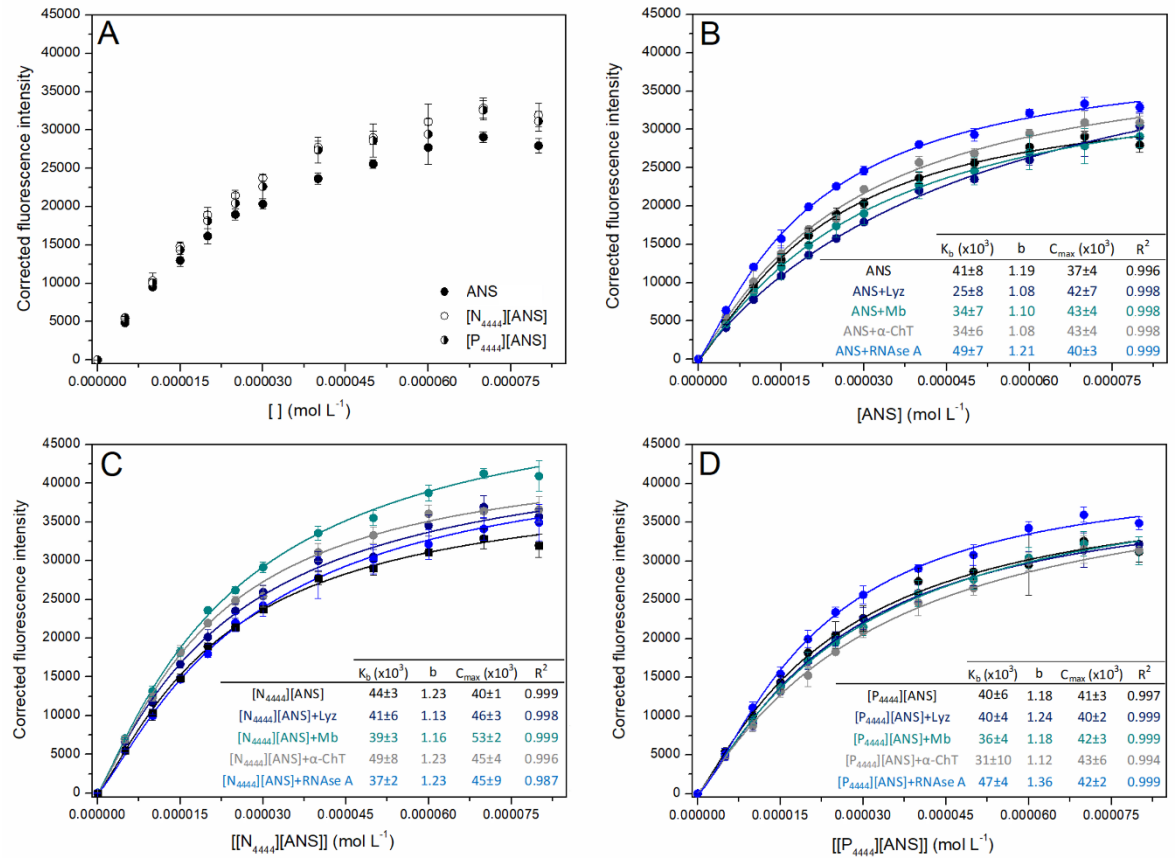

Fig. 5.3. Binding isotherms of ANS, [N_{4444}][ANS], and [P_{4444}][ANS] in the absence of proteins (A). Binding isotherms of ANS (B), [N_{4444}][ANS] (C), and [P_{4444}][ANS] (D) in the presence of Lyz, Mb, α-ChT, and RNAse A (20 μg mL^{-1}), along with the estimated binding parameters: binding constant (K_b), binding process cooperativity (b), maximum fluorescence intensity (C_{max}), and coefficient of determination (R^2). Results are presented as the mean and standard deviation of at least three independent assays, with lines representing the best fit to Eq. 3.

5.4. Conclusions

Herein, three novel ANS-based GUMBOS ([N_{4444}][ANS], [N_{6666}][ANS], and [P_{4444}][ANS]) were successfully synthesized from ANS dye via simple ion metatheses reactions, and their potential as fluorescent probes for study of protein-membrane binding was investigated. It was found that [N_{4444}][ANS] and [P_{4444}][ANS] display enhanced optical properties when compared to parent ANS and [N_{6666}][ANS]. These two GUMBOS also showed improved lipophilicity as well as good thermal stability, which is why they were selected for subsequent binding studies. Although membrane saturation occurred at the same concentration range for [N_{4444}][ANS], [P_{4444}][ANS], and ANS, slightly enhanced fluorescence signals were observed for synthesized GUMBOS as compared to parent ANS dye. Additionally, different responses were obtained for each probe upon addition of proteins, which demonstrates the

impact of protein properties (e.g., surface hydrophobicity) on their binding ability to lipid membranes. No major changes were observed in the binding process cooperativity (b) or maximum fluorescence intensity (C_{max}), which suggests that proteins and ANS-based GUMBOS synthesized herein compete for the same binding sites on membranes. Overall, these findings provide valuable information for design of ANS-based GUMBOS with improved properties as probes. Moreover, this GUMBOS-based strategy is operationally simple and requires relatively small concentrations of reagents, which makes it attractive for high-throughput analyses.

SUPPLEMENTARY MATERIAL

Characterization of EB-based GUMBOS

$[N_{4444}][ANS]$

^{1}H NMR (400.15 MHz, CD_3OD, ppm): δ 8.38 (dd, *J* 7.4, 1.5, 1H, H2); 7.91 (dd, *J* 8.2, 1.4, 1H, H4); 7.58 (dd, *J* 7.7, 1.4, 1H, H7); 7.44 (dd, *J* 8.0, 1.4, 1H, H5); 7.41–7.35 (m, 2H, H3 and H6); 7.20–7.15 (m, 4H, 2 x H10 and 2x H11); 6.81–6.76 (m, 1H, H12); 3.18–3.14 (m, 4 x 2H, -NC$\underline{H}_2$CH$_2$CH$_2$CH$_3$); 1.63–1.55 (m, 4 x 2H, -NCH$_2$C$\underline{H}_2$CH$_2$CH$_3$); 1.40–1.31 (m, 4 x 2H, -NCH$_2$CH$_2$C$\underline{H}_2$CH$_3$); 0.98 (t, *J* 7.4, 4 x 3H, -NCH$_2$CH$_2$CH$_2$C$\underline{H}_3$). ^{13}C NMR (100.62 MHz, CD_3OD, ppm): δ 146.2 (C9); 141.7 (C8); 141.1 (C1); 138.8 (C4a); 134.0 (C4); 129.9 (C11); 128.7 (C2); 127.2 (C6); 124.8 (C3); 124.0 (C8a); 122.6 (C5); 120.7 (C12); 118.5 (C10); 117.6 (C7); 59.4 (-N$\underline{C}$H$_2$CH$_2$CH$_2$CH$_3$); 24.8 (-NCH$_2\underline{C}$H$_2$CH$_2$CH$_3$); 20.7 (-NCH$_2$CH$_2\underline{C}$H$_2$CH$_3$); 13.9 (-NCH$_2$CH$_2$CH$_2\underline{C}$H$_3$).

$[N_{6666}][ANS]$

^{1}H NMR (400.15 MHz, CD_3OD, ppm): δ 8.38 (dd, *J* 7.4, 1.5, 1H, H2); 7.90 (dd, *J* 8.2, 1.4, 1H, H4); 7.57 (dd, *J* 7.7, 1.4, 1H, H7); 7.44 (dd, *J* 8.0, 1.4, 1H, H5); 7.38 (q, 2H, H3 and H6); 7.20–7.15 (m, 4H, 2 x H10 and 2x H11); 6.80–6.76 (m, 1H, H12); 3.20 (quint, *J* 5.1, 3.4, 4 x 2H, -NC$\underline{H}_2$CH$_2$CH$_2$CH$_2$CH$_2$CH$_3$); 1.64 (quint, *J* 7.4, 8.0, 4 x 2H, -NCH$_2$C$\underline{H}_2$CH$_2$CH$_2$CH$_2$CH$_3$); 1.34–1.39 (m, 12 x 2H, -NCH$_2$CH$_2$C$\underline{H}_2$C$\underline{H}_2$C$\underline{H}_2$CH$_3$); 0.93 (quint, *J* 7.4, 8.0, 4 x 3H, -NCH$_2$CH$_2$CH$_2$CH$_2$CH$_2$C$\underline{H}_3$). ^{13}C NMR (100.62 MHz, CD_3OD, ppm): δ 146.2 (C9); 141.1 and 141.6 (C1 + C8); 138.8 (C4a); 134.1 (C4); 130.0 (C11); 128.7 (C2); 127.2 (C6); 124.8 (C3); 124.0 (C8a); 122.6 (C5); 120.7 (C12); 118.5 (C10); 117.7 (C7); 59.6 (-N$\underline{C}$H$_2$CH$_2$CH$_2$CH$_2$CH$_2$CH$_3$); 32.4 (-NCH$_2$CH$_2$CH$_2$CH$_2\underline{C}$H$_2$CH$_3$); 27.0 (-NCH$_2$CH$_2\underline{C}$H$_2$CH$_2$CH$_2$CH$_3$); 23.5 (-NCH$_2$CH$_2$CH$_2\underline{C}$H$_2$CH$_2$CH$_3$); 22.7 (-NCH$_2\underline{C}$H$_2$CH$_2$CH$_2$CH$_2$CH$_3$); 14.3 (-NCH$_2$CH$_2$CH$_2$CH$_2$CH$_2\underline{C}$H$_3$).

$[P_{4444}][ANS]$

^{1}H NMR (400.15 MHz, CD_3OD, ppm): 8.38 (dd, *J* 7.4, 1.5, 1H, H2); 7.90 (dd, *J* 8.2, 1.5, 1H, H4); 7.57 (dd, *J* 7.6, 1.2, 1H, H7); 7.44 (dd, *J* 8.1, 1.5, 1H, H5); 7.40–7.35 (m, 2H, H3 and H6); 7.20–7.15 (m, 4H, 2 x H10 and 2x H11); 6.80–6.76 (m, 1H, H12); 2.15 (bs, 4 x 2H, -PC$\underline{H}_2$CH$_2$CH$_2$CH$_3$); 1.50 (bs, 4 x 2H, -PCH$_2$CH$_2$C$\underline{H}_2$CH$_3$ and 4 x 2H, -PCH$_2$C$\underline{H}_2$CH$_2$CH$_3$); 0.97 (bs, 4 x 3H, -PCH$_2$CH$_2$CH$_2$C$\underline{H}_3$). ^{13}C NMR (100.62 MHz, CD_3OD, ppm): δ 146.2 (C9); 141.7 (C8); 141.2 (C1); 138.8 (C4a); 134.1 (C4); 130.0 (C11); 128.7 (C2); 127.2 (C6); 124.8

(C3); 124.1 (C8a); 122.6 (C5); 120.7 (C12); 118.5 (C10); 117.6 (C7); 25.0–24.3 (-$PCH_2\underline{C}H_2\underline{C}H_2CH_3$); 19.3–18.9 (-$P\underline{C}H_2CH_2CH_2CH_3$); 13.6 (-$PCH_2CH_2CH_2\underline{C}H_3$).

Analysis of ^{1}H NMR spectra of [N_{4444}][ANS] (Fig. S5.1) revealed two sets of signals: one corresponding to the aliphatic protons of N_{4444}^{+} and the other to the aromatic protons of ANS anion. Resonance signals of methyl protons at the end of the cation alkyl side chains appeared at 0.98 ppm and aliphatic ethylene protons were seen between 1.63 and 1.31 ppm. Protons registered at δ = 3.18–3.14 ppm were assigned to the ethylene groups directly bound to the central nitrogen atom. The first set of aromatic protons corresponds to the phenyl ring of ANS^{-} and signals in the low field area of the ^{1}H spectrum were attributed to protons of the naphthalene group. The recorded signals were in good agreement with assignments reported in the literature for ANS (55, 56).

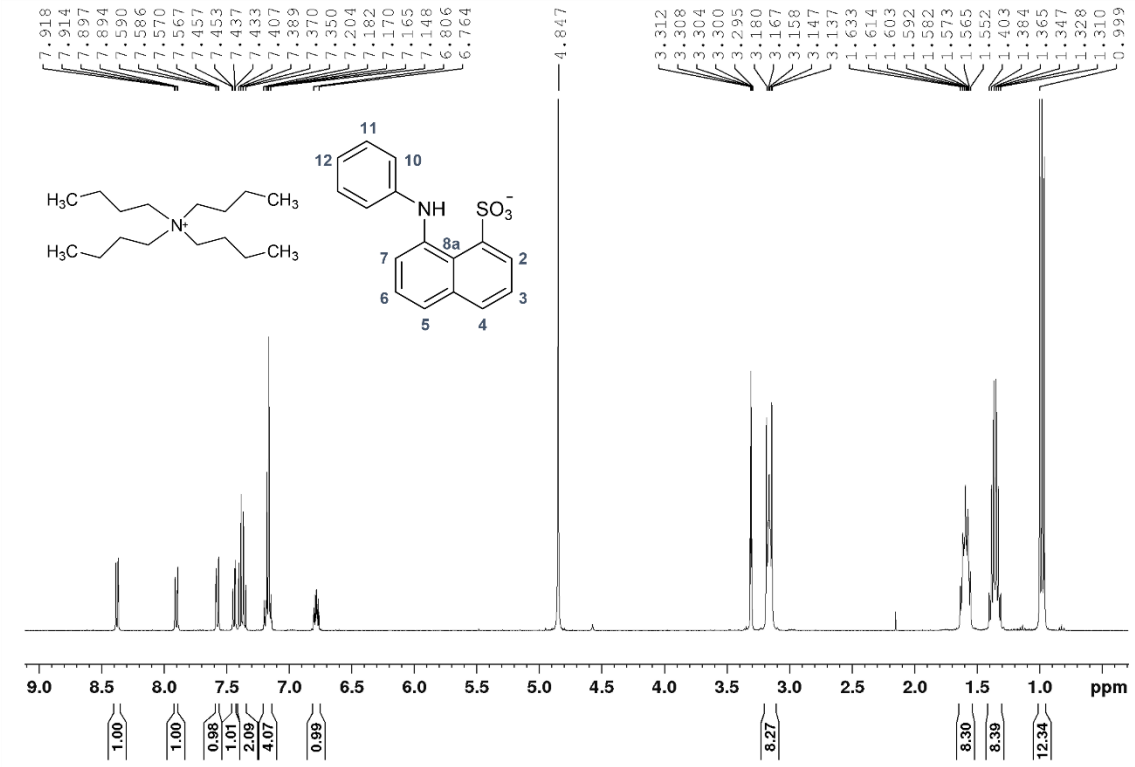

Fig. S5.1. ^{1}H NMR spectrum of [N_{4444}][ANS].

Carbon signals in the range of 59.4–13.9 ppm (Fig. S5.2) were directly assigned as they showed HSQC correlations with the respective protons in the cation (Fig. S5.3). Resonance signals of carbons from ANS^{-} were attributed based on their correlation with protons in HSQC and HMBC spectra (Figs. S5.3 and S5.4, respectively). Experimental chemical shift values were similar to the expected ones (55, 56).

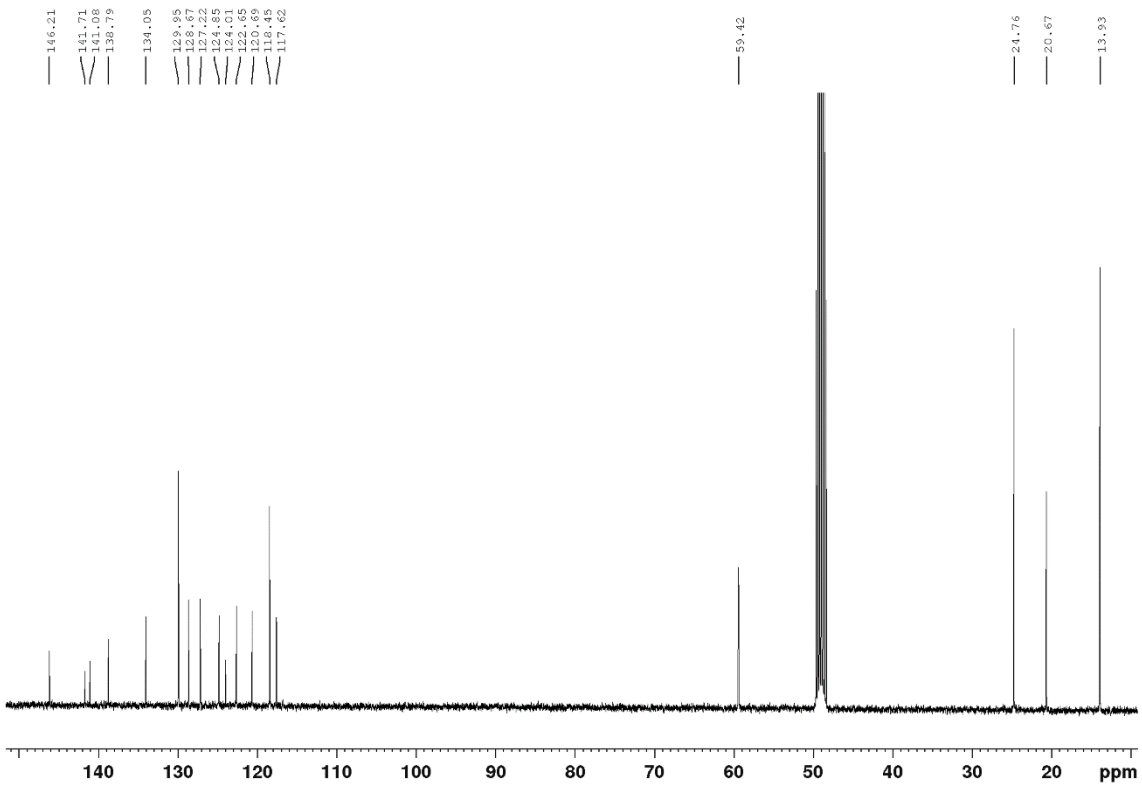

Fig. S5.2. ^{13}C NMR spectrum of $[N_{4444}][ANS]$ GUMBOS.

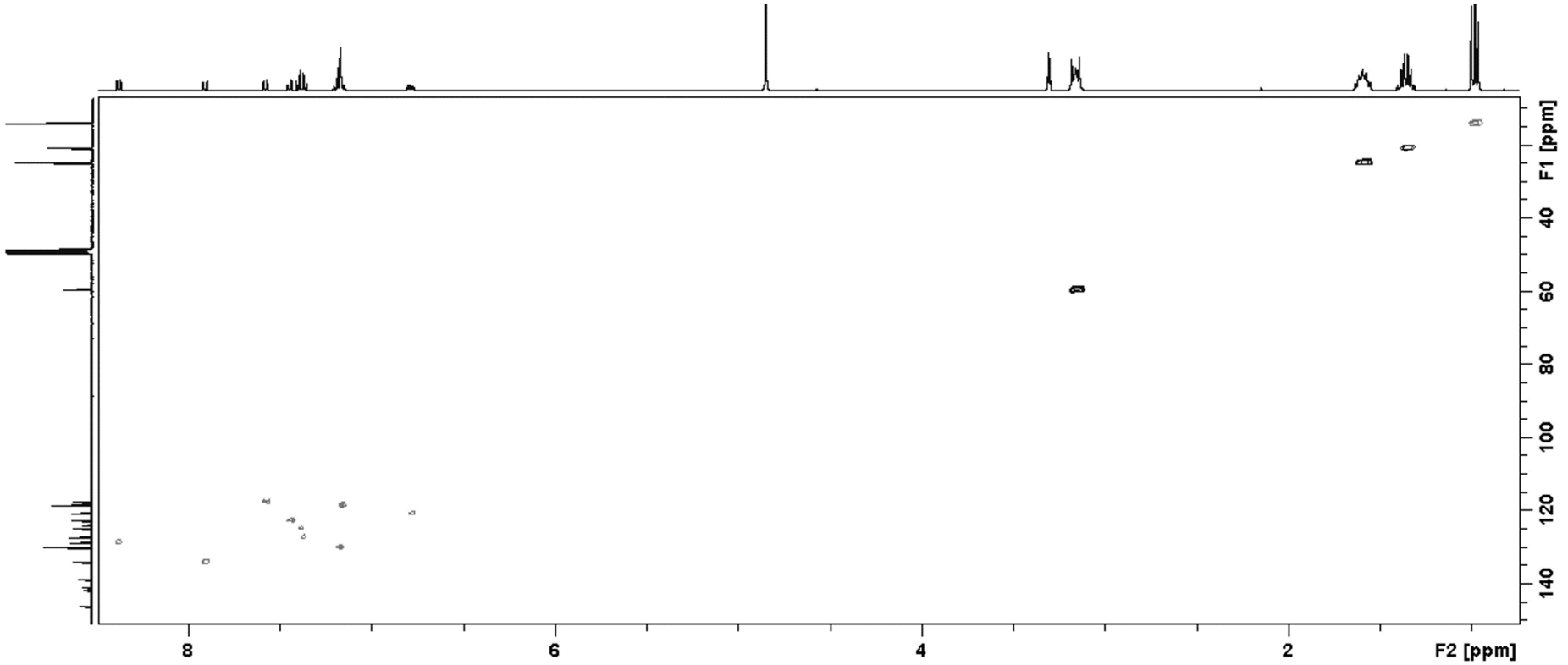

Fig. S5.3. HSQC spectrum of $[N_{4444}][ANS]$.

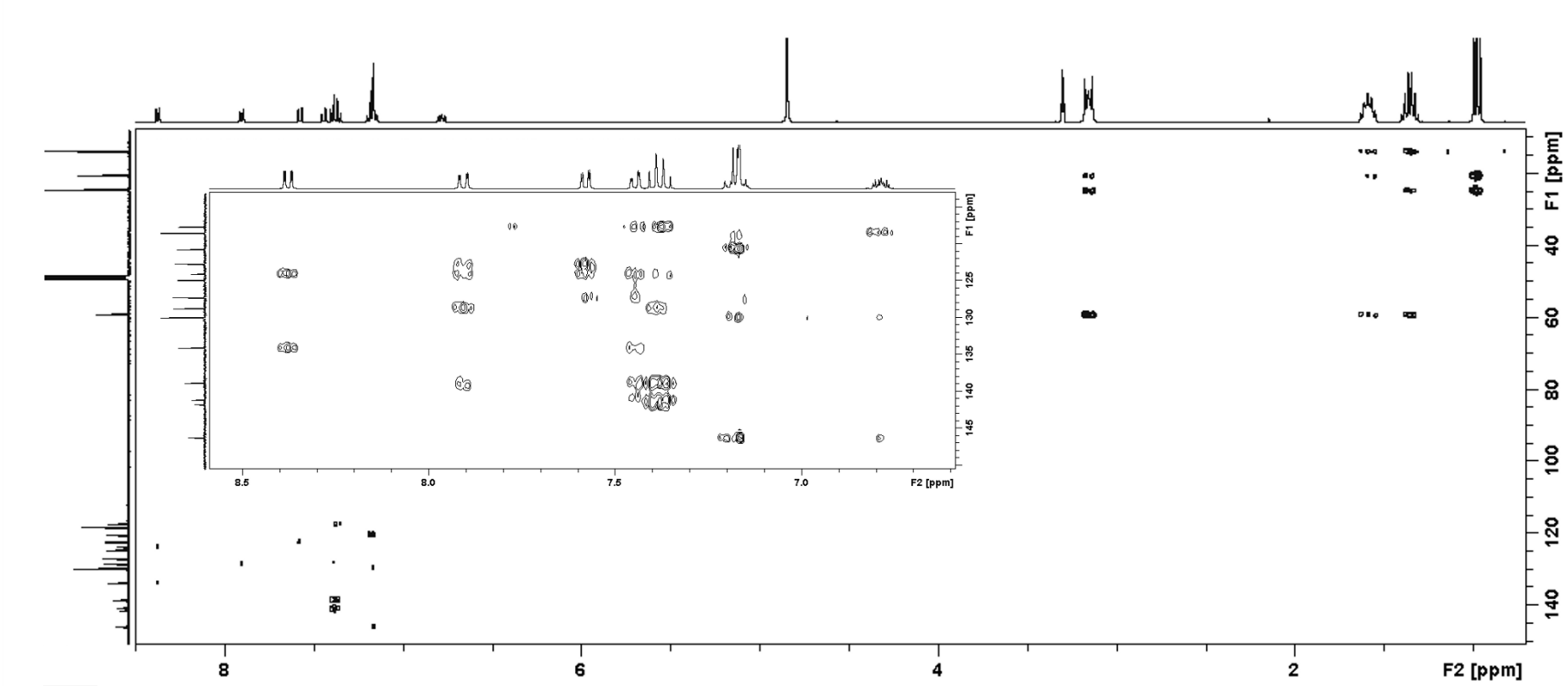

Fig. S5.4. HMBC spectrum of [N_{4444}][ANS] and respective inset.

The ^{1}H and ^{13}C signals of $[N_{6666}][ANS]$ GUMBOS (Figs. S5.5 and S5.6, respectively) were quite similar to those found for $[N_{4444}][ANS]$, which is not surprising due to the chemical resemblance between these compounds, with the only difference being the length of alkyl side chains (six *versus* four carbons).

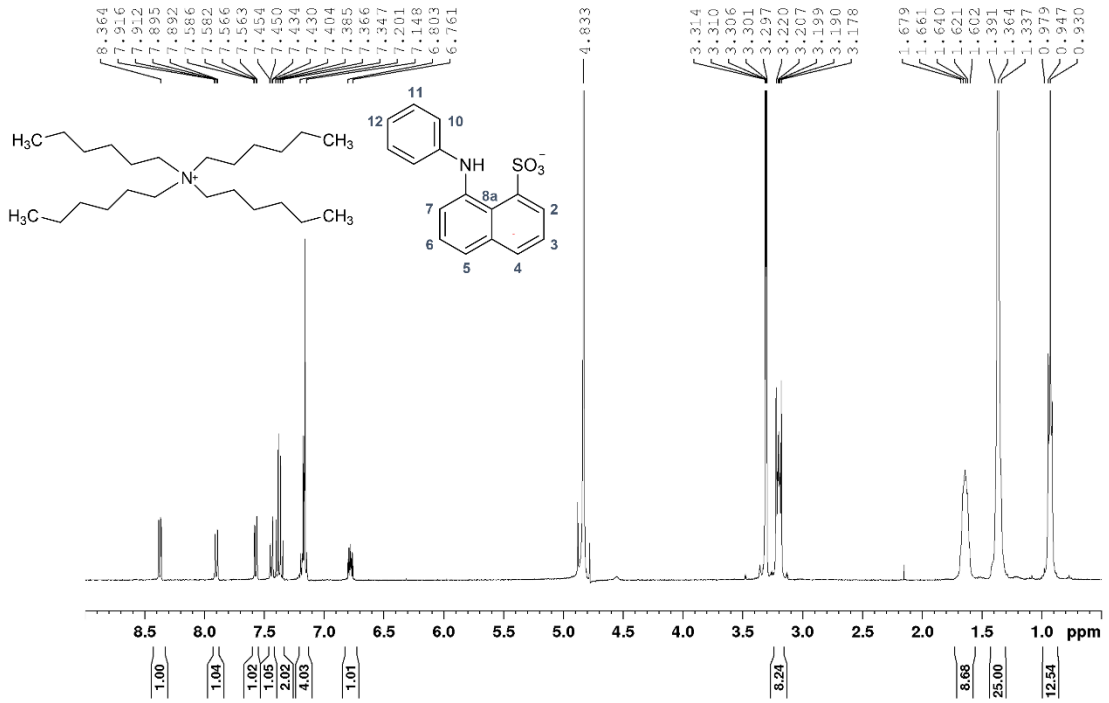

Fig. S5.5. ^{1}H spectrum of $[N_{6666}][ANS]$ GUMBOS.

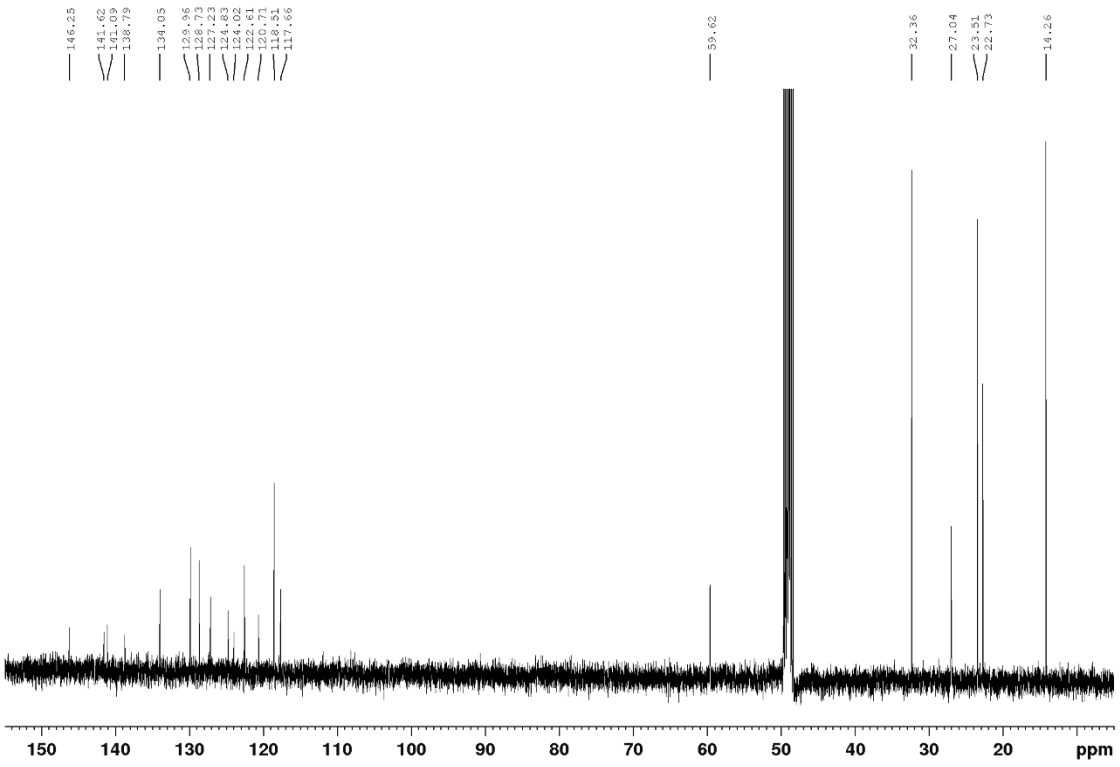

Fig. S5.6. ^{13}C spectrum of $[N_{6666}][ANS]$ in CD_3OD.

Aliphatic protons and carbons appeared at 3.20–0.93 and 59.6–14.3 ppm, respectively. Carbons were assigned based on their HSQC and HMBC correlations (Figs. S5.7 and S5.8, respectively). Additionally, the aromatic peaks of ANS anion were found to be virtually equal to those of $[N_{4444}][ANS]$, and in line with previously reported values (55, 56).

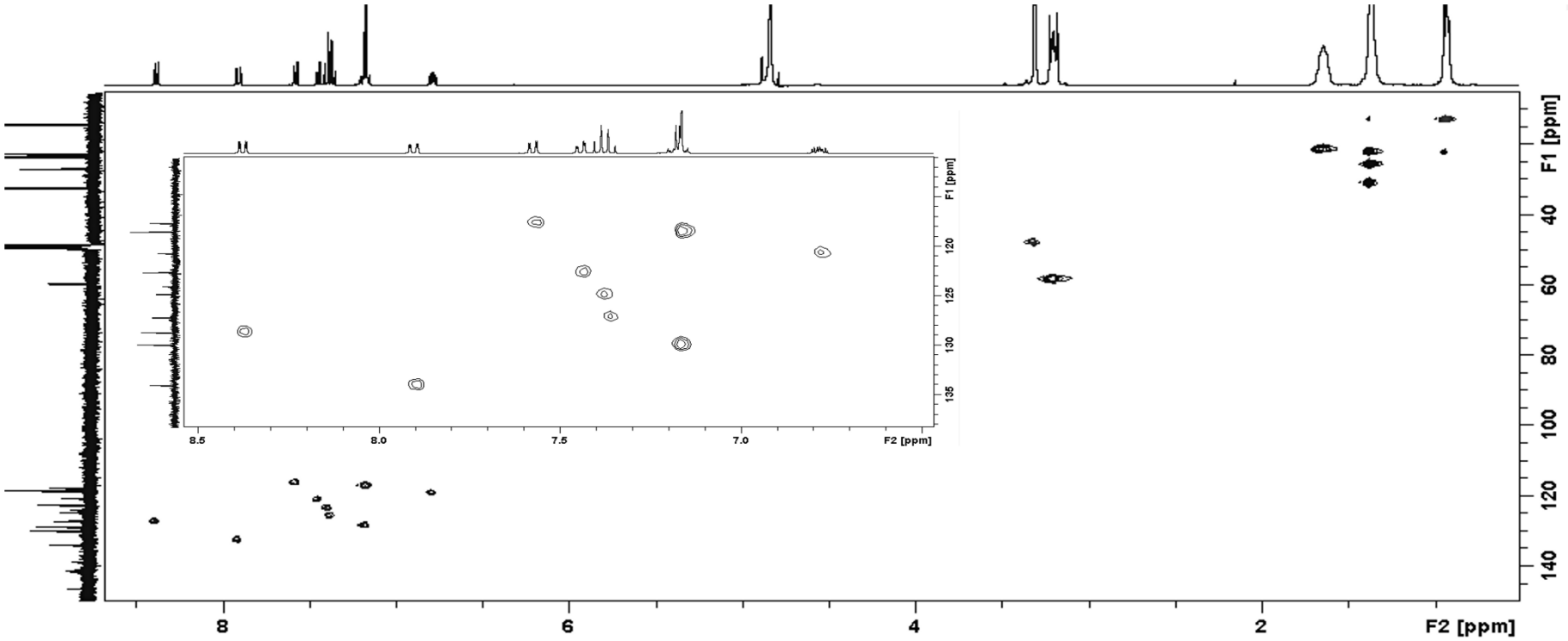

Fig. S5.7. HSQC spectrum of [N_{6666}][ANS] GUMBOS and respective inset.

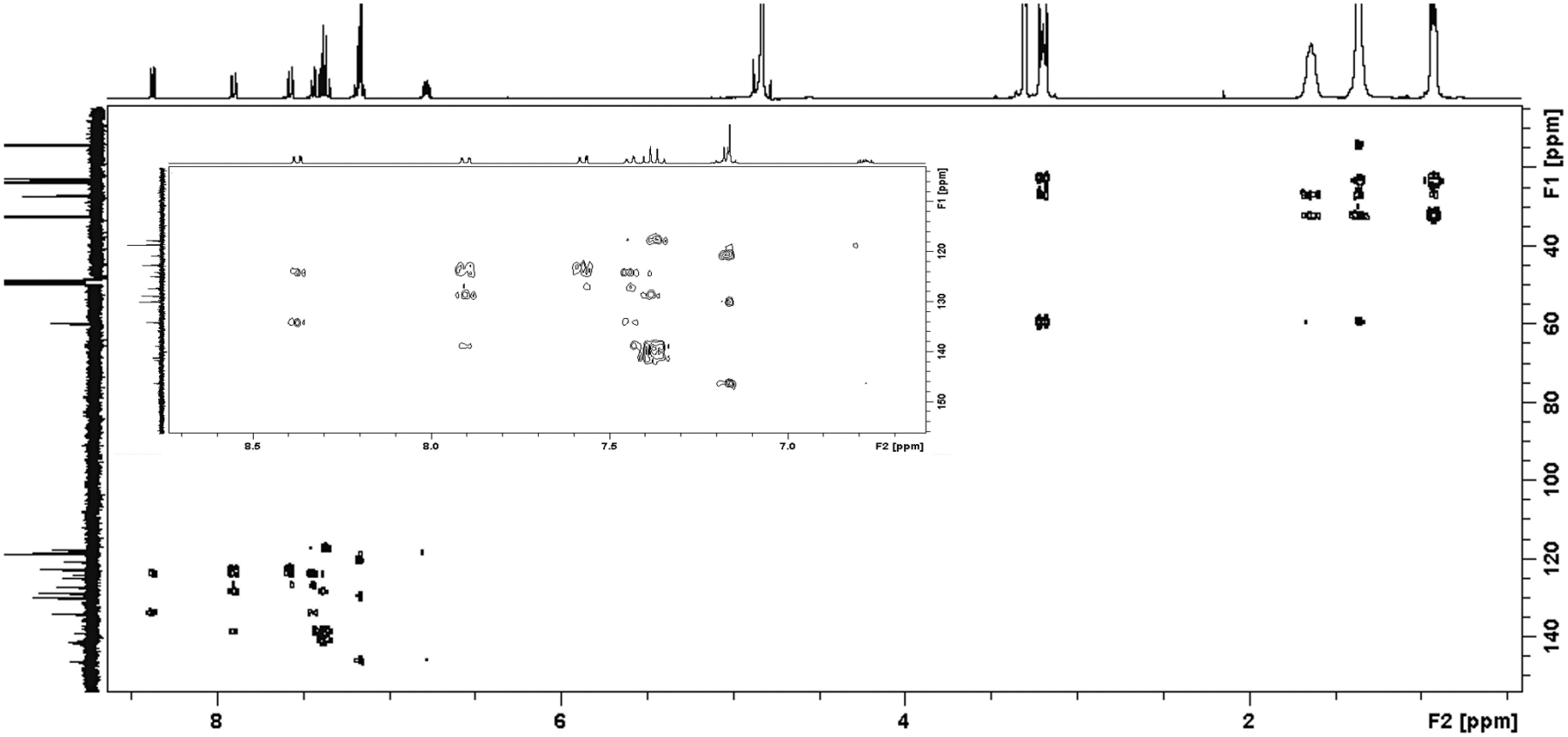

Fig. S5.8. HMBC spectrum of [N_{6666}][ANS] and respective inset.

Regarding [P_{4444}][ANS] GUMBOS, the terminal -CH_3 and -CH_2- protons of cation alkyl side chains appeared as broad singlets at δ = 0.97 and 2.15–1.50 ppm, respectively (Fig. S5.9). These signals were found at lower chemical shift values than those for [N_{4444}][ANS]. Moreover, resonance signals of protons in the middle of the alkyl chain (-$PCH_2C\underline{H}_2C\underline{H}_2CH_3$) have similar neighboring, thus appearing as a single peak in the ^{1}H spectrum. The stronger electron-withdrawing effect of nitrogen atom compared to phosphorus in the cation can explain the different chemical shifts of -NCH_2- protons *versus* -PCH_2- (from 3.18–3.14 to 2.15 ppm, respectively). Similar to [N_{4444}][ANS] GUMBOS, aromatic peaks were assigned to the protons of ANS anion. Chemical shifts were very close and in line with reported values (55, 56).

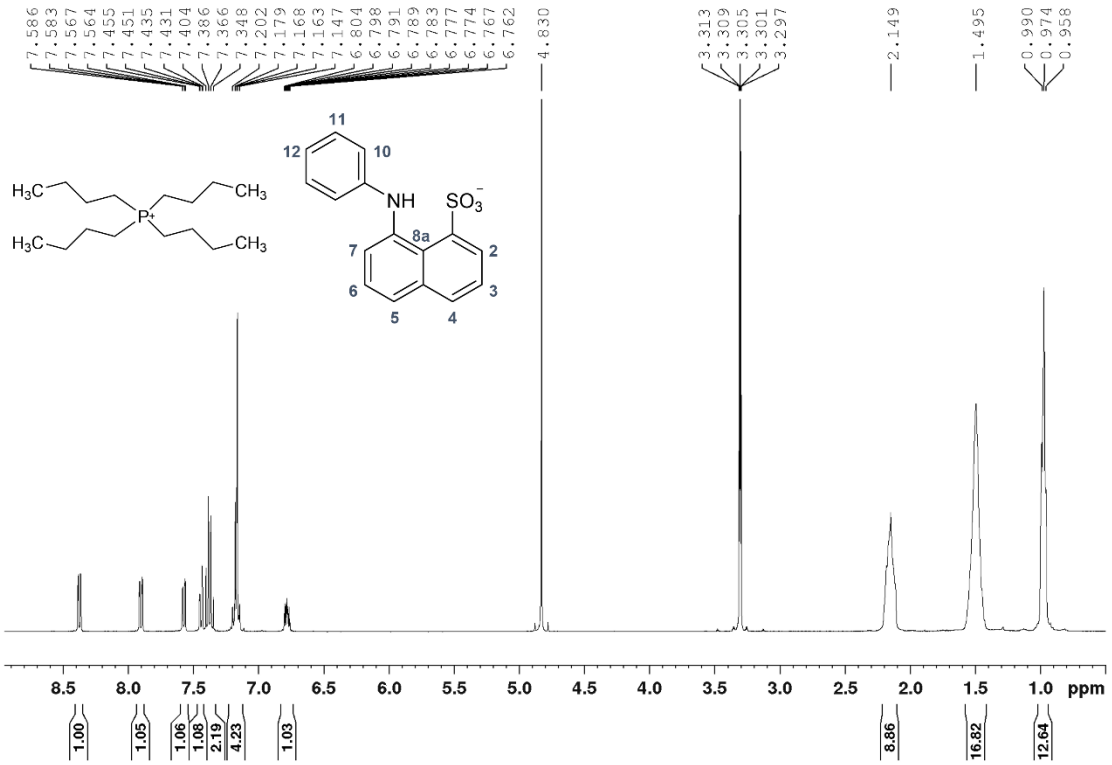

Fig. S5.9. ^{1}H spectrum of [P_{4444}][ANS].

Regarding the assignment of carbons present in [P_{4444}][ANS] GUMBOS (Fig. S5.10), the HSQC spectrum (Fig. S5.11) showed peaks from 25.0 to 13.6 ppm, which were correlated with signals attributed to protons of the aliphatic chains of P_{4444}^+. Once again, carbons in the middle of the chain (-$PCH_2C\underline{H}_2C\underline{H}_2CH_3$) had similar neighboring and appeared closer in the ^{13}C spectrum. The chemical shift is significantly lower than that verified for similar carbons in the [N_{4444}][ANS] GUMBOS. For example, the signal assigned to carbons of -

PCH_2- groups is shifted to a higher field, varying from 59.4 ppm in $[N_{4444}][ANS]$ to approximately 19 ppm in $[P_{4444}][ANS]$. This difference can be justified by the influence of cation's central atom (N or P).

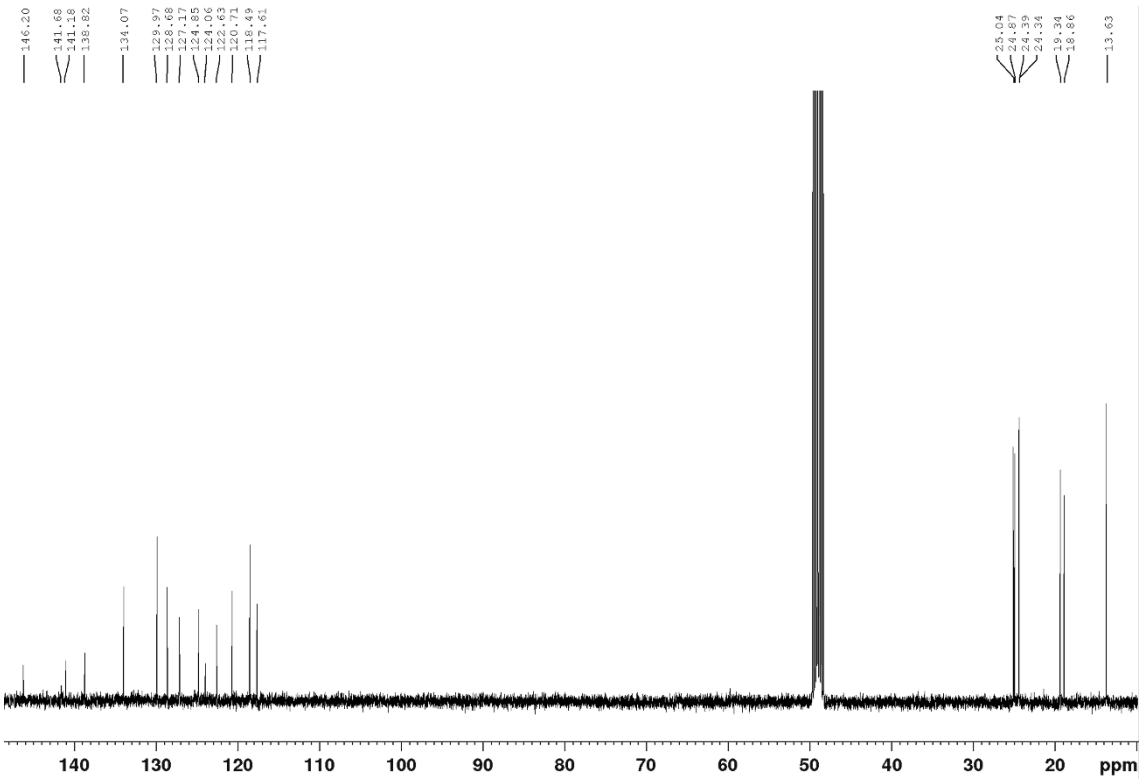

Fig. S5.10. ^{13}C spectrum of $[P_{4444}][ANS]$ GUMBOS.

Analysis of HSQC and HMBC spectra (Figs. S5.11 and S5.12) allowed the unequivocal assignment of peaks attributed to carbons present in the ANS anion, which appeared in the low-field region. Their chemical shift values were in good agreement with the values described in the literature (55, 56).

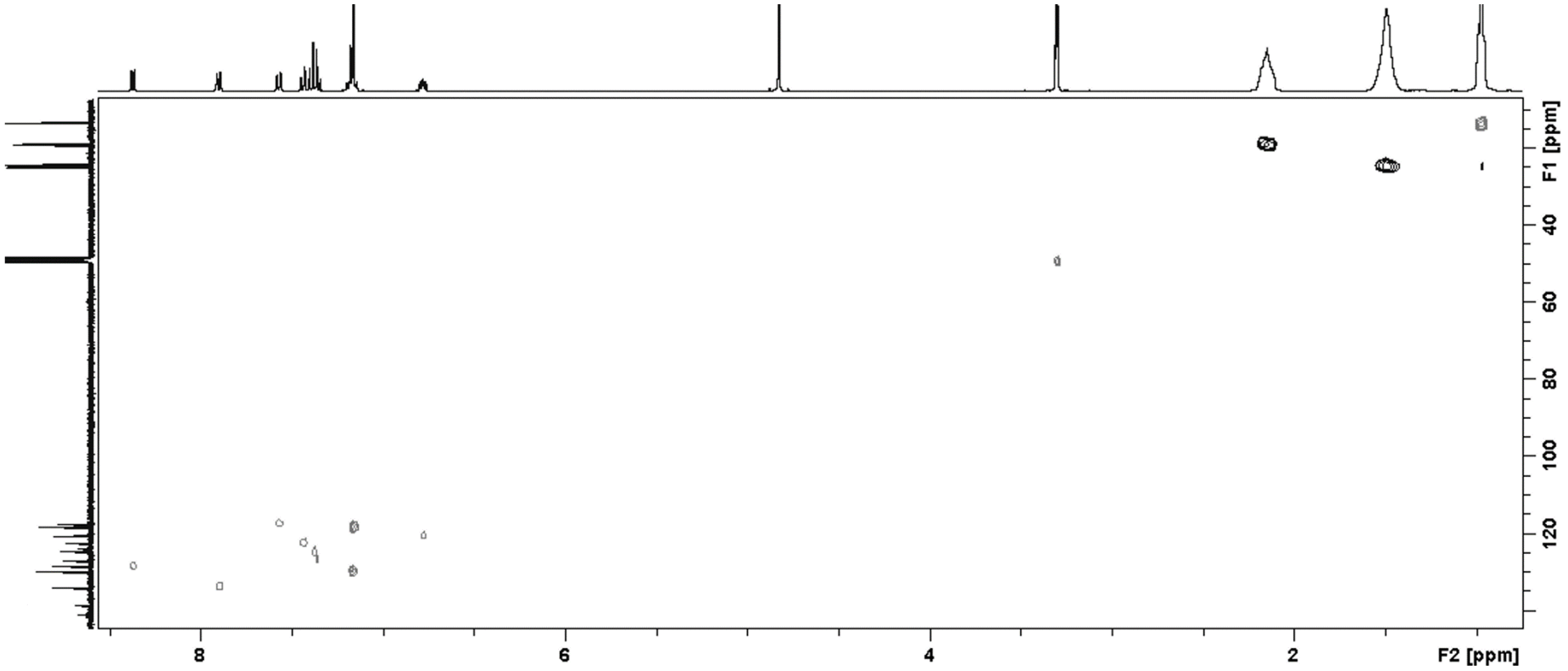

Fig. S5.11. HSQC spectrum of $[P_{4444}][ANS]$.

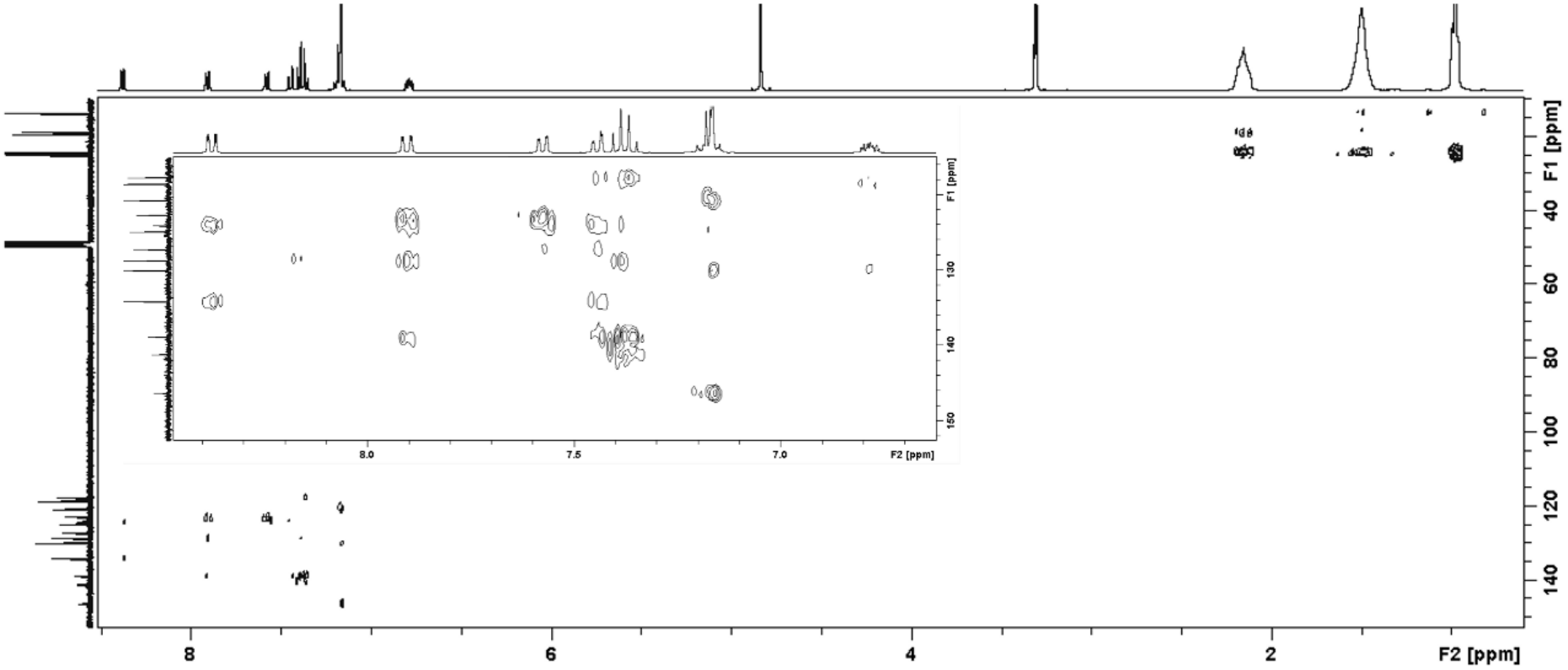

Fig. S5.12. HMBC spectrum of [P_{4444}][ANS] and respective inset.

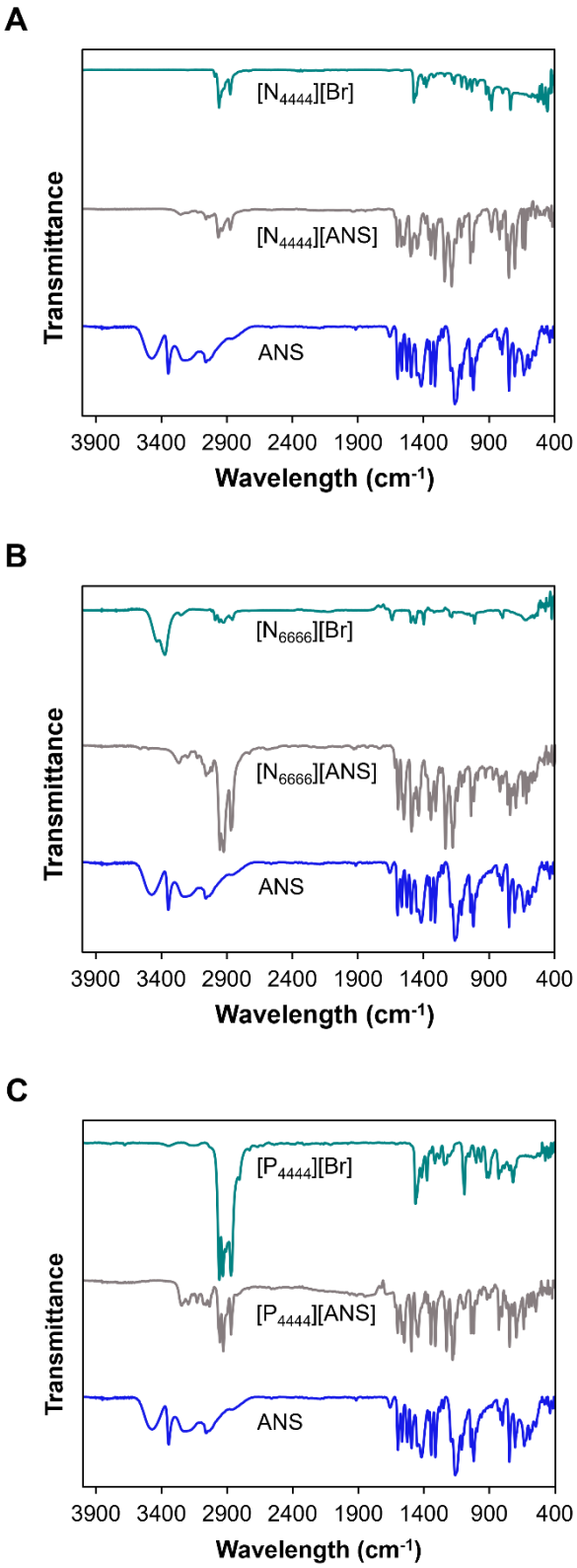

Fig. S5.13. Overlay of FTIR spectra of starting materials (green and blue) and resulting GUMBOS (grey): (A) $[N_{4444}][ANS]$, (B) $[N_{6666}][ANS]$, and (C) $[P_{4444}][ANS]$.

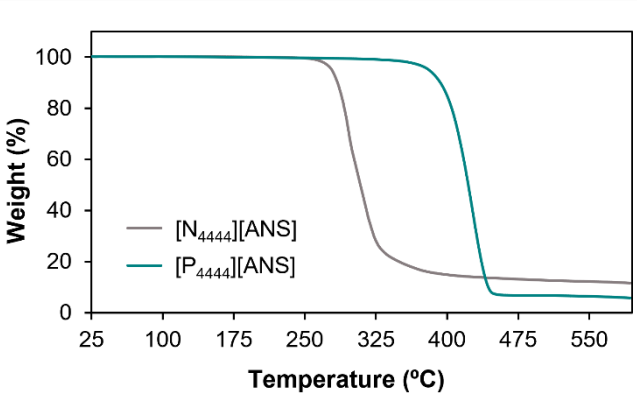

Fig. S5.14. TGA spectra of ANS-based GUMBOS.

Table S5.1. ESI-MS analysis of synthesized compounds.

GUMBOS	Ionic formula		ESI-MS (positive mode)		ESI-MS (negative mode)	
	Cation	Anion	Expected mass (*m/z*)	Obtained mass (*m/z*)	Expected mass (*m/z*)	Obtained mass (*m/z*)
$[N_{4444}][ANS]$	$C_{16}H_{36}N^+$		242.2842	242.2848		298.0548
$[N_{6666}][ANS]$	$C_{24}H_{52}N^+$	$C_{16}H_{12}NO_3S^-$	354.4094	354.4109	298.0543	298.0547
$[P_{4444}][ANS]$	$C_{16}H_{36}P^+$		259.2549	259.2562		298.0547

Table S5.2. Half weight loss temperature ($T_{50\%}$) and melting point of ANS-based GUMBOS.

GUMBOS	$T_{50\%}$ (ºC)	Melting point (ºC)[a]
$[N_{4444}][ANS]$	308	108
$[P_{4444}][ANS]$	422	95

[a] For $[NH_4][ANS]$, m.p. = 237 ºC (TCI America).

References

1. Goni FM. Non-permanent proteins in membranes: when proteins come as visitors (review). Mol Membr Biol. 2002;19(4):237-45.

2. Whited AM, Johs A. The interactions of peripheral membrane proteins with biological membranes. Chem Phys Lipids. 2015;192:51-9.

3. Wymann MP, Schneiter R. Lipid signalling in disease. Nat Rev Mol Cell Biol. 2008;9(2):162-76.

4. Muller MP, Jiang T, Sun C, Lihan MY, Pant S, Mahinthichaichan P, et al. Characterization of Lipid-Protein Interactions and Lipid-Mediated Modulation of Membrane Protein Function through Molecular Simulation. Chem Rev. 2019;119(9):6086-161.

5. Wood WG, Eckert GP, Igbavboa U, Muller WE. Amyloid beta-protein interactions with membranes and cholesterol: causes or casualties of Alzheimer's disease. Biochim Biophys Acta-Biomembr. 2003;1610(2):281-90.

6. Peters I, Igbavboa U, Schutt T, Haidari S, Hartig U, Rosello X, et al. The interaction of beta-amyloid protein with cellular membranes stimulates its own production. Biochim Biophys Acta-Biomembr. 2009;1788(5):964-72.

7. Zhao HX, Lappalainen P. A simple guide to biochemical approaches for analyzing protein-lipid interactions. Mol Biol Cell. 2012;23(15):2823-30.

8. Czogalla A, Grzybek M, Jones W, Coskun U. Validity and applicability of membrane model systems for studying interactions of peripheral membrane proteins with lipids. Biochim Biophys Acta Mol Cell Biol Lipids. 2014;1841(8):1049-59.

9. Ferreira H, Lucio M, Lima JLFC, Matos C, Reis S. Effects of diclofenac on EPC liposome membrane properties. Anal Bioanal Chem. 2005;382(5):1256-64.

10. Lucio M, Ferreira H, Lima JLFC, Reis S. Interactions between oxicams and membrane bilayers: an explanation for their different COX selectivity. Med Chem. 2006;2:447–56.

11. Pinheiro M, Arede M, Caio JM, Moiteiro C, Lucio M, Reis S. Drug-membrane interaction studies applied to N '-acetyl-rifabutin. Eur J Pharm Biopharm. 2013;85(3):597-603.

12. Escriba PV, Gonzalez-Ros JM, Goni FM, Kinnunen PKJ, Vigh L, Sanchez-Magraner L, et al. Membranes: a meeting point for lipids, proteins and therapies. J Cell Mol Med. 2008;12(3):829-75.

13. Deleu M, Crowet JM, Nasir MN, Lins L. Complementary biophysical tools to investigate lipid specificity in the interaction between bioactive molecules and the plasma membrane: A review. Biochim Biophys Acta-Biomembr. 2014;1838(12):3171-90.

14. Cardamone M, Puri NK. Spectrofluorimetric assessment of the surface hydrophobicity of proteins. Biochem J. 1992;282:589-93.
15. Gasymov OK, Glasgow BJ. ANS fluorescence: Potential to augment the identification of the external binding sites of proteins. BBA-Proteins Proteomics. 2007;1774(3):403-11.
16. Hawe A, Sutter M, Jiskoot W. Extrinsic fluorescent dyes as tools for protein characterization. Pharm Res. 2008;25(7):1487-99.
17. Pohl WG, Teissié J. The use of fluorescent probes for studying the interaction of proteins with black lipid membranes. Z Naturforsch C Biosci. 1975;30:147-51.
18. Sankhala RS, Damai RS, Swamy MJ. Correlation of Membrane Binding and Hydrophobicity to the Chaperone-Like Activity of PDC-109, the Major Protein of Bovine Seminal Plasma. PLoS One. 2011;6(3):13.
19. Azzi A. The application of fluorescent probes in membrane studies. Q Rev Biophys. 1975;8:237-316.
20. Kachel K, Asuncion-Punzalan E, London E. The location of fluorescence probes with charged groups in model membranes. Biochim Biophys Acta-Biomembr. 1998;1374(1-2):63-76.
21. Wang N, Faber EB, Georg GI. Synthesis and Spectral Properties of 8-Anilinonaphthalene-1-sulfonic Acid (ANS) Derivatives Prepared by Microwave-Assisted Copper(0)-Catalyzed Ullmann Reaction. ACS Omega. 2019;4(19):18472-7.
22. Polak J, Graz M, Wlizlo K, Szalapata K, Kapral-Piotrowska J, Paduch R, et al. Bioactive Properties of a Novel Antibacterial Dye Obtained from Laccase-Mediated Oxidation of 8-Anilino-1-naphthalenesulfonic Acid. Molecules. 2022;27(2):16.
23. Perez RL, Ayala CE, Warner IM. Group of Uniform Materials Based on Organic Salts (GUMBOS): A Review of Their Solid State Properties and Applications. In: Sohel Murshed SM, editor. Ionic Liquids - Thermophysical Properties and Applications: IntechOpen; 2021.
24. Azevedo AMO, Sousa C, Chen M, Ayala CE, Perez RL, Santos JLM, et al. Protein discrimination using erythrosin B-based GUMBOS in combination with UV-Vis spectroscopy and chemometrics. Talanta. 2022;240:11.
25. Warner IM, El-Zahab B, Siraj N. Perspectives on Moving Ionic Liquid Chemistry into the Solid Phase. Anal Chem. 2014;86(15):7184-91.
26. Azevedo AMO, Santos JLM, Warner IM, Saraiva MLMFS. GUMBOS and nanoGUMBOS in chemical and biological analysis: A review. Anal Chim Acta. 2020;1133:180-98.
27. Chen M, Bhattarai N, Cong MY, Perez RL, McDonough KC, Warner IM. Mitochondria targeting IR780-based nanoGUMBOS for enhanced selective toxicity towards cancer cells. RSC Adv. 2018;8(55):31700-9.

28. Bhattarai N, Chen M, Perez RL, Ravula S, Strongin RM, McDonough K, et al. Comparison of Chemotherapeutic Activities of Rhodamine-Based GUMBOS and NanoGUMBOS. Molecules. 2020;25(14):13.
29. Magalhaes LM, Nunes C, Lucio M, Segundo MA, Reis S, Lima JLFC. High-throughput microplate assay for the determination of drug partition coefficients. Nat Protoc. 2010;5(11):1823-30.
30. Azevedo AMO, Costa SPF, Dias AFV, Marques AHO, Pinto PCAG, Bica K, et al. Anti-inflammatory choline based ionic liquids: Insights into their lipophilicity, solubility and toxicity parameters. J Mol Liq. 2017;232:20-6.
31. Pereira-Leite C, Nunes C, Bozelli JC, Schreier S, Kamma-Lorger CS, Cuccovia IM, et al. Can NO-indomethacin counteract the topical gastric toxicity induced by indomethacin interactions with phospholipid bilayers? Colloid Surf B-Biointerfaces. 2018;169:375-83.
32. Zhang H. Thin-Film Hydration Followed by Extrusion Method for Liposome Preparation. In: D'Souza GGM, Zhang H, editors. Liposomes: Methods and Protocols. 2622. 3rd eds ed. New York: Humana; 2023. p. 57-63.
33. Taylor KMG, Morris RM. Thermal analysis of phase transition behaviour in liposomes. Thermochim Acta. 1995;248:289-301.
34. Lucio M, Ferreira H, Lima JLFC, Matos C, de Castro B, Reis S. Influence of some anti-inflammatory drugs in membrane fluidity studied by fluorescence anisotropy measurements. Phys Chem Chem Phys. 2004;6(7):1493-8.
35. Coutinho A, Prieto M. Ribonuclease T1 and alcohol dehydrogenase fluorescence quenching by acrylamide: A laboratory experiment for undergraduate students. J Chem Educ. 1993;70(5):425-8.
36. Pereira-Leite C, Carneiro C, Soares JX, Afonso C, Nunes C, Lucio M, et al. Biophysical characterization of the drug-membrane interactions: The case of propranolol and acebutolol. Eur J Pharm Biopharm. 2013;84(1):183-91.
37. Barros AEB, Carvalho FAO, Alves FR, Carvalho JWP, Tabak M. Denaturant effects on HbGp hemoglobin as monitored by 8-anilino-1-naphtalene-sulfonic acid (ANS) probe. Int J Biol Macromol. 2015;74:327-36.
38. Vaughan SR, Speller NC, Chhotaray P, McCarter KS, Siraj N, Perez RL, et al. Class specific discrimination of volatile organic compounds using a quartz crystal microbalance based multisensor array. Talanta. 2018;188:423-8.
39. de Castro B, Gameiro P, Lima JLFC, Matos C, Reis S. Interaction of drugs with hexadecylphosphocholine micelles. Derivative spectroscopy, acid-base and solubility studies. Mater Sci Eng C-Biomimetic Supramol Syst. 2001;18(1-2):71-8.

40. de Castro B, Gameiro P, Lima JLFC, Matos C, Reis S. A fast and reliable spectroscopic method for the determination of membrane-water partition coefficients of organic compounds. Lipids. 2001;36(1):89-96.
41. Ferreira H, Lucio M, de Castro B, Gameiro P, Lima JLFC, Reis S. Partition and location of nimesulide in EPC liposomes: a spectrophotometric and fluorescence study. Anal Bioanal Chem. 2003;377(2):293-8.
42. Brittes J, Lucio M, Nunes C, Lima JLFC, Reis S. Effects of resveratrol on membrane biophysical properties: relevance for its pharmacological effects. Chem Phys Lipids. 2010;163(8):747-54.
43. Parmar A, Sharma S. Derivative UV-vis absorption spectra as an invigorated spectrophotometric method for spectral resolution and quantitative analysis: Theoretical aspects and analytical applications: A review. Trac-Trends Anal Chem. 2016;77:44-53.
44. Loureiro DRP, Soares JX, Lopes D, Macedo T, Yordanova D, Jakobtorweihen S, et al. Accessing lipophilicity of drugs with biomimetic models: A comparative study using liposomes and micelles. Eur J Pharm Sci. 2018;115:369-80.
45. Galpothdeniya WIS, Fronczek FR, Cong MY, Bhattarai N, Siraj N, Warner IM. Tunable GUMBOS-based sensor array for label-free detection and discrimination of proteins. J Mat Chem B. 2016;4(8):1414-22.
46. Kagimoto J, Fukumoto K, Ohno H. Effect of tetrabutylphosphonium cation on the physico-chemical properties of amino-acid ionic liquids. Chem Commun. 2006(21):2254-6.
47. Jordan AN, Siraj N, Das S, Warner IM. Tunable near-infrared emission of binary nano- and mesoscale GUMBOS. RSC Adv. 2014;4(54):28471-80.
48. Lopez-Martin I, Burello E, Davey PN, Seddon KR, Rothenberg G. Anion and cation effects on imidazolium salt melting points: A descriptor modelling study. ChemPhysChem. 2007;8(5):690-5.
49. Zhang H, Li MT, Yang BL. Design, Synthesis, and Analysis of Thermophysical Properties for Imidazolium-Based Geminal Dicationic Ionic Liquids. J Phys Chem C. 2018;122(5):2467-74.
50. Grancelli A, Morros A, Cabanas ME, Domenech O, Merino S, Vazquez JL, et al. Interaction of 6-fluoroquinolones with dipalmitoylphosphatidylcholine monolayers and liposomes. Langmuir. 2002;18(24):9177-82.
51. Regmi BP, Galpothdeniya WIS, Siraj N, Webb MH, Speller NC, Warner IM. Phthalocyanine- and porphyrin-based GUMBOS for rapid and sensitive detection of organic vapors. Sens Actuator B-Chem. 2015;209:172-9.
52. Yoshimoto N, Yoshimoto M, Yasuhara K, Shimanouchi T, Umakoshi H, Kuboi R. Evaluation of temperature and guanidine hydrochloride-induced protein-liposome

interactions by using immobilized liposome chromatography. Biochem Eng J. 2006;29(3):174-81.

53. Has C, Sivadas P, Das SL. Insights into Membrane Curvature Sensing and Membrane Remodeling by Intrinsically Disordered Proteins and Protein Regions. J Membr Biol. 2022;255(2-3):237-59.

54. Bakk A, Hoye JS, Hansen A. Apolar and polar solvation thermodynamics related to the protein unfolding process. Biophys J. 2002;82(2):713-9.

55. NMRShiftDB2 database. Available at: https://nmrshiftdb.nmr.uni-koeln.de/portal/js_pane/P-Results/nmrshiftdbaction/showDetailsFromHome/molNumber/20208017(accessed on 7th July 2023).

56. PubChem. Available at: https://pubchem.ncbi.nlm.nih.gov/compound/8-Anilino-1-naphthalenesulfonic-acid#section=Spectral-Information (accessed on 7th July 2023).

Chapter 6

A GUMBOS-based strategy for overcoming therapeutic limitations of rose bengal

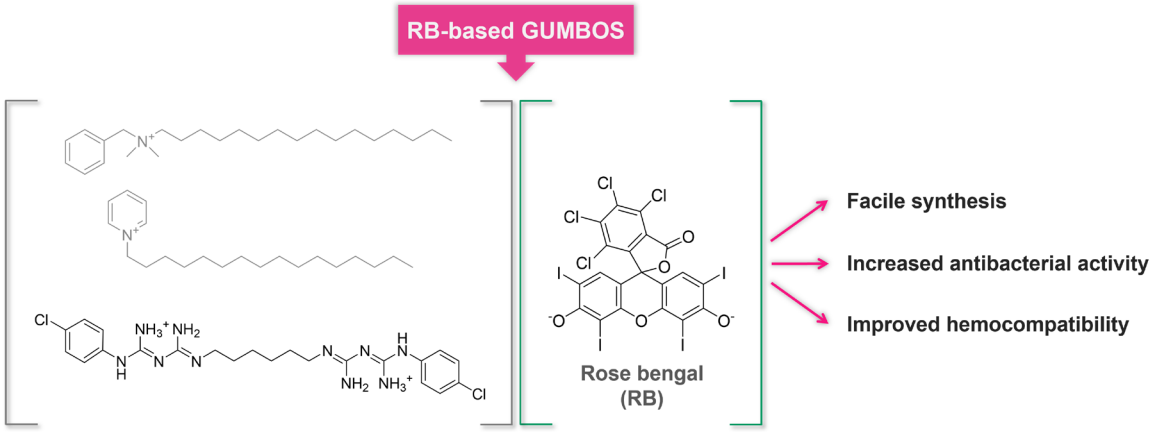

Highlights

- Three novel rose bengal-based GUMBOS were synthesized and characterized.
- GUMBOS showed improved activity towards *S. aureus* DSM 2569 and *E. faecalis*.
- [CHX][RB] was found to be active against *E. coli*, with a MIC of 8–1 μg mL^{-1}.
- The lowest hemolytic activity was also observed for [CHX][RB] (free Hb < 5%).

Manuscript submitted as "Azevedo AMO, Seabra CL, Moniz T, Nunes C, Ayala CE, Rangel M, Reis S, Santos JLM, Warner IM, Saraiva MLMFS. A GUMBOS-based strategy for overcoming therapeutic limitations of rose bengal".

Abstract

The therapeutic use of rose bengal (RB) has been limited by its anionic nature, high water solubility, and short half-life. In this study, RB was converted into a *g*roup of *u*niform *m*aterials *b*ased on *o*rganic *s*alts (GUMBOS) via ion metathesis reactions to replace its sodium counterions with distinct cationic antiseptics (i.e., benzyldimethylhexadecylammonium, BDHA; cetylpyridinium, C_{16}Py; and chlorhexidine, CHX). The potential use of RB-based GUMBOS as antibacterial agents was investigated against a panel of Gram-positive and Gram-negative bacteria, namely *Staphylococcus aureus* (*S. aureus*), methicillin-resistant *S. aureus* (MRSA), *Enterococcus faecalis* (*E. faecalis*), *Pseudomonas aeruginosa* (*P. aeruginosa*), and *Escherichia coli* (*E. coli*). The micro-broth dilution method was used to determine the minimum inhibitory concentration (MIC) of synthesized GUMBOS as well as their parent compounds and unreacted stoichiometric mixtures. Hemolytic effects were further studied using human red blood cells. When compared to parent compounds and unreacted mixtures, GUMBOS showed equal or improved activity towards the non-resistant strain of *S. aureus* (i.e., DSM 2569) and *E. faecalis*. Additionally, [CHX][RB] was found to be active against *E. coli* with a MIC of 8–1 μg mL^{-1}, being 64 times more potent than RB and the corresponding unreacted mixture. The [CHX][RB] GUMBOS also showed the lowest hemolytic activity among all tested compounds and mixtures (percentage of hemolysis < 5%). Overall, these results demonstrated that this GUMBOS-based strategy can improve the antibacterial activity of RB against Gram-positive bacteria and extend its spectrum of action towards *E. coli*, which could further contribute to safety improvements in multiple industries.

Keywords: Antibacterial activity; GUMBOS; Hemocompatibility; Rose bengal.

6.1. Introduction

Rose bengal (RB) is a polyhalogenated fluorescein derivative that has been used to evaluate ocular surface damage in patients with dry eye disease and to assess the severity of hepatic dysfunction, especially in cases where liver biopsy is not feasible or reliable (1-3). Additionally, several studies have demonstrated the potential of using RB for cancer and antimicrobial therapy, either alone or in combination with clinically used drugs (4-7). However, the dianionic charge at physiological pH (pK_a1 = 1.89, pK_a2 = 3.93), high water solubility (100 g L^{-1}), and short half-life (30 min) have limited its clinical applications (8-10). The dianionic nature and poor lipophilicity of RB decrease its ability to cross cell membranes and hinder the interaction with negatively charged organelles (e.g., mitochondria) and Gram-negative bacteria, resulting in decreased cellular uptake and accumulation. Furthermore, the reduced half-life limits its tissue accumulation and leads to the need for multiple administrations to achieve the desired outcome (11-14).

Two primary strategies have been proposed to overcome the limitations of RB dye and enhance its therapeutic potential (12). The first involves chemical modification of the xanthene core or benzyl group to obtain RB derivatives with improved lipophilicity (11, 15), while the second focuses on developing delivery systems to increase cell uptake efficiency (16, 17). For example, conjugates of RB with cationic peptides and polymers were found to be effective against both Gram-positive and Gram-negative bacteria (18-20). This can be ascribed to electrostatic interactions between the positively-charged conjugates and the lipopolysaccharides (LPS) of the Gram-negative outer membrane, which result in increased permeability and, ultimately, bacterial cell death (20, 21). Despite the great promise of these strategies, RB derivatives often require multi-step synthetic procedures with low product yields. Further, cationic conjugates can suffer from low stability and biocompatibility (21-23).

GUMBOS (*g*roup of *u*niform *m*aterials *b*ased on *o*rganic *s*alts) have attracted increasing attention recently due to their ease of synthesis and great tunability. In fact, GUMBOS can be synthesized from well-known compounds in their salt forms using a simple metathesis reaction and do not require laborious purification steps (24-26). Additionally, many GUMBOS properties, including lipophilicity and toxicity, can be easily modulated by changing the cation-anion combination, which makes this approach a resource-efficient and more cost-effective tool for designing RB derivatives (27, 28).

In this study, the synthesis of three novel RB-based GUMBOS was performed, where the RB anion is ion-paired with distinct cationic antiseptics, namely benzyldimethylhexadecylammonium (BDHA), cetylpyridinium (C_{16}Py), and chlorhexidine (CHX). Their antibacterial efficacy was investigated against a panel of clinically relevant

Gram-positive and Gram-negative bacteria. Results were compared with those obtained for unreacted stoichiometric mixtures and parent compounds to confirm the potential of synthesized GUMBOS as alternative antibacterial agents. Moreover, hemolytic effects were examined as an initial study to determine if these RB-GUMBOS could be safe for use as therapeutic agents, in particular, in humans.

6.2. Material and methods

6.2.1. Chemicals and solvents

RB disodium salt ($[Na]_2[RB]$), benzyldimethylhexadecylammonium chloride ([BDHA][Cl]), chlorhexidine diacetate ($[CHX][CH_3COO]_2$), hexadecylphosphocholine (HePC), *N*-(2-hydroxyethyl)piperazine-*N*′-(2-ethanesulfonic acid) (HEPES) hemisodium salt, cation-adjusted Müeller-Hinton broth (MHB-II), isopropyl alcohol (IPA), 0.85% (w/v) sodium chloride (NaCl) solution, and Triton™ X-100 were all obtained from Sigma-Aldrich (St. Louis, MO). NaCl salt was acquired from PanReac AppliChem (Darmstadt, Germany). Cetylpyridinium chloride ($[C_{16}Py][Cl]$), tryptic soy agar (TSA), tryptic soy broth (TSB), and dimethylsulfoxide (DMSO) were purchased from Merck KGaA (Darmstadt, Germany). Deuterated chloroform ($CDCl_3$, 99.80%) and hexadeuterodimethylsulfoxide (DMSO-d_6, 99.96%) with 0.03% (v/v) tetramethylsilane were obtained from Eurisotop (Saarbrücken, Germany).

HEPES buffer (0.01 mol L^{-1}, pH 7.4) was obtained by dissolving HEPES in ultrapure water (Milli-Q, 18.2 MΩ cm) and adjusting ionic strength to 0.1 mol L^{-1} with NaCl. A stock suspension of HePC (600 µmol L^{-1}) was prepared in HEPES buffer, and then a working suspension of 100 µmol L^{-1} was obtained by diluting the stock suspension with the same buffer. RB-based GUMBOS were dissolved in DMSO and kept in the dark to avoid photodegradation. Before membrane partition studies, these stock solutions were diluted in HEPES buffer to a concentration of 48 µmol L^{-1}. For the evaluation of antibacterial activity, dilution was performed in MHB-II medium (final concentration of DMSO = 2%).

6.2.2. Instrumentation

Proton (^1H, 400.15 MHz) and carbon (^{13}C, 100.62 MHz) nuclear magnetic resonance (NMR) spectra were recorded using a Bruker Avance III 400, equipped with a pulse gradient unit (z-gradient of 50.0 G cm^{-1}). Bruker's TopSpin software version 4.0.1 was used for spectra acquisition and processing. Samples were prepared by dissolving $[BDHA]_2[RB]$ and $[C_{16}Py]_2[RB]$ in $CDCl_3$, and [CHX][RB] in DMSO-d_6. Chemical shifts (δ) were reported in

ppm and coupling constants (*J*) in Hz. Multiplicities were abbreviated as follows: s, singlet; d, doublet; t, triplet; and m, multiplet.

A Thermo Scientific LTQ-Orbitrap XL mass spectrometer was externally calibrated using a standard kit provided by the manufacturer. This mass spectrometer was operated in positive and negative ionization mode with the capillary voltage set to 3 kV, sheath gas flow to 6, and temperature of ion transfer capillary to 275 °C. Spectra were recorded for *m/z* values between 250 and 2000 in the Fourier transform (FT) mode with a resolution of 60,000 FWHM (full width at half maximum). Samples were prepared in methanol prior to analysis and directly infused into the electrospray ion source at a flow rate of 10 μL min^{-1} using the syringe pump of the mass spectrometer. High-resolution mass spectrometry (HRMS) and NMR analyses were performed at "Laboratório de Análise Estrutural, Centro de Materiais da Universidade do Porto (CEMUP), Portugal".

Infrared (IR) spectra were collected from 4000 to 600 cm^{-1} using a PerkinElmer Frontier spectrometer equipped with an attenuated total reflectance (ATR) accessory. The number of scans and resolution were set to 32 and 4 cm^{-1}, respectively. A MEL-TEMP® apparatus was used to determine the melting point range of synthesized materials. Thermogravimetric analysis (TGA) was performed on a TA Discovery TGA550 instrument. Approximately 1 mg of GUMBOS was heated from 25 to 595 ºC at a rate of 10 ºC min^{-1}.

Optical properties were studied using a Jasco V-660 spectrophotometer, equipped with a 1 cm quartz cuvette. Ultraviolet-visible (UV-Vis) spectra were recorded from 300 to 700 nm using a bandwidth of 5 nm. Partition and hemolysis assays were performed on a Cytation 3 imaging reader from BioTek Instruments.

6.2.3. Synthesis and characterization of GUMBOS

RB-based GUMBOS were synthesized using a single-step ion-exchange metathesis reaction (29). Sodium cations of RB dye were exchanged with $BDHA^+$, $C_{16}Py^+$, and CHX^{2+} (Table 6.1). Following a procedure similar to that described by Cole et al., both cation and anion were dissolved in water, or a mixture of water and IPA, and stirred for 48 h in the dark at room temperature (24). The resulting precipitates were washed several times with cold water to remove excess dye and by-products. Washed precipitates were then freeze-dried. NMR, FTIR, and MS provided structural information on the synthesized compounds. TGA was used to investigate their thermal stability. Detailed characterization data can be found in Supplementary Material (Figs. S6.1 and S6.2, and Tables S6.1–S6.3).

Table 6.1. Chemical structures and molar ratios of the ions used in GUMBOS synthesis.

GUMBOS	Cation	Anion	Molar ratio (Cation:Anion)
$[BDHA]_2[RB]$	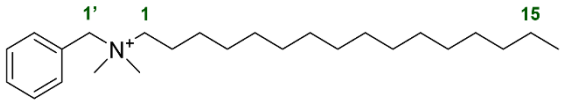 Benzyldimethylhexadecylammonium [BDHA]	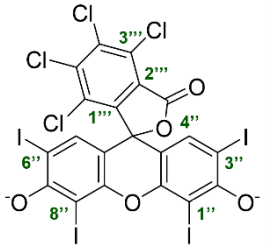 Rose bengal [RB]	2:1
$[C_{16}Py]_2[RB]$	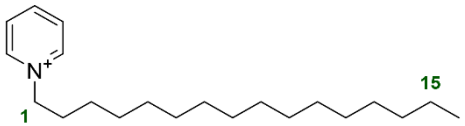 Cetylpyridinium [C_{16}Py]		2:1
[CHX][RB]	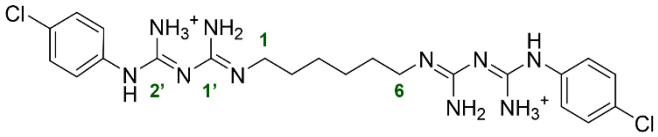 Chlorhexidine [CHX]		1:1

6.2.4. Micellar/water partitioning

The lipophilicities of synthesized RB-GUMBOS and parent RB dye were further evaluated through determination of micelle/water partition coefficients (K_p) by derivative UV-Vis spectrophotometry, as previously described (30, 31). Briefly, 50 µL of each GUMBOS solution in HEPES buffer (final concentration = 8 µmol L^{-1}) were added to a microplate containing increasing concentrations of HePC (0–200 µmol L^{-1}). References were prepared according to the same procedure but in the absence of GUMBOS, which was replaced by HEPES buffer. After an incubation period of 30 min at 37 ºC, spectra were collected from 450 to 650 nm. Data analyses were performed using the K_p calculator spreadsheet developed by Magalhaes and coworkers (30). First, each reference spectrum was subtracted from the corresponding sample spectrum, and then a second derivative spectrum was generated to minimize the effects of light scattering from HePC micelles and improve the resolution of overlapping bands (32). Second derivative values measured at 560 nm (wavelength at which light scattering was negligible) were plotted against HePC concentrations, and K_p (mol L^{-1}) was determined by fitting Eq. 1 to experimental data using a nonlinear least-squares regression method (30):

$$D_T = D_W + \frac{(D_L - D_W)K_p[L]}{1 + K_p[L]} \qquad (1)$$

where D is the second derivative intensity obtained from absorbance values of the total amount of GUMBOS (D_T), and GUMBOS in the lipid (D_L) and aqueous (D_W) phases. [L] is the concentration of HePC and K_p the partition coefficient (both expressed in mol L^{-1}).

6.2.5. Bacterial strains and growth conditions

The Gram-positive and Gram-negative bacterial strains used in this study were the following: *Staphylococcus aureus* (*S. aureus*) DSM 2569 (susceptible strain), *S. aureus* ATCC 6538 (biofilm-forming strain), methicillin-resistant *S. aureus* (MRSA) ATCC 33592, *Enterococcus faecalis* (*E. faecalis*) ATCC 29212, *Pseudomonas aeruginosa* (*P. aeruginosa*) DSM 1117, and *Escherichia coli* (*E. coli*) ATCC 25922. DSM and ATCC strains were purchased from DSMZ-German Collection of Microorganisms and Cell Cultures GmbH (Braunschweig, Germany) and American Type Culture Collection (Manassas, VA), respectively.

All strains were cultured on TSA plates for 24 h at 37 ºC and then grown overnight (16–18 h) on TSB medium at the same temperature under agitation (150 rpm). Subsequently, bacteria were harvested by centrifugation (2500 *g*, 10 min), washed with phosphate-buffered saline (0.1 mol L^{-1}, pH 7.4), and their concentrations adjusted to 1×10^8 CFU mL^{-1}

($OD_{600\ nm}$ = 0.1) using MHB-II medium. Before evaluating the antibacterial activity of synthesized compounds, bacterial suspensions were further diluted to 2×10^5 CFU mL^{-1} in the same medium.

6.2.6. Antibacterial activities of synthesized GUMBOS

The minimum inhibitory concentration (MIC) of RB-based GUMBOS, parent compounds, and unreacted mixtures were determined using the micro-broth dilution method described by Wiegand et al. (33), which follows CLSI (34) and EUCAST (35) guidelines. Briefly, 150 µL of each compound were added to a 96-well microplate (non-treated, round bottom) containing bacterial suspension at a final concentration of 1×10^5 CFU mL^{-1}, and then serial two-fold dilutions were performed to obtain concentrations ranging from 512 to 0.25 µg mL^{-1}. After incubation for 24 h at 37 ºC, MIC was recorded as the lowest concentration inhibiting bacterial growth (absence of turbidity and pellet formation). The minimum bactericidal concentration (MBC) was assessed by plating on TSA medium the content of the first three wells where no growth was observed. Subsequently, plates were incubated for 24 h at 37 ºC and the number of colony-forming units (CFU) was counted. MBC was defined as the lowest concentration of compound killing 99.9% of the initial inoculum. Experiments were also conducted in the presence of light for comparison purposes, and *S. aureus* DSM 2569, *E. faecalis* ATCC 29212, *P. aeruginosa* DSM 1117, and *E. coli* ATCC 25922 were used as model bacteria. The microplate was irradiated for 30 min using an in-house developed light source, which consists of gallium phosphate green light-emitting diodes (LEDs) attached to a polymethyl methacrylate surface and achieves an illuminance of 3500 lux (Table S6.1).

6.2.7. Hemolysis assay

Before assessing the hemolytic effects of synthesized compounds, fresh blood samples collected from four healthy volunteers and kindly provided by “Serviço de Hematologia Clínica, Centro Hospitalar Universitário do Porto”, were centrifuged for 5 min at 955 *g* and 4 ºC using an Allegra X-15R centrifuge. The upper layers (plasma and buffy coat) were carefully removed and discarded, and the sedimented red blood cells (RBCs) were washed three times with 0.85% (w/v) NaCl. Subsequently, RBCs were diluted to a final concentration of 4% (v/v) in the same saline solution, and 100 µL of the resultant suspension were seeded into a 96-well plate. An equal volume of each concentration of GUMBOS and controls was added to the respective wells and incubated for 1 h at 37 ºC. The supernatant containing hemoglobin released from lysed RBCs was transferred to a new plate, and absorbance was measured at 415 and 690 nm. Finally, the percentage of hemolysis was calculated using the following equation:

$$\text{Hemolysis (\%)} = \frac{\text{Abs}_{\text{sample}} - \text{Abs}_{\text{negative control}}}{\text{Abs}_{\text{positive control}} - \text{Abs}_{\text{negative control}}} \times 100 \qquad (2)$$

where Abs is the corrected absorbance obtained by subtracting the absorbance at 690 nm from that measured at 415 nm. RBCs in 0.85% NaCl were used as the negative control, while RBCs treated with 1% (v/v) Triton™ X-100 served as the positive control (100% hemolysis).

The same procedure was followed to determine the percentage of hemolysis caused by the parent compounds and unreacted stoichiometric mixtures.

6.3. Results and discussion

6.3.1. Structural characterization and thermal stability of the synthesized GUMBOS

The chemical structures of synthesized compounds were determined by analysis of NMR (^{1}H and ^{13}C), FTIR, and HRMS data. Proton and carbon chemical shifts were assigned based on 1D and 2D ^{1}H–^{1}H COSY (correlation spectroscopy), ^{1}H–^{13}C HSQC (heteronuclear single quantum coherence), and ^{1}H–^{13}C HMBC (heteronuclear multiple bond coherence) experiments. Integration of proton NMR signals further confirmed the expected stoichiometric ratio of cation to anion, which was determined as 2:1 for $[BDHA]_2[RB]$ and $[C_{16}Py]_2[RB]$, and 1:1 for [CHX][RB]. Peaks corresponding to the starting materials were observed in the FTIR spectra of the resulting GUMBOS (Fig. S6.1). For example, the characteristic peaks of RB dye appear around 1626, 1544, 1450, and 1344 cm^{-1}, indicating the presence of a –C=O group and aromatic C=C bonds in synthesized compounds (36, 37). Analyses of the positive ion mode mass spectra showed peaks at *m/z* values of 360.3632, 304.3005, and 253.1097, which correspond to BDHA, C_{16}Py, and CHX cations. RB anion was detected in the negative ion mode for all synthesized GUMBOS. Moreover, good agreement was found between experimental and theoretical masses (Table S6.2).

The thermal behavior of RB-based GUMBOS was examined using TGA. Fig. S6.2 shows the weight loss curves for all compounds and Table S6.3 lists the temperatures at which their weight was reduced by 50% ($T_{50\%}$). It was determined that thermal stability is affected by the nature of the cation, i.e., the thermal stability increased in the following order: $[BDHA]_2[RB] < [C_{16}Py]_2[RB] <$ [CHX][RB]. This result is in line with previous reports for the impact of cation on thermal stability of ionic compounds (38-40). In particular, the highest thermal stability observed for the [CHX][RB] GUMBOS is likely the result of an increased

number of aromatic rings and extended conjugation in the case of CHX.

6.3.2. UV-Vis spectral properties of RB-based GUMBOS

The optical properties of synthesized compounds were investigated using UV-Vis spectroscopy. As shown in Fig. 6.1, the absorption profile of RB-based GUMBOS is similar to that of $[Na]_2[RB]$ with an intense band at 565 nm, a shoulder at 526 nm, and a lower intensity band at approximately 330 nm (41, 42). These absorption bands can be assigned to the origin, $S_0 \rightarrow S_1$, and $S_0 \rightarrow S_2$ transitions, respectively (41). Moreover, the increase in absorbance can be explained by the surfactant properties of the cations used to form GUMBOS. Other groups have reported changes in the spectral properties of RB upon addition of surfactants (43, 44).

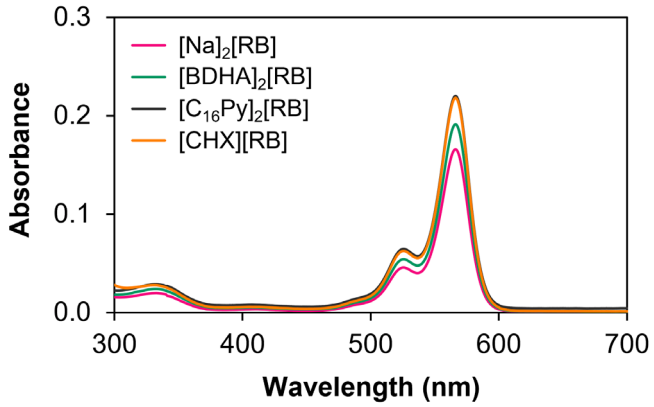

Fig. 6.1. UV-Vis absorption spectra of $[Na]_2[RB]$ and RB-based GUMBOS (2 μmol L^{-1}) in DMSO.

6.3.3. Melting point and lipophilicity of the synthesized compounds

The impact of cation exchange on GUMBOS physicochemical properties was evaluated through determination of their melting point and lipophilicity. It was found that the exchange of Na^+ by $BDHA^+$, $C_{16}Py^+$, and CHX^{2+} (large organic cations) led to a reduction in the melting point (Table S6.4), thus corroborating previous findings (29, 45). The decrease in melting point was less pronounced for [CHX][RB] than for other GUMBOS and can be attributed to the stoichiometric ratio of cation to anion as well as to cation symmetry, which results in a higher degree of lattice matching and stronger ionic interactions. Additionally, the similarity between melting point ranges of $[BDHA]_2[RB]$ and $[C_{16}Py]_2[RB]$ could be attributed to the length of the side chain (n = 15 in both cations) (28, 46, 47).

In order to assess the lipophilicity of synthesized compounds, partition coefficients were measured using HePC micelles as model membranes. Fig. 6.2 shows an example of the absorption (A) and second derivative (B) spectra of [CHX][RB] as well as the variation of

second derivative values (λ = 560 nm) with increasing concentrations of lipid (C). The partition coefficients determined for $[Na]_2[RB]$ and RB-based GUMBOS are listed in Table 6.2. Analyses of data suggest that lipophilicity is affected by cation's chemical structure, similar to what has been reported for other GUMBOS (29, 45). Additionally, the surfactant properties of $BDHA^+$ and CHX^{2+} may help explain the reduction in GUMBOS lipophilicity as compared to the parent dye ($[Na]_2[RB]$). For example, Jabbari and Teymoori demonstrated that the partition coefficient of gemfibrozil and ibuprofen decreases in the presence of surfactants, which follows an opposite trend to that observed for solubility (48).

Table 6.2. Partition coefficients (expressed as K_p and logD) of $[Na]_2[RB]$ and RB-based GUMBOS in micelles of HePC at pH 7.4 and 37 ºC. Results are the mean ± standard deviation of three replicates.

Compound	K_p (L mol^{-1})	K_p[a]	logD
$[Na]_2[RB]$	32344 ± 649	79664 ± 1598	4.90 ± 0.01
$[BDHA]_2[RB]$	24910 ± 1715	61355 ± 4224	4.79 ± 0.03
$[C_{16}Py]_2[RB]$	38792 ± 3246	95546 ± 7995	4.98 ± 0.04
[CHX][RB]	11722 ± 501	28871 ± 1233	4.46 ± 0.02

[a] Dimensionless values were obtained by dividing molar partition coefficients by HePC molar volume (0.406 L mol^{-1}) (30).

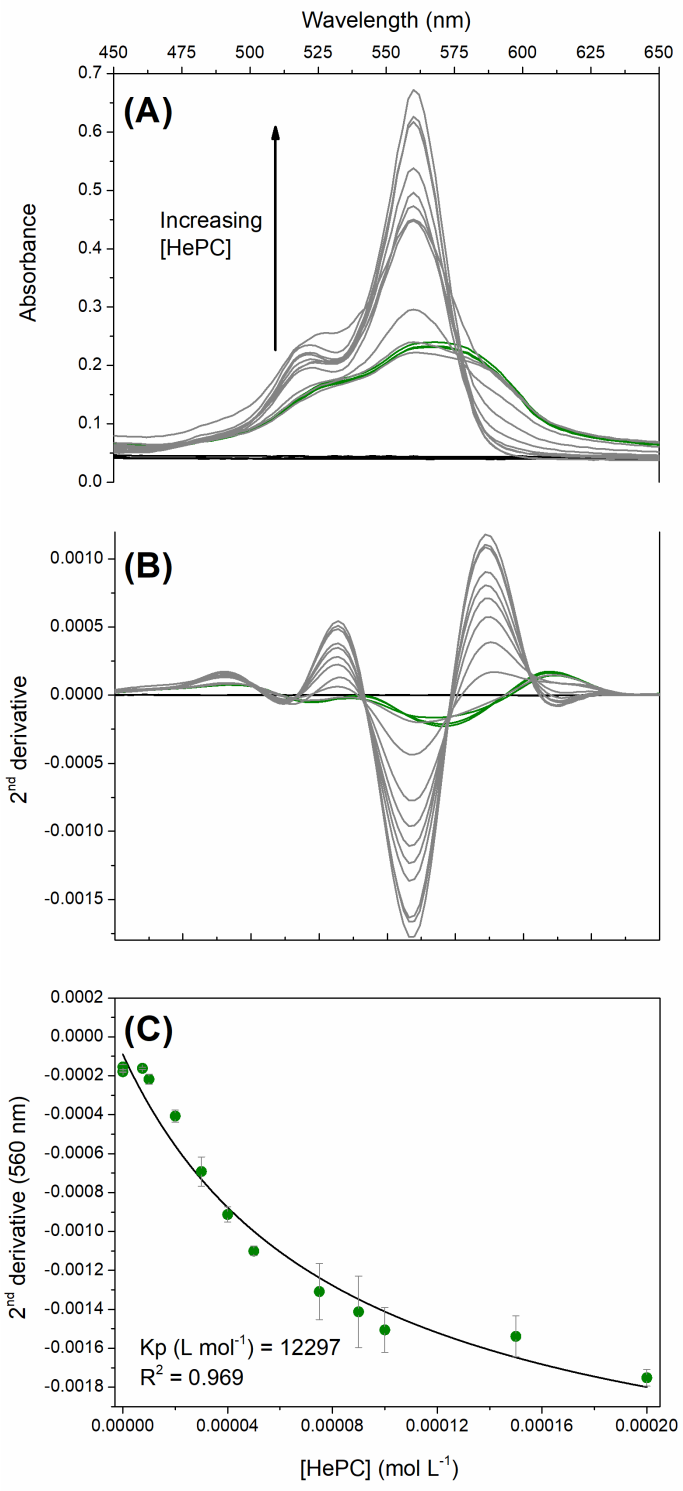

Fig. 6.2. (A) Absorption and (B) second derivative spectra of [CHX][RB] (8 μmol L^{-1}) in the absence (**–**) and presence of increasing concentrations of HePC (**–**), and micelles without GUMBOS (**–**). (C) Plot of second derivative values at 560 nm as a function of HePC micellar concentration and their fit using a nonlinear least squares regression method. Note: Some error bars are smaller than the corresponding markers.

6.3.4. Antibacterial activities of RB-based GUMBOS

Following the characterization of synthesized GUMBOS, their antibacterial activities against Gram-positive and Gram-negative bacteria in the absence and presence of light were evaluated. Results (Table S6.5) showed that, in most cases, exposure to green light does not potentiate the antibacterial effect of tested compounds. For this reason, along with advantages in terms of time, costs, and technical simplicity, it was decided to proceed with studies in the absence of irradiation.

RB-based GUMBOS were found to be equally or more effective than parent compounds and unreacted mixtures towards *S. aureus* DSM 2569 and *E. faecalis*, with MIC and MBC values in the range of 2–0.5 and 4–0.5 μg mL^{-1}, respectively (Table 6.3). *S. aureus* ATCC 6538 and MRSA were slightly less susceptible than the non-resistant strain (i.e., *S. aureus* DSM 2569). Analysis of results further revealed that *P. aeruginosa* was not susceptible to either RB-GUMBOS or unreacted mixtures, suggesting that the selected antiseptics do not potentiate the antibacterial activity of RB either as a reacted ion pair or a mixture for this microbe. This result is not surprising since *P. aeruginosa* has shown decreased susceptibility and resistance to many antimicrobial agents, including quaternary ammonium compounds and biguanides (49-51). Moreover, several authors have reported that RB is more active against Gram-positive (e.g., *S. aureus*) than Gram-negative (e.g., *P. aeruginosa* and *E. coli*) bacteria, which can be attributed to differences in composition and structure of the cell envelope (52-55). For example, LPS is the major component of the external leaflet of the Gram-negative outer membrane and forms a permeability barrier to large, hydrophobic, and anionic compounds such as RB (21, 56-58).

Among the synthesized GUMBOS, [CHX][RB] was determined to be the most effective against Gram-positive bacteria and *E. coli*, with the latter exhibiting a MIC of 8–1 μg mL^{-1} (64 times lower than that of the corresponding unreacted mixture and $[Na]_2[RB]$). These findings can be explained as the result of different stoichiometric ratios of precursor ions (1:1 *versus* 2:1) and their impact on the structural configuration of GUMBOS (24). Additionally, the lower lipophilicity of [CHX][RB] can lead to greater penetration into *E. coli* cells and result in increased antibacterial efficacy (21, 59). The susceptibility of *S. aureus* to CHX is not affected by its mixture with RB. However, RB-GUMBOS were determined to improve bactericidal activity when compared to the unreacted mixture. It is worth noting that *S. aureus* isolates with reduced susceptibility to CHX are characterized by a MIC equal to or greater than 4 μg mL^{-1} (60, 61).

Table 6.3. MICs and MBCs (μg mL^{-1}) of GUMBOS, parent compounds, and unreacted stoichiometric mixtures against Gram-positive and Gram-negative bacteria.

		Bacterial species											
		Gram-positive								Gram-negative			
		S. aureus DSM 2569		*S. aureus* ATCC 6538		MRSA ATCC 33592		*E. faecalis* ATCC 29212		*P. aeruginosa* DSM 1117		*E. coli* ATCC 25922	
		MIC	MBC	MIC	MBC	MIC	MBC	MIC	MBC	MIC	MBC	MIC	MBC
GUMBOS	$[BDHA]_2[RB]$	2–1	2	8–2	16–8	4–2	8–4	1–0.5	1–0.5	>512	>512	>512	>512
	$[C_{16}Py]_2[RB]$	1–0.5	4–1	2–1	16–2	2	8–4	0.5	0.5	>512	>512	>512	>512
	[CHX][RB]	0.5	4–1	1	16–4	2	32–16	0.5	1–0.5	>512	>512	8–1	64–8
Parent compounds	$[Na]_2[RB]$	8–4	8	4	8–4	2	4–2	4–2	4–2	>512	>512	>512	>512
	[BDHA][Cl]	0.5	2	0.5	4–2	1	2	0.5	1–0.5	32	256–128	4–8	32–16
	$[C_{16}Py][Cl]$	0.5	2	0.5	2–1	4–1	16–8	0.5	2–0.5	128–64	256–128	8	16
	$[CHX][CH_3COO]_2$	0.5	2	0.5	2	0.5	2	2–0.5	4–1	2	8	0.5	16–4
Unreacted mixtures	2 BDHA:1 RB	2–1	4–2	1–0.5	4–1	2–1	16–2	4–2	1	>512	>512	>512	>512
	2 $C_{16}Py$:1 RB	0.5	2	2–1	16–4	2	4–2	0.5	0.5	>512	>512	>512	>512
	1 CHX:1 RB	0.5	8	1–0.5	16–8	2–0.5	2–0.5	1–0.5	1–0.5	>512	>512	>512	>512

6.3.5. Hemocompatibility of the synthesized GUMBOS

In order to evaluate the hemocompatibility of RB-based GUMBOS and further determine if they are safe for clinical use in humans, a hemolysis assay was performed. Human RBCs were used as a model system for studying the hemolytic effects of synthesized RB-GUMBOS as well as their starting materials and unreacted stoichiometric mixtures (Fig. 6.3). RB-based GUMBOS (Fig. 6.3A) were found to be more hemocompatible than the corresponding parent compounds (Fig. 6.3B). Moreover, [CHX][RB] showed decreased hemolytic activity as compared to the unreacted mixture (Fig. 6.3C), producing a percentage of hemolysis lower than 5% as recommended by ASTM F756-17 (62). This finding can be explained by the reduced lipophilicity of [CHX][RB] (about three times lower than that of $[Na]_2[RB]$), which limits its ability to penetrate the RBCs membrane (63, 64). As a result of its improved hemocompatibility and extended antibacterial activity, it was determined that [CHX][RB] GUMBOS may be a potentially valuable alternative for treating bacterial infections.

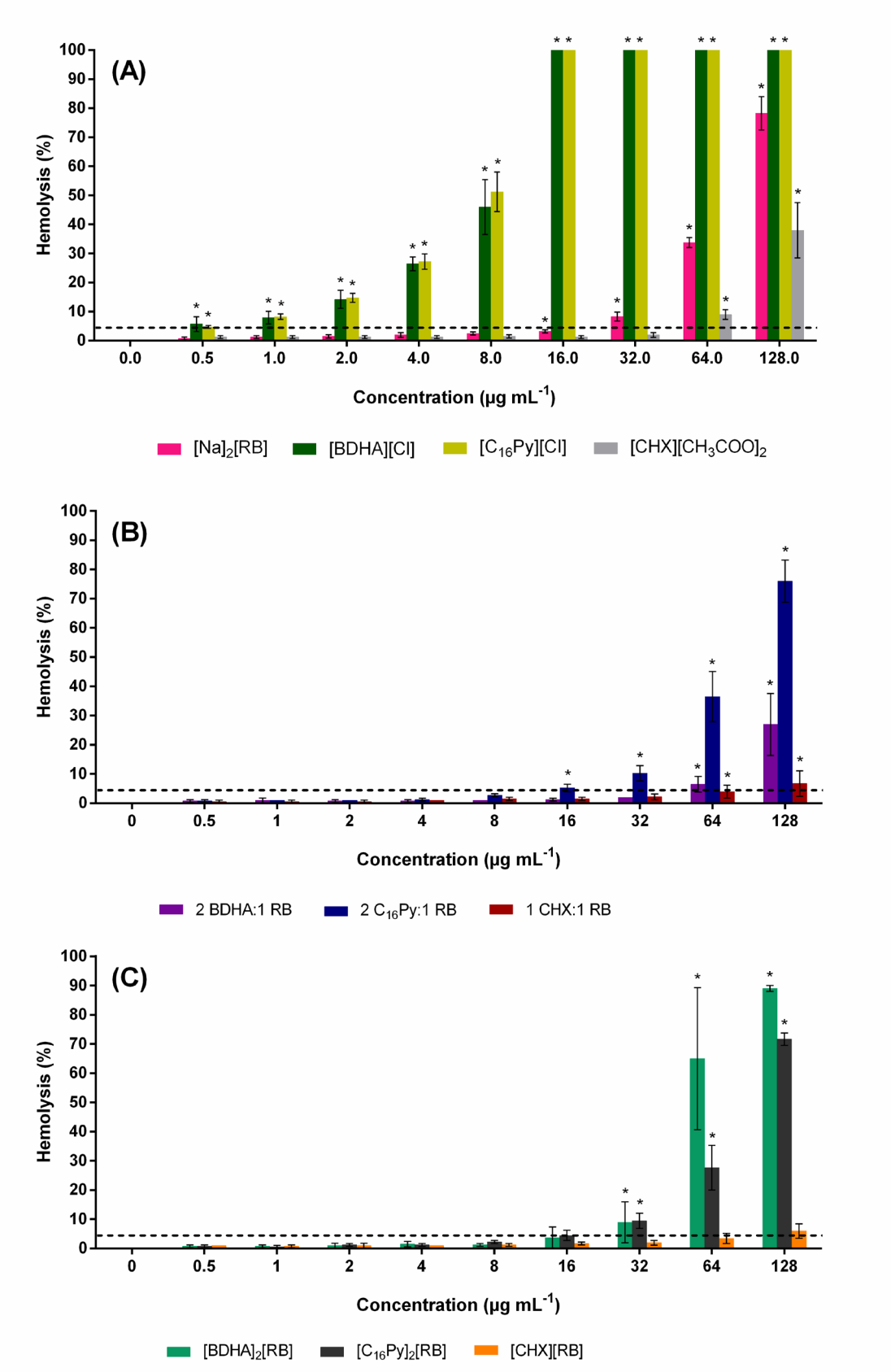

Fig. 6.3. Percentage of hemolysis (mean ± standard deviation) after incubation of human RBCs with different concentrations of (A) GUMBOS, (B) starting materials, and (C) unreacted mixtures. RBCs

in saline solution (0.85%) and Triton™ X-100 (1% v/v) were used as negative and positive controls, respectively. Statistically significant differences between each concentration and the negative control (untreated RBCs) were assessed using the non-parametric Kruskal-Wallis test (*P < 0.05). Dash line represents 5% hemolysis.

6.4. Conclusions

In this study, three RB-based GUMBOS were prepared using a single-step ion-exchange metathesis reaction. The properties of these RB-GUMBOS were studied, and their potential efficacy as antibacterial agents was examined. The synthesized GUMBOS proved to be equally or more effective than parent compounds and unreacted mixtures towards *S. aureus* DSM 2569 and *E. faecalis*. Moreover, [CHX][RB] was found to be active against the Gram-negative *E. coli*, with a MIC that is 64 times lower than that of RB dye and the corresponding unreacted mixture. The [CHX][RB] GUMBOS was also determined to produce the lowest percentage of hemolysis (< 5%) among all tested compounds and mixtures; thus, these results demonstrate that RB properties can be easily tuned by changing the cation. Additionally, the simplicity of the synthetic procedure and the possibility to strategically incorporate different biologically active cations, make this method a promising tool for development of cost-effective alternatives to RB. The obtained results further confirm the potential of this GUMBOS approach to improve antibacterial efficacy against Gram-positive strains and expand the spectrum of action towards Gram-negative bacteria.

SUPPLEMENTARY MATERIAL

Characterization of RB-based GUMBOS

$[BDHA]_2[RB]$

^{1}H NMR (400.15 MHz, $CDCl_3$, ppm): δ 7.57 (s, 2H, H4'', H5''); 7.38 (m, 2x 5H, -CH_2-Bn); 4.41 (s, 2x 2H, 1' -NCH_2-); 3.16 (s, 2x 2H, 1 -NCH_2-); 2.94 (s, 2x 6H, -N(CH_3)$_2$); 1.74 (s, 2x 2H, 2 -CH_2-); 1.25 (s, 2x 26H, 3-15 -CH_2-); 0.88 (t, *J* 6.4, 2x 3H, -CH_3). ^{13}C NMR (100.62 MHz, $CDCl_3$, ppm): δ 172.8 (C2'', C7''); 158.0 (C1a'', C8a''); 144.5 (C1'''); 137.8 (C4'', C5''); 133.2, 130.8, 129.4 (-CH_2-Bn); 134.3, 126.9, 122.2, 116.4, 112.1 (aromatic C_q from xanthene core and Cl-substituted ring); 96.7 (C3'', C6''); 68.0 (1' -NCH_2-); 63.9 (1 -NCH_2-); 49.7 (-N(CH_3)$_2$); 29.5 (3-15 -CH_2-); 22.9 (2 -CH_2-); 14.2 (-CH_3).

$[C_{16}Py]_2[RB]$

^{1}H NMR (400.15 MHz, $CDCl_3$, ppm): δ 8.94 (d, 2x 2H, -Py); 8.32 (t, 7.6, 2x H, -Py); 7.88 (t, 7.1, 2x 2H, -Py); 7.47 (s, 2H, H4'', H5''); 4.56 (t, 7.7, 2x 2H, 1-NCH_2-); 1.91 (t, 7.3, 2x 2H, 2 -CH_2-); 1.22 (m, 2x 26H, 3-15 -CH_2-); 0.88 (t, 6.9, 2x 3H, -CH_3). ^{13}C NMR (100.62 MHz, $CDCl_3$, ppm): δ 172.8 (C2'', C7''); 158.0 (C1a'', C8a''); 144.9 (C1'''); 137.8 (C4'', C5''); 145.4, 128.8 (-Py); 112.3 (aromatic C_q from xanthene core); 96.9 (C3'', C6''); 62.9 (1 -CH_2-); 32.3 (2 -CH_2-); 30.0, 29.9, 26.6, 23.1 (3-15 -CH_2-); 14.3 (-CH_3).

[CHX][RB]

^{1}H NMR (400.15 MHz, DMSO-d_6, ppm): δ 9.79, 9.52 (s, 2x 1H, -NH-); 7.99, 7.63 (s, 2x 2H, -NCH_2-); 7.36 (s, 2H, H4'', H5''); 7.29 (s, 2x 4H, -Bn); 7.10, 6.82 (s, 2x 3H, -NCH_3^+-); 1.43, 1.24 (s, 12H, H1-6). ^{13}C NMR (100.62 MHz, DMSO-d_6, ppm): δ 172.2, 157.8 (C=O, RB); 137.6 (C4'', C5''); 129.1, 122.3, 111.4 (-Bn); 97.1, 75.9 (C3'', C6''); 26.5 (C1-6).

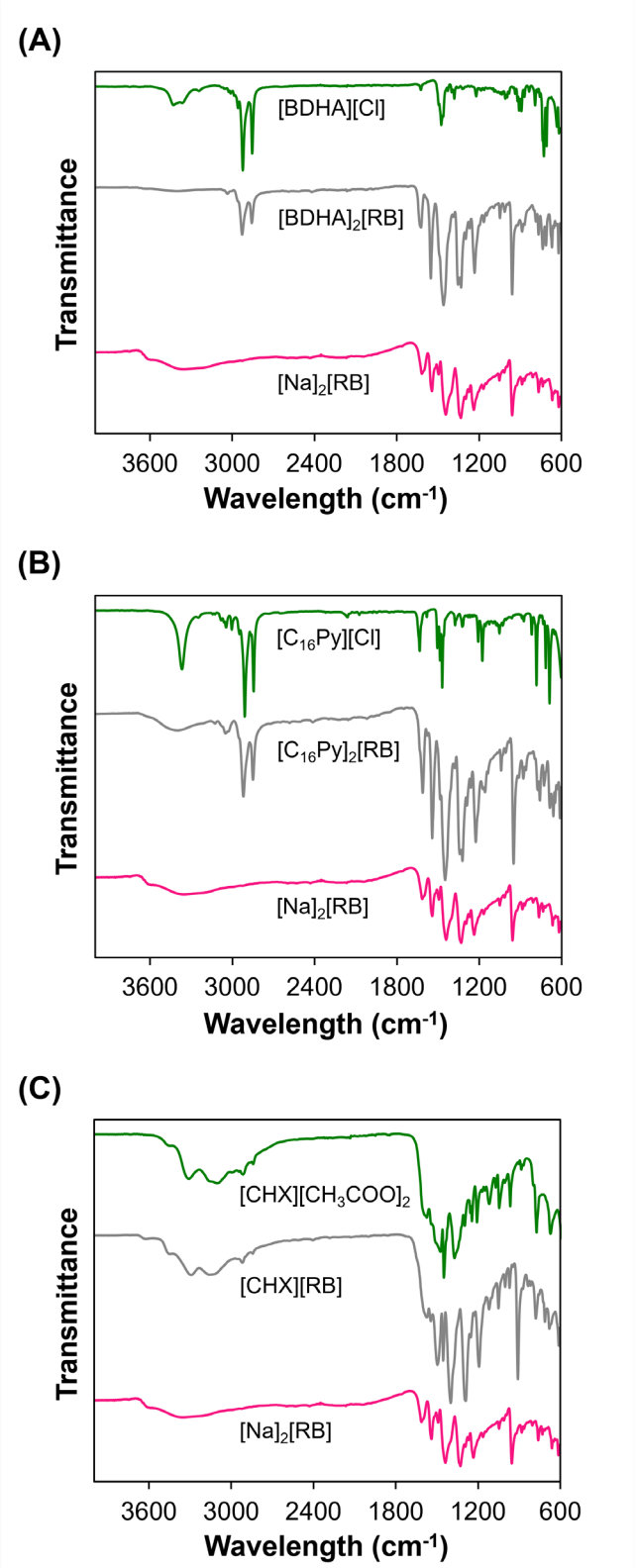

Fig. S6.1. Overlay of FTIR spectra of bulk materials (green and pink) and resulting GUMBOS (grey): (A) $[BDHA]_2[RB]$, (B) $[C_{16}Py]_2[RB]$, and (C) [CHX][RB].

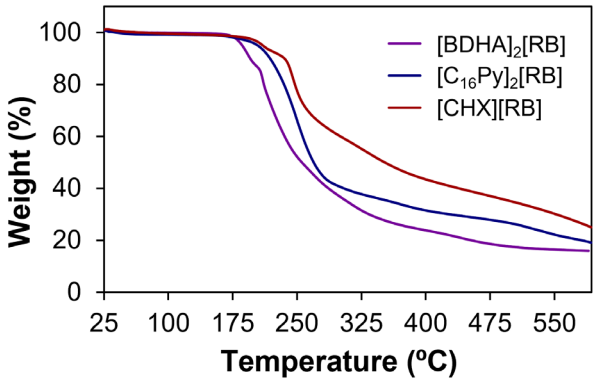

Fig. S6.2. TGA spectra of RB-based GUMBOS

Table S6.1. Green LED irradiation parameters.

Peak wavelength	565 nm
Output current	15 mA
Luminous flux	220 lm
Emission angle	120º
Distance[a]	5 cm
Illuminance	3500 lux

[a] Distance from the top of the microplate.

Table S6.2. ESI-MS analysis of synthesized GUMBOS.

GUMBOS	Ionic formula		ESI-MS (positive mode)		ESI-MS (negative mode)	
	Cation	Anion	Expected mass (*m/z*)	Obtained mass (*m/z*)	Expected mass (*m/z*)	Obtained mass (*m/z*)
$[BDHA]_2[RB]$	$C_{25}H_{46}N^+$		360.3625	360.3632		972.4975
$[C_{16}Py]_2[RB]$	$C_{21}H_{38}N^+$	$C_{20}H_3Cl_4I_4O_5^-$	304.2999	304.3005	972.4889	972.4967
[CHX][RB]	$C_{22}H_{32}Cl_2N_{10}^{2+}$		253.1089	253.1097		972.4956

Table S6.3. TGA data of RB-based GUMBOS.

GUMBOS	$T_{50\%}$ (ºC)[a]
$[BDHA]_2[RB]$	255
$[C_{16}Py]_2[RB]$	269
[CHX][RB]	352

[a] $T_{50\%}$ = 50% weight loss temperature.

Table S6.4. Melting point range (ºC) of synthesized compounds.

GUMBOS	Melting range (ºC)
$[BDHA]_2[RB]$	85–100
$[C_{16}Py]_2[RB]$	90–110
[CHX][RB]	209–215

For $[Na]_2[RB]$, m.p. > 300 ºC (Thermo Fisher Scientific).

Table S6.5. MICs and MBCs (μg mL^{-1}) of GUMBOS (A), parent compounds (B), and unreacted stoichiometric mixtures (C) against Gram-positive and Gram-negative bacteria. For comparison purposes, experiments were conducted in the presence and absence of light.

		Bacterial species															
		Gram-positive								Gram-negative							
		S. aureus DSM 2569				*E. faecalis* ATCC 29212				*P. aeruginosa* DSM 1117				*E. coli* ATCC 25922			
		MIC[a]	MBC[a]	MIC[b]	MBC[b]	MIC[a]	MBC[a]	MIC[b]	MBC[b]	MIC[a]	MBC[a]	MIC[b]	MBC[b]	MIC[a]	MBC[a]	MIC[b]	MBC[b]
A	$[BDHA]_2[RB]$	2	32	2–1	2	1	1	1–0.5	1–0.5	>512	>512	>512	>512	>512	>512	>512	>512
	$[C_{16}Py]_2[RB]$	1	2	1–0.5	4–1	0.5	0.5	0.5	0.5	>512	>512	>512	>512	>512	>512	>512	>512
	[CHX][RB]	0.5	2	0.5	4–1	0.5	0.5	0.5	1–0.5	>512	>512	>512	>512	1	4	8–1	64–8
B	$[Na]_2[RB]$	4	4	8–4	8	4	4	4–2	4–2	>512	>512	>512	>512	>512	>512	>512	>512
	[BDHA][Cl]	0.5	2	0.5	2	0.5	1	0.5	1–0.5	32	128	32	256–128	4	8	8–4	32–16
	$[C_{16}Py][Cl]$	0.5	8	0.5	2	0.5	2	0.5	2–0.5	128	256	128–64	256–128	8	8	8	16
	$[CHX][CH_3COO]_2$	0.5	2	0.5	2	0.5	4	2–0.5	4–1	2	8	2	8	0.5	>4	0.5	16–4
C	2 BDHA:1 RB	1	16	2–1	4–2	1	1	4–2	1	256	>512	>512	>512	>512	>512	>512	>512
	2 C_{16}Py:1 RB	0.5	2	0.5	2	0.5	0.5	0.5	0.5	>512	>512	>512	>512	>512	>512	>512	>512
	1 CHX:1 RB	0.5	8	0.5	8	32	32	1–0.5	1–0.5	>512	>512	>512	>512	>512	>512	>512	>512

[a] Exposure to green light for 30 min.

[b] Dark conditions.

References

1. Doughty MJ. Rose bengal staining as an assessment of ocular surface damage and recovery in dry eye disease-A review. Contact Lens Anterior Eye. 2013;36(6):272-80.
2. Madl AC, Liu CZ, Cirera-Salinas D, Fuller GG, Myung D. A Mucin-Deficient Ocular Surface Mimetic Platform for Interrogating Drug Effects on Biolubrication, Antiadhesion Properties, and Barrier Functionality. ACS Appl Mater Interfaces. 2022;14(16):18016-30.
3. Gamlen TR, Triger DR, Ackery DM, Fleming JS, Grant RW, Kenny RW, et al. Quantitative liver imaging using 131-I Rose Bengal as an index of liver function and prognosis. Gut. 1975;16(9):738-43.
4. Amescua G, Arboleda A, Nikpoor N, Durkee H, Relhan N, Aguilar MC, et al. Rose Bengal Photodynamic Antimicrobial Therapy: A Novel Treatment for Resistant Fusarium Keratitis. Cornea. 2017;36(9):1141-4.
5. Perez-Laguna V, Garcia-Luque I, Ballesta S, Perez-Artiaga L, Lampaya-Perez V, Samper S, et al. Antimicrobial photodynamic activity of Rose Bengal, alone or in combination with Gentamicin, against planktonic and biofilm Staphylococcus aureus. Photodiagnosis Photodyn Ther. 2018;21:211-6.
6. Qin JZ, Kunda N, Qiao GL, Calata JF, Pardiwala K, Prabhakar BS, et al. Colon cancer cell treatment with rose bengal generates a protective immune response via immunogenic cell death. Cell Death Dis. 2017;8:9.
7. Innamarato P, Morse J, Mackay A, Asby S, Beatty M, Blauvelt J, et al. Intralesional injection of rose bengal augments the efficacy of gemcitabine chemotherapy against pancreatic tumors. BMC Cancer. 2021;21(1):12.
8. Klaassen CD. Pharmacokinetics of rose bengal in the rat, rabbit, dog, and Guinea pig. Toxicol Appl Pharmacol. 1976;38(1):85-100.
9. Batistela VR, Pellosi DS, de Souza FD, da Costa WF, Santin SMD, de Souza VR, et al. pK(a) determinations of xanthene derivates in aqueous solutions by multivariate analysis applied to UV-Vis spectrophotometric data. Spectroc Acta Pt A-Molec Biomolec Spectr. 2011;79(5):889-97.
10. Demartis S, Anjani QK, Volpe-Zanutto F, Paredes AJ, Jahan SA, Vora LK, et al. Trilayer dissolving polymeric microneedle array loading Rose Bengal transfersomes as a novel adjuvant in early-stage cutaneous melanoma management. Int J Pharm. 2022;627:14.
11. Panzarini E, Inguscio V, Dini L. Overview of Cell Death Mechanisms Induced by Rose Bengal Acetate-Photodynamic Therapy. Int J Photoenergy. 2011;2011:11.
12. Demartis S, Obinu A, Gavini E, Giunchedi P, Rassu G. Nanotechnology-based rose Bengal: A broad-spectrum biomedical tool. Dyes Pigment. 2021;188:14.

13. Demartis S, Rassu G, Murgia S, Casula L, Giunchedi P, Gavini E. Improving Dermal Delivery of Rose Bengal by Deformable Lipid Nanovesicles for Topical Treatment of Melanoma. Mol Pharm. 2021;18(11):4046-57.
14. Sztandera K, Gorzkiewicz M, Martins ASD, Pallante L, Zizzi EA, Miceli M, et al. Noncovalent Interactions with PAMAM and PPI Dendrimers Promote the Cellular Uptake and Photodynamic Activity of Rose Bengal: The Role of the Dendrimer Structure. J Med Chem. 2021;64(21):15758-71.
15. Rubekina AA, Kamzeeva PN, Alferova VA, Shustova EY, Kolpakova ES, Yakovchuk EV, et al. Hydrophobic Rose Bengal Derivatives Exhibit Submicromolar-to-Subnanomolar Activity against Enveloped Viruses. Biomolecules. 2022;12(11):11.
16. Wang BK, Wang JH, Liu Q, Huang H, Chen M, Li KY, et al. Rose-bengal-conjugated gold nanorods for in vivo photodynamic and photothermal oral cancer therapies. Biomaterials. 2014;35(6):1954-66.
17. Anjani QK, Demartis S, Volpe-Zanutto F, Li HH, Bin Sabri AH, Gavini E, et al. Fluorescence-Coupled Techniques for Determining Rose Bengal in Dermatological Formulations and Their Application to Ex Vivo Skin Deposition Studies. Pharmaceutics. 2023;15(2):21.
18. Costley D, Nesbitt H, Ternan N, Dooley J, Huang YY, Hamblin MR, et al. Sonodynamic inactivation of Gram-positive and Gram-negative bacteria using a Rose Bengal-antimicrobial peptide conjugate. Int J Antimicrob Agents. 2017;49(1):31-6.
19. Nakonieczna J, Wolnikowska K, Ogonowska P, Neubauer D, Bernat A, Kamysz W. Rose Bengal-Mediated Photoinactivation of Multidrug Resistant Pseudomonas aeruginosa Is Enhanced in the Presence of Antimicrobial Peptides. Front Microbiol. 2018;9:15.
20. Shrestha A, Kishen A. Polycationic Chitosan-Conjugated Photosensitizer for Antibacterial Photodynamic Therapy. Photochem Photobiol. 2012;88(3):577-83.
21. Li CC, Lin FM, Sun W, Wu FG, Yang H, Lv RJ, et al. Self-Assembled Rose Bengal-Exopolysaccharide Nanoparticles for Improved Photodynamic Inactivation of Bacteria by Enhancing Singlet Oxygen Generation Directly in the Solution. ACS Appl Mater Interfaces. 2018;10(19):16715-22.
22. Chen HJ, Zhou XB, Wang AL, Zheng BY, Yeh CK, Huang JD. Synthesis and biological characterization of novel rose bengal derivatives with improved amphiphilicity for sono-photodynamic therapy. Eur J Med Chem. 2018;145:86-95.
23. Sztandera K, Marcinkowska M, Gorzkiewicz M, Janaszewska A, Laurent R, Zablocka M, et al. In Search of a Phosphorus Dendrimer-Based Carrier of Rose Bengal: Tyramine Linker Limits Fluorescent and Phototoxic Properties of a Photosensitizer. Int J Mol Sci. 2020;21(12):20.

24. Cole MR, Hobden JA, Warner IM. Recycling Antibiotics into GUMBOS: A New Combination Strategy to Combat Multi-Drug-Resistant Bacteria. Molecules. 2015;20(4):6466-87.
25. Perez RL, Ayala CE, Warner IM. Group of Uniform Materials Based on Organic Salts (GUMBOS): A Review of Their Solid State Properties and Applications. In: Sohel Murshed SM, editor. Ionic Liquids - Thermophysical Properties and Applications: IntechOpen; 2021.
26. Lopez KM, Hobden JA, Warner IM. Octenidine/carbenicillin GUMBOS as potential treatment for oropharyngeal gonorrhoea. J Antimicrob Chemother. 2020;75(12):3576-81.
27. Warner IM, El-Zahab B, Siraj N. Perspectives on Moving Ionic Liquid Chemistry into the Solid Phase. Anal Chem. 2014;86(15):7184-91.
28. Azevedo AMO, Santos JLM, Warner IM, Saraiva MLMFS. GUMBOS and nanoGUMBOS in chemical and biological analysis: A review. Anal Chim Acta. 2020;1133:180-98.
29. Azevedo AMO, Sousa C, Chen M, Ayala CE, Perez RL, Santos JLM, et al. Protein discrimination using erythrosin B-based GUMBOS in combination with UV-Vis spectroscopy and chemometrics. Talanta. 2022;240:11.
30. Magalhaes LM, Nunes C, Lucio M, Segundo MA, Reis S, Lima JLFC. High-throughput microplate assay for the determination of drug partition coefficients. Nat Protoc. 2010;5(11):1823-30.
31. Azevedo AMO, Costa SPF, Dias AFV, Marques AHO, Pinto PCAG, Bica K, et al. Anti-inflammatory choline based ionic liquids: Insights into their lipophilicity, solubility and toxicity parameters. J Mol Liq. 2017;232:20-6.
32. Parmar A, Sharma S. Derivative UV-vis absorption spectra as an invigorated spectrophotometric method for spectral resolution and quantitative analysis: Theoretical aspects and analytical applications: A review. Trac-Trends Anal Chem. 2016;77:44-53.
33. Wiegand I, Hilpert K, Hancock REW. Agar and broth dilution methods to determine the minimal inhibitory concentration (MIC) of antimicrobial substances. Nat Protoc. 2008;3(2):163-75.
34. Clinical and Laboratory Standards Institute, Performance standards for antimicrobial susceptibility testing, Sixteenth informational supplement. Wayne, PA: CLSI document M100-S16CLSI; 2006.
35. European Committee for Antimicrobial Susceptibility Testing (EUCAST) of the European Society of Clinical Microbiology and Infectious Diseases (ESCMID), Determination of minimum inhibitory concentrations (MICs) of antibacterial agents by broth dilution. Clin Microbiol Infect. 2003;9(8):7.
36. Anju VT, Paramanantham P, Lal SBS, Sharan A, Alsaedi MH, Dawoud TMS, et al. Antimicrobial photodynamic activity of rose bengal conjugated multi walled carbon

nanotubes against planktonic cells and biofilm of Escherichia coli. Photodiagnosis Photodyn Ther. 2018;24:300-10.

37. Kumar S, Meena VK, Hazari PP, Sharma SK, Sharma RK. Rose Bengal attached and dextran coated gadolinium oxide nanoparticles for potential diagnostic imaging applications. Eur J Pharm Sci. 2018;117:362-70.

38. Cao YY, Mu TC. Comprehensive Investigation on the Thermal Stability of 66 Ionic Liquids by Thermogravimetric Analysis. Ind Eng Chem Res. 2014;53(20):8651-64.

39. Jordan AN, Siraj N, Das S, Warner IM. Tunable near-infrared emission of binary nano- and mesoscale GUMBOS. RSC Adv. 2014;4(54):28471-80.

40. Vaughan SR, Speller NC, Chhotaray P, McCarter KS, Siraj N, Perez RL, et al. Class specific discrimination of volatile organic compounds using a quartz crystal microbalance based multisensor array. Talanta. 2018;188:423-8.

41. Fleming GR, Knight AWE, Morris JM, Morrison RJS, Robinson GW. Picosecond fluorescence studies of xanthene dyes. J Am Chem Soc. 1977;99(13):4306-11.

42. Rauf MA, Graham JP, Bukallah SB, Al-Saedi MAS. Solvatochromic behavior on the absorption and fluorescence spectra of Rose Bengal dye in various solvents. Spectrochim Acta A-Mol Biomol Spectrosc. 2009;72(1):133-7.

43. Kapoor RC, Jain MK, Mishra VN. Fluorescence and absorption spectra of Rose-Bengal dye in the presence of surfactants. J Lumines. 1981;22(4):429-39.

44. Bilski P, Holt RN, Chignell CF. Premicellar aggregates of Rose Bengal with cationic and zwitterionic surfactants. J Photochem Photobiol A-Chem. 1997;110(1):67-74.

45. Galpothdeniya WIS, Fronczek FR, Cong MY, Bhattarai N, Siraj N, Warner IM. Tunable GUMBOS-based sensor array for label-free detection and discrimination of proteins. J Mat Chem B. 2016;4(8):1414-22.

46. Lopez-Martin I, Burello E, Davey PN, Seddon KR, Rothenberg G. Anion and cation effects on imidazolium salt melting points: A descriptor modelling study. ChemPhysChem. 2007;8(5):690-5.

47. Zhang H, Li MT, Yang BL. Design, Synthesis, and Analysis of Thermophysical Properties for Imidazolium-Based Geminal Dicationic Ionic Liquids. J Phys Chem C. 2018;122(5):2467-74.

48. Jabbari M, Teymoori F. An insight into effect of micelle-forming surfactants on aqueous solubilization and octanol/water partition coefficient of the drugs gemfibrozil and ibuprofen. J Mol Liq. 2018;262:1-7.

49. Tabata A, Nagamune H, Maeda T, Murakami K, Miyake Y, Kourai H. Correlation between resistance of Pseudomonas aeruginosa to quaternary ammonium compounds and expression of outer membrane protein OprR. Antimicrob Agents Chemother. 2003;47(7):2093-9.

50. Morita Y, Tomida J, Kawamura Y. Responses of Pseudomonas aeruginosa to antimicrobials. Front Microbiol. 2014;4:8.

51. Zheng XK, Zhang XY, Zhou BB, Liu SX, Chen WF, Chen LQ, et al. Clinical characteristics, tolerance mechanisms, and molecular epidemiology of reduced susceptibility to chlorhexidine among Pseudomonas aeruginosa isolated from a teaching hospital in China. Int J Antimicrob Agents. 2022;60(1):9.

52. Silhavy TJ, Kahne D, Walker S. The Bacterial Cell Envelope. Cold Spring Harbor Perspect Biol. 2010;2(5):16.

53. Wen X, Zhang XS, Szewczyk G, El-Hussein A, Huang YY, Sarna T, et al. Potassium Iodide Potentiates Antimicrobial Photodynamic Inactivation Mediated by Rose Bengal in In Vitro and In Vivo Studies. Antimicrob Agents Chemother. 2017;61(7):15.

54. Kurosu M, Mitachi K, Yang JS, Pershing EV, Horowitz BD, Wachter EA, et al. Antibacterial Activity of Pharmaceutical-Grade Rose Bengal: An Application of a Synthetic Dye in Antibacterial Therapies. Molecules. 2022;27(1):21.

55. Gurianov Y, Meistelman M, Albo Y, Nisnevitch M, Nakonechny F. Antibacterial Activity of Rose Bengal Entrapped in Organically Modified Silica Matrices. Int J Mol Sci. 2022;23(7):15.

56. Dahl TA, Midden WR, Neckers DC. Comparison of photodynamic action by rose bengal in Gram-positive and Gram-negative bacteria. Photochem Photobiol. 1988;48(5):607-12.

57. Nikaido H. Molecular basis of bacterial outer membrane permeability revisited. Microbiol Mol Biol Rev. 2003;67(4):593-656.

58. Ebbensgaard A, Mordhorst H, Aarestrup FM, Hansen EB. The Role of Outer Membrane Proteins and Lipopolysaccharides for the Sensitivity of Escherichia coli Antimicrobial Peptides. Front Microbiol. 2018;9:13.

59. Manoil D, Filieri A, Schrenzel J, Bouillaguet S. Rose bengal uptake by E. faecalis and F. nucleatum and light-mediated antibacterial activity measured by flow cytometry. J Photochem Photobiol B-Biol. 2016;162:258-65.

60. Horner C, Mawer D, Wilcox M. Reduced susceptibility to chlorhexidine in staphylococci: is it increasing and does it matter? J Antimicrob Chemother. 2012;67(11):2547-59.

61. Horner C, Utsi L, Coole L, Denton M. Epidemiology and microbiological characterization of clinical isolates of Staphylococcus aureus in a single healthcare region of the UK, 2015. Epidemiol Infect. 2017;145(2):386-96.

62. ASTM, Standard Practice for Assessment of Hemolytic Properties of Materials. West Conshohocken, PA: ASTM International; 2017.

63. Schmitt MA, Weisblum B, Gellman SH. Interplay among folding, sequence, and lipophilicity in the antibacterial and hemolytic activities of alpha/beta-peptides. J Am Chem Soc. 2007;129(2):417-28.

64. Goncalves ARP, Paredes X, Cristino AF, Santos FJV, Queiros CSGP. Ionic Liquids-A Review of Their Toxicity to Living Organisms. Int J Mol Sci. 2021;22(11):50.

Chapter 7

Development of an automated yeast-based spectrophotometric method for toxicity screening: application to ionic liquids, GUMBOS, and deep eutectic solvents

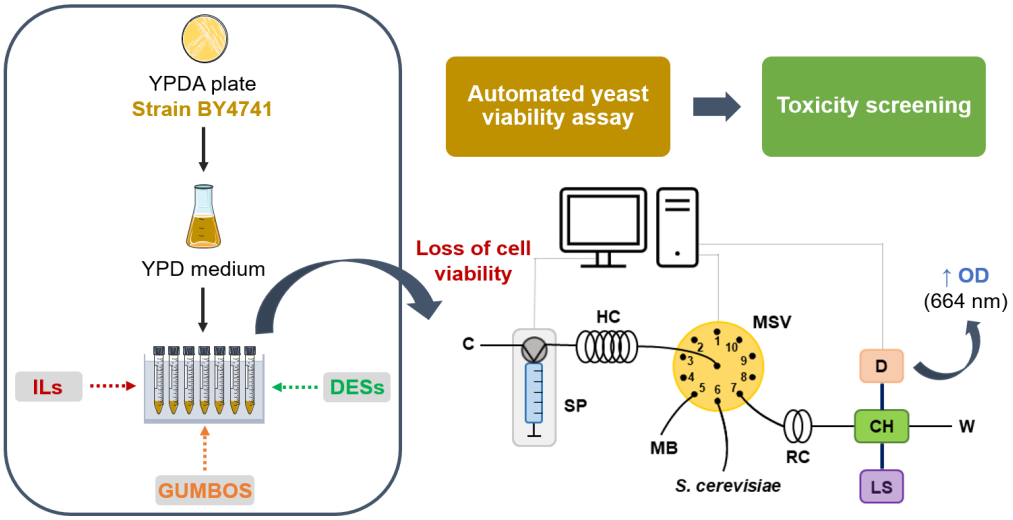

Highlights

- A yeast-based spectrophotometric assay was implemented using an SIA flow system.
- This assay was applied toward toxicity evaluation of ILs, GUMBOS, and DESs.
- IC_{50} values correlated with compound structures and observed toxicities.
- The developed method may be used as an alternative tool for toxicity screening.

Manuscript published after international peer review as "Azevedo AMO, Vilaranda AG, Neves AFDC, Sousa MJ, Santos JLM, Saraiva MLMFS. Development of an automated yeast-based spectrophotometric method for toxicity screening: Application to ionic liquids, GUMBOS, and deep eutectic solvents. Chemosphere. 2021;277:8".

Abstract

Saccharomyces cerevisiae has been used as a eukaryotic model organism for studying the toxic effects of various compounds. In this context, an automated spectrophotometric method based on the enzymatic reduction of methylene blue dye to a colorless product by living yeast cells was implemented in a sequential injection analysis system. Loss of yeast viability/impaired metabolic activity was monitored by an increase in optical density at 664 nm. To prove the usefulness of this approach, the toxicity of ILs (ionic liquids), GUMBOS (group of uniform materials based on organic salts), and DESs (deep eutectic solvents) was examined. Differences obtained between IC_{50} values confirmed the impact of structural elements on each compounds' toxicity. While DESs appeared to be less toxic than ILs, GUMBOS were found to be among the most toxic compounds to yeast cells and thus can be viewed as promising antimicrobial candidates. The automated methodology showed satisfactory repeatability and reproducibility (RSD < 9%), which is in good agreement with Green Chemistry principles. In fact, the method required consumption of only 40 µL of reagents and produced less than 2 mL of effluents per cycle. Thus, the developed assay can be used as an alternative tool for toxicity screening.

Keywords: Deep eutectic solvents; GUMBOS; Ionic liquids; *Saccharomyces cerevisiae*; Toxicity.

7.1. Introduction

European Union regulation No 1907/2006, concerning registration, evaluation, authorization, and restriction of chemicals (REACH), is intended to protect both the environment and human health from hazardous substances. Furthermore, this regulation encourages reduction of testing on vertebrate animals (e.g., mammals and fish), by suggesting alternative methods such as structure-activity relationship models or *in vitro* experiments (1). In this regard, enzymatic inhibition and cell-based assays have proven to be useful for toxicity screening, with distinct advantages including simplicity, rapidity, and cost-saving. These methods also avoid ethical and reliability issues regarding animal research. In fact, interspecies differences and stress-induced changes in physiological parameters can limit the usefulness of animal data for predicting human toxicity (2, 3).

Due to short generation times, rapid growth in inexpensive media, as well as industrial and environmental relevance, microorganisms have been used as indicators of toxicity of chemicals. Yeasts, Gram-negative and Gram-positive bacteria are among the most used microorganisms for such applications and can provide further insights into chemical mechanisms of action (4, 5). The budding yeast *Saccharomyces cerevisiae* (*S. cerevisiae*) offers several advantages over other toxicity models, including simple structure, high homology to mammalian systems, and a fully sequenced genome that can be easily manipulated. In addition, this eukaryotic model organism tolerates a wide range of temperature and pH values, in addition to simple and inexpensive handling (6-8). *S. cerevisiae* has been used to study the toxic effects of several organic/inorganic compounds and nanoparticles, including ionic liquids (9, 10), selenium (11), cadmium (12), silver and copper oxide nanoparticles (13, 14).

Several methods have been employed for determining yeast viability, e.g., the percentage of living cells in a suspension upon exposure to toxic compounds. One of the most frequently used, and the standard in microbiology, is based on counting the number of colony-forming units (CFU) on agar plates, which reflects the number of living cells in a given suspension. However, this method is laborious, time-consuming, and often inaccurate. In this regard, there are also commercially available staining kits to assess live/dead cells, that rely on measuring other parameters such as metabolic activity or cell membrane integrity. However, these methods are relatively expensive, demand specialized equipment and a trained operator (15-17). Due to its unique mode of operation, sequential injection analysis (SIA) appears to be a suitable approach for evaluation of yeast viability and toxicity screening. In fact, since the selection valve, propulsion device, and detector are all automated, it is possible to precisely control assay conditions, reduce the need for operator intervention, and ensure good measurement reproducibility. Additionally, this flow

technique allows reduction in reagent consumption and waste generation (18, 19). Several studies have already confirmed that SIA is a cost-effective tool for implementation of bioassays using whole cells and their application to toxicity studies (20-22).

The interest in ILs as environmentally friendly alternatives to conventional organic solvents is motivated by their unique features, namely low vapor pressure and flammability, great thermal and chemical stability, as well as unique solvation capability for both polar and nonpolar molecules (23, 24). However, several studies have demonstrated that ILs are not as innocuous as initially believed, with some being poorly biodegradable and highly toxic (25). Deep eutectic solvents (DESs) have emerged as alternatives that overcome some limitations associated with ILs. For example, DESs can be easily prepared by mixing a hydrogen bond acceptor (HBA) with a hydrogen bond donor (HBD) at an appropriate molar ratio followed by heating under mild conditions, and thus avoiding purification steps. Additionally, a large number of biodegradable, cheap, and renewable compounds can be used as HBAs or HBDs, making these solvents less expensive and more sustainable than ILs (26, 27).

Although increasing attention has been placed on use of ILs and DESs, much less importance has been given to 'GUMBOS' (*g*roup of *u*niform *m*aterials *b*ased on *o*rganic *s*alts). These novel materials are solid-state analogues of ILs and have thus expanded the number of possible applications of ionic liquid chemistry (28, 29). However, additional toxicity studies are required to clarify the effects of DESs and GUMBOS on the environment and human health to determine if they are safer than ILs. The aim of the study presented here is to develop an automated yeast-based assay that may be applicable as alternative screening tool for evaluating the toxicity of chemical compounds in early stages of development. To prove the suitability of this method, the toxic effects of ILs, GUMBOS, and DESs were assessed.

7.2. Materials and methods

7.2.1. Reagents

Benzyldimethylhexadecylammonium chloride and methylene blue (MB) were purchased from Alfa Aesar and Riedel-de Häen, respectively. Glucose and dimethylsulfoxide (DMSO) were obtained from Merck. All other reagents were purchased from Sigma-Aldrich and used without further purification.

Phosphate buffer (0.1 mol L^{-1}, pH 5.8) was prepared by mixing 460 mL of a 0.2 mol L^{-1} NaH_2PO_4 solution with 40 mL of a Na_2HPO_4 solution of the same concentration, and further

diluting to 1 L using high purity water (Milli-Q, resistivity of 18.2 MΩ.cm). This buffer solution was employed as carrier in the flow system and used for preparation of a 0.20 mmol L^{-1} MB solution. For the yeast-based assay, solutions with increasing concentrations of ILs and DESs (from 25 to 2500 µmol L^{-1}), were prepared daily in the same buffer. The poorly-water soluble EB-based GUMBOS were first dissolved in DMSO, and then working standards were obtained by diluting the stock solution with phosphate buffer (2% DMSO final concentration).

7.2.2. Synthesis of GUMBOS and DESs

EB-based GUMBOS were prepared using a simple metathesis reaction (30). The sodium cations of EB dye were exchanged using three bulky organic cations (BAC, benzyldimethylhexadecylammonium; N_{11116}, hexadecyltrimethylammonium; and P_{4444}, tetrabutylphosphonium) at a molar ratio of 1.1 to 2. Both cation and anion were dissolved using phosphate buffer pH 7.4 and then stirred for 24 h at room temperature. Finally, GUMBOS were washed several times with water to remove any byproduct and subsequently freeze-dried.

DESs were synthesized using procedures reported in the literature (31-33). Briefly, eutectic mixtures were prepared by stirring and heating the two components in an oil bath at 80/100 ºC until a homogeneous liquid was obtained. The compounds 1-butyl-3-methylimidazolium chloride ([bmim][Cl]), choline chloride ([chol][Cl]), and tetrabutylammonium chloride ($[N_{4444}][Cl]$) were used as HBAs, and mixed with zinc chloride ($ZnCl_2$), urea (U), and glycerol (Gly), at respective molar ratios of 1:1, 1:2, and 1:5. The synthesized compounds were vacuum dried prior to toxicity evaluation, and then stored in an anhydrous atmosphere until further use. Chemical structures, names, and abbreviations of the ions, HBAs, and HBDs used to form the ILs, GUMBOS, and DESs tested in this work are provided in Fig. S7.1.

7.2.3. Yeast strain and culture conditions

S. cerevisiae BY4741 (MATa *his3*Δ1 *leu2*Δ0 *met15*Δ0 *ura3*Δ0) used in this study was grown on YPDA plates (1% w/v yeast extract, 2% w/v bacto-peptone, glucose, and agar) at 30 ºC for 48 h, and further maintained at 4 ºC for 2 weeks. Prior to toxicity testing, *S. cerevisiae* cells were subcultured in medium of the same composition, but without agar (YPD medium), and incubated overnight using a shaking water bath (30 ºC, 100 rpm). Cells from the mid-exponential growth phase (OD_{600nm} = 0.5-0.6) were separated into two fractions, one of which was boiled for 2 min. Five different mixtures of heat-killed and living *S. cerevisiae* cells (V_f = 2 mL) were also prepared and used as viability standards. Afterwards, yeast cells were harvested by centrifugation (5250 *g*, 15 min), washed twice with 4 mL of phosphate

buffer solution (0.1 mol L^{-1}, pH 5.8), and resuspended in 2 mL of the same buffer. Cell suspensions and MB dye were then alternatively aspirated into the flow system.

7.2.4. Toxicity assessment

For toxicity evaluation, yeast cells from the original culture medium (OD_{600nm} = 0.5-0.6) were harvest and washed as described in the subsection above. Then, pellets were resuspended in 200 µL of tested compounds (10–2500 µmol L^{-1} concentration range) and incubated for a 2 h period at room temperature. In parallel, an equal volume of acetic acid solution (180 mmol L^{-1}, pH 3.0) was added to a tube containing the same cell concentration. This tube served as a positive control since acetic acid is known to induce loss of cell viability in *S. cerevisiae* (34). To further assess the effect of DMSO on cell viability, yeast cells were treated with the same percentage of organic solvent (2%), which caused only a slight loss of yeast viability, similar to what has been previously reported (35). After the incubation time, cells were harvest, washed twice, and resuspended in the same volume (2 mL) of 0.1 mol L^{-1} phosphate buffer (pH 5.8). These cell suspensions were then used to build dose-response curves of ILs, GUMBOS, and DESs.

7.2.5. Flow apparatus

The SIA system used for evaluating yeast cell viability upon exposure to tested compounds is depicted in Fig. 7.1. This system comprises a bi-directional syringe pump (Crison Burette 1S, Alella, Spain) and a 10-port multiposition Cheminert® selection valve (VICI-Valco Instruments, Houston, USA). The automatic burette was equipped with a single 5 mL glass syringe (Hamilton, Bonaduz, Switzerland), which was connected to a solenoid valve. Optical density (OD) measurements were acquired using an Ocean Optics USB4000 spectrometer fitted with an LS-1-LL tungsten halogen light source and a 1 cm cuvette holder (CH), where a flow cell was placed with internal volume of 18 µL (Hellma 178.712-QS, Müllheim, Germany). The CH was connected to the light source and miniature spectrometer using two optical fibers with a core diameter of 600 µm (Ocean Optics, QP600-2-UV-BX).

All flow lines, including the holding and reaction coils (HC and RC), were constructed using polytetrafluoroethylene tubing of 0.8 mm internal diameter. Both HC and RC were shaped using a figure eight configuration and respective lengths of 2 and 0.15 m. The syringe pump (SP), multiposition selection valve (MSV), and spectrometer were connected to a computer using a RS-232C interface and controlled using homemade software written in Visual Basic (22). Data acquisition was performed using Ocean Optics' SpectraSuite software.

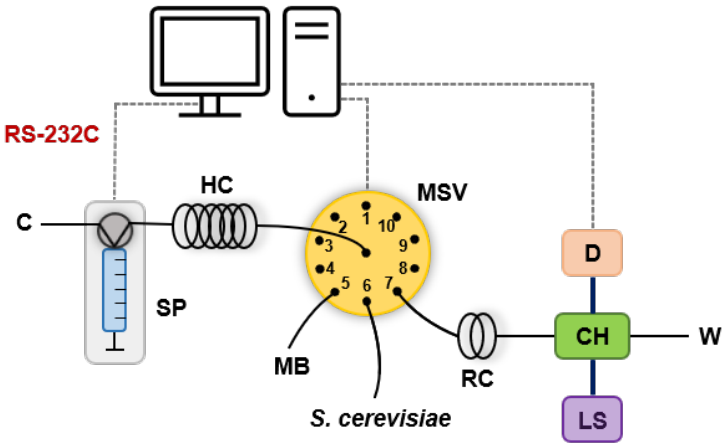

Fig. 7.1. Schematic representation of the SIA system used to evaluate yeast cell viability. C, carrier (phosphate buffer 0.1 mol L^{-1}, pH 5.8); SP, syringe pump (5 mL syringe capacity); HC, holding coil (2 m length); MSV, multiposition selection valve; MB, methylene blue; *S. cerevisiae*, *Saccharomyces cerevisiae* cells; RC, reaction coil (0.15 m length); CH, cuvette holder (connected to the light source and spectrometer via optical fibers); D, detector (664 nm); LS, light source; W, waste.

7.2.6. Sequential injection procedure

To assess loss of cell viability (%) after treatment with selected compounds, a five-step analytical cycle was established (Table 7.1). Briefly, two aliquots of 10 µL of MB dye and *S. cerevisiae* cells were alternatively aspirated into the HC (steps 1–4). The flow was then reversed, and the aspirated sequence was propelled through the RC into the detector flow cell (step 5). Loss of yeast viability/impaired metabolic activity was shown by an increase in OD at 664 nm (36). Toxicity results were expressed as concentration of tested compound that reduced cell viability by 50% (IC_{50}) and were calculated from dose-response curves using polynomial equations. One-way ANOVA-Tukey's test and t-test were used to compare IC_{50} values and determine statistically significant differences between compounds containing the same cation or anion.

Table 7.1. Protocol sequence for evaluation of yeast cell viability in the absence and presence of tested compounds.

Step	Valve position	Flow rate (mL min^{-1})	Volume (µL)	Time (s)	Description
1	5	0.5	10	1.2	Aspiration of MB
2	6	0.5	10	1.2	Aspiration of *S. cerevisiae*
3	5	0.5	10	1.2	Aspiration of MB
4	6	0.5	10	1.2	Aspiration of *S. cerevisiae*
5	7	1.0	1875	112.5	Propulsion to the detector

7.3. Results and discussion

In this section, we describe development and optimization of an automated spectrophotometric method for toxicity screening. The *S. cerevisiae*-based assay was implemented in a SIA system and relied on ability of living yeast cells to enzymatically reduce MB dye to a colourless product (15). Following exposure to compounds under study, loss of cell viability/decreased metabolic activity was evidenced through an increase in OD signal at 664 nm.

7.3.1. Optimization of the automated yeast-based assay

The first step in developing the automated procedure was adaptation of a previously described MB dye reduction test to a SIA format (36). Then, the assay was optimized in a strictly aqueous medium using a univariate approach. Results were analysed by considering the difference in OD signal between heat-killed and living *S. cerevisiae* cells. Optimized parameters and selected values are presented in Table 7.2. More detailed information can be found in Supplementary Material (Fig. S7.2).

Table 7.2. Results of optimization of the automated yeast viability assay.

Parameter	Range	Selected value
Buffer pH	5.8–7.4	5.8
MB concentration (mmol L^{-1})	0.04–0.20	0.20
MB and yeast volumes (µL)	10–25	20
Propulsion flow rate (mL min^{-1})	0.5–1.5	1.0
RC length (m)	0.15–0.30	0.15

The pH of phosphate buffer used to prepare MB dye solution and *S. cerevisiae* cell suspensions, as well as carrier in the flow system, was studied within the range of 5.8–7.4, with a value of 5.8 being chosen. MB concentration was analyzed between 0.04 and 0.20 mmol L^{-1}, with results showing an increase in difference in OD signal between heat-killed and living yeast cells with increments of dye concentration up to 0.20 mmol L^{-1}. This concentration was then selected for final studies. Higher concentrations were not tested since they could affect yeast plasma membrane functions (36).

After fixing the concentration of MB dye, its volume was tested over the range 10–25 µL. It was observed that OD signals reached maximum difference at a volume of 20 µL and then decreased. Influence of yeast suspension volume was also studied under the same experimental conditions. Results showed enhancement of signal difference between heat-killed and living cells in the range of 10 to 20 µL. Thus, this volume was selected in order to obtain maximum sensitivity.

A flow rate of 0.5 mL min^{-1} was adopted for aspiration of MB dye and yeast suspension, ensuring good compromise between repeatability and sampling rate. The propulsion flow rate was studied between 0.5 and 1.5 mL min^{-1}, with best results being obtained by propelling the aspirated zone to the detector at a flow rate of 1.0 mL min^{-1}. In this way, dilution of aliquots is avoided without sensitivity prejudice.

A RC was positioned between the MSV and CH and its length studied between 0.15 and 0.30 m, with RC of 0.15 m finally selected. Smaller reactors were not considered because they would not guarantee proper mixing conditions.

Regarding order of aspiration of *S. cerevisiae* cells and MB dye into the HC, best results were achieved when MB was aspirated first. Double intercalation of MB and yeast was fixed in the optimized analytical cycle since it resulted in highest OD signals' difference among tested sequences. A solution of acetic acid 180 mmol L^{-1} (pH 3.0) was used as a positive control, allowing study of mixing efficiency and establishing the contact time between yeast cells and tested compounds.

A seven-point calibration curve was obtained by plotting the percentage of cell viability loss (υ) against OD measured at 664 nm (x). Regression analysis was then applied to estimate the following equation: υ = 1014 (±87) x - 199 (±22), R^2 = 0.9944. The repeatability of SIA procedure was calculated using relative standard deviation (RSD) of ten consecutive measurements in absence and presence of [bmim][Ac] (2500 μmol L^{-1}). The obtained values were 7.9 and 8.7%, respectively. These results are satisfactory, particularly if we consider that they illustrate the performance of an automated assay using whole cells and solutions with high viscosity. Additionally, the flow system displayed acceptable reproducibility with an RSD of 6.5% (n = 7). Under optimized conditions, it was possible to conduct 31 cycles per hour, producing less than 2 mL of effluent in each.

7.3.2. Application of the automated spectrophotometric assay for toxicity evaluation of ILs, GUMBOS, and DESs

After optimizing assay conditions, the effect of eleven ILs, three GUMBOS, and three DESs on yeast cell viability was assessed. The tested compounds possessed different chemical structures, incorporating various cations and anions in the case of ILs/GUMBOS or distinct HBAs and HBDs for DESs. In general, the percentage of cell viability loss increased in the presence of all compounds under study and was concentration-dependent. Dose-response curves are provided in Fig. 7.2 and calculated IC_{50} values are listed in Table S7.1, and also shown in Fig. 7.3.

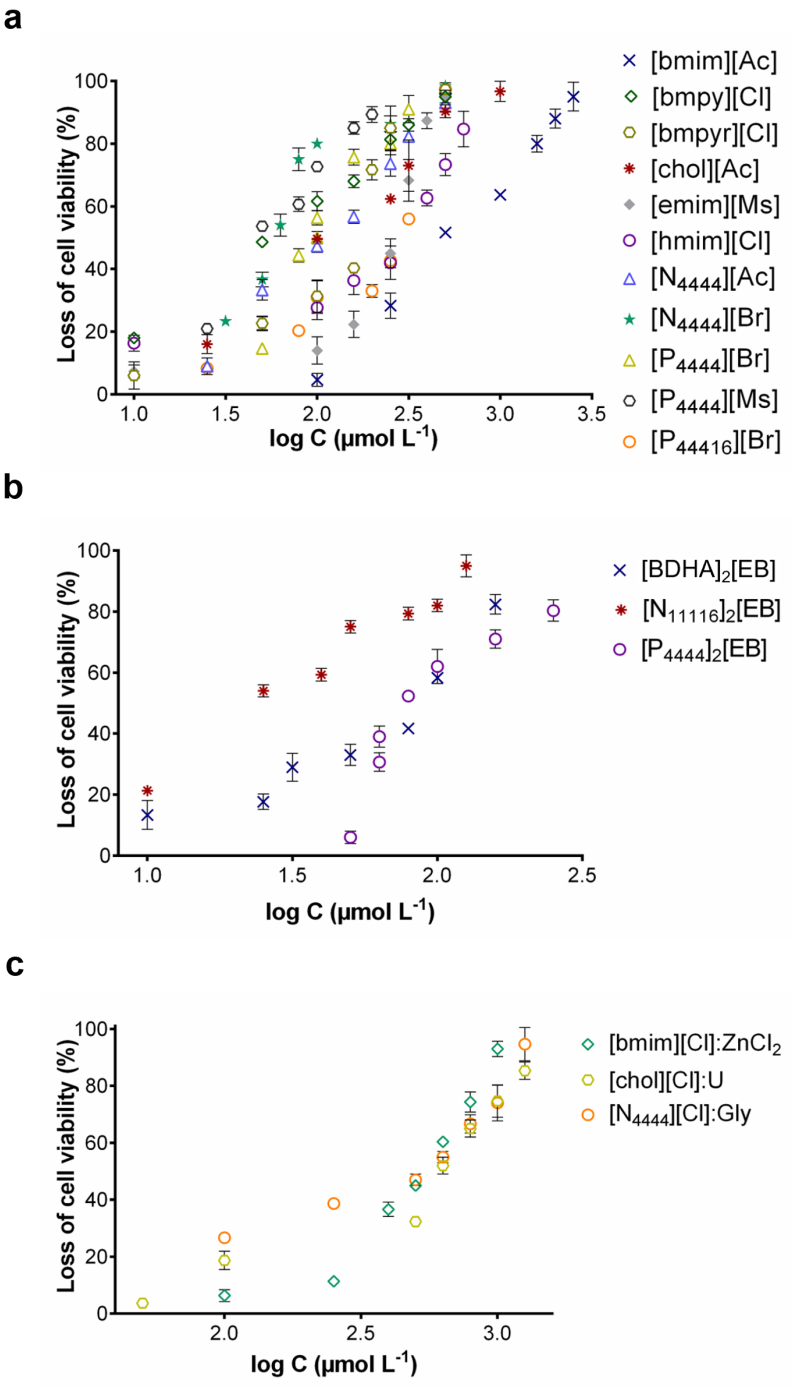

Fig. 7.2. Percentage of loss of yeast cell viability after 2 h exposure to different concentrations of (a) ILs, (b) GUMBOS, and (c) DESs. Each point and error bar represents the mean and standard deviation of three independent experiments performed in triplicate. Some error bars are smaller than the symbols.

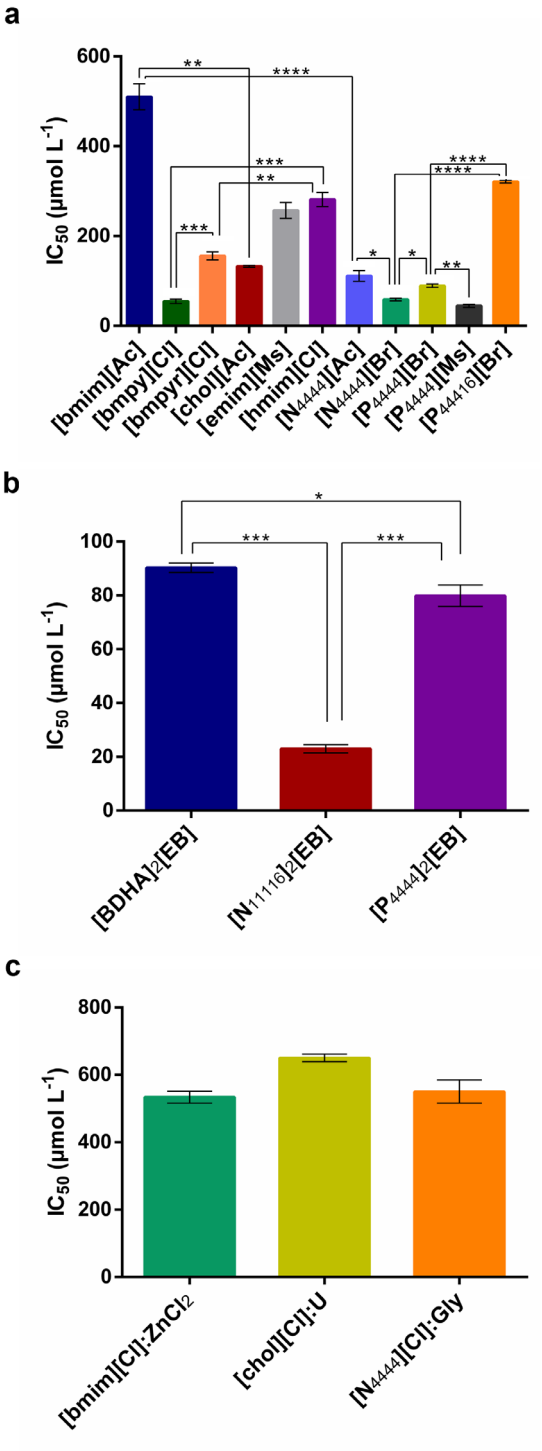

Fig. 7.3. IC_{50} values (μmol L^{-1}) obtained for (a) ILs, (b) GUMBOS, and (c) DESs. These values were calculated from the dose-response curves shown in Fig. 7.2. Statistically differences between compounds containing the same cation or anion was assessed by use of GraphPad Prism software *via* one-way ANOVA-Tukey's test or t-test (*P ≤ 0.05, **P ≤ 0.01, ***P ≤ 0.001, and ****P ≤ 0.0001).

7.3.2.1. ILs

Cation's impact on yeast viability was assessed by resorting to six main cores: ammonium, choline, imidazolium, phosphonium, pyridinium, and pyrrolidinium. When comparing the non-aromatic pyrrolidinium ([bmpyr][Cl], IC_{50} = 156 ± 9 µmol L^{-1}) with the aromatic pyridinium-based IL ([bmpy][Cl], IC_{50} = 55 ± 5 µmol L^{-1}), a three-fold increase in toxicity towards yeast cells was observed. Other authors have also found that the pyridinium cation is more toxic towards freshwater organisms (e.g. *Pseudokirchneriella subcapitata* and *Daphnia magna*), as well as cell lines (for example, MCF7) than the pyrrolidinium core (37-39). Additionally, it was noticed that the pyridinium cationic head group exerts a greater toxic effect on *S. cerevisae* cells than the imidazolium cation ([hmim][Cl], IC_{50} = 282 ± 16 µmol L^{-1}), which concurs with previous findings obtained for *Vibrio fischeri* (21, 40). In fact, a six-membered ring such as the pyridinium cation is known to be more toxic than the imidazolium five-membered ring (25, 41).

After exposure of yeast cells to the ILs $[N_{4444}][Br]$ (IC_{50} = 59 ± 3 µmol L^{-1}) and $[P_{4444}][Br]$ (IC_{50} = 89 ± 4 µmol L^{-1}), which have the same anion, it was verified that the phosphonium core is less toxic than the ammonium one. Kumar and Malhotra also reported that phosphonium-based ILs are less cytotoxic and more active against human tumor cells when compared with their ammonium analogues (42). This is likely because the phosphonium head group is bulkier than its nitrogen-containing derivative, leading to a decrease in positive charge density and thus weaker electrostatic interactions (43, 44). Furthermore, the toxicity mechanism of quaternary ammonium compounds seems to be related to disruption of yeast plasma membrane (45, 46). Statistically significant differences were also found between the pairs [bmim][Ac]/$[N_{4444}]$[Ac] and [bmim][Ac]/[chol][Ac] (P = 0.0001 and 0.0038, respectively). These results support previous reports that ammonium-based ILs exhibit higher toxicity than those containing imidazolium cations (47, 48). A distinct toxicity mechanism from that proposed for imidazolium-based ILs may explain these observed differences. In fact, ILs incorporating the imidazolium cation appear to act by targeting yeast mitochondria (9).

The effect of side chain length on cell viability was assessed by comparing results obtained with the ILs $[P_{4444}][Br]$ and $[P_{44416}][Br]$. In contrast to expectation, $[P_{44416}][Br]$ was found to be about four times less toxic than $[P_{4444}][Br]$ (IC_{50} = 321 ± 3 vs 89 ± 4 µmol L^{-1}). This result is corroborated by other studies, which have found a relationship between loss of antimicrobial activity and increase in phosphonium alkyl chain length (49-51). It has been noticed that from a certain side chain length, toxicity cannot be increased due to the "cut-off" effect (51, 52). Additionally, different explanations have been proposed for this phenomenon, including poor solubility and a reduction in uptake of high molecular weight compounds due to steric effects (50, 53).

After studying the impact of cation and alkyl chain length on ILs' toxicity towards *S. cerevisiae* cells, the influence of common anions (acetate, bromide, and methanesulfonate) was further assessed. Evaluation of results showed that the anion used also affects ILs' toxic behavior, thus confirming previous observations (25, 54). Moreover, the most statistically significant difference was observed between $[P_{4444}][Br]$ and $[P_{4444}][Ms]$ ($P = 0.0036$), with the last one being the most toxic among tested ILs. This may be attributed to the high aqueous solubility and toxicity of methanesulfonate anion (55, 56). Phosphonium ILs containing methanesulfonate as the anionic counterpart also showed extremely high toxicity against *Drosophila melanogaster* S2 cells (55).

7.3.2.2. GUMBOS

The IC_{50} values of EB-based GUMBOS ranged from 23 ± 1 ($[N_{11116}]_2[EB]$) to 90 ± 2 μmol L^{-1} ($[BAC]_2[EB]$), demonstrating the impact of cationic head group on yeast cell viability. Similar to what was observed for ILs, linear ammonium cation (N_{11116}^+) was found to be more toxic towards *S. cerevisiae* cells than phosphonium (P_{4444}^+). However, and in accordance to what is described in the literature, inclusion of a benzyl group at one of the cation's alkyl side chains leads to reduction of toxicity (48). Overall, the toxicity of cations to yeast cells followed the trend: $N_{11116}^+ > P_{4444}^+ > BAC^+$.

When compared with other tested compounds, EB-based GUMBOS are among the most toxic, which is not surprising since other authors have reported that EB dye can induce DNA damage in HepG2 cells and enhance oxidative stress in CHO cell line (57, 58). Additionally, previous reports have shown that EB-mediated photodynamic therapy is effective against *Candida albicans*, *Enterococcus hirae*, *Escherichia coli*, *Listeria innocua*, and *Staphylococcus aureus* planktonic cells and biofilms (59, 60). These results support the potential use of EB-based GUMBOS for therapeutic purposes.

7.3.2.3. DESs

Results obtained in this study corroborate the belief that DESs are less toxic than ILs, as evidenced by higher IC_{50} values (Table S7.1) (61). It was also observed that toxicity of DESs is composition-dependent, which is in good agreement with previous findings (61, 62). In fact, [bmim][Cl]:$ZnCl_2$ (1:1) displayed the greatest toxicity towards *S. cerevisiae* cells, which can be attributed to the toxic properties of metal component ($ZnCl_2$). Other studies have also found that $ZnCl_2$-based DESs showed the highest inhibition zone diameter against tested fungi (*Aspergillus niger*, *Candida cylindracea*, *Lentinus tigrinus*, and *Phanerochaete chrysosporium*) and the lowest lethal concentration for the fish *Cyprinus carpio* (63, 64) In contrast, the use of natural raw materials, e.g., urea and glycerol, resulted in compounds

with decreased toxicity (65, 66). Macario and colleagues reported that [chol][Cl]:U do not significantly affect MNT-1 cell viability, thus corroborating our results (67).

7.4. Conclusions

In this study, we have developed a new spectrophotometric method based on SIA for assessing the toxic effect of different groups of compounds on yeast cells. This assay focuses on the ability of living *S. cerevisiae* cells to enzymatically reduce MB dye to a colorless product. Thus, the toxicity of ILs, GUMBOS, and DESs could be simply monitored by an increase in OD at 664 nm, proving to be a good alternative to more laborious and time-consuming methods, while following Green Chemistry principles.

Differences obtained between IC_{50} values highlight the impact of a given compounds' chemical structure on its toxicity. In fact, it was observed that ILs containing pyridinium and ammonium cations or with methanesulfonate anion caused a higher toxicity effect on yeast cells. Although GUMBOS are among the compounds with lowest IC_{50} values, this potential disadvantage suggest use as promising candidates for antimicrobial applications. In contrast to GUMBOS, and as expected, DESs demonstrated lower toxicity than ILs. Finally, it is worth mentioning that results gathered from this work may complement available toxicity data, thus providing guidance for design of less harmful or even task-specific compounds.

SUPPLEMENTARY MATERIAL

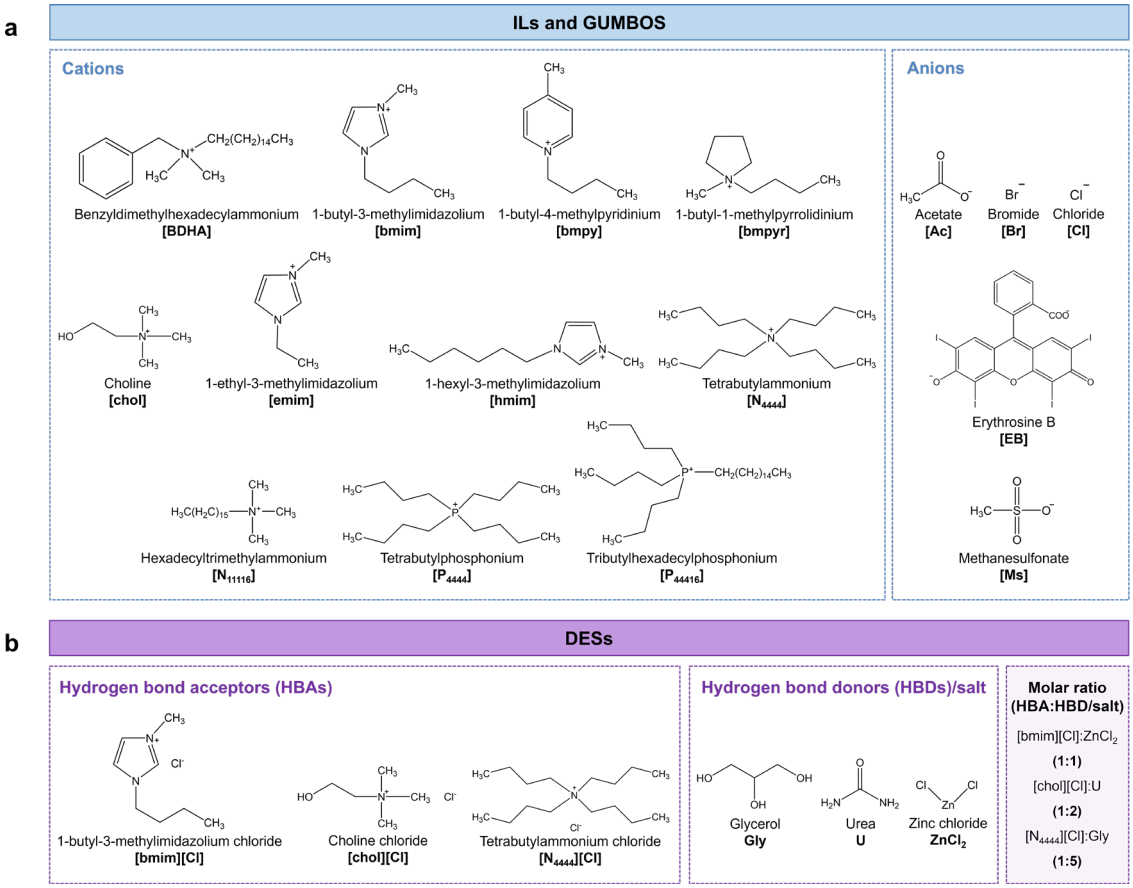

Fig. S7.1. (a) Chemical structures, names, and abbreviations of the cations and anions reported in this work. (b) Hydrogen bond acceptors and hydrogen bond donors/salt used for synthesis of DESs.

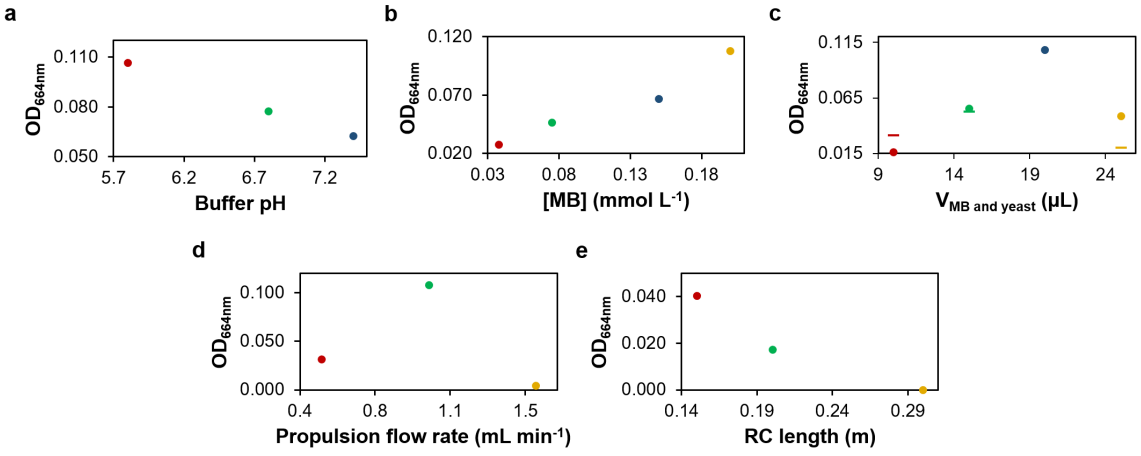

Fig. S7.2. Effect of (a) buffer pH, (b) MB concentration, (c) MB (circles) and yeast (lines) volumes, (d) propulsion flow rate, and (e) RC length on OD signal at 664 nm.

Table S7.1. Toxicity of the studied compounds towards yeast cells expressed as IC_{50} values (µmol L^{-1}), which represents the concentration necessary to reduce cell viability by 50%. *S. cerevisiae* cells were exposed to the tested compounds for 2 h at room temperature.

Class	Compound	Concentration range (µmol L^{-1})	IC_{50} (µmol L^{-1})
ILs	[bmim][Ac]	100–2500	510 ± 29
	[bmpy][Cl]	10–500	54 ± 4
	[bmpyr][Cl]	10–500	156 ± 9
	[chol][Ac]	25–1000	133 ± 2
	[emim][Ms]	10–500	257 ± 18
	[hmim][Cl]	10–650	282 ± 16
	$[N_{4444}][Ac]$	25–1000	111 ± 12
	$[N_{4444}][Br]$	30–500	59 ± 3
	$[P_{4444}][Br]$	50–500	89 ± 4
	$[P_{4444}][Ms]$	25–500	46 ± 3
	$[P_{44416}][Br]$	25–500	321 ± 3
GUMBOS	$[BDHA]_2[EB]$	10–150	90 ± 2
	$[N_{11116}]_2[EB]$	10–125	23 ± 1
	$[P_{4444}]_2[EB]$	25–250	80 ± 4
DESs	[bmim][Cl]:$ZnCl_2$	100–1000	534 ± 18
	[chol][Cl]:U	50–1250	651 ± 11
	$[N_{4444}]$[Cl]:Gly	100–650	552 ± 33

References

1. EC. Regulation No 1907/2006 [Available from: http://data.europa.eu/eli/reg/2006/1907/2014-04-10.

2. Rehberger K, Kropf C, Segner H. In vitro or not in vitro: a short journey through a long history. Environ Sci Eur. 2018;30:12.

3. Kim TW, Che JH, Yun JW. Use of stem cells as alternative methods to animal experimentation in predictive toxicology. Regul Toxicol Pharmacol. 2019;105:15-29.

4. Gaytan BD, Vulpe CD. Functional toxicology: tools to advance the future of toxicity testing. Front Genet. 2014;5:10.

5. Sivapragasam M, Moniruzzaman M, Goto M. An Overview on the Toxicological Properties of Ionic Liquids toward Microorganisms. Biotechnol J. 2020;15(4):9.

6. Rodriguez CE, Shinyashiki M, Froines J, Yu RC, Fukuto JM, Cho AK. An examination of quinone toxicity using the yeast Saccharomyces cerevisiae model system. Toxicology. 2004;201(1-3):185-96.

7. Tian J, Ji ZH, Wang FB, Song MY, Li H. The Toxic Effects of Tetrachlorobisphenol A in Saccharomyces cerevisiae Cells via Metabolic Interference. Sci Rep. 2017;7:10.

8. Martin-Yken H. Yeast-Based Biosensors: Current Applications and New Developments. Biosensors-Basel. 2020;10(5):19.

9. Dickinson Q, Bottoms S, Hinchman L, McIlwain S, Li S, Myers CL, et al. Mechanism of imidazolium ionic liquids toxicity in Saccharomyces cerevisiae and rational engineering of a tolerant, xylose-fermenting strain. Microb Cell Fact. 2016;15:13.

10. Missoun F, de los Rios AP, Ortiz-Martinez V, Salar-Garcia MJ, Hernandez-Fernandez J, Hernandez-Fernandez FJ. Discovering Low Toxicity Ionic Liquids for Saccharomyces cerevisiae by Using the Agar Well Diffusion Test. Processes. 2020;8(9):18.

11. Herrero E, Wellinger RE. Yeast as a model system to study metabolic impact of selenium compounds. Microb Cell. 2015;2(5):139-49.

12. Ozturk M, Metin M, Altay V, De Filippis L, Unal BT, Khursheed A, et al. Molecular Biology of Cadmium Toxicity in Saccharomyces cerevisiae. Biol Trace Elem Res. 2021:15.

13. Kasemets K, Kaosaar S, Vija H, Fascio U, Mantecca P. Toxicity of differently sized and charged silver nanoparticles to yeast Saccharomyces cerevisiae BY4741: a nano-biointeraction perspective. Nanotoxicology. 2019;13(8):1041-59.

14. Chen XQ, Zhang RX, Sun J, Simth N, Zhao MY, Lee J, et al. A novel assessment system of toxicity and stability of CuO nanoparticles via copper super sensitive Saccharomyces cerevisiae mutants. Toxicol Vitro. 2020;69:10.

15. Kwolek-Mirek M, Zadrag-Tecza R. Comparison of methods used for assessing the viability and vitality of yeast cells. FEMS Yeast Res. 2014;14(7):1068-79.

16. Nandy SK, Knudsen PB, Rosenkjaer A, Lantz AE, Thykaer J, Workman M. A high-throughput method for quantifying metabolically active yeast cells. Yeast. 2015;32(6):461-8.
17. Feizi A, Zhang YB, Greenbaum A, Guziak A, Luong M, Chan RYL, et al. Rapid, portable and cost-effective yeast cell viability and concentration analysis using lensfree on-chip microscopy and machine learning. Lab Chip. 2016;16(22):4350-8.
18. Mesquita RBR, Rangel AOSS. A review on sequential injection methods for water analysis. Anal Chim Acta. 2009;648(1):7-22.
19. van Staden JF. Application of phthalocyanines in flow- and sequential-injection analysis and microfluidics systems: A review. Talanta. 2015;139:75-88.
20. Costa SPF, Justina VD, Bica K, Vasiloiu M, Pinto PCAG, Saraiva MLMFS. Automated evaluation of pharmaceutically active ionic liquids' (eco)toxicity through the inhibition of human carboxylesterase and Vibrio fischeri. J Hazard Mater. 2014;265:133-41.
21. Costa SPF, Pinto PCAG, Lapa RAS, Saraiva MLMFS. Toxicity assessment of ionic liquids with Vibrio fischeri: An alternative fully automated methodology. J Hazard Mater. 2015;284:136-42.
22. Costa SPF, Cunha E, Azevedo AMO, Pereira SAP, Neves AFDC, Vilaranda AG, et al. Microfluidic Chemiluminescence System with Yeast Saccharomyces cerevisiae for Rapid Biochemical Oxygen Demand Measurement. ACS Sustain Chem Eng. 2018;6(5):6094-101.
23. Vekariya RL. A review of ionic liquids: Applications towards catalytic organic transformations. J Mol Liq. 2017;227:44-60.
24. Singh SK, Savoy AW. Ionic liquids synthesis and applications: An overview. J Mol Liq. 2020;297:23.
25. Costa SPF, Azevedo AMO, Pinto PCAG, Saraiva MLMFS. Environmental Impact of Ionic Liquids: Recent Advances in (Eco)toxicology and (Bio)degradability. ChemSusChem. 2017;10(11):2321-47.
26. Zhang QH, Vigier KD, Royer S, Jerome F. Deep eutectic solvents: syntheses, properties and applications. Chem Soc Rev. 2012;41(21):7108-46.
27. Song Z, Hu XT, Wu HY, Mei MC, Linke S, Zhou T, et al. Systematic Screening of Deep Eutectic Solvents as Sustainable Separation Media Exemplified by the CO2 Capture Process. ACS Sustain Chem Eng. 2020;8(23):8741-51.
28. Warner IM, El-Zahab B, Siraj N. Perspectives on Moving Ionic Liquid Chemistry into the Solid Phase. Anal Chem. 2014;86(15):7184-91.
29. Azevedo AMO, Santos JLM, Warner IM, Saraiva MLMFS. GUMBOS and nanoGUMBOS in chemical and biological analysis: A review. Anal Chim Acta. 2020;1133:180-98.

30. Galpothdeniya WIS, Fronczek FR, Cong MY, Bhattarai N, Siraj N, Warner IM. Tunable GUMBOS-based sensor array for label-free detection and discrimination of proteins. J Mat Chem B 2016;4(8):1414-22.
31. Abbott AP, Capper G, Davies DL, Rasheed RK, Tambyrajah V. Novel solvent properties of choline chloride/urea mixtures. Chem Commun. 2003(1):70-1.
32. Liu YT, Chen YA, Xing YJ. Synthesis and characterization of novel ternary deep eutectic solvents. Chin Chem Lett. 2014;25(1):104-6.
33. Mjalli FS, Naser J, Jibril B, Alizadeh V, Gano Z. Tetrabutylammonium Chloride Based Ionic Liquid Analogues and Their Physical Properties. J Chem Eng Data. 2014;59(7):2242-51.
34. Trindade D, Pereira C, Chaves SR, Manon S, Corte-Real M, Sousa MJ. VDAC regulates AAC-mediated apoptosis and cytochrome c release in yeast. Microb Cell. 2016;3(10):369-79.
35. Sadowska-Bartosz I, Paczka A, Molon M, Bartosz G. Dimethyl sulfoxide induces oxidative stress in the yeast Saccharomyces cerevisiae. FEMS Yeast Res. 2013;13(8):820-30.
36. Bonora A, Mares D. A Simple Colorimetric Method For Detecting Cell Viability in Cultures of Eukaryotic Microorganisms. Curr Microbiol. 1982;7(4):217-22.
37. Pretti C, Chiappe C, Baldetti I, Brunini S, Monni G, Intorre L. Acute toxicity of ionic liquids for three freshwater organisms: Pseudokirchneriella subcapitata, Daphnia magna and Danio rerio. Ecotox Environ Safe. 2009;72(4):1170-6.
38. Pham TPT, Cho CW, Yun YS. Structural effects of ionic liquids on microalgal growth inhibition and microbial degradation. Environ Sci Pollut Res. 2016;23(5):4294-300.
39. Kumar RA, Papaiconomou N, Lee JM, Salminen J, Clark DS, Prausnitz JM. In Vitro Cytotoxicities of Ionic Liquids: Effect of Cation Rings, Functional Groups, and Anions. Environ Toxicol. 2009;24(4):388-95.
40. Montalban MG, Hidalgo JM, Collado-Gonzalez M, Banos FGD, Villora G. Assessing chemical toxicity of ionic liquids on Vibrio fischeri: Correlation with structure and composition. Chemosphere. 2016;155:405-14.
41. Ventura SPM, Goncalves AMM, Sintra T, Pereira JL, Goncalves F, Coutinho JAP. Designing ionic liquids: the chemical structure role in the toxicity. Ecotoxicology. 2013;22(1):1-12.
42. Kumar V, Malhotra SV. Study on the potential anti-cancer activity of phosphonium and ammonium-based ionic liquids. Bioorg Med Chem Lett. 2009;19(16):4643-6.
43. Arning J, Stolte S, Boschen A, Stock F, Pitner WR, Welz-Biermann U, et al. Qualitative and quantitative structure activity relationships for the inhibitory effects of

cationic head groups, functionalised side chains and anions of ionic liquids on acetylcholinesterase. Green Chem. 2008;10(1):47-58.

44. Agatemor C, Ibsen KN, Tanner EEL, Mitragotri S. Ionic liquids for addressing unmet needs in healthcare. Bioeng Transl Med. 2018;3(1):7-25.

45. McDonnell G, Russell AD. Antiseptics and disinfectants: Activity, action, and resistance. Clin Microbiol Rev. 1999;12(1):147-79.

46. Kapitanov IV, Jordan A, Karpichev Y, Spulak M, Perez L, Kellett A, et al. Synthesis, self-assembly, bacterial and fungal toxicity, and preliminary biodegradation studies of a series of L-phenylalanine-derived surface-active ionic liquids. Green Chem. 2019;21(7):1777-94.

47. Pretti C, Chiappe C, Pieraccini D, Gregori M, Abramo F, Monni G, et al. Acute toxicity of ionic liquids to the zebrafish (Danio rerio). Green Chem. 2006;8(3):238-40.

48. Ventura SPM, Silva FAE, Goncalves AMM, Pereira JL, Goncalves F, Coutinho JAP. Ecotoxicity analysis of cholinium-based ionic liquids to Vibrio fischeri marine bacteria. Ecotox Environ Safe. 2014;102:48-54.

49. Cieniecka-Roslonkiewicz A, Pernak J, Feder-Kubis J, Ramani A, Robertson AJ, Seddon KR. Synthesis, anti-microbial activities and anti-electrostatic properties of phosphonium-based ionic liquids. Green Chem. 2005;7(12):855-62.

50. Ventura SPM, Marques CS, Rosatella AA, Afonso CAM, Goncalves F, Coutinho JAP. Toxicity assessment of various ionic liquid families towards Vibrio fischeri marine bacteria. Ecotox Environ Safe. 2012;76:162-8.

51. Ventura SPM, de Barros RLF, Sintra T, Soares CMF, Lima AS, Coutinho JAP. Simple screening method to identify toxic/non-toxic ionic liquids: Agar diffusion test adaptation. Ecotox Environ Safe. 2012;83:55-62.

52. Wu SG, Li FF, Zeng LB, Wang CY, Yang YR, Tan ZJ. Assessment of the toxicity and biodegradation of amino acid-based ionic liquids. RSC Adv. 2019;9(18):10100-8.

53. Stolte S, Matzke M, Arning J, Boschen A, Pitner WR, Welz-Biermann U, et al. Effects of different head groups and functionalised side chains on the aquatic toxicity of ionic liquids. Green Chem. 2007;9(11):1170-9.

54. Mena IF, Diaz E, Palomar J, Rodriguez JJ, Mohedano AF. Cation and anion effect on the biodegradability and toxicity of imidazolium- and choline-based ionic liquids. Chemosphere. 2020;240:9.

55. Rahman M, O'Donnell JM, Brazel CS. Cytotoxicity of Plasticizers and Ionic Liquids Using Drosophila melanogaster S2 Cell Culture. Chem Eng Technol. 2011;34(3):429-38.

56. Egorova KS, Ananikov VP. Toxicity of Ionic Liquids: Eco(cyto)activity as Complicated, but Unavoidable Parameter for Task-Specific Optimization. ChemSusChem. 2014;7(2):336-60.

57. Chequer FMD, Venancio VP, Bianchi MLP, Antunes LMG. Genotoxic and mutagenic effects of erythrosine B, a xanthene food dye, on HepG2 cells. Food Chem Toxicol. 2012;50(10):3447-51.

58. Demirkol O, Gumusay OA, Cerit I. Effect of erythrosine and phloxine from xanthene food dyes on oxidative stress in Chinese hamster ovary cells. Food Sci Technol. 2020;40(4):1009-13.

59. Costa ACBP, Rasteiro VMC, Pereira CA, Rossoni RD, Junqueira JC, Jorge AOC. The effects of rose bengal- and erythrosine-mediated photodynamic therapy on Candida albicans. Mycoses. 2012;55(1):56-63.

60. Silva AF, Borges A, Freitas CF, Hioka N, Mikcha JMG, Simoes M. Antimicrobial Photodynamic Inactivation Mediated by Rose Bengal and Erythrosine Is Effective in the Control of Food-Related Bacteria in Planktonic and Biofilm States. Molecules. 2018;23(9):18.

61. Hayyan M, Looi CY, Hayyan A, Wong WF, Hashim MA. In Vitro and In Vivo Toxicity Profiling of Ammonium-Based Deep Eutectic Solvents. Plos One. 2015;10(2):18.

62. Wen Q, Chen JX, Tang YL, Wang J, Yang Z. Assessing the toxicity and biodegradability of deep eutectic solvents. Chemosphere. 2015;132:63-9.

63. Juneidi I, Hayyan M, Hashim MA. Evaluation of toxicity and biodegradability for cholinium-based deep eutectic solvents. RSC Adv. 2015;5(102):83636-47.

64. Juneidi I, Hayyan M, Ali OM. Toxicity profile of choline chloride-based deep eutectic solvents for fungi and Cyprinus carpio fish. Environ Sci Pollut Res. 2016;23(8):7648-59.

65. Hayyan M, Mbous YP, Looi CY, Wong WF, Hayyan A, Salleh Z, et al. Natural deep eutectic solvents: cytotoxic profile. SpringerPlus. 2016;5:12.

66. Halder AK, Natalia M, Cordeiro DS. Probing the Environmental Toxicity of Deep Eutectic Solvents and Their Components: An In Silico Modeling Approach. ACS Sustain Chem Eng. 2019;7(12):10649-60.

67. Macario IPE, Oliveira H, Menezes AC, Ventura SPM, Pereira JL, Goncalves AMM, et al. Cytotoxicity profiling of deep eutectic solvents to human skin cells. Sci Rep. 2019;9:9.

Chapter 8

Concluding remarks and future perspectives

8.1. Concluding remarks

The research presented in this dissertation is primarily focused on use of GUMBOS (and nanoGUMBOS) as optical probes and antibacterial agents. In this dissertation, a total of ten novel GUMBOS were strategically designed and synthesized via simple ion-exchange metathesis reactions with select cations. The simplicity of synthesis of these organic ionic materials allowed development of relatively low-cost and labor-efficient approaches for protein analyses (chapters 2–4). The possibility of designing GUMBOS for a targeted purpose, along with the ease of modulating their properties, motivated synthesis of ANS- and RB-based GUMBOS, which were further investigated as fluorescent probes for protein-membrane binding studies (chapter 5) and antibacterial agents (chapter 6), respectively. Toxic effects were also evaluated using human RBCs (chapter 6) and *S. cerevisiae* cells (chapter 7) to ensure a more sustainable development of this class of materials.

In Chapter 2, four EB-based GUMBOS were synthesized and evaluated for their ability to discriminate individual proteins and protein mixtures. Percentages of correct assignments varied from 86.5 to 100.0% depending on GUMBOS chemical structure and buffer pH. Best results were obtained using $[P_{4444}]_2[EB]$ and $[N_{4444}]_2[EB]$ at pH 6.0 after 5 min of incubation. Under optimized conditions, it was also possible to distinguish between mixtures containing different proportions of Alb and Mb (20% + 80%, 40% + 60%, 60% + 40%, and 80% + 20%). Evaluation of overall results suggested that it is not necessary to use an assembly of multiple EB-based probes to discriminate proteins, and that cationic tuning of EB can broaden its sensing capability beyond traditionally employed low pH values.

In Chapter 3, the abilities of $[P_{4444}]_2[EB]$ and $[N_{4444}]_2[EB]$ GUMBOS to distinguish serum and non-serum proteins at concentrations as low as 0.05 μg mL^{-1} were investigated. Although these two GUMBOS were determined to successfully discriminate proteins at 20 μg mL^{-1} (chapter 2), a range of concentrations is necessary to determine their potential for qualitative and quantitative analyses as changes in protein levels may help early diagnosis and allow prompt treatment. It was determined that $[P_{4444}]_2[EB]$ and $[N_{4444}]_2[EB]$ can discriminate proteins at concentrations lower than those described for other sensing systems (e.g., ≥ 5.0 μg mL^{-1}). Additionally, it was demonstrated that cation exchange can

expand the detection range to as low as 0.5 μg mL^{-1} (i.e., 3 times lower than that described for the parent dye).

In Chapter 4, $[P_{4444}]_2$[EB] was converted into nanoGUMBOS, and its potential for protein discrimination and quantification was examined. Sonication time and CD templating were investigated for impact on discrimination performance of $[P_{4444}]_2$[EB] nanoGUMBOS, with best results obtained for 5 min of sonication in the absence of CD template. Under these conditions, the synthesized nanoGUMBOS successfully distinguished proteins at concentrations lower than those reported in the literature (i.e., 2.0 μg mL^{-1}). Moreover, $[P_{4444}]_2$[EB] nanoGUMBOS was able to discriminate between protein mixtures of Lyz, Cyt c, and Hb and showed great promise for quantification of Alb. This nanoGUMBOS approach also involved relatively small volumes of reagents, which makes this strategy an attractive option for high-throughput applications. Ultimately, the results presented in chapters 2 to 4 support potential use of GUMBOS (and nanoGUMBOS) in combination with UV-Vis spectroscopy and chemometric tools for qualitative and quantitative analyses of proteins. Moreover, these proposed strategies offer several advantages as compared to conventional analytical methods, e.g. simplicity, rapidity, and cost-effectiveness. In fact, these GUMBOS (and nanoGUMBOS) approaches are label-free, require only 5 min of incubation, and avoid the use of expensive instrumentation.

In Chapter 5, the ANS anion was ion-paired with distinct cations (N_{4444}, N_{6666}, and P_{4444}), and the resulting GUMBOS were investigated as fluorescent probes for study of protein-membrane binding. The $[N_{4444}]$[ANS] and $[P_{4444}]$[ANS] GUMBOS were found to display improved optical properties and lipophilicity as compared to the parent dye, which demonstrates the potential of this GUMBOS strategy to fine-tune ANS properties. These findings can also provide relevant information for designing GUMBOS with ameliorated properties. Protein addition to membrane-bound probes resulted in distinct fluorescence responses, showing the impact of surface hydrophobicity of proteins on the binding process. Moreover, results suggested that proteins compete with GUMBOS for DMPC binding sites.

In Chapter 6, three novel GUMBOS were synthesized using RB anionic dye and distinct cationic antiseptics, and their potential use as antibacterial agents was examined. RB-based GUMBOS proved to be equally effective (or more effective) than the individual parent dye and cationic antiseptics as well as the unreacted mixtures of RB and cationic antiseptics towards *S. aureus* DSM 2569 and *E. faecalis*. Moreover, [CHX][RB] was determined to be active against Gram-negative *E. coli*, with a MIC that was 64 times lower than that of the parent dye and the corresponding unreacted mixture. This GUMBOS was also found to produce the lowest percentage of hemolysis (< 5%) among all tested compounds and mixtures, which suggests potential safety for clinical use in humans. Overall, the obtained results demonstrate the ability to strategically incorporate different biologically active

cations, making this strategy a promising tool for development of cost-effective alternatives to RB without traditional pitfalls.

In Chapter 7, an automated yeast-based spectrophotometric assay was developed for the first time. This assay was then applied to a set of GUMBOS, ILs, and DESs in order to assess its potential as a toxicity screening tool. Differences in IC_{50} values confirmed impact of chemical structure on the toxicity of each compound. For example, ILs containing pyridinium and ammonium cations or with methanesulfonate anion were determined to have a higher toxic effect on *S. cerevisiae* cells. GUMBOS and DESs were respectively found to be among the most and least toxic compounds. However, this apparent disadvantage of EB-based GUMBOS could serve as motivation for further studies as antimicrobial agents. Moreover, the obtained results may complement available toxicity data and guide the design of less harmful and more task-specific compounds. The proposed method further allows rigorous control of reaction conditions and a decrease in reagents consumption and effluents production.

8.2. Future perspectives

Although the studies presented in this dissertation are far from exhaustive, they can serve as a starting point for additional future research. EB-based GUMBOS and nanoGUMBOS showed great promise as optical probes for protein analyses (chapters 2–4), but more work could be done to elucidate the mechanism of protein discrimination. As part of future studies, it is also planned to extend application of these developed approaches to more complex proteins and real samples with challenging matrices (e.g., blood and urine). Another possible research direction is to study the effect of cation variation on nanoGUMBOS properties, and subsequently on their ability to discriminate and quantify protein analytes.

Following the work presented in Chapter 5, it would be of interest to study the membrane location of ANS-based GUMBOS, which can be performed by using fluorescence quenching with probes such as trimethylammonium-diphenylhexatriene (TMA-DPH). Additionally, liposome composition could be modified through use of lipid mixtures or incorporation of proteins to more closely resemble biological membranes. One future direction that could be explored is analyses of a broader panel of proteins, including membrane proteins.

Despite the great promise of [CHX][RB] as an antibacterial agent (chapter 6), it is important to elucidate its pharmacokinetics and pharmacodynamics through additional in vitro and in vivo studies. For example, membrane models capable of mimicking lipid composition of

bacterial cell membranes could be used to clarify the mechanism of action of this GUMBOS. It would also be important to evaluate the antibacterial efficacy of [CHX][RB] against clinical isolates of *E. coli* from patients resistant to standard antibiotic therapies and investigate bacterial resistance to this GUMBOS. Since *E. coli* is commonly found in wounds, [CHX][RB] GUMBOS could further be used topically as an alternative treatment option. Moreover, [CHX][RB] could be converted into nanoGUMBOS and incorporated into hydrogels to investigate topical antibacterial applications.

A possible future direction for work described in Chapter 7 is application of the developed automated yeast-based assay to a larger number of compounds in order to obtain a deeper understanding of structure-toxicity relationship, and establish cation and anion trends. It would also be of interest to exploit the antimicrobial properties of the tested EB-based GUMBOS and investigate their therapeutical potential.

Finally, all GUMBOS synthesized in this dissertation were obtained by combining a select anion (i.e., EB, ANS, or RB) with distinct cations, and changes in the properties of the parent dye were attributed to cationic exchange. To further confirm GUMBOS tunability it would be important to design, synthesize, and investigate GUMBOS derived from cationic compounds using anion variation.

Sustainable and task-specific (nano)GUMBOS for chemical and biological analysis

Ana Marta de Oliveira Azevedo

Faculdade de Farmácia